Characterisation of a new mobile absolute quantum gravimeter : application in groundwater storage monitoring

Anne-Karin Cooke

THÈSE POUR OBTENIR LE GRADE DE DOCTEUR DE L'UNIVERSITÉ DE MONTPELLIER

En Géosciences

École doctorale GAIA : Biodiversité, Agriculture, Alimentation, Environnement, Terre, Eau

Unité de recherche Géosciences Montpellier – UMR 5243

Characterisation of a new mobile absolute quantum gravimeter: Application in groundwater storage monitoring

Présentée par Anne-Karin COOKE
Le 30 Octobre 2020

Sous la direction de Cédric CHAMPOLLION

Devant le jury composé de

Cédric CHAMPOLLION, Maître de conferences, Géosciences Montpellier	Directeur de thèse
Stéphane MAZZOTTI, Professeur, Géosciences Montpellier	Examinateur
Sylvain BONVALOT, Directeur de recherche, IRD, GET Toulouse	Examinateur
Andreas GÜNTNER, Professor, GFZ, Potsdam University	Rapporteur
Majken Caroline LOOMS ZIBAR, Associate Professor, Department of Geosciences and Natural Resource Management, University of Copenhagen	Rapportrice

UNIVERSITÉ DE MONTPELLIER

Acknowledgements

There are numerous people that deserve my uttermost gratitude. It is not possible to name everyone who contributed to this PhD thesis, but I have to start somewhere: First and foremost, I want to thank Cédric Champollion for the supervision, support and inspiration! In these three years, there was always an open space to think aloud, for discussion, the exchange of ideas, and fair communication. I am grateful for the trust and freedom. Then, I'd like to thank Nicolas Le Moigne for the technical support, advice, and critical thinking. I am grateful for all the inspiring discussions I had at Muquans: It was a pleasure to work with Camille Janvier and Pierre Vermeulen. I am impressed by the rigorous love for detail. Furthermore, my thanks go to Bruno Desruelle, Laura Antoni-Micollier, and Vincent Ménoret. Needless to say, everyone, I encountered at Muquans deserves my gratitude. I could learn a lot from everyone I met at Muquans and at Géosciences Montpellier.

Also, I'd like to thank Sébastien Merlet for the valuable input and critical view on the planning of experiments and feedback on the paper. I furthermore want to thank everyone else in my comité de suivi, Séverin Pistre, Jean Chèry, and Benoit Ildefonse, for the fruitful discussions. On other occasions, I had the chance to exchange thoughts on my work with Olivier Francis, Philippe Jousset, Marvin Reich, and many others.

In the ITN Enigma, I had the unique opportunity to meet many incredible researchers, in the network itself, the industrial partners, and the advisory board. Special thanks go to the aspiring, multicultural, and fun bunch of ESRs: We were a great team!

I am grateful for all the enriching experiences with people I met in Montpellier and Bordeaux: I am not going to name all the fellow PhD students, post-docs, senior researchers and technical staff I had the pleasure to interact with. Also at the Enigma summer school, at conferences, in seminars - the list is endless.

And I want to thank all my dear friends in France and around the world that accompanied me, old friends, that stayed by my side and new friends who came into my life during these three years.

Last but not least I want to express my tremendous gratitude towards my partner and my family, whose support and constant belief in me has been amazing. I am truly blessed to have you in my life!

All measurement presented here are from the Larzac observatory hosted by OSU OREME (http://www.oreme.org) and SNO H+ (http://hplus.ore.fr/). Larzac observatory and instrumentation are mainly funded by the CNRS INSU, ANR, Montpellier University, OZCAR, RESIF and Occitanie region.

ENIGMA ITN has received funding from European Union's Horizon 2020 research and innovation programme under the Marie Sklodowska-Curie Grant Agreement N°722028.

Synthesis

Quantum gravimeters provide the possibility of continuous, high-frequency absolute gravity monitoring while remaining user-friendly and transportable. This thesis assessed high precision performance measures of the first commercial absolute quantum gravimeters AQG#A01 and AQG#B01 developed by Muquans. This was carried out in comparison with high precision absolute and relative gravimeters and additional geophysical and environmental data, in controlled conditions and experiments in view of future deployment in field conditions. Both AQG devices allow stable measurements of g of several weeks. Significant drifts in time have not been observed. The two instruments have been transported and re-installed several times between sites and had been successfully applied in different conditions. The sensitivity of the AQG#A01 is better than 10 nm·s^{-2} after 24 h, which the AQG#B01 achieves after only one hour in a calm environment. For noisier environments, the sensitivity after one hour of the AQG#B01 is 20 to 30 nm·s^{-2}. The repeatability of the AQG#B01 is reported as better than 50 nm·s^{-2}. Changes of instrument tilt and external temperature (20 - 30 °C) and combination of both did not influence the measurement of gravitational attraction. These results were also confirmed during two weeks of acquisition in an urban garage during which the measurement of g remained unaffected by fast temperature changes. A rainfall event at the Larzac geodetic observatory caused a gravity increase of 100 nm·s^{-2} in December 2019, which was detected with the AQG#B01 in agreement with the superconducting relative gravimeter (GWR, iGrav#002) and corresponding Bouguer slab approximation. The potential gain in precision and time saved makes the AQG#B01 a promising instrument for e.g. large-scale gravity mapping. Such studies were formerly only feasible using a relative gravimeter that requires repeated acquisition loops and a reference absolute gravimeter for drift corrections. The AQG#B01 can be used without a reference instrument: It provides stable, repeatable measurements of absolute gravity while being transportable and user-friendly. Continuous monitoring at high precision allows for studies of high temporal resolution at different scales. The AQG#B01 would especially be suited for the monitoring of transient mass changes at duration (e.g. a few weeks) that are too short to justify the effort of installing a stationary, superconducting gravimeter. To reliably detect transient phenomena, a drift-free and repeatable determination of g is required for which e.g. spring relative gravimeters are not suitable. Some aspects are still under investigations, such as the potential effect of the sensor head's orientation, the Coriolis effect, on the measurement of g and the assessment of the accuracy regarding differences between the AQG#B01 and the absolute gravimeter (Micro-g LaCoste, FG5#228) that is used as a reference. Time-lapse ground-based gravimetry is increasingly applied in subsurface hydrology to monitor water storage dynamics. The complementary spatial sensitivities of gravity and vertical gravity gradients (VGG) can be used to deduct the spatial characteristics of subsurface mass changes. VGG were estimated from one year of monthly relative gravity surveys on three different heights on three locations inside the Larzac observatory. The repeatability of VGG estimations was found to be better than 23 $\pm$ 9 E. The study suggests the influence of heterogeneous soil saturation patterns on VGG and the potential of differential VGG monitoring in resolving spatial mass distributions. Observed time-lapse, differential VGG changes provided additional constraints to the subsurface model. Combined VGG and gravity monitoring in hydrogeology is a promising new approach for hydrogeophysical subsurface imaging, which could find practical application in gravity monitoring during hydraulic aquifer testing.

Contents

List of Figures

List of Tables

Résumé

La gravimétrie est l'étude des variations spatiales et temporelles du champ de gravité terrestre, ces variations pouvant être liées à des changements de distribution de masse étudiés dans diverses disciplines des sciences de la Terre. Les applications incluent la géodésie et la géodynamique à grande échelle comme la tectonique et la subsidence lent (Camp et al. (2011); Hwang et al. (2010)) ainsi que incluant la déformation de la croûte et le soulèvement isostatique glaciaire (Mazzotti et al. (2011); Olsson et al. (2019)). La gravimétrie s'est par ailleurs avérée être un outil d'évaluation des aléas naturels tels que le suivi de l'activité volcanique (Bonvalot, Diament, and Gabalda (1998), Carbone et al. (2017)), la cartographie des vides souterrains ou l'étude des tremblements de terre (Imanishi (2004)). Les applications dans le domaine de l'énergie et des ressources comprennent les champs géothermiques (Pearson-Grant, Franz, and Clearwater (2018)), les réservoirs de stockage de CO_2 (Sugihara et al. (2017)) ou les installations de recharge artificielle des eaux souterraines (Kennedy, Ferré, and Creutzfeldt (2016)). Les méthodes gravimétriques trouvent en outre une application dans le contexte de l'exploration et de la prospection pétrolières et minérales (par exemple Ferguson et al. (2007); Hinze, Von Frese, and Saad (2013)). En hydrologie, la mesure de la gravité offre des possibilités de surveiller la dynamique de stockage des ressources en eaux souterraines locales et à l'échelle du paysage (par exemple Creutzfeldt et al. (2008); Creutzfeldt et al. (2010); Jacob et al. (2010); Hector et al. (2014); Hector et al. (2015); Fores, Champollion, Moigne, Bayer, et al. (2016); Güntner et al. (2017)) et même les taux d'évapotranspiration (Van Camp et al. (2016)). Les applications et les domaines de recherche sur la gravité active ont été largement examinés par Crossley, Hinderer, and Riccardi (2013) et Camp et al. (2017).

Les gravimètres sont des appareils qui mesurent l'attraction gravitationnelle g à la surface de la Terre. Les gravimètres peuvent être caractérisés par leurs performances de mesure. La répétabilité d'une mesure fait référence à l'accord entre des mesures répétées et est généralement évaluée en effectuant plusieurs changements d'emplacement répétés entre les mesures. La sensibilité (ou précision) d'un gravimètre est une incertitude relative et se réfère au plus petit changement d'accélération gravitationnelle que le gravimètre est capable de détecter. Nous parlons de stabilité comme de l'absence de dérive instrumentale significative dans le temps ou de bruit corrélé. La précision d'une mesure de gravité décrit dans quelle mesure elle peut être considérée comme correcte en termes absolus et fait référence à l'incertitude d'une mesure par rapport à un étalon absolu (Niebauer (2015)).

Les gravimètres relatifs détectent l'attraction gravitationnelle indirectement en mesurant la force nécessaire pour annuler la gravitation en stabilisant une masse d'essai et sont utilisés pour surveiller les changements de gravité relative dans le temps ou dans l'espace. Ces dispositifs

montrent des dérives qui peuvent devenir importantes en quelques jours (gravimètres à ressort) ou quelques mois (gravimètres supraconducteurs) (Camp et al. (2017)). Les gravimètres relatifs nécessitent un étalonnage régulier avec des gravimètres absolus comme stations de référence et des mesures répétées en boucle ou absolues pour éliminer les dérives dans les levés de terrain (Hector and Hinderer (2016); Kennedy and Ferré (2015)). Ils peuvent être sensibles aux changements de température (par exemple avec un gravimètre à ressort relatif comme dans Fores, Champollion, Moigne, and Chery (2016)). Les gravimètres relatifs les plus sensibles sont les gravimètres supraconducteurs et atteignent une haute précision d'environ 0,1 $nm.s^{-2}$ tout en mesurant en continu à une fréquence d'échantillonnage de 1 Hz. Ils sont basés sur la lévitation magnétique au lieu d'un ressort mécanique (Hinderer, Crossley, and Warburton (2015)).

Les gravimètres absolus estiment la norme de l'accélération gravitationnelle g en chute libre verticale dans le vide (Niebauer et al. (1995)). Les gravimètres absolus sont principalement basés sur un rétroréflecteur cubique en chute libre dans une chambre à vide avec une incertitude instrumentale de l'ordre de quelques dizaines de $nm.s^{-2}$ (Niebauer (2015)). Les gravimètres absolus actuellement disponibles ne sont pas adaptés à une surveillance continue en raison de pièces mécaniques à durée de vie limitée. Cela limite le nombre d'expériences de chute libre et nécessite une maintenance fréquente des instruments. Leur fonctionnement nécessite généralement un niveau de compétence technique élevé et ils ne peuvent être mis en oeuvre par un non-spécialiste.

La détection quantique offre de nouvelles possibilités pour la mesure de l'inertie et le développement de gravimètres quantiques absolus. Le principe général de mesure d'un gravimètre quantique absolu (AQG) est celui de l'interférométrie matière-ondes ((Peters, Chung, and Chu (2001)); Merlet et al. (2010)). Les atomes peuvent être exploités comme masses de test ainsi que comme outil pour mesurer le chemin parcouru afin de détecter la gravité (Peters, Chung, and Chu (2001)). Réalisation de laboratoire, le gravimètre à atome froid (CAG) développé au LNE-SYRTE dans le cadre de la balance Kibble a démontré des performances inédites tant en sensibilité qu'en précision. Il a depuis participé à International Comparisons of Absolute Gravimeters (ICAG) montrant une meilleure sensibilité à court terme que les gravimètres absolus et un budget de précision rigoureusement quantifié (Jiang et al. (2012); Francis et al. (2013); Gillot et al. (2014)). De nombreux instituts de recherche et entreprises privées travaillent sur différentes réalisations de gravimètres à atomes froids (Geiger et al. (2020)) comme GAIN (Allemagne; Hauth et al. (2013)) ou WAG-H5-1 (Chine; Huang et al. (2019)). Une manipulation robuste des atomes, étape cruciale vers la réalisation d'un instrument de terrain, a été réalisée par piégeage et détection d'atomes sans qu'il soit nécessaire d'aligner plusieurs composants optiques. Ceci a été réalisé grâce à un seul réflecteur pyramidal creux, permettant

un fonctionnement avec un seul faisceau optique, et conduisant à une mise en œuvre compacte (après Bodart et al. (2010)). Un examen exhaustif de l'état de l'art des capteurs à inertie gravitationnelle à atome froid, des différents types de capteurs, des applications et des différences de performances a été fourni par Geiger et al. (2020). Le premier gravimètre disponible dans le commerce (AQG#A) basé sur cette technologie a été développé par Muquans. La conception compacte a permis un instrument mobile qui ne nécessite pas de formation spéciale pour mise en oeuvre. Les progrès de la correction à la volée des effets externes ont contribué à la création d'un instrument compact et stable de haute sensibilité mesurant à une fréquence d'échantillonnage de 2 Hz. Une stabilité meilleure que 10 $nm.s^{-2}$ pendant un mois de fonctionnement a été observée, et la répétabilité de l'instrument a été préalablement quantifiée pour être du même ordre de grandeur (Ménoret et al. (2018)) pendant 24 h.

Conclusion

L'objectif principal de cette thèse était l'évaluation des mesures de performance de haute précision des gravimètres quantiques absolus en comparaison avec des gravimètres absolus et relatifs de haute précision et des données géophysiques et environnementales complémentaires. Deux gravimètres quantiques absolus, les Muquans AQG#A01 et AQG#B01, ont été évalués en se concentrant sur des mesures de performance importantes: précision, sensibilité, stabilité et répétabilité. Des mesures de plusieurs semaines ont été réalisées à trois endroits différents: l'observatoire du Larzac, Géosciences Montpellier et Trappes (près de Paris).

La characterisation de l'AQG#B01 a été réalisé dans des conditions contrôlées et via de nombreuses expériences en vue d'un déploiement futur sur le terrain. Les principaux objectifs de cette étude sont d'évaluer la stabilité et la répétabilité du premier gravimètre quantique absolu de terrain en vue d'un déploiement futur en tant que gravimètre de terrain pour des applications hydrogéophysiques. L'évaluation se fait lors de mesures et d'expériences en continu (impact d'orientation ou de transport) en comparaison avec des gravimètres absolus et relatifs. La sensibilité aux changements d'inclinaison et de température ainsi que l'interaction entre les deux sont d'une importance cruciale pour évaluer l'aptitude de l'AQG#B01 en tant qu'instrument de terrain. Sa sensibilité aux variations de température ambiante est évaluée en effectuant des tests dans un environnement contrôlé. Enfin, des recommandations sont présentées pour l'utilisation future de l'AQG#B01 dans des expériences sur le terrain.

De l'expérience de ces expériences, on peut conclure ce qui suit:

- Un arrêt, un démontage, un transport et un redémarrage complet réussis ont été obtenus avec les deux instruments lors de plusieurs déplacements
- Mesure sans dérive de g sur plusieurs semaines avec les deux appareils AQG

AQG-A01

En complément de l'étude de Ménoret et al. (2018), les résultats supplémentaires suivants ont été obtenus pour l'AQG#A01:

- Dans un environnement à faible bruit (Larzac), l'AQG-A01 atteint une sensibilité inférieure à 10 nm·s^{-2} après 24 h d'intégration de données
- La sensibilité et la stabilité montrent une forte variabilité due à des oscillations subjournalières
- Ces oscillations sont susceptibles d'être liées à l'instabilité laser, mais la corrélation n'est pas systématiquement reproductible sur tous les sites d'étude
- Estimation du gradient de gravité vertical (VGG) basé sur des mesures sur trépieds de deux hauteurs différentes avec l'AQG-A01 moins précis que l'estimation VGG avec un gravimètre relatif CG6

AQG-B01

Sur la base de l'expérience acquise avec l'AQG#A01, la version de suivi sur le terrain (AQG#B01) comprend des améliorations considérables en termes de sensibilité et de stabilité. La caractérisation de l'AQG#B01 pour les applications sur le terrain s'est concentrée sur les conditions potentielles du terrain ayant un impact sur la température, l'inclinaison et l'orientation de la tête du capteur.

Les principales conclusions sont les suivantes:

- Dans les environnements à faible bruit (observatoire du Larzac), l'AQG-B01 a montré une sensibilité de 10 nm·s^{-2} après 1 h
- La sensibilité après 24 h d'intégration des données est proche de celle de l'iGrav-002 à l'observatoire du Larzac
- Dans les environnements bruyants (Montpellier), la sensibilité est comprise entre 20 et 30 nm·s^{-2} après 1 h
- La répétabilité a été quantifiée à 3 nm·s^{-2} avec un écart type de 25 nm·s^{-2}
- Surveillance des changements de masse hydrologique: Accord entre les résidus gravimétriques mesurés avec l'iGrav et l'AQG-B01
- Fonctionnement fiable dans des conditions contrôlées avec une plage de température extérieure comprise entre 20 et 30 ° C sur plusieurs semaines

- Aucun effet d'une interaction potentielle entre la température et l'inclinaison de la tête du capteur sur la mesure de g observée
- Fonctionnement fiable pendant deux semaines dans un garage, aucun impact observé des changements rapides de température, des niveaux de bruit accrus ou des mouvements d'air lors de l'ouverture des portes de garage
- Montpellier: Δg entre AQG-B01 et FG5-228 était de 44 nm·s^{-2} avec un écart type de 66 nm·s^{-2} ($g_{AQG-B} < g_{FG5}$)
- Larzac: Δg entre AQG-B01 et FG5-228 était de 110 nm·s^{-2} avec un écart type de 31 nm·s^{-2} ($g_{AQG-B} > g_{FG5}$)

Prochaines étapes proposées

Des informations pratiques pourraient être tirées de la caractérisation des instruments présentée dans cette thèse. Cependant, l'étude n'est pas exhaustive, car l'évaluation du budget d'incertitude d'un gravimètre reste une tâche complexe. Dans un proche avenir, les tests suivants sont importants:

- L'impact de l'orientation de la tête du capteur (effet Coriolis) sur la mesure de g doit être approfondi
- Le suivi de plusieurs mois pour évaluer la stabilité à long terme
- La répétabilité et la transportabilité doivent être répétées: déplacements supplémentaires entre Montpellier et le Larzac (et autres lieux)

Études appliquées potentielles

Le gain potentiel de précision et de gain de temps fait de l'AQG#B01 un instrument prometteur pour, par exemple, la cartographie gravimétrique à grande échelle. Ces études n'étaient auparavant réalisables qu'en utilisant un gravimètre relatif qui nécessite des boucles d'acquisition répétées et un gravimètre absolu de référence pour les corrections de dérive. L'AQG#B01 peut être utilisé sans instrument de référence: il fournit des mesures stables et reproductibles de la gravité absolue tout en étant transportable et ergonomique. Surveillance temporelle des changements de masse, par exemple des signaux hydrogéophysiques, sur d'autres sites, sont envisagés. La surveillance continue à haute précision permet des études de haute résolution temporelle à différentes échelles. L'AQG#B01 serait particulièrement adapté pour la surveillance des changements de masse transitoires à des durées (par exemple quelques semaines) trop courtes pour justifier l'effort d'installation d'un gravimètre supraconducteur. Pour détecter de manière fiable les phénomènes transitoires, une détermination sans dérive et répétable de g est nécessaire pour

laquelle les gravimètres à ressort ne conviennent pas.

Surveillance des gradients verticaux de gravité

Lier les caractéristiques spatiales et temporelles des observations gravimétriques aux phénomènes et caractéristiques géophysiques est au cœur de la discipline. La cartographie des anomalies de gravité spatiale peut être utilisée pour détecter les contrastes de densité du sous-sol tels que déployés dans l'exploration et la prospection pétrolières et minérales (par exemple Ferguson et al. (2007); Hinze, Von Frese, and Saad (2013)) ou pour la détection de dépressions souterraines (Jacob et al. (2018)). Les résidus temporels subsistent après correction des séries chronologiques gravimétriques pour les effets connus tels que les signaux de marée et les variations de pression atmosphérique. Ces résidus peuvent être attribués à des changements de masse locaux (Crossley, Hinderer, and Riccardi (2013); Camp et al. (2017)).

Les effets hydrologiques globaux et locaux de la gravité sur les observations gravimétriques sont causés par la déformation de la croûte et l'attraction newtonienne des masses d'eau (Llubes et al. (2004); Harnisch and Harnisch (2006); Linage, Hinderer, and Rogister (2007); Neumeyer et al. (2008); Longuevergne et al. (2009), Wziontek et al. (2009)). Les signaux hydrologiques dans les données gravimétriques au sol se produisent principalement à des échelles de temps et de longueur intermédiaires (heures en années, mètres en kilomètres). De plus, ils peuvent être fortement dépendants du site et complexes à déterminer (Harnisch and Harnisch (2006)).

L'hydrogravimétrie comme l'une des méthodes d'exploration hydrogéophysique émergentes fournit une approche spatialement intégrative et non invasive pour l'imagerie souterraine. La principale caractéristique des mesures gravimétriques est leur nature intégrant la profondeur qui comprend les contributions des changements de masse locaux et distants. Cela a trouvé son application dans les bilans massiques contraignants pour les estimations du stockage total de l'eau (TWS). Il facilite la caractérisation des écoulements souterrains dans les aquifères hétérogènes où les mesures ponctuelles hydrologiques classiques manquent de représentativité (Binley et al. (2015)). Par exemple, dans les karsts fortement hétérogènes, les niveaux d'eau provenant de forages uniques peuvent ne pas être représentatifs de la dynamique globale de la teneur en eau souterraine (Hartmann et al. (2014)). La gravimétrie au sol offre un outil important pour détecter les changements de masse locaux qui sont trop faibles pour la gravimétrie spatiale à grande échelle mais trop éloignés ou répartis dans l'espace pour être représentés dans des mesures de points hydrologiques, comme le montrent des études hydrogravimétriques récentes dans les régions karstiques (Mazzilli et al. (2012); Mouyen et al. (2019)).

La force de la gravimétrie est à la fois son principal inconvénient en raison de la non-unicité des solutions d'inversion de gravité et de la difficulté à résoudre la distribution spatiale des

masses telles que la déduction de la profondeur et les informations directionnelles. Malgré ces défis, la séparation et l'identification des signaux peuvent être obtenues par l'inclusion d'autres techniques géophysiques, géodésiques ou hydrologiques et l'analyse de la signature temporelle du changement de gravité. Cette hydrogravimétrie hybride accélérée est ainsi capable de contraindre et de quantifier les changements de stockage de l'eau (WSC) et de séparer les zones contributives et les processus impliqués (Naujoks et al. (2007); Naujoks et al. (2010)), tels que les précipitations (Meurers, Camp, and Petermans (2007), Delobbe et al. (2019)), l'humidité du sol (Krause et al. (2009)), l'évapotranspiration (Van Camp et al. (2016)) et le ruissellement et les rejets de surface (Lampitelli and Francis (2010); Creutzfeldt et al. (2013), Piccolroaz et al. (2015)), les changements de stockage de l'eau du captage (Hasan et al. (2008)) Hector et al. (2014), Hector et al. (2015); Güntner et al. (2017)) ou pour surveiller les installations de recharge artificielle des eaux souterraines (Davis, Li, and Batzle (2008); Kennedy, Ferré, and Creutzfeldt (2016)).

L'effet gravitationnel des changements de masse d'eau (par exemple un événement de précipitation) est généralement simplifié sous la forme d'une dalle homogène et infinie (plaque de Bouguer) d'une colonne d'eau. Cette hypothèse peut ne pas s'appliquer dans les aquifères hétérogènes (par exemple les karsts). Le signal de gravité intégrant la profondeur n'inclut pas d'informations sur la distribution spatiale des masses. Contrairement aux mesures de l'intensité du champ gravitationnel, le gradient de gravité vertical (VGG) est sensible aux changements de masse latéraux. Les sensibilités spatiales complémentaires de la gravité et des VGG peuvent être utilisées pour déduire conjointement les caractéristiques spatiales des changements de masse dans le sous-sol. Dans cette étude, nous avons évalué la précision de la surveillance des VGG à l'aide de gravimètres de terrain relatifs placés sur des trépieds dans un cadre d'observatoire contrôlé et avons relié nos résultats au contexte hydrogéologique du site d'étude. Les VGG ont été estimés à partir de relevés mensuels de gravité relative sur trépieds de différentes hauteurs sur trois piliers en béton de l'observatoire géodésique du Larzac dans le sud de la France, entre décembre 2017 et novembre 2018. La répétabilité des estimations VGG basées sur cette méthode a été estimée à 23 $\pm$ 9 E. Des changements de VGG de $\sim$ 80 Eotvos (1 E = $10^{-9}\mathrm{s}^{-2}$) en un an sur l'un des emplacements de mesure ont été observés. En l'absence d'autres changements de masse, les changements de VGG étaient liés aux sources possibles de changement de stockage d'eau à proximité. Premièrement, l'impact de l'effet parapluie (protection du bâtiment contre les précipitations) a été testé comme une source potentielle de changements VGG et s'est avéré limité à quelques E. Deuxièmement, les distributions possibles de porosité souterraine ont été générées dans la simulation stochastique géostatistique et sélectionnées pour obéissez aux changements observés de gravité et de VGG ainsi qu'aux différences entre les emplacements de mesure. Les

données conjointes de gravité et de gradient de gravité ont réduit la gamme de simulations cohérente avec les données. Nous discutons en outre du potentiel des mesures de VGG comme une nouvelle technique potentielle pour résoudre spatialement les changements de masse dans un contexte hydrogéologique.

L'estimation du gradient de gravité vertical basée sur des boucles répétées réalisées avec un gravimètre à ressort relatif sur trépied est une méthode longue qui ne permet pas une résolution temporelle élevée. La mesure prend environ une journée de travail et un post-traitement approfondi est nécessaire pour une correction adéquate des dérives et autres effets. Nous avons quantifié la répétabilité des estimations VGG à 23 $\pm$ 9 E. Pour la différence de hauteur de 117,5 cm entre les mesures, 20 E se réfère à 23,5 nm·s^{-2} erreur.

Les simulations géostatistiques stochastiques réalisées montrent d'éventuelles distributions spatiales des propriétés souterraines qui conduiraient à des différences de VGG entre les piliers de plusieurs dizaines de E tout en limitant les variations de gravité à quelques dizaines de nm·s^{-2}. Nous avons supposé une plage de porosité en cohérence avec les diagraphies de forage et les résultats d'inversion des études hydrogéophysiques précédentes. Cette étude a montré que la surveillance des VGG est sensible à une hétérogénéité souterraine locale qui autrement ne serait pas visible dans la série gravimétrique seule. Les gradients de gravité permettent d'accéder à l'hétérogénéité de la surface et à l'emplacement des changements de masse. Contrairement aux mesures gravimétriques uniques qui représentent des mesures intégratives de profondeur, les gradients de gravité donnent accès à des informations au-delà des limites de l'approximation de plaque de Bouguer classiquement utilisée en hydrogravimétrie. Nous recommandons, cependant, d'affiner d'abord les paramètres de simulation sur la base de variogramme directionnel et d'inversion avec des données fournies par d'autres méthodes d'imagerie géophysique. Afin de mieux comprendre les processus souterrains du site du Larzac qui montrent potentiellement une influence détectable sur les estimations VGG, nous suggérons une approche conjointe de surveillance supplémentaire de la teneur en eau du sol, de simulations stochastiques affinées et de développement de modèles hydrologiques. Des études répétées de tomographie de résistivité électrique ajouteraient des informations sur les changements de saturation saisonniers à partir desquels d'autres modèles de variogramme directionnel pourraient être ajustés, ce qui limiterait les simulations géostatistiques et augmenterait le réalisme hydrogéologique. La dynamique du stockage de l'eau karstique et la distribution de la porosité ont été résolues par une surveillance ERT à long terme (Watlet et al. (2018)). Des profils ERT supplémentaires à différents angles du bâtiment pourraient aider à identifier l'anisotropie locale en appliquant l'ajustement de variogramme directionnel (Carrière et al. (2013)).

Impact du gradient de gravité vertical sur la comparaison gravimétrique

L'observatoire du Larzac offre des conditions favorables pour la surveillance gravimétrique en raison de l'environnement peu bruyant, de la température contrôlée et d'un suivi hydrogéophysique supplémentaire sur le site. Cependant, son aptitude à la comparaison gravimétrique en termes de précision est limitée par la variabilité spatiale et temporelle du champ gravitationnel local. Les piliers en béton dépassent de 0,5 m de la surface du sol, provoquant des gradients de gravité verticaux non linéaires (courbure) dans les 2 premiers mètres au-dessus de la surface du pilier. Les différences entre les courbures observées et simulées causées par les piliers en béton suggèrent l'impact d'une hétérogénéité souterraine supplémentaire. La cartographie précise de la courbure est limitée par la sensibilité de la méthode d'estimation VGG disponible. Il est recommandé d'effectuer des comparaisons gravimétriques dans les observatoires où les piliers sont idéalement intégrés dans une plaque de béton plus grande et plate. Des mesures avec plusieurs déplacements entre les piliers de l'observatoire du Larzac sont recommandées. De plus, l'observatoire du Larzac est exposé aux changements d'humidité du sol dans la zone non saturée environnante. Leur impact sur les mesures de gravité en raison de l'incertitude liée à la correction VGG peut être potentiellement important. En un mot, le suivi des VGG peut être résumé dans les points suivants.

Variations de VGG temporelles observées

- Un an de levés gravimétriques mensuels réalisés avec un gravimètre relatif CG5 sur trois hauteurs différentes sur trois piliers
- Répétabilité de l'estimation VGG quantifiée à 23 $\pm$ 9 E
- 80 E changement observé sur le pilier du point de mesure p_3
- Les VGG sur les piliers p_1 et p_2 ne montrent pas de tendances significatives
- Plusieurs dizaines d'E de bruit VGG time-lapse peuvent conduire à des décalages de gravité non négligeables lors de la comparaison de gravimètres

Surveillance différentielle VGG comme méthode hydrogéophysique

Les changements observés de VGG ont été étudiés à la recherche du changement de masse correspondant.

- Impact simulé de l'effet parapluie (zone de construction protégeant le sous-sol des précipitations) sur le VGG de l'ordre de quelques E
- L'impact de l'hétérogénéité du sous-sol a été étudié à l'aide d'une simulation géostatistique stochastique
- Les données combinées de gravité et de différence VGG ont considérablement réduit le

nombre de réalisations souterraines simulées appropriées

- Aucune corrélation significative entre les propriétés simulées du sous-sol et les structures géologiques existantes (cavité, orientation de la fracture)
- Effet de la topographie locale sur VGG estimé négligeable
- Des simulations simplifiées concernant les variations de stockage de l'eau à l'emplacement de deux forages à 20 m de profondeur montrent des changements de gravité et de VGG dans l'ordre de grandeur des changements observés

Prochaines étapes

- Simulations raffinées avec des paramètres d'anisotropie mieux contraints, basées sur des mesures de saturation supplémentaires
- Recherches complémentaires sur l'impact de la dynamique temporelle des stockages souterrains
- Potentiel d'estimation VGG avec AQG-B: surveillance plus efficace, sensibilité attendue 21 E et répétabilité de 6,3 $\pm$ 53 E

Un autre objectif de cette thèse était le développement de nouvelles méthodes de gravimétrie dans le contexte de l'hydrologie. Dans cette thèse, la surveillance time-lapse des VGG a été testée à l'aide de gravimètres relatifs disponibles. La précision et les limites attendues de la méthode ont été évaluées. L'étude suggère l'influence de l'hétérogénéité dans la saturation des sols sur les VGG. Les résultats discutés dans cette thèse font allusion au potentiel de la surveillance différentielle des VGG dans la résolution des distributions spatiales de masse en hydrogéologie.

1 General objectives and outline

The hydrological cycle drives the transport and transformation of water and its compounds in the atmosphere, geosphere, and biosphere where they are susceptible to physical, biological, geochemical interactions. These processes take place in an area referred to as the critical zone, a layer spanning the Earth that comprises the upper atmosphere to deep aquifers, functioning as habitat, and providing life-sustaining resources. In the Anthropocene, the critical zone is increasingly shaped and controlled by human activity. The majority of yearly available freshwater in surface and groundwater is consumed by humanity (Vörösmarty et al. (2005)). Economic development, population growth, and increased consumption lead to a global water demand growing at a rate of about 1% annually. Many regions worldwide are classified as water-stressed due to over-exploitation of freshwater resources. Climate change adds further uncertainty and erratic nature to water supply due to shifts in the seasonality of global water distribution patterns. Groundwater as the largest freshwater reservoir is a resource of increasing importance as overexploitation of surface water sources fuels a shift towards enhanced groundwater use. Complex interactions between increasing world-wide groundwater extraction and climate change effects put further pressure on water supply. Surface water availability declines due to increasing precipitation variability which leads to changes in groundwater recharge rates (UN (2020); Green (2016)). Groundwater extraction for crop irrigation is on the rise. Global food security and ecosystem functioning are therefore increasingly dependent on the responsible handling of subsurface water resources. Successful sustainable groundwater management requires a precise understanding of water storage dynamics. The feasibility of utilization plans is tested in model experiments that are developed on the basis of observations. Data and model results are used to identify subsurface structures and key processes and to quantify the current and to predict future states of the resource. Groundwater systems are complex systems. Sedimentation, deformation, pedogenesis, and other processes over various time-scales have shaped heterogeneous and often variably saturated soils, sediments, and bedrock compartments. Aquifer hydraulic property heterogeneity ranges from features of pore-scale media, to fracture networks and the connectivity of aquifer systems in larger catchments.

The correct representation of these heterogeneous systems in hydrological models remains challenging. One important step forward is innovation in the field of subsurface monitoring to inform model development and to increase realism. In the last decades, numerous geophysical methods found applications in hydrology, and new sensing techniques emerged, giving rise to the new field of hydrogeophysics. The link between a measurable, physical unit (e.g. electric resistivity) and information on subsurface properties (e.g. water content) are described as petrophysical or hydrogeological relationships. Hydrogeophysical methods range from ground-penetrating radar

(GPR), electromagnetic induction (EMI), and electric resistivity tomography (ERT), seismic refraction, nuclear magnetic resonance (NMR) to direct current (DC) resistivity, induced polarization (IP), self-potential (SP). For a comprehensive and extensive review refer to Binley et al. (2015). The development of new joint utilisations of existing geophysical monitoring methods in the context of hydrogeology goes hand in hand with recent advances in imaging, simulation, and interpretation thanks to improved algorithms, computational power, and data accessibility.

In the context of quantitative hydrology, total water storage, and storage change are the variables of interest. Hydrological storage can be defined as the water volume stored within a catchment. Storage and its distribution among different reservoirs (such as groundwater, soil moisture, or snow) represent meaningful state variables of the hydrological system which is further discussed as a catchment comparison metric. However, the heterogeneity of storage at different scales make this variable the most difficult to accurately quantify. A further distinction can be made between total storage and active storage, the latter refers to the storage volumes that retain and release water. Classical hydrological methods are often mainly point-measurements with limited spatial representativeness. Another challenge lies in bridging between spatial and temporal scales, oftentimes governed by different hydrological processes and interactions between storages (McNamara et al. (2011)).

Water storage can be characterised by the involved masses which can be detected due to their influence on the Earth's gravity field. The interest in the determination of the gravitational attraction experienced on the surface of the Earth is rooted in fundamental physics and Earth exploration and gave rise to the discipline of gravimetry. The monitoring of gravity changes caused by mass changes is a non-invasive, integrated way that offers advantages for hydrology. Especially the potential of constraining the estimation of total water storage is of particular interest. The relatively young field of hydrogravimetry has meanwhile developed into an aspiring branch of hydrogeophysics.

Progress in gravimetry is largely based on the improvement of measuring methods, this includes the development of new devices as well as their deployment in unprecedented applications.

This doctoral thesis focuses on the emergence of new technologies in absolute gravimetry using new quantum sensing methods. Quantum gravimetry has become an innovative industrial development environment and a very active field of research, bringing together new technologies and experts from various disciplines. Three main directions in this field can be identified as (Geiger et al. (2020)):

1. **Performance improvements in terms of instrument sensitivity and accuracy.**
2. **Design and development of gravimeter architecture towards increased porta-**

bility, compactness, ease-of-use and reduced production costs.

3. **Field tests and expansion of field applications.**

This thesis contributes to the third research direction by focusing on the following general objectives:

1. **Assessment of high precision performance measures of two absolute quantum gravimeters in comparison with high precision absolute and relative gravimeters and additional geophysical and environmental data in**

   a) observatory conditions

   b) during experiments and in controlled, modified conditions

   Objective 1 b) aims at evaluating the dynamic range of the instruments and their performance in preparation for testing the applicability under terrain conditions.

2. **Development of new methods in gravimetry in the context of hydrology.**

The numerous potential applications of absolute quantum gravimeters exceed the scope of this thesis. The focus is on the recent advances that open up new trajectories in hydrogeological research in particular. This new generation of gravimeters offers the possibility to reliably acquire gravity data more easily. This would make more hydrological field sites accessible to this method and allow for the testing of new approaches and hypotheses.

This thesis begins with an instrumental part focused on the technical characterisation of new gravity instruments. In a second step, it aims at throwing a bridge to specific applications in hydrogeology. The outline is structured accordingly. Chapter 2 focuses on instrument validation and presents the two new absolute quantum gravimeter devices that were assessed in the scope of this manuscript. It closes with a conclusion on their applicability in the investigated conditions. It further discusses the state of the AQG devices in the context of existing gravimeters. Chapter 3 presents the potential of joint gravity and gravity gradient monitoring in hydrogeology in combination with hydrological modelling. Chapter 4 discusses perspectives on the potential of hydrogravimetric methods in the specialised case of aquifer property estimation.

2 Introduction

2.1 Gravitational attraction and potential

"The magnitude of the gravitational force between two masses is proportional to each mass and inversely proportional to the square of their separation" (Newton (1686)).

The attractive force between a point mass m_1 and a point mass m_2 at distance r in a Cartesian coordinate system:

$$\overrightarrow{F} = -G\frac{m_1 m_2}{\vec{r^2}}, \tag{1}$$

with G being the gravitational constant $\mathrm{G} = 6.674\,083\,1 \times 10^{-11}\,\mathrm{m^3{\cdot}kg^{-1}{\cdot}s^{-2}}$.

The distance r is given by:

$$r = [(x - x')^2 + (y - y')^2 + (z - z')^2]^{\frac{1}{2}}, \tag{2}$$

where the co-ordinates of the two points in space are (x,y,z) and (x', y', z') in a Cartesian co-ordinate system.

The gravitational attraction **g** at a point P is essential a vector field, defined as the gradient

$$\mathbf{g}(P) = \nabla U(P) \tag{3}$$

of the gravitational potential

$$U(P) = G\frac{m}{r}. \tag{4}$$

Because the gravitational field is a conservative force field, (that is, the work required to move a test particle from one point to another is path- independent), it can be expressed as the gradient of a potential field. Gravitational attraction of a mass δm is given by:

$$\mathbf{g}(P) = -G\frac{\delta m}{r^2}\hat{r}, \tag{5}$$

with the unit vector $\hat{r}$ directed from the centre of the mass to the observation point P. The attraction of several masses is an additive superposition of their individual gravitational attractions (Newton (1686); Blakely (1995)).

2.2 Terrestrial gravity field

The vertical gravitational attraction experienced on the surface of Earth due to its mass and the Earth's rotation is in the order of 9.81 $\mathrm{m.s^{-2}}$ (referred to as g). A commonly used unit of g

is the Gal, named after Galileo (0.01 m.s^{-2}). Gravimetry nowadays focuses on processes on the level of μGals, which equals 10 nm.s^{-2} in the Système Internationale (SI). One μGal is in the order of 10^{-9} g.

The gravitational field of the Earth is not constant in time and space. Changes in the Earth's shape, rotation and density distribution cause gravity field variations. Gravity anomalies are deviations from a reference model, the theoretical static gravity field of the Earth, whereas gravity residuals are temporal signals after correction for known variations (Crossley, Hinderer, and Riccardi (2013)).

The hereafter described spatial and temporal variations of the Earth's gravity field can be linked to changes in above-ground, atmospheric and subsurface mass distribution and can find application in various disciplines of the Earth sciences. Gravimetry covers a vast range in observation scale. It deals with the shape of the whole Earth and the geodetic geoid, or local small-scale density changes such as underground cavities. Gravimetry further ranges from space-borne satellite observations to deep seafloor exploration, studying processes as short-term and erratic as earthquakes in fractions of seconds or continuous over geological time-scales of millennia.

2.2.1 Spatial anomalies and corrections

The Earth's shape is described in relation to a reference ellipsoid, a theoretical approximation of the geoid surface. Observed gravity on a given location on the Earth is a superposition of gravity anomalies as a result of local density variations. The observed gravity comprises of the gravitational attraction of the reference model, the outward centrifugal force due to the earth's rotation and the sum of various effects of the local gravitational field.

The **Free-Air** correction accounts for the effect of the distance from the surface of the reference geoid, thus the elevation above mean sea level. The free air effect $\delta_{g_{FA}}$ is the gravity anomaly $\delta\gamma$ per altitude difference:

$$\delta_{g_{FA}} = \frac{\delta\gamma}{\delta h} \approx \frac{-2_{g_0}}{R} H, \tag{6}$$

yielding a nominal value of -3086 nm·s^{-2}m^{-1} . The effect of the average "normal" mass between sea level and observation location is the **Bouguer** correction. It is defined as the gravitational attraction of a horizontally infinite slab dependent on the slab thickness h.

$$g_{sb} = 2\pi G\rho h, \tag{7}$$

Topography or terrain g_t is of interest to terrestrial gravimetry focused on local effects, as the masses of the terrain around and their distribution below and above the measurement point need to be considered. This effect refers to specific local **geological** crust density variations.

By definition, the complete Bouguer anomaly includes these anomalies and can be obtained from the observed gravity value after subtracting the Free-Air, simple Bouguer and topographic anomalies:

$$\Delta g_{cb} = g_{obs} - g_{FA} - g_{sb} - g_t - g_0 \tag{8}$$

(Blakely (1995)).

2.2.2 Time-variable gravity field

Apart from spatial variations, time-variable gravity effects influence gravity measurements both due to mass attraction and Earth's surface deformation. A gravity time series can be decomposed into these additive effects. They can be categorized by their physical origin, their periodicity or erraticism, and their temporal and spatial scale and frequency (Crossley, Hinderer, and Riccardi (2013)). This section gives an overview on time-variable gravity signals and methods of correction for these effects. Furthermore, their geophysical origin and the processes of scientific interest are discussed. Firstly, **periodic** signals are discussed.

2.2.2.1 Solid Earth and ocean tides

The largest effects in terms of amplitude are variations of the gravitational field experienced at or near the earth's surface arising from (i) the gravitational fields of the sun and of the moon (and, to a much lesser extent, of nearby planets) which vary as a consequence of the relative motion between the earth and these bodies, and (ii) the earth's deformational responses to these changing fields. The deformational responses of the earth include solid earth tides and ocean tides. The chart in Figure 2.1 (Agnew (2015); p. 164) describes the processing flow starting at the origin of tidal forces caused by celestial bodies to the impact on both solid Earth, core and oceanic water masses. The gravity effect results from direct, Newtonian attraction and from surface displacement due to crust deformation. Extraction of tidal signals in gravity series can be facilitated by knowledge on environmental gravity effects. The strongest time-variable signals are caused by the solid Earth tides, reaching more than 3000 $\mathrm{nm{\cdot}s^{-2}}$ of amplitude.

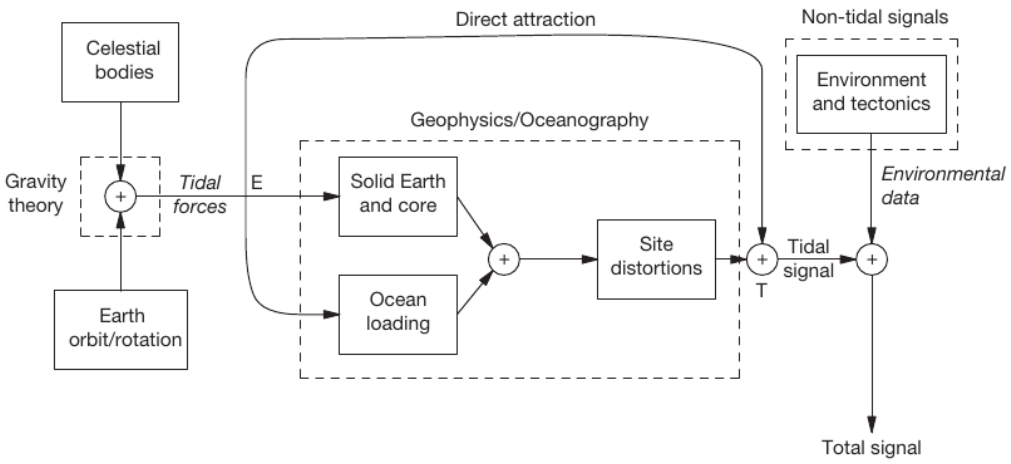

Figure 2.1: Flowchart from tidal forces to tidal signal (from Agnew, 2015, p. 164).

The tidal influence on the Earth's gravity field are described as the tidal potential from which spherical harmonics can be derived, showing long-term, diurnal term and semi-diurnal harmonics, as a combined effect of celestial body attraction and the Earth's rotation. The tidal potential can be decomposed into latitude and longitude related terms and the spectrum of the tidal harmonics can be described by their period duration in hours and frequency, phase and amplitude. These tidal wave properties are listed in tidal generating potential catalogs, obtained from analytical or numerical spectral analysis. From these theoretical models, tidal parameters can be derived, consisting of an amplitude factor and a phase difference, which serve as transfer functions with the aim to determine the tidal gravimetric factors (Agnew (2015)).

Various tidal potential catalogues and corresponding softwares for tidal analysis and prediction exist, e.g. the programs Baytap based on the tidal catalogue of Tamura et al. (2007), VAV (Ducarme et al. (2006)) or ETERNA (Wenzel (1996)) and find application in gravimetrical studies. Mikolaj, Reich, and Güntner (2019) compare the root-mean-square error for the mentioned three solid Earth tidal correction programs for several measurement locations on the globe and found an uncertainty of less than 2 nm·s^{-2}.

2.2.2.2 Polar motion effects

The Earth's rotation axis moves relative to a reference frame and changes as a superposition of two frequencies of an annual wobble and the Chandler wobble with a period of 433 days. The superposition of both wobbles causes a period of approximately seven years. Changes of the axis change the centrifugal forces at a given location, causing crust deformation and changes in measurable gravity (Wahr (1985)). The International Earth rotation and Reference systems Service provides daily pole coordinate series and predicted values for several weeks (Bizouard and Gambis (2009); Bizouard et al. (2018)).

Nonperiodic signals can be caused by atmospheric loading, gravity effects of the masses of the oceans caused by changes in ocean temperature and non-tidal ocean currents, volcanic activity and diverse mechanisms of crust deformation or seismicity (Crossley, Hinderer, and Riccardi (2013)).

2.2.2.3 Atmospheric pressure

Atmospheric Pressure effects are the combined effects of mainly Newtonian attraction of the atmospheric masses and surface deformation due to their load, typically about 3 nm·s^{-2} hPa^{-1}. The local atmospheric effect within 50 km radius of the measurement location is the dominant contributer (about 90%), while regional and global atmospheric load effects contribute only a few percent (Merriam (1992)). Site-specific atmospheric admittance factors can be derived from tidal analysis using long-term gravity and barometric series in order to distinguish the signals.

The gravimetric effect $\delta g_{atmosphere}$ caused by the local atmosphere is linearly related to the difference in barometric pressure relative to a fixed, nominal pressure reference P_{nom} times the admittance coefficient α. The nominal pressure P_{nom} is estimated from the altitude above sea level h as:

$$P_{nom} = 1013.25 \times (1 - \frac{0.0065h}{288.15})^{5.2559}. \tag{9}$$

Given the pressure P at a time t we can obtain

$$\delta g_{atmosphere} = \alpha \times (P(t) - P_{nom}). \tag{10}$$

(Crossley, Hinderer, and Rosat (2002))

2.2.2.4 Uncertainty of time-variable gravity corrections

The described time-variable effects that contribute to the observed gravity residual can be summarised and are ordered according to their frequency range in the following equation (Crossley, Hinderer, and Riccardi (2013)):

$$g_{obs} = \delta g_{disturbances} + \delta g_{tides} + \delta g_{atmosphere} + \delta g_{polar\ motion} + \delta g_{instrumental\ drift}$$

$$+\delta g_{hydrology} + \delta g_{other\ processes}$$

Disturbances are local, site-specific short-term noise sources, such as microseismicity, anthropogenic activity or earthquakes) or errors of instrument operation. Systematic long-term instrumental drift depends on the gravimeter and can be determined by calibration with other

instruments. “Other processes” are remaining, mainly slow, long-term gravity changes or short-term events.

Long-term and large-scale geodynamic processes can be resolved by gravity time series. Such long-term gravity trends are caused by crust deformation (Mazzotti et al. (2007)), tectonics and slow subsidence (Camp et al. (2011)). Storage changes of large water masses can be due to ice melt, withdrawal or redistribution driven by climate, such as the glacial viscoelastic isostatic adjustment uplift (e.g. Mazzotti et al. (2011); Olsson et al. (2019)). These mass changes impact crustal elastic loading and hence gravity.

Earthquakes can cause numerous gravity effects occurring at different times during a seismic event. Potential preseismic, coseismic and postseismic gravity effects have been detected (Imanishi (2004); Imanishi et al. (2009)) and can be modelled from the gravity series (Wang, Lorenzo-Martı'n, and Roth (2006)). Earthquakes can cause response oscillations of the Earth known as seismic elastic normal modes (Rosat (2005)).

Depending on the process of interest, further effects should be corrected for, such as global hydrology and nontidal ocean loading. A complete removal of extraneous effects has not been achieved yet, residual tidal and atmospheric pressure signals remain. The residual uncertainty in these corrections in terms of root mean square error has been estimated to be up to 2.6 $\mathrm{nm{\cdot}s^{-2}}$ for global atmospheric and 1.6 $\mathrm{nm}s^{-2}$ for nontidal ocean loading, respectively (Mikolaj, Reich, and Güntner (2019)). Various global hydrological models are available for continental water storage. Commonly used are surface models as part of the GLDAS framework (Rodell et al. (2004)). Further options are e.g. ERA Interim (Dee et al. (2011)) or MERRA-2 (Gelaro et al. (2017)). Models correcting for large-scale hydrology have been found to be the largest source of 3.8 $\mathrm{nm{\cdot}s^{-2}}$ uncertainty. General errors for the correction in time-variable effects in terms of root mean square error ranged between 0.5 $\mathrm{nm{\cdot}s^{-2}}$ for hourly data and 6.7 $\mathrm{nm{\cdot}s^{-2}}$ over periods of 6 months. Improvements are likely to be gained from modelling seasonal global hydrological effects (Mikolaj, Reich, and Güntner (2019)). Global 3D models and maps of terrestrial gravity, resulting from surface deformation and Newtonian attraction of atmospheric, oceanic and continental hydrological mass retribution processes are available from the EOST loading service (Boy and Hinderer (2006); Boy and Lyard (2008); Boy et al. (2009)).

2.2.2.5 Hydrology

The standard model is referred to as the combined corrections for signals that are known and relatively straight forward to model, namely tides, atmospheric pressure, polar motion, and instrument drift (Hinderer, Crossley, and Warburton (2015)). Residual effects can, to some extent, be attributed to local **hydrological mass changes**, which occur in form of rainfall, soil

moisture changes, groundwater storage, surface water mass, or snow and ice cover changes. The simplest approximation to describe the gravity effect of a horizontal layer of soil water is given by a Bouguer slab. Given the density of water ρ_{water}, soil porosity θ and the slab thickness h

$$\delta g = 2\pi G \rho_{water} \theta h \tag{11}$$

a flat slab of 1 mm water height would cause 0.42 nms^{-2} residual gravity signal δg (e.g. Deville (2013)). Gravity variations caused by hydrology were originally regarded as noise in geodetic and geodynamical applications. Long-term gravimetric observation series conducted with superconducting gravimeters (SG) at the geodetic station Strasbourg showed seasonal variations that can be partially attributed to hydrological mass changes (Amalvict et al. (2004)).

Hydrogravimetry has recently developed into a discipline that covers all components of the hydrological cycle: evapotranspiration, condensation, precipitation, infiltration, percolation and runoff. Gravity monitoring along-side with other methods contributes to the investigation of multi-scale temporal-spatial hydrological fluxes. This field of research represents one of the main topics of this thesis.

2.2.3 Further applications of gravimetry

Gravimetric methods find further applications in the context of oil and mineral exploration and prospecting. Gravimetry used to be the predominant geophysical exploration methods before becoming increasingly overshadowed by seismometry. Great potential lies in joint surveys with seismic and magnetic methods in which changes in lithologic densities are explored for the detection of deposits or fluids (e.g. Hinze, Von Frese, and Saad (2013)), e.g. applied in the Prudhoe Bay Oil field (Ferguson et al. (2007)).

Recently, gravimetry has advanced as an important tool in natural hazard assessment such as monitoring and prediction of volcanic activity though observation of mantel mass movements (Bonvalot, Diament, and Gabalda (1998); Carbone and Greco (2007); Carbone et al. (2017); Carbone et al. (2020)). Other examples are the detection of subsidence (Hwang et al. (2010)) and associated risks in urban construction and planning (e.g. Pacheco-Martı'nez et al. (2015)) or mapping of Karst cavities (Mochales et al. (2007)). Mouyen et al. (2012) identified gravity changes caused by erosion and typhoon related land-slides. Examples for applications in energy and resources are the monitoring of geothermal fields (Sugihara and Ishido (2008); Pearson-Grant, Franz, and Clearwater (2018)) or CO2 storage reservoirs (Sugihara et al. (2017)).

Last but not least, gravimetry measures one of the four fundamental forces present in our universe, and is a tool and research object in fundamental physics and metrology (Merlet et al.

(2008); Stock (2012)).

The examples described in this chapter aim at providing a broad overview of the manifold applications in gravimetry. It nevertheless remains a selection without claiming completeness. Further applications and active gravity research fields have been reviewed by Crossley, Hinderer, and Riccardi (2013) and Camp et al. (2017).

2.3 Gravimeters

Instruments to measure the gravitational attraction of the Earth's surface are called gravimeters. Today a diverse range of gravimeters based on different measurement principles exist that are used for various purposes. Before going into detail, key concepts concerning the assessment and comparison of gravimeter performance need to be introduced.

Accuracy

The accuracy of a gravity measurement describes to which extent it can be considered as correct in absolute terms. It refers to the uncertainty of a measurement relative to an absolute standard that can only be determined by comparison with a more accurate instrument, which is usually done during national and international inter-comparison campaigns such as The International Comparison of Absolute Gravimeters (ICAG) including several absolute gravimeters of different providers ((Jiang et al. (2012); Francis et al. (2013); Gillot et al. (2014)). The accuracy of a measurement is affected by systematic errors.

Precision

The precision (or sensitivity) of a gravimeter is a relative uncertainty and refers to the smallest change in gravitational acceleration that the gravimeter is able to detect. It essentially refers to the last significant digit of a measurement output and is determined by instrumental and environmental noise levels. Precision can increase with increasing averaging interval. This procedure is, however, often limited by noise of lower frequencies. The influence of the averaging duration is given by the spectral noise density in gravitational acceleration per square root of frequency. Signal precision or sensitivity can be assessed by time series analysis of frequency stability, as by the Allan variance (Allan (1966)) given as:

$$\sigma_y^2(\tau) = \frac{1}{2}\langle(\bar{y}_{i+1} - \bar{y}_i)^2\rangle, \tag{12}$$

with the observation time t and the $\bar{y}_i$ as the i^{th} fractional frequency:

$$\bar{y}_i = \frac{1}{\tau}\int_0^{\tau} y(i\tau + t)dt. \tag{13}$$

After a Fourier-tranform of the series y into $S_y(f)$ one can write:

$$\sigma_y^2(\tau) = \int_0^{\infty} S_y(f)\frac{2sin^4\pi\tau f}{(\pi\tau f)^2}df, \tag{14}$$

with the Allan variance transfer function

$$|H_A(f)|^2 = \frac{2\sin^4\pi\tau f}{(\pi\tau f)^2}. \tag{15}$$

Repeatability

The repeatability of a measurement refers to the agreement between repeated measurements and is usually assessed by carrying out several repeated location changes in between measurements. Repeatability is dependent on precision, environmental noise, and other error sources (Niebauer (2015)).

2.3.1 Absolute gravimeters

Absolute gravimeters measure the instantaneous gravitational attraction at a particular location. This has been implemented based on the principle of a test mass experiencing the gravitational force of the Earth, either on a pendulum or in vertical free fall. Pendula were discovered as a measuring device for time (Galileo in 1602, Huygens in 1657), first used as gravimeters in 1749 by Bouguer and later developed into the Kater pendulum by Kater in 1818 (Figure 2.6, Angelis et al. (2008)). The measurement of g is based on the simple relationship between the period T and the length L given by

$$T = 2\pi\sqrt{\frac{L}{g}} \tag{16}$$

This set-up achieves an accuracy of 10^{-4} g (Kater (1818); Niebauer (2015)). Pendulum gravimeters were used until the first half of the 20th century and reached an accuracy of about 10^{-5} g (Marson (2012)).

Free-fall or ballistic gravimeters sense gravity by obtaining the gravitational acceleration experienced by a test mass during free fall from the change in vertical fall velocity over a distance. The emergence of high precision time measurements, progress in laser and vacuum led to considerable improvements in absolute gravimetry in the second half of the 20th century. Absolute gravime-

ters based on this principle essentially share the same basic architecture: The main component is a vacuum chamber in which a test mass is dropped and caught. It is released to experience free-fall and monitored during this process. The chamber needs to allow for efficient shielding from external forces (e.g. electromagnetic) and a vertical trajectory of the test mass during fall. For the measurement to be precise in the order of 1e-9, the time and distance references need to be exact in the order of 1e-9. The distance can be measured in an optical interferometer (Mach-Zehnder or Michelson), time with atom clocks. The whole set-up should be isolated from seismic noise which can be achieved through passive or active compensation mechanisms (Niebauer (2015)). More recent implementations of absolute gravimeters use quantum interferometers to measure the acceleration experienced by the test mass, as will be explained in more detail in section 2.4.

2.3.1.1 Micro-g LaCoste FG5-X

The most used commercial absolute gravimeter is the FG5X model by Micro-g LaCoste (Figure 2.2, LaCoste (2020)). Its principal components are a vacuum chamber, an in-line Mach-Zender interferometer with an iodine-stabilized laser, and a 'super spring' for active microseismic compensation. A corner-cube retroreflector serves as the test mass. A detailed description of the architecture, technical specification, and operation is given in Niebauer et al. (1995).

The laser beam is split and recombined using mirrors, the resulting interference fringes are sensed by a photodiode and transformed into an electrical output. Over 20 cm free-fall length, about 200 time and distance measurement data points of the falling cube are taken. The post-processing software fits a parabolic function to the data. A first guess of the vertical gravity gradient is required. The test mass's positions x_i and at a point in time t_i and hence the fall trajectory can be calculated with the following adjusted equation of motion that is extended by the effect of the vertical gravity gradient.

$$x_i = x_0 + v_0 + \frac{1}{2} g_0 \tilde{t_i^2} + \frac{1}{6} \gamma v_0 \tilde{t_i^3} + \frac{1}{24} \gamma g_0 \tilde{t_i^4} \tag{17}$$

$$\tilde{t} = t_i - \frac{(x_i - x_0)}{c} \tag{18}$$

The initial position, velocity and acceleration are given as x_0, v_0 and g_0, respectively, c refers to the speed of light.

The a priori vertical gravity gradient is that of the Free-Air gradient of -3086 nm·s^{-2}m^{-1}. Gravity gradients are expressed in the unit of Eotvos (1 $E = 10^{-9}$ s^{-2}). If the vertical gravity gradient estimation has an uncertainty of 1 % (about 30 E) the estimated gravity value acquires an error of 1.9 nm·s^{-2} along the 0.2 m fall length (Niebauer et al. (1995)). To reduce this error source a

well-estimated local vertical gravity gradient at the height of the measurement is necessary. The FG5's instrumental uncertainty has been assessed to be 11 nm·s^{-2} with a standard deviation of 50 to 80 nm·s^{-2} in favourable conditions. The scatter of individual measurements (drops) tend to be 100 nm·s^{-2} and FG5 devices tend to show 10-20 nm·s^{-2} consistency among them (Niebauer (2015)). As an absolute gravimeter, the FG5 usually does not show an instrumental drift over time and serves as a reference for the calibration of other gravimeters. It requires regular international comparison among absolute gravimeters. The repeatability of AG measurements has indeed been estimated as of 1 nm·s^{-2}y^{-1} (M. V. Camp, Williams, and Francis (2005)). However, assembling, operation and maintenance require high technical skills and experience and are operated by trained personnel.

Figure 2.2: FG5-X absolute gravimeter by Micro-g LaCoste Inc., 2020.

Another device by Micro-g LaCoste Inc. is the A-10 absolute gravimeter (LaCoste (2008)). It is a portable terrain version based on the same principle as the FG5. The uncertainty of these gravimeters has been quantified as of 100 nm·s^{-2} (Falk et al. (2011)). Schmerge and Francis (2006) characterised the standard deviation (16 ± 6 nm·s^{-2}) and repeatability (29 ± 15 nm·s^{-2})

of the A10#008. They define the standard devation as the scatter of a measurement set and repeatability as the standard deviation of different set-ups.

2.3.2 Relative gravimeters

Relative gravimeters do not measure the gravitational attraction directly but infer gravity from the force needed to counteract gravitation and to stabilize a test mass. They are hence suited to monitor gravity changes and have been widely used in spatial gravity mapping and time-lapse surveys. Lacking long-term stability, they require regular calibration with absolute gravimeters as reference stations and show variable drifts that can become important within days (spring gravimeters) or months (superconducting gravimeters) (Camp et al. (2017)).

2.3.2.1 Spring gravimeters

Spring gravimeters started replacing pendulum gravimeters and became commercially available in the 1930s, such as the metal spring gravimeters provided by the manufacturer LaCoste and Romberg. An elastic spring in equilibrium shows a spring elongation δL of

$$\delta L = \frac{mg}{k} \tag{19}$$

that is determined by its elastic constant k and the involved mass m. In knowledge of k and the test mass m, g can be obtained from the elongation L. The performance of relative gravimeters is limited by the elongation measurement and spring hysteresis (Figure 2.6, Angelis et al. (2008)).

Spring gravimeters are still the most commonly available relative gravimeters. Most spatial gravity surveys and monitoring of relative gravity changes have been carried out with spring gravimeters, as they are less expensive, smaller, and easier to use and maintain than absolute gravimeters (Niebauer (2015)). State-of-the-art relative spring gravimeters rely on quartz springs that show higher stability than metal springs. The fused quartz stabilise the test mass electro-statically. The voltage representing the electrostatic feedback needed to counteract the gravitational force on the spring is translated into gravity using a linear calibration coefficient. The commercially most common quartz spring relative gravimeters are Scintrex CG5 (Scintrex (2014)) and recently the CG6 Autograv as the leading device (Scintrex (2018); Figure 2.3, Bertrand (2019), RESIF (2020)).

Figure 2.3: Scintrex CG5 and CG6 devices as part of RESIF's GMob mobile gravimeter facility, in test at the Géosciences Montpellier laboratory (Bertrand, 2019).

The uncertainty of the CG5 measurement depends on various factors, causing errors of up to several tens of $\mathrm{nm{\cdot}s^{-2}}$ each, such as instrument tilt, temperature, spring hysteresis, calibration errors and others. The origin and order of magnitude of these error sources as well as possibilities for their mitigation during operation are discussed in Lederer (2009) and Christiansen, Lund, et al. (2011). Adequate relaxation times need to be respected before acquisition starts, as transport of the instrument in a non-vertical position can cause off-sets lasting hours (Reudink et al. (2014)). Fores, Champollion, Moigne, and Chery (2016) show the need for adequate correction of temperature effects in terrain surveys. The main issue remains the drift correction and the occurrence of nonlinear short-term drifts. Instrumental drift tends to be linear for a couple of hours and can turn into later nonlinear trends. Additional tares occur often during surveys. Repetitions and loops are required to identify and remove these outliers and the drift. Survey precision and repeatability depend on the careful reduction of error sources, repeated measurements, and revisiting of survey locations as well as thorough post-processing. In order to be able to compare survey results of campaigns lasting days to weeks, a least-squares network adjustment needs to be carried out with open-source software readily available for these purposes (Kennedy and Ferré (2015); Hector and Hinderer (2016)). Further data quality improvements can be achieved by other post-processing techniques such as filtering for microseismic noise as suggested by Boddice et al. (2018). CG5 devices show a sensitivity of less than 10 $\mathrm{nm{\cdot}s^{-2}}$ (less for

CG6) and a field repeatability is around 50 nm·s^{-2}. Acquisition frequency lies at 6 Hz, allowing for repeated set cycles. Averaged output values are displayed for a user-defined set size (Scintrex (2014)), usually between 30 seconds and 90 seconds. Linear drifts can be several thousands of nm·s^{-2} per day for CG5 devices (e.g. Merlet et al. (2008)), for CG6 the manufacturer reports drifts of less than 2000 nm·s^{-2} per day (Scintrex (2018)).

The latest generation of mechanical spring gravimeter is the gPhoneX by Micro-g LaCoste and Romberg (LaCoste (2013)). In terms of noise level and precision, it competes with other spring gravimeters such as the Scintrex CG5, as drift rates are much lower. With less than 3 nm·s^{-2} precision after one hour integration, it finds application in several geophysical studies (e.g. Fores et al. (2019)). However, compared to superconducting gravimeters (presented hereafter), these drifts are still important and complicated to model due to their strong nonlinearity. Only after several weeks a drift rate of 150 nm·s^{-2} can be achieved. The gPhone is a device of higher stability than quartz spring gravimeters but about ten times noisier than SG. The lack of long-term stability reduces their suitability for long-term gravity change monitoring (Riccardi, Rosat, and Hinderer (2011)).

2.3.2.2 Superconducting gravimeters

Unlike the mechanical spring in the previously discussed relative gravimeters, superconducting gravimeters (SG) keep a test mass steady in an extremely stable magnetic field that is generated by exploiting the resistance-reducing, superconducting properties based on the Meissner effect (e.g. Tinkham (2004)) of a cooled-down niobium sphere surrounded by wire coils. The magnetic field generated by the coils around induces currents in the superconducting sphere, the interaction between both generated the levitation force (Goodkind (1999)). Acceleration forces such as gravity and ground vibrations cause a displacement of the test mass, usually a sphere of less than 3 cm radius. The output signal is a voltage, it gives the current in the coil necessary to generate a magnetic force to keep the sphere relatively in place within the case. A schematic view of the interior of the SG is depicted in Figure 2.4.

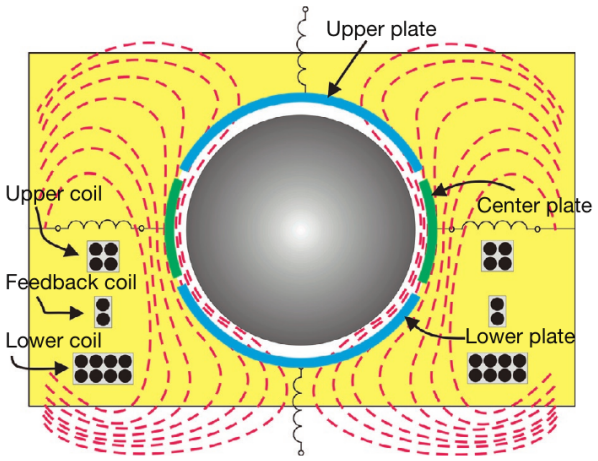

Figure 2.4: Nb sphere kept stable within the magnetic field (from Hinderer et al., 2015; p. 67).

The thermal and mechanical stability of the set-up allows for very low instrument drift. SG time-series are characterised by relatively small and linear drifts that can be modelled and removed with additional absolute measurements. For most SG they tend to be few tens of $nm{\cdot}s^{-2}$ per year, often below 40 $nm{\cdot}s^{-2}{\cdot}y^{-1}$. The GWR#C021 operated at the Membach geodetic observatory, Belgium, showed an instrumental drift as low as a few 10 $nm{\cdot}s^{-2}{\cdot}y^{-1}$, best described by an exponential law. However, for time-series of less than a decade, linear drift models are accurate enough (M. V. Camp and Francis (2006)). Right after installation exponential drifts can occur that can later be modelled as linear with time (Camp, Viron, and Warburton (2013)). Otherwise, errors in drift correction could lead to misinterpretation as trends of geophysical phenomena (M. V. Camp and Francis (2006)). SG instrumental drift determination relies on regular comparisons with AG measurements to separate instrumental drift and signal. Logically, the long-term SG precision is dependent on the reproducibility of FG5 measurements, the latter estimated to be at 16 $nm{\cdot}s^{-2}$ (M. V. Camp, Williams, and Francis (2005)).

Due to the lack of a more precise reference, SG precision is determined by inference. The smallest detectable gravity change in the frequency domain has been quantified as 1 nGal (0.01 $nm{\cdot}s^{-2}$) and 1 $nm{\cdot}s^{-2}$ or better in the time domain (Hinderer, Crossley, and Warburton (2015)). Practically, data are averaged to minutes, yielding a precision of 0.1 - 0.3 $nm{\cdot}s^{-2}$. SG precision has been shown to be superior to that of other gravimeters over a large spectral band (Riccardi, Rosat, and Hinderer (2011)).

Voltage changes need to be accurately converted into real gravity changes. This is usually done by calibration using absolute gravimeters (mostly FG5). The coefficient is obtained by fitting the temporal variations of current measured by the SG and those of gravity measured by the absolute gravimeter. The calibration factor can be determined the most precisely during the time period of large tidal signals in the gravity data. Francis and Dam (2002) demonstrated

that SG calibration to a precision of about 0.1 % is achievable within a minimum of four days in order to cover large enough tidal amplitudes. Calibration procedures can be applied in two ways. SG data can vice versa improve the determination of gravity changes monitored with AG (Camp, Viron, and Warburton (2013)). Once the instrumental drift is well characterised, the SG can be used as a reference for the calibration of spring gravimeters, yielding overall good results (Meurers (2002)).

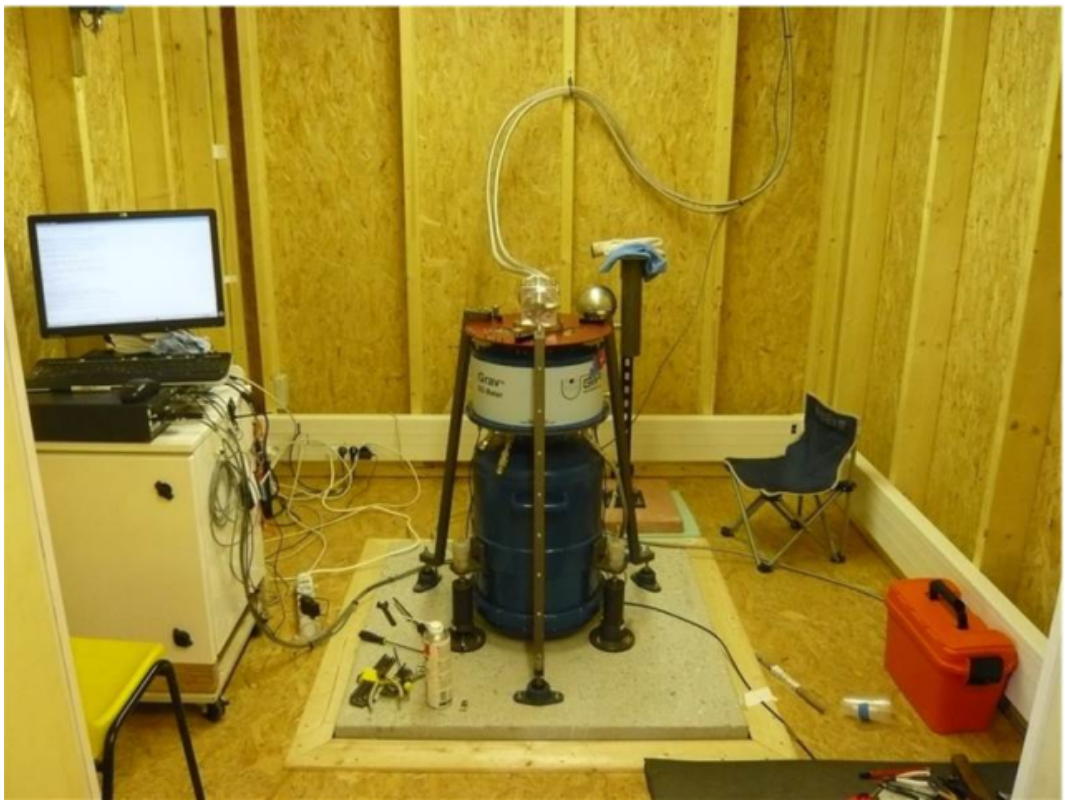

Figure 2.5: GWR iGrav-002 operating at the Larzac observatory, France, since 2011 (Le Moigne, 2019; RESIF).

SG can detect gravity variations from seconds to decades, enabling reliable long-term monitoring while resolving short-term variations. Due to their small temporal drift and high precision, SG have shown to cover very different phenomena at a large range of temporal and spatial scales, contributing to scientific achievements in many disciplines. The SG's classical function is that of long-term monitoring observatory instruments, due to their limited transportability and the time needed to make the instrument operational. The most recent generation of devices such as the iGrav by GWR Instruments, Inc. (Warburton, Pillai, and Reineman (2010)) does not lose their high performance after transportation if 4 K operating temperatures are maintained (Schäfer, Jousset, Güntner, et al. (2020)). Transportable enclosures are available and increase their mobility and application in various terrains in hydrology (e.g. Güntner et al. (2017)) or geothermal fields (Schäfer, Jousset, Toledo, et al. (2020)). Obviously, their transportability remains limited compared to those of spring gravimeters. The high precision of the SG is one of

the causes of its major contributions towards the determination and description of time-variable gravity signals. The quality of e.g. tidal models is largely due to analysis based on SG time series. An in-depth review of SG use and research has been provided by Hinderer, Crossley, and Warburton (2015). The iGrav#002 operating at the Larzac observatory, France (Moigne (2019), RESIF (2020)) is shown in Figure 2.5.

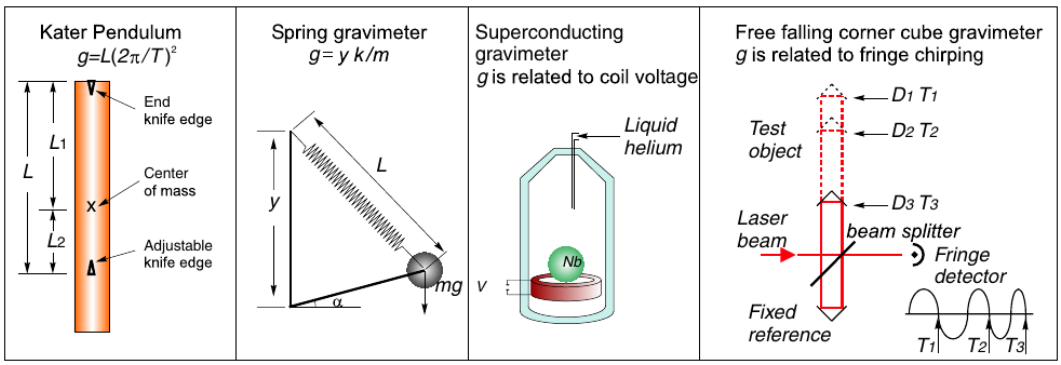

Figure 2.6: Working principles of a Kater pendulum, spring gravimeter, superconducting and free-fall corner cube gravimeter; from de Angelis et al., 2009, p. 8.

2.3.2.3 MEMS

Other devices for gravity monitoring are micro-electromechanical systems (MEMS). These low-cost microscopic electronic devices are used to measure acceleration which provides the possibility to serve as a compact, low-cost, and transportable gravimeter. A demonstrated sensitivity of 400 $\mathrm{nm.s^{-2}\sqrt{Hz}^{-1}}$ allowed for the sensing of tidal signals (Middlemiss et al. (2016)) and a standard deviation of about 560 $\mathrm{nm{\cdot}s^{-2}}$ in field tests (Middlemiss et al. (2017)). They show relatively high noise levels but upon further improvements could be used in spatially distributed applications (Middlemiss et al. (2017)). Promising new monitoring methods arise from the coupling of spatially distributed MEMS and absolute gravity measurements as an anchoring reference. Such a high-resolution gravity imaging system with MEMs gravimeters and an absolute quantum gravimeter is currently in development in the context of volcanic activity monitoring at Mount Etna (Italy) (Carbone et al. (2020)).

2.3.3 Airborne and spaceborne gravimetry

Airborne and satellite gravimeter missions complement terrestrial gravity measurements and allow for studies at larger spatial scales. Their temporal resolution is however limited and they are less suited to study temporal variations. Airborne gravity surveys are usually obtained by gravity monitoring in an airplane. Gravity estimation requires very precise positioning and velocity determination using GPS. Accuracies of 10.000 $\mathrm{nm{\cdot}s^{-2}}$ (1 milliGal) at a resolution of a few kilometers have been reported (Forsberg and Olesen, 2010). In 2002 NASA (US) and

DLR (Germany) launched the Gravity Recovery and Climate Experiment (GRACE) satellite mission, orbiting the Earth until 2017 and continued by GRACE-Follow On (GRACE-FO) since 2018. Two twin satellites orbit at 450 km altitude and use K-Band microwave ranging to measure their distance (about 220 km). The spatio-temporal variations of the geopotential manifest in distance changes between the satellites. Non-gravitational effects on their motion are monitored and corrected using GNSS and accelerometer data. This allows for continuous gravity measurements at a resolution of several hundreds of km. GRACE time series find application in global-scale monitoring of geoid height and gravity field (Tapley (2004)). Gravity changes of 10 $\mathrm{nm{\cdot}s^{-2}}$ can be resolved drift-free at a temporal resolution of one month and a spatial resolution of about 1,500 km (Schmidt et al. (2006)). One key scientific interest of GRACE is to monitor global hydrological changes. Regional (200 km^2) estimates of averaged water storage time-series have been compared to terrestrial gravity measurements, allowing for cross-validation between space-borne and local gravity monitoring and hydrological models and showing relatively good agreement (e.g. Neumeyer et al. (2006)). Frappart and Ramillien (2018) provide a review on the contributions of the first GRACE mission in hydrology.

2.4 Quantum gravimeters

A recent and promising line of research is focused on absolute gravimetry based on cold-atom quantum interferometers. Quantum interferometers are mainly based on two technological breakthroughs in the late 20th century, one of them being matter-wave interferometry and the other atom laser cooling techniques. The exploitation of the wave-matter duality of atoms has led to unprecedented applications in physics and dates back to developments in quantum theory by Broglie (1924).

A matter wave can be described by the de Broglie wavelength, expressed as the Planck constant h divided by the atom's momentum p as:

$$\lambda_{matterwave} = \frac{h}{p} = \frac{h}{Mv}. \tag{20}$$

Momentum p is given by the atomic mass M times the velocity v. The matter waves in a quantum interferometer can be seen as analogous to the laser beams in an optical interferometer.

The atoms are slowed down by laser cooling and trapping. These Nobel-winning techniques (Chu (1998)) can reach as low as a few μKelvin. Under these low-temperature conditions, their velocity and position can be controlled, increasing the signal-to-noise ratio of the interference pattern at the interferometer output. Longer interaction times increase sensitivity to external

fields as such the Earth's gravity field. For atoms cooled down to 1 μK this wavelength can be larger than 1 μm (Angelis et al. (2008)). These low temperatures (in the order of μK) allow for well-controlled atom trajectories (Peters, Chung, and Chu (2001); Santos and Bonvalot (2016); Geiger et al. (2020)). Advancements in cold atom technologies in order to realize a quantum interferometer emerged in the late 1980s (Bordé (1989)) and were first demonstrated in 1991 (Kasevich and Chu (1991)). The manipulation of cold atoms has since then developed into high precision spectroscopy and atomic clocks.

The atom interferometer works analogously to a two-wave optical interferometer such as the Mach-Zender interferometer as shown in Figure 2.7 (Angelis et al. (2008)).

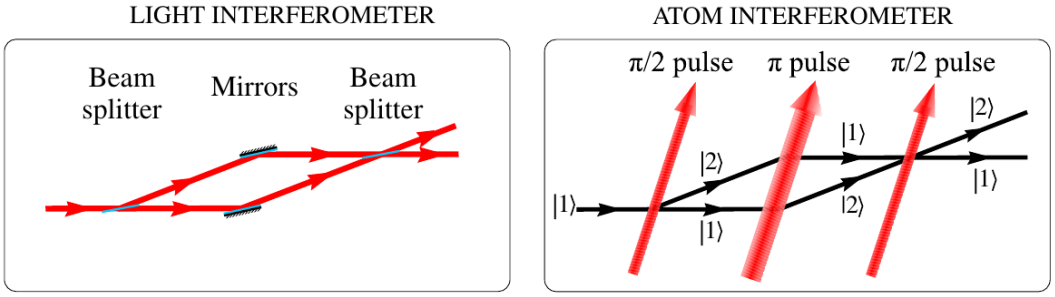

Figure 2.7: Conceptual differences between an optical interferometer (left) and an atom interferometer (right); from de Angelis et al, 2009, p. 2.

Optical beam-splitters and mirrors of corner-cube free-fall optical interferometers are replaced by counter-propagating laser pulses. As shown in Figure 2.8, the atoms are split into two partial wave packets, redirected and recombined by Raman transitions induced by three laser pulses at specific intervals. The atoms wave packets are essentially distinguished by their atomic state. The Raman transitions that the atoms undergo are basically changes between two fundamental atomic states initiated by the lasers characterised by their wavevectors k_1 and k_2 or angular frequencies ω_1 and ω_2. The elements used are mainly alkali metals (mostly Rubidium and Cesium) for cooling, trapping and manipulation wavelength are well-known and easy to produce.

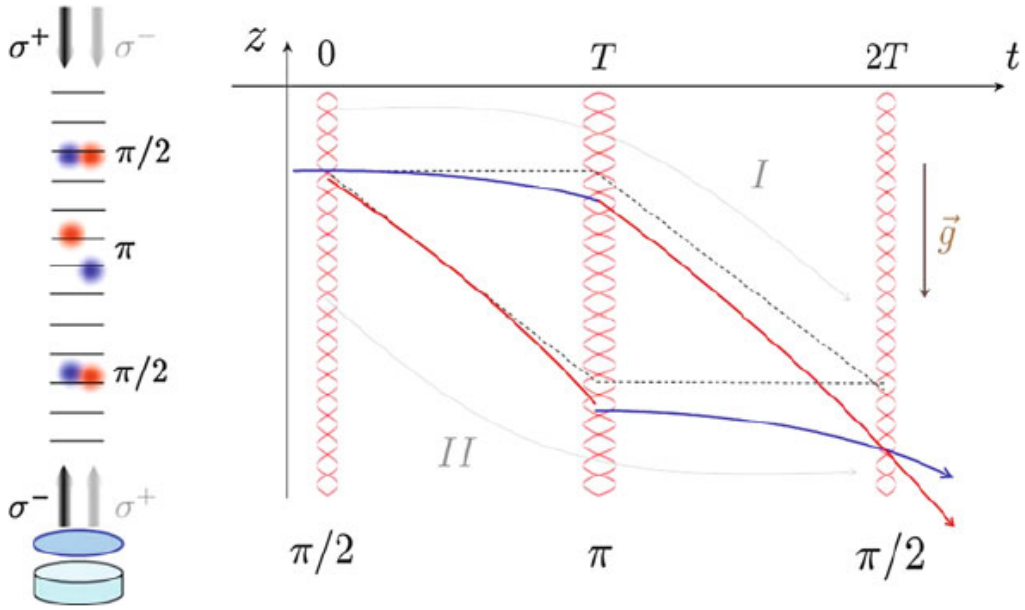

Figure 2.8: Schematic depiction of the atomic trajectories in an atom interferometer; from dos Santos and Bonvalot, 2016, p. 2.

The first Raman pulse splits the matter-wave by placing atoms in a superposition of the coupled states, basically exploiting the quantum superpositions of the atom's momentum. The second Raman pulse deflects the wave by causing an exchange of the atomic states, equivalent to the mirrors in an optical interferometer. The third pulse recombines the two wave packets, equivalent to the second splitter in an optical set-up. The interferometer phase, the difference in phase accumulated while travelling along the two interferometer paths, depends on the phases at the corresponding atom cloud position. The atomic wave functions inherit the phase difference of the counter-propagating lasers as in 21:

$$\Delta\Phi = \phi_1 - 2\phi_2 + \phi_3. \tag{21}$$

2.4.1 Atom interferometers as inertial sensors

Inertial sensing, particularly gravitational acceleration, is one of the most studied applications of atom interferometry. A cloud of cold atoms can be used as a test mass and tool to measure the travelled path in order to sense gravity (Peters, Chung, and Chu (2001)). Due to the cloud acceleration, a Doppler-effect induced shift in frequency appears and modifies the probed transition. The frequency of the laser seen by the atoms is subjected to this Doppler effect, due to the atoms' expression of the Doppler shift.

In order to maintain the resonance condition on the atom, the Doppler-effect induced shift in frequency $\delta\omega$ is compensated by a matching change in Raman laser frequency, also called

frequency chirp. A chirp is a signal in which the frequency changes with time:

$$\delta\omega(t) = at \tag{22}$$

. The laser frequency is thus

$$f_{laser} = f_0 + at \tag{23}$$

. When the compensation is correctly adjusted, the frequency induced by the Doppler effect equals the frequency chirp of the laser, so we can write:

$$f_{Doppler} = f_{Laser} \tag{24}$$

as

$$a_0 = k_{eff} g \tag{25}$$

. Their precise scanning allows to determine g from

$$g = \frac{a_0}{k_{eff}} \tag{26}$$

. Further systematic effects need to be taken into account when relating phase shifts and g measurements (e.g. Wolf and Tourrenc (1999)).

2.4.1.1 Architecture of a quantum gravimeter

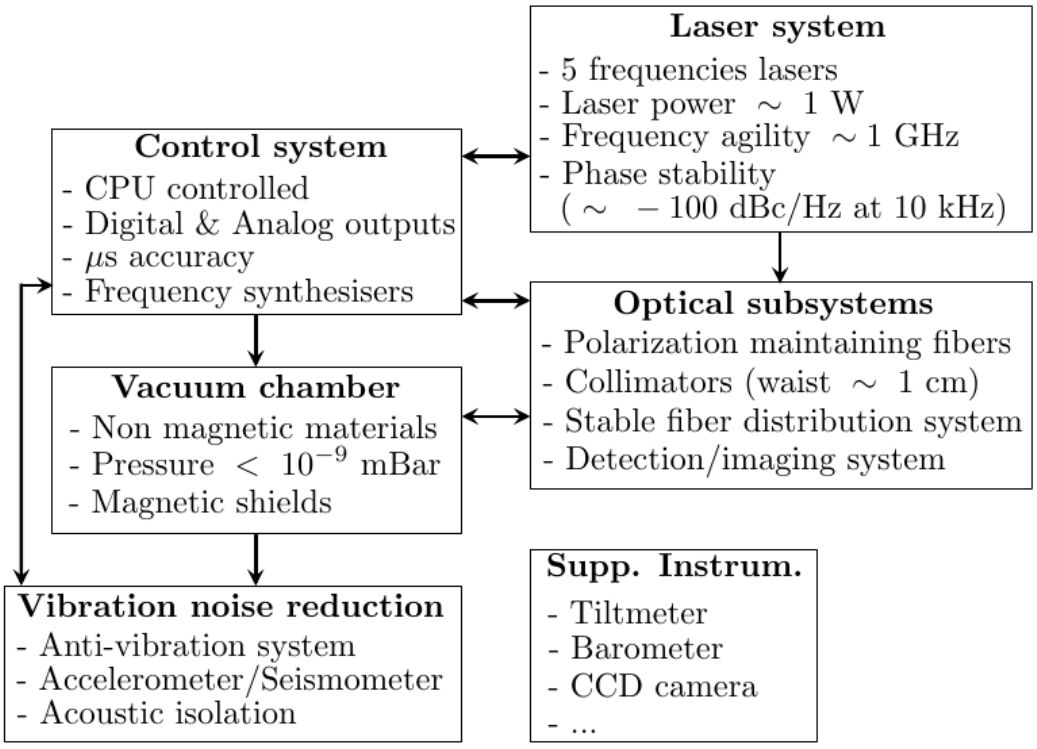

Figure 2.9: Quantum gravimeter system requirements; from Geiger at al., 2020, p. 3.

The architecture of a quantum gravimeter follows to some extent the previously mentioned architecture of mechanical absolute gravimeters but extends these with very specific features (Figure 2.9). First and foremost, a **vacuum chamber** and an **atom source** is required. The **laser system** is required for atom cooling, manipulation, and detection, supported by an additional **optical system**. A **control system** digitalises the output and allows to operate the instrument. Further devices concerning noise reduction and **stabilisation** can be mounted.

2.4.1.2 Sensitivity and accuracy

As for all absolute gravimeters, the higher the precision of the measurement of time and length units, the more precise the measurement of the gravitational acceleration. The smallest measurable change in g is closely related to the smallest frequency adjustment, or chirp a:

$$\delta g \approx \frac{\delta a}{k_{eff}} = \frac{\delta f}{kT} \tag{27}$$

. To guarantee reliable performance and accurate measurement of g, laser frequencies need to be kept stable. Gouët et al. (2008) identify the contributing noises sources and their impact on a quantum gravimeter's sensitivity. Several systematic effects are contained in the uncertainty budget, such as for instance atomic wavefront distortion caused by optical aberrations (Santos

and Bonvalot (2016); Trimeche et al. (2017); Geiger et al. (2020)). Research and development will certainly continue to focus on the mitigation of these effects. The signal-to-noise ratio (SNR) of the detection and by the interference contrast. At the middle fringe of the interference pattern, sensitivity is given by

$$\frac{\delta g}{g} = \frac{1}{k_{eff} g T^2 SNR} \tag{28}$$

.

Phase noise is defined as fluctuations of the Raman laser phases, adding to the interferometer phase noise. This type of noise source consists of various properties of the laser system, such as the uncertainty of the reference quartz oscillator, the laser phase lock, microwave frequency synthesis, or light shifts. However, the dominant limit to sensitivity tends to be external noise. Vibrations and their impact increase with the interrogation time T, defined by the length of the free-fall dropping chamber. The instrument's sensitivity tends to be limited by microseismic noise correction. There are various ways to achieve this, such as sensor isolation using e.g. a super spring stabilisation. Passive and active systems combined with accelerometers and seismometers can provide on-the-fly laser adjustment or post-correction (Gouët et al. (2008)). Externally introduced vibrations of the experimental set-up can cause displacements of the self-reflecting mirror.

Peters, Chung, and Chu (2001) first showed that measuring g with an atomic interferometer could reach a precision of $2 \times 10^{-8} g$ after 1.3 s and $1 \times 10^{-10} g$ after two days integration time (10 nm·s^{-2} $\approx 10^{-9} g$). Their measurement agreed within 7 $\pm$ 7 nm·s^{-2} with a corner-cube absolute gravimeter.

Another example of a laboratory realization is the Cold Atom Gravimeter (CAG-1) developed at LNE-SYRTE (Louchet-Chauvet et al. (2011)), which compares well to the accuracy and precision reached by FG5 absolute gravimeters (Gillot et al. (2014)). The highest sensitivities after one second have been reported as $1.4 \times 10^{-8} g$, clearly exceeding those for the FG5#206 of $4 \times 10^{-8} g$ (Gouët et al. (2008)). Louchet-Chauvet et al. (2011) report a sensitivity after 1 s of 700 nm·s^{-2} for the FG5#209 and between 600 and 140 nm·s^{-2} for the CAG (depending on measurement location). A comparison between the CAG and the FG5#220 agree within 43 $\pm$ 64 nm·s^{-2} (Merlet et al. (2010)). International comparisons of absolute gravimeters (e.g. the ECAG-2011 in Walferdange, Luxembourg; Francis et al. (2013)) show similar ranges. An exhaustive review on the state-of-the-art of cold-atom gravito-inertial sensors, different sensor types, applications, and differences in performance has been provided by Geiger et al. (2020).

To summarise, the high performance in terms of sensitivity and accuracy of laboratory versions has been demonstrated. Recently, quantum gravimetry matured into mobile devices that started leaving the laboratory environment: commercial, absolute quantum gravimeters have become available. The capability of continuous, drift-free absolute gravity monitoring with a low-maintenance, transportable device combines several characteristics that were previously only possible to cover by joint campaigns of relative and absolute gravimeters. There are several questions that arise with this new type of instrument. First of all, their fundamental performance requires precise quantification. This is achieved in controlled test conditions, especially regarding the determination of accuracy and systematic effects. The devices have only been available for a short time, hence the reproducibility of their measurements needs to be characterised. These analyses will prepare future participation in international comparisons of absolute gravimeters (ICAG), which have been visited by the SYRTE CAG (Jiang et al. (2012); Francis et al. (2013); Gillot et al. (2014)). In the next step, their suitability to measure in harsher environments (e.g. temperature changes) is a key criterion from a point of view of geophysical research. Moreover, there are practical aspects to evaluate as the commercial absolute quantum gravimeters aim at ease of use. The experiments carried out in this thesis provide a report on the user-friendliness of the specific devices in use. One of the objectives of the development of these instruments is to reach a broader, interdisciplinary clientele in order to expand the range of scientific applications. Making quantum gravimetry available for the user without the requirement of a background in quantum physics increases the scientific scope of this technology and possible study cases. Another trajectory is the potential expansion of gravimetry beyond classical applications in geodesy and geophysics to touch the community of e.g. environmental hydrology, as discussed in this thesis. As outlined in the general objectives, this thesis represents a contribution in the light of these questions.

3 Instrument validation

As of 2020, 50 research groups and 7 private companies worldwide are involved in quantum gravimeter development (Geiger et al. (2020)). One of these companies is Muquans, a French high-precision quantum technology company, founded in 2011 and based in Talence, near Bordeaux, France. Their field of expertise covers laser and optical technologies, opto-mechanical assemblies, and atom cooling and trapping as well as ultra-high vacuum technologies among others. Their products involve atomic clocks, custom laser and optical solutions, and time and frequency transfer products. Among their main products are quantum gravity sensors (Muquans (2020)).

3.1 AQG#A01

Muquans develops and produces the commercially available quantum gravimeters AQG#A and AQG#B. The architecture is described hereafter, followed by considerations on the instrument's measurement performance. The main features include:

- An innovative-patented optical design allows for robust atom manipulation using a single beam in a hollow pyramidal reflector
- Continuous absolute measurements from a few seconds to several months are possible, at a measurement frequency of 2 Hz
- Ground vibration noise is compensated actively in real-time without mechanical isolation
- High reliability, fibered laser technology
- Their devices are transportable, compact, and easy to operate and maintain for non-specialists

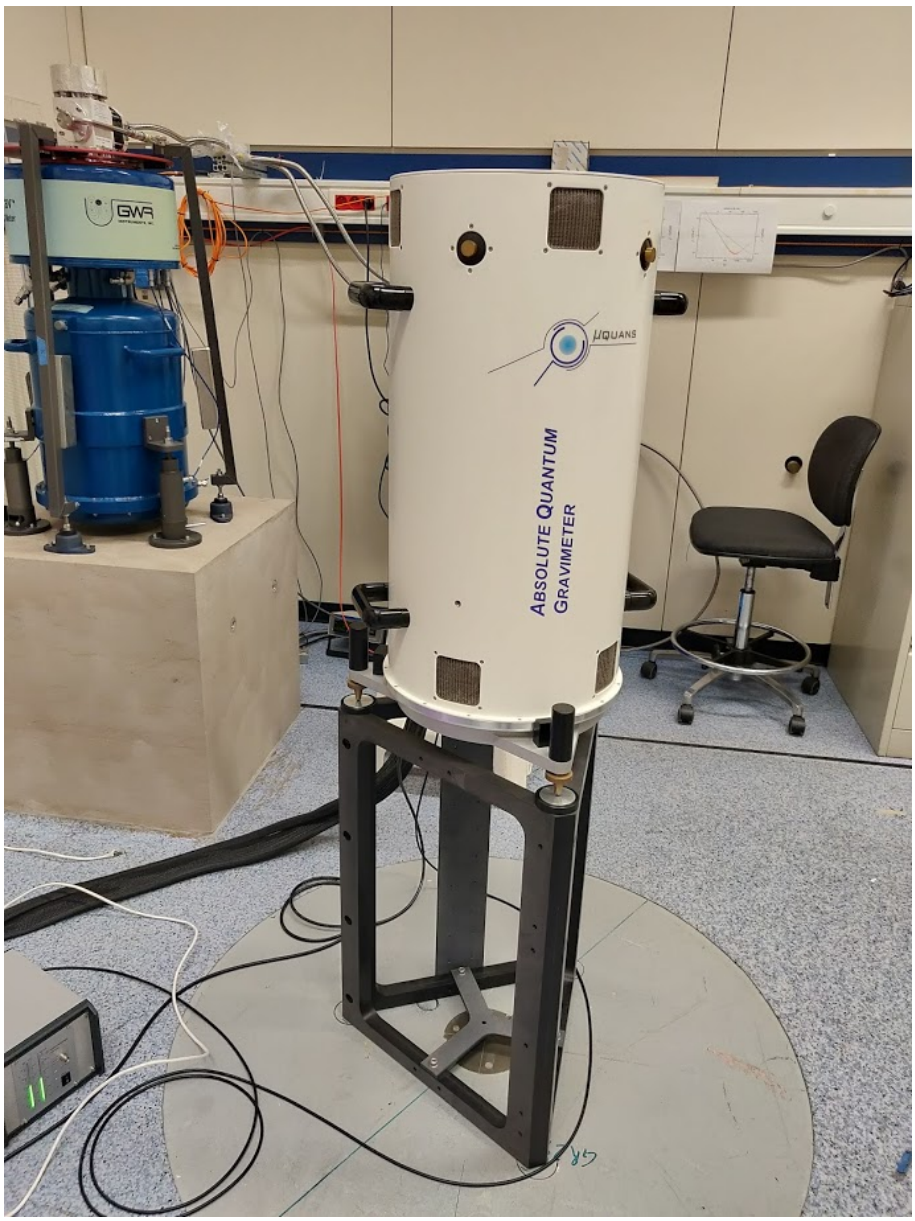

Figure 3.1: The AQG-A01 on a tripod in the LNE laboratory (Trappes) on 01/10/2019. Photo: Cooke

3.1.1 Architecture

The Muquans AQGs consist of two physical sub-units, the sensor head and the control system connected by approximately 5 m of cables.

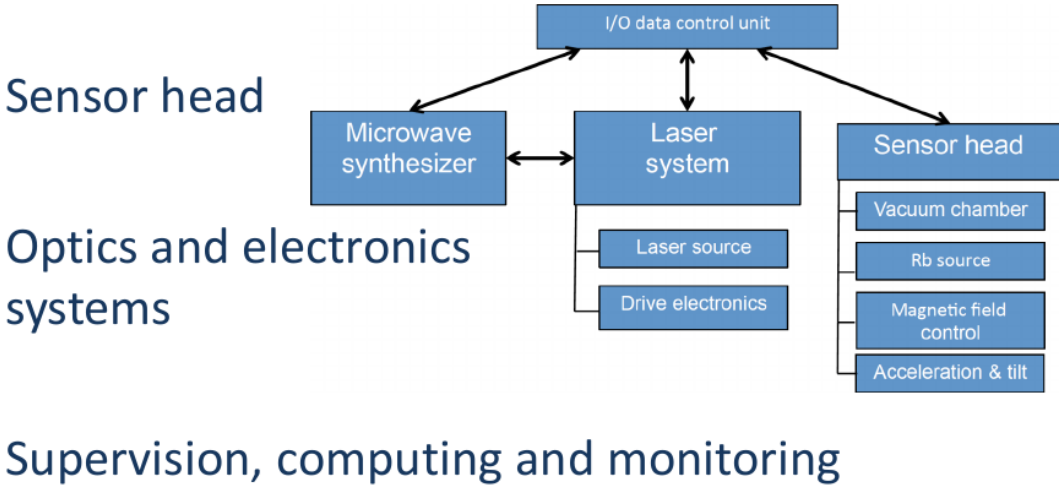

Figure 3.2: Schematic overview of the functional subunits comprising of the sensor head, optics and electronics system as well as the aspect of supervision and monitoring. Muquans, 2017.

3.1.1.1 Sensor head

The core of the instrument is the sensor head in which the atom manipulations and detection take place. It includes the vacuum chamber in which the atom clouds are prepared and selected, then experience free-fall and are detected. The Rubidium source is located in the sensor head, the control of the magnetic field and acceleration and tilt are measured here. The vacuum chamber has been emptied to a pressure of 10^{-9} mbar. The vacuum is kept stable through active and passive pumping systems. In Figure 3.3 the general principle of atom manipulations occurring in the vacuum chamber is depicted in a simplified way. Firstly, atoms are loosened from the Rubidium filaments and 10^7 atoms are trapped in a magneto-optical-trap (MOT) and then cooled down to a temperature of less than 2 μK in optical molasses. After atomic state preparation and selection, the lasers are shut and leave the atoms to experience free fall in the vacuum chamber as to be seen on the second panel from the left in Figure 3.3. Atom detection using photodiodes happens at the lower part of the vacuum chamber inside the sensor head. Details are described in Ménoret et al. (2018). The accelerometer on top of the sensor head allows for real-time vibration correction. Vibrations are recorded during free fall and directly processed and compensated for. Sensor head tilts are compensated as inclinometers register the instrument's tilt in x and y-direction.

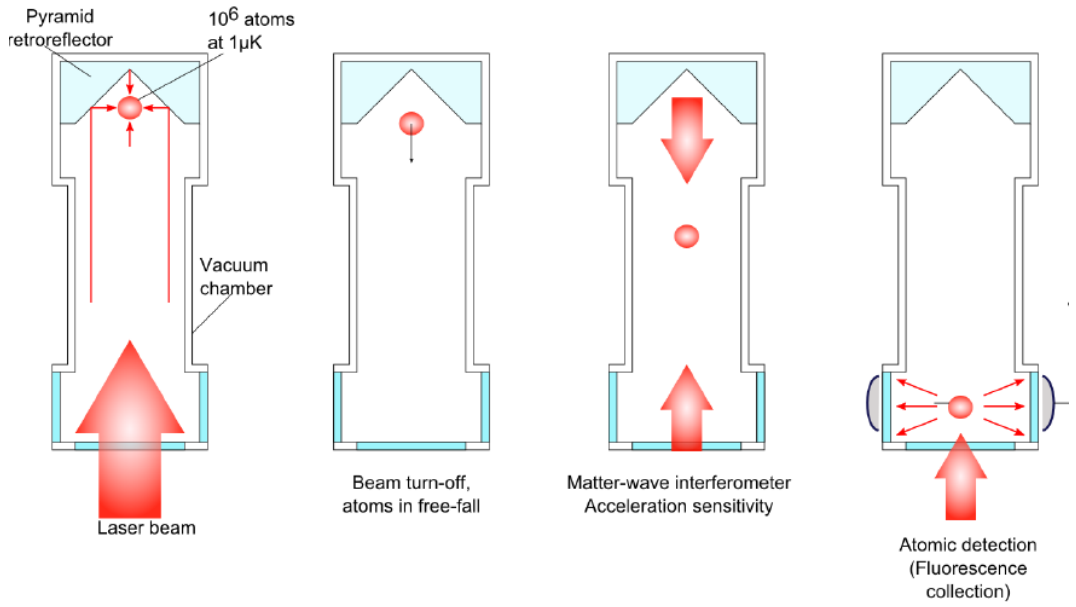

Figure 3.3: Schematic description of measurement sequence in the vacuum chamber. Source: Muquans.

3.1.1.2 Optical system

The laser systems consist of a laser source as well as the drive electronics. The optical system creates a precise and stable light source with a wavelength of 780 nm based on a 1560 nm seed laser and amplifiers using fibered optics. The system consists of three main lasers, the master laser responsible for frequency stabilization and two slave lasers, responsible for atom manipulation and interrogation.

The measurement sequence is realised with a single laser beam (instead of up to eight) based on novel patented opto-mechanical architecture. This is made possible by a compact hollow pyramidal reflector (after Bodart et al. (2010)) that achieves atom trapping and detection without the necessity to align several optical components, leading to increases in compactness and robustness.

3.1.1.3 Electronic system

The electronic system's main purpose is laser diode control and feedback. Temperature, current, and frequency stability are continuously checked. The microwave synthesizer is one of the crucial components of the AQG. Several frequencies are generated to allow for the correct operation of the system and checked with a high precision quartz. This is in particular important for the laser frequency chirp that is needed to compensate for the Doppler effect.

3.1.1.4 Supervision and computing

All these three components, the microwave synthesizer, laser system, and sensor head communicate with the data control unit in order to work together properly. The instrument is monitored during the measurement sequence. The on-board supervision systems check an exhaustive list of diagnostic parameters. They further allow for corrections to be computed in real-time such as vibrations recorded by the accelerometer mounted on the top of the sensor head or the laser phase that is updated within each cycle.

3.1.2 Installation and operation

The laser and electronics sum up to dimensions of 100 x 50 x 70 cm^3 and a weight of 75 kg. The sensor head has a height of 70 cm and 38 cm diameter, weighing about 25 kg. The power consumption lies at 250 W. Correct connection of cables between the units and procedure of the power-up are well described and instructions easy to follow. Installation is easily possible in less than 20 minutes by a non-specialist (Ménoret et al. (2018)). The AQG#A01 is a user-friendly instrument and can be started by one person, the know-how can quickly be obtained and does not require much training. Once the AQG is set-up and connected to the PC the AQG GUI software requires certain manual input, such as the location information, previously measured height of the tripod, choice of applied gravity corrections, and vertical gravity gradient. Then the manual tilt levelling is required. The tilt is adjusted by turning the screws on the tripod for x and y and is displayed on the PC screen with instructions in which directions to turn. The software allows for a manual, step-wise start by initializing each step by clicking on it. Otherwise, the option of the automatic start-up can be chosen. The software first launches accelerometer powering and stabilization. After the electronic systems reached a thermally stable state in less than an hour, the lasers are locked on their reference frequencies and the laser amplifiers are adjusted. As a next step atom trapping is checked to be operational. Then, laser frequencies are calibrated, an initial gravity measurement is conducted and the quartz is calibrated. These calibrations are crucial for the accuracy of the gravity measurement. At the same time, they do not require input from the user and can be repeated if necessary or start automatically if inconsistencies are detected. Upon successful completion of the calibration steps, the measurement sequence can be started.

3.1.3 Output and post-processing

The gravity data is saved by the AQG software as raw data (the 2 Hz recordings) and as processed data that includes the averaged data over a 10-minute interval.

- raw vertical gravity and standard deviation

- corrected vertical gravity and standard deviation

All gravity data are given in nm·s^{-2}. The applied corrections are listed in the file, which includes the corrections for instrumental effects and specific set-up (Muquans (2020)):

- **Quartz**

Similar as in an atom clock, the frequency of the Rubidium clock transitions are measured and compared to the theoretical value f_{th}, from which the quartz-correction g_{quartz} is calculated from:

$$\delta g_{quartz} = g_{raw}(\frac{f_{Rb} - f_{th}}{f_{th}}), \tag{29}$$

with f_{th} being known as 6834682611 Hz.

- **Tilt**

The effective tilt θ_{eff} is calculated from the two measured horizontal tilts θ_x and θ_y from:

$$\tan^2 \theta_{eff} = \tan^2 \theta_x + \tan^2 \theta_y, \tag{30}$$

causing the measured g_{obs} to be smaller than the actual value of g if the instrument is tilted. The correction can be obtained from:

$$g_{obs} = g_{act} \cos \theta_{eff}. \tag{31}$$

- **Systematic effects**

Systematic effects are design-specific contributions to the uncertainty budget of the instrument that have been quantified by the developer at this point in time.

- **Height**

The height correction is required to transfer the gravity measurement to ground level. The user has to enter the vertical gravity gradient to be applied and the height of the tripod, measured manually during set-up. Additionally, the instrument-specific installation height of the measurement is needed in order to gain:

$$\delta g_{height} = VGG(h_{tripod} + h_{installation}). \tag{32}$$

- laser polarization

Furthermore, environmental effects are corrected for:

- Atmospheric pressure

- solid Earth tide
- ocean tide
- polar motion

according to commonly used procedures, as well as further recorded variables

- atmospheric pressure (hPa)
- external temperature (°C)
- sensor head temperature (°C)
- vacuum chamber temperature (°C)
- laser temperature (°C)
- tiltmeter temperature (°C)
- X tilt (mrad) , X tilt standard deviation (mrad)
- Y tilt (mrad), Y tilt standard deviation (mrad)

laser properties:

- Frequency offset of the saturated absorption spectroscopy (Hz)
- Laser polarisation angles ϕ and η (rad) of the two lasers: (1) cooler laser and (2) re-pumper

3.1.4 Uncertainty budget and performance of the AQG#A01

Preceding studies show the high precision of the AQG#A01. Instrument performance had been assessed at two locations with different levels of vibration noise. At the Muquans laboratories in Talence, France, an urban area and part of greater Bordeaux, the standard deviation after one hour reached 10.7 nm·s^{-2}, 8.5 nm·s^{-2} after 24 h. The sensitivity during five days of acquisition in late 2016 reached 600 nm.s$^{-2}\sqrt{\text{Hz}}^{-1}$. Measurements in a geodetic observatory (Geodetic Observatory (GEK) Larzac, rural area) in summer 2017 yielded a sensitivity of 500 nm.s$^{-2}\sqrt{\text{Hz}}^{-1}$ with a standard deviation 9.4 nm·s^{-2} for the whole series. Possible hydro-geophysical signals and uncertainty linked to the atmospheric pressure corrections and tidal model have been discussed as additional error sources. No measurable drift was observed between July 25th, 2017 and September 4th, 2017. This stability during a bit over a month of below 10 nm·s^{-2} was confirmed with FG5#228 measurements on these dates. The AQG#01 showed a small-scale repeatability of less than 10 nm·s^{-2} on three independent pillars within the same room. The authors conclude with the aim of characterizing all systematic effects in order to obtain a complete accuracy budget, aiming at 50 nm·s^{-2} of absolute accuracy and a repeatability and stability of 10 nm·s^{-2} (Ménoret et al. (2018)).

3.2 Methods

3.2.1 Aims and outline

The earlier presented investigations and contributions to the uncertainty budget of the AQG#A01 resulting from previous studies demonstrate the high sensitivity, stability, and repeatability of the instrument. The objective of the work carried out in the scope of this thesis study is to continue investigations that contribute to a better understanding of the instrument's performance and to define contributions to the uncertainty budget more precisely. In general, high precision instruments tend to be evaluated by the user for specific applications to improve the understanding of the instrument and its performance in different conditions during acquisition. The investigations presented hereafter consist of repetition and expansion of previous studies. The AQG#A01 has been characterised based on its stability and sensitivity, using absolute gravity data obtained with the Micro-g LaCoste FG5#228 as a reference in this case.

Repeatability is assessed by carrying out several location changes. These included different scales in the distance and temporal delay. Small-scale movement on several independent concrete pillars within the same laboratory from one day to another. Large-scale repeatability test was conducted by moving the instrument between Montpellier and the Larzac, almost 100 km in distance, during two surveys each, respectively, allowing for several weeks in between the surveys.

The results of the large-scale repeatability assessment between Montpellier and the Larzac have been reported in (Le Moigne et al. (2019)) and in the publication in review "Evaluation of the capacities of a field absolute quantum gravimeter (AQG#B01)" enclosed in this thesis.

3.2.2 Sites and instruments

The obtained gravity data has been evaluated for three different locations: Larzac Observatory, Géosciences Montpellier, and LNE (Trappes).

The Larzac Observatory (Geodetic Observatory in Karstic Environment: GEK) on the site La Jasse in L'hospitalet-du-Larzac offers a calm environment and serves as a study site for hydro-geophysical monitoring. It offers access to numerous hydro-meteorological and geodetic long-term monitoring. A supra-conducting gravimeter, the iGrav#002 by GWR Instruments, Inc., is installed on the central concrete pillar in the observatory building. Its performance is described in Fores, Champollion, Moigne, Bayer, et al. (2016). Data recorded by a STS2 seismometer installed on the Larzac site is made available by RESIF. All measurements from the Larzac observatory are hosted by OSU OREME and SNO H+. Larzac observatory and instrumentation are mainly funded by the CNRS INSU, ANR, Montpellier University, RESIF, and Occitanie region. Géosciences Montpellier is located in building 22 on the campus Triolet of the University of Montpellier and provides two rooms in the cellar for gravimeter operation.

The laboratory of SYRTE LNE at Trappes (île de France) serves as an observatory for the Watt Balance project and instrument development and testing. A well-characterised and controlled laboratory with stable concrete pillars constructed for these specific purposes. The AQG has been set up on point GR 29 in the LNE laboratories in Trappes where series of continuous measurements of g between July 23rd and August 23rd, 2019 has been obtained. A description of the room in the facility is given by Merlet et al. (2008).

Relative gravimeters Scintrex CG5#1151 and CG6#120 were present at all three sites. The Micro-g LaCoste FG5#228 served as an absolute gravity reference at the Larzac site and in Montpellier.

3.2.3 Data-processing and analysis

Polar motion and solid Earth and ocean tide corrections have been generated with the TSOFT software package developed at the Royal Observatory of Belgium (M. V. Camp and Vauterin (2005)). This feature is already integrated into the AQG software and was calculated additionally in TSOFT for the iGrav and FG5 series. Polar coordinates were obtained from the International Earth rotation and Reference Systems Service (IERS). Site-specific combined ocean and solid Earth tidal parameters were used for the Larzac site (Fores, Champollion, Moigne, Bayer, et al.

(2016)). A local atmospheric pressure admittance of -2.71574 $nm.s^{-2}hPa^{-1}$(Fores, Champollion, Moigne, Bayer, et al. (2016)) was applied for the Larzac site and a general admittance factor of -3.280 $nm.s^{-2}hPa^{-1}$ for Montpellier. FG5 and iGrav raw time series were corrected for all these effects. The iGrav raw data in Volt was converted into nm·s^{-2} using a calibration factor of -901.269 $nm.s^{-2}V^{-1}$ (Champollion, 2020, personal communication). The Larzac site offers precipitation monitoring through rain gauges, the data available at OSU OREME. The gravity and seismometer time series were investigated for their auto-correlation and cross-correlation with recorded instrumental and environmental variables.

3.3 Results and discussion

3.3.1 Stability

Stability was assessed during gravity monitoring at the three sites (Larzac observatory, Géosciences Montpellier, and LNE Trappes).

3.3.1.1 Daily averages

The acquisition starting December 2018 at the Larzac observatory provided the benefit of assessing the temporal variation of the gravity residuals in comparison with other absolute and relative gravimeters. Gravity residuals of the AQG#A01, FG5#228, and iGrav#002 obtained during the acquisition at the Larzac in December 2018 and January 2019 are shown in Figure 3.4. The differences between the AQG#01 and iGrav#002 residuals vary within the AQG#A01's daily standard deviation. Based on two absolute FG5#228 measurements, no significant drift in time was observed for the AQG#A01. The AQG#A01 series shows an average daily standard deviation of 35 nm·s^{-2}. The later acquisition in the Larzac observatory in February/March 2019 showed coherent temporal variations for the three gravimeters (Figure 3.5). As shown in Figure 3.6 the gravity residuals for the acquisition carried out in Montpellier in March and April 2019 show an average daily standard deviation of 50 nm·s^{-2}. This is also the case for the gravity series obtained in May and June 2019. The daily gravity residuals for the Trappes site are shown in Figure 3.7. Monitoring of g over several weeks on the three sites presented as daily averages shows high stability and coherence with the complementary FG5 and iGrav measurements. The results further suggest that the AQG#A01 does not show a drift during continuous measurements of about one month.

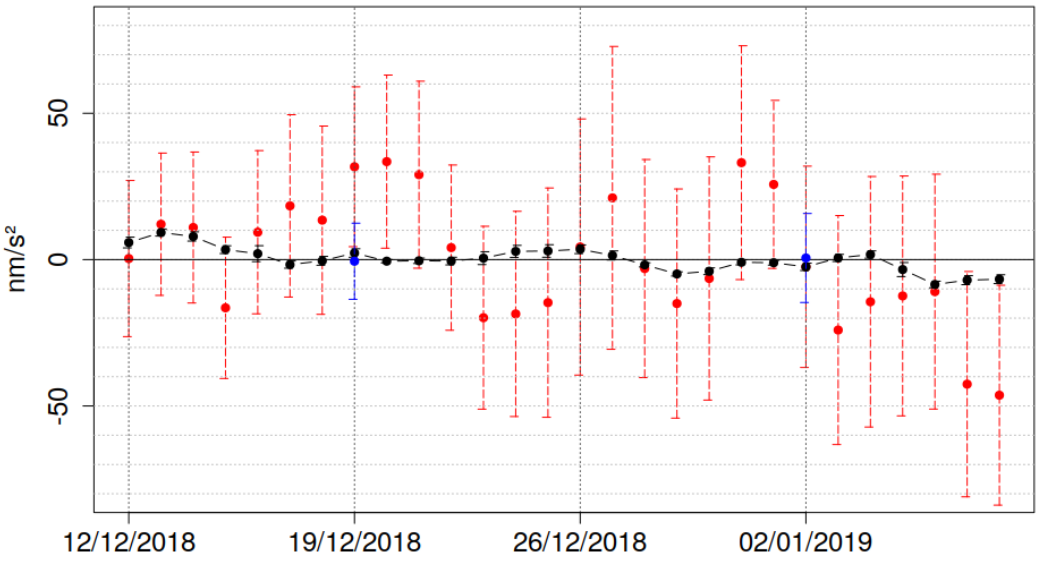

Figure 3.4: Daily corrected gravity residuals (of the mean) in nm.s^{-2}, for the AQG-A01 (red), iGrav-002 (black) and FG5-228 (blue) at the Larzac observatory 12/12/2018 - 08/01/2019

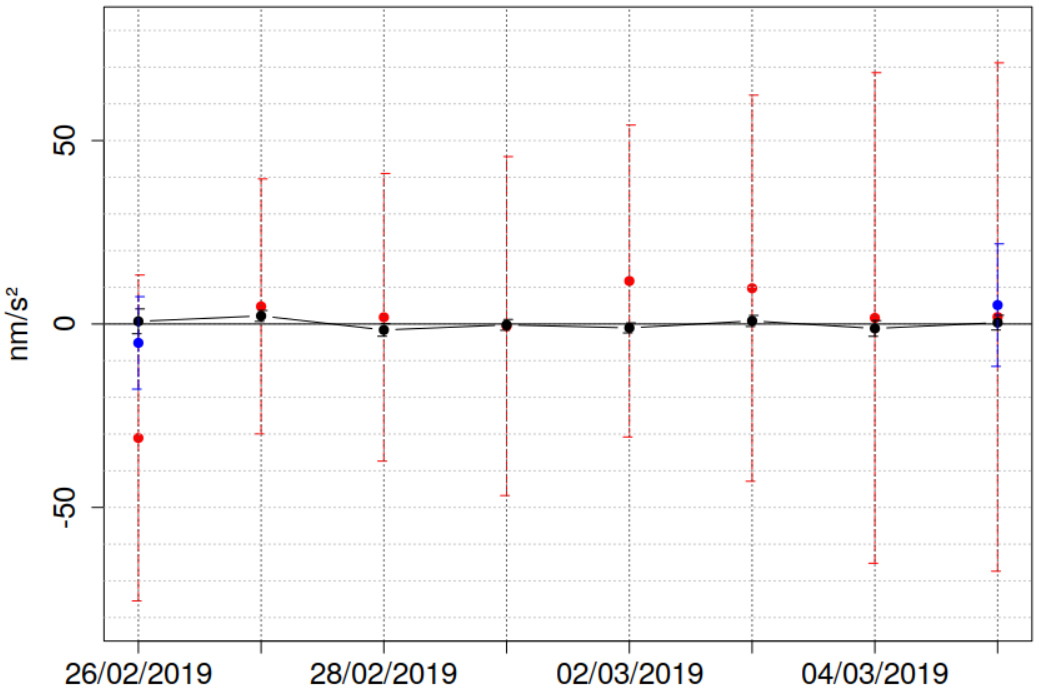

Figure 3.5: Daily corrected gravity residuals (of the mean) in nm.s^{-2}, for the AQG-A01 (red), iGrav-002 (black) and FG5-228 (blue) at the Larzac observatory, 26/02 - 06/03/2019.

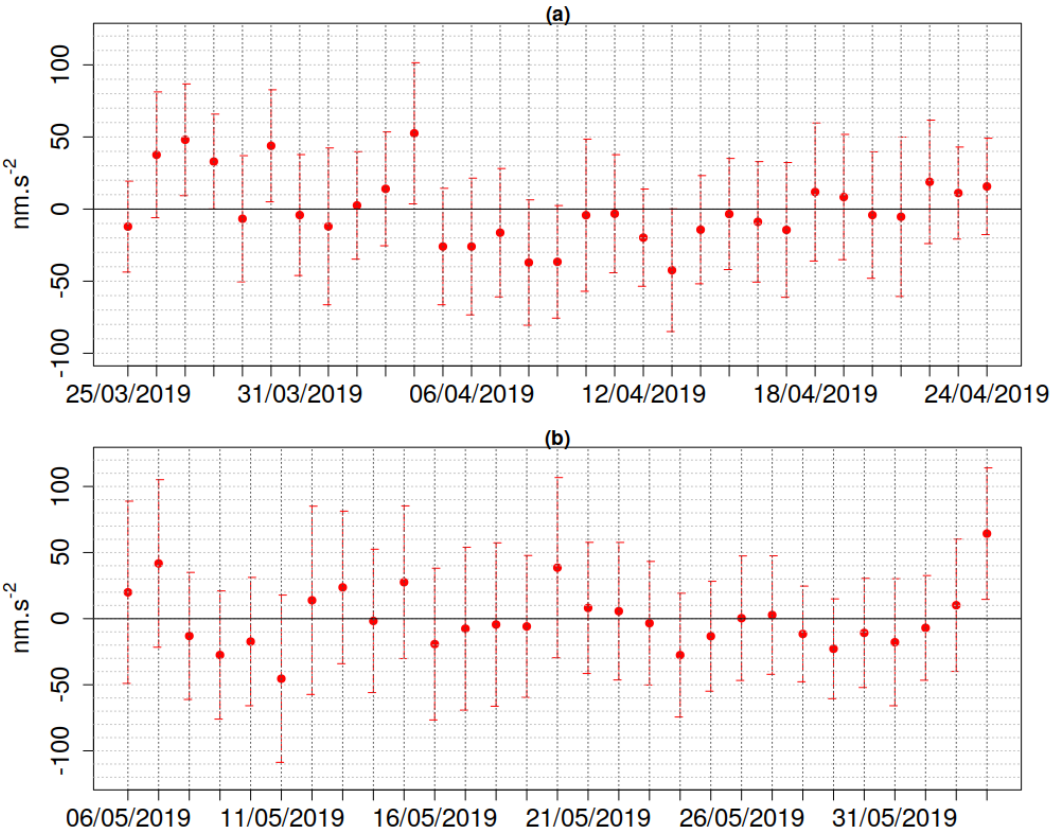

Figure 3.6: Daily averaged gravity residuals (of the mean) in nm.s^{-2}, obtained with the AQG-A01 at Géosciences Montpellier, 25/03 - 24/04/2019 (panel (a)) and 06/05 - 03/06/2019 (panel (b)).

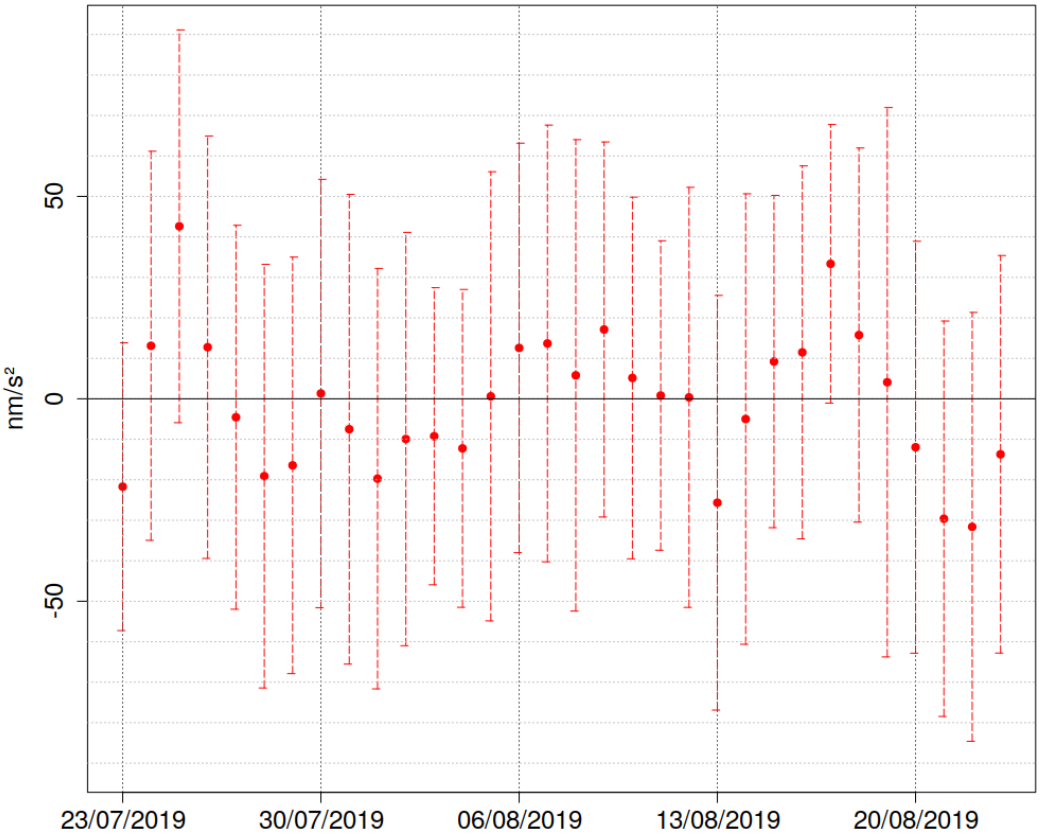

Figure 3.7: Daily gravity residuals from the mean in nm.s^{-2} obtained with the AQG-A01 at LNE (Trappes), 23/07 - 23/08/2019.

3.4 Sensitivity

Figure 3.8 compares the achieved sensitivities for the five data sets: One gravity series at Trappes and two gravity series at both Géosciences Montpellier and the Larzac observatory, respectively.

The series recorded at the Larzac recorded in December 2018 - January 2019 reaches 20 nm·s^{-2} after one hour. The short series ($\sim$ one week) recorded in February 2019 shows initially higher noise levels for averaging intervals of less than one hour. After one hour it decreases more linearly and achieves a sensitivity of better than 10 nm·s^{-2} after 24 h, whereas the longer series ($\sim$ 1 month) does not drop below the 10 nm·s^{-2} benchmark. As a comparison, the Allan deviation of the iGrav#002 gravity residuals for the time period 12/12/2018 - 08/01/2019 (Figure 3.9) at the Larzac observatory is at 0.5 nm·s^{-2} after one hour and at 2 nm·s^{-2} after 24 h. For the time series at the Larzac site a sensitivity of 500 nm.s$^{-2}\sqrt{\text{Hz}}^{-1}$ has been observed (Le Moigne et al. (2019)), which matches the previously observed sensitivity during continuous operation in 2017 (Ménoret et al. (2018)).

The two series in Montpellier (red and blue curves) show a very similar behaviour, the Montpellier series are at 28 nm·s^{-2} after one hour and at 17 nm·s^{-2} (March/April) and 21 nm·s^{-2} (May/June) after one hour. The Allan deviation increases for averaging intervals in the

range of a few hours, showing a maximum of 33 nm·s^{-2} before decreasing. At 24 h, the Allan deviations of the Montpellier series show fluctuations and do not fall below 10 nm·s^{-2}.

The series recorded at Trappes (orange curve) shows a lower Allan deviation after one hour than the Montpellier series. For integration times of a few hours, its Allan deviation increases again, but decreases to better than 10 nm·s^{-2} after 24 h.

Long-term drifts are not visible in any of the curves, as the Allan deviation does not rise again for longer integration times. Sensitivity after one hour depends on the site, as does the amplitude of the increase between one and 24 h.

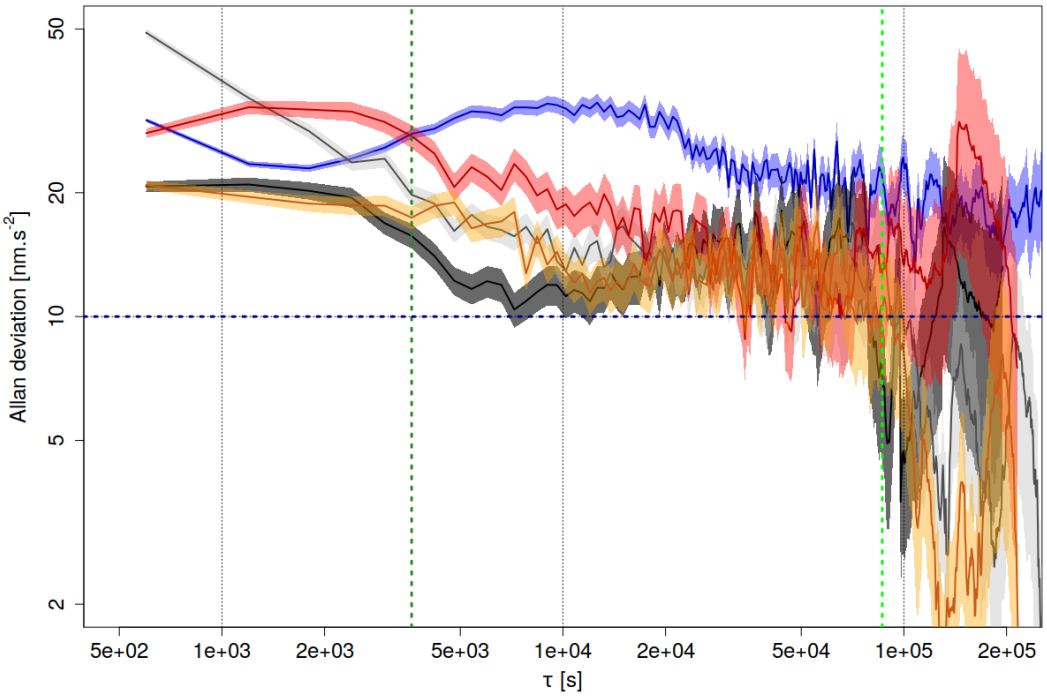

Figure 3.8: Allan deviation in nm.s^{-2} for two series at each site, Montpellier and Larzac, respectively. Géosciences Montpellier March-April 2019 (red), May-June 2019 (blue). Larzac December 2018-January 2019 (black), February 2019 (lightgrey). Trappes July-August 2019 (orange). The horizontal blue dashed line shows the sensitivity benchmark of 10 nm.s^{-2}, the dark green vertical dashed line signifies the integration period of 1 h, the light green line refers 24 h.

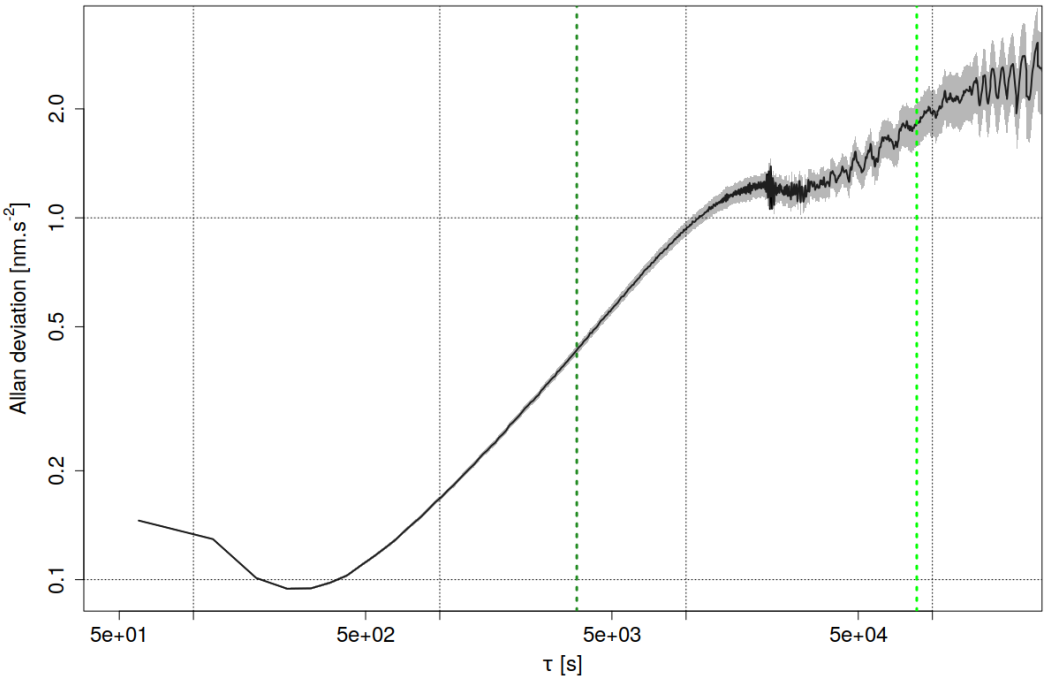

Figure 3.9: Allan deviation of 1-minute gravity residuals obtained with iGrav-002 at GEK (Larzac), 12/12/2018 - 08/01/2019. The horizontal blue dashed line shows the sensitivity benchmark of 10 nm.s^{-2}, the dark green vertical dashed line signifies the integration period of 1 h, the light green line refers 24 h.

Moreover, the Allan deviation after one hour was calculated for each day of the series at all sites. At Montpellier, the sensitivity after one hour of averaging varies between 20 and 35 nm·s^{-2} in March 2019 (Figure 3.15), showing similar values between 15 and 33 nm·s^{-2} in May/June (Figure 3.16). For Trappes, these values vary in a similar range of 15 to 35 nm·s^{-2}. At the Larzac observatory, the sensitivity after one hour is slightly better than at the other two sites, showing between 10 and 30 nm·s^{-2} (Figure 3.13), not exceeding 30 nm·s^{-2} at any day of the series. For the Larzac site, the Christmas holidays show increased noise levels, which could be possibly be linked to increased traffic on the highway A75 at approximately 1 km distance. At Montpellier and Trappes, no clear difference in short-term sensitivity between weekdays and weekend is visible.

Figures 3.11, 3.10 and 3.12 show day and nighttime (10 p.m. - 6 a.m.) sensitivity for the three sites. For the Montpellier series, the difference is the least clear. For certain time intervals, a distinct nighttime decrease in noise level is visible in the Larzac and Trappes series. For both sites, this distinction occurs at different time intervals.

Generally, high variability of precision is observed. The observed sensitivity of the AQG#A01 appears to mainly depend on the site. After 24 h, the AQG#A01 can achieve a sensitivity of less than 10 nm·s^{-2} for the Larzac site. The analyses showed no clear and reproducible patterns of influences on the level of sensitivity regarding the day of the week or time of day.

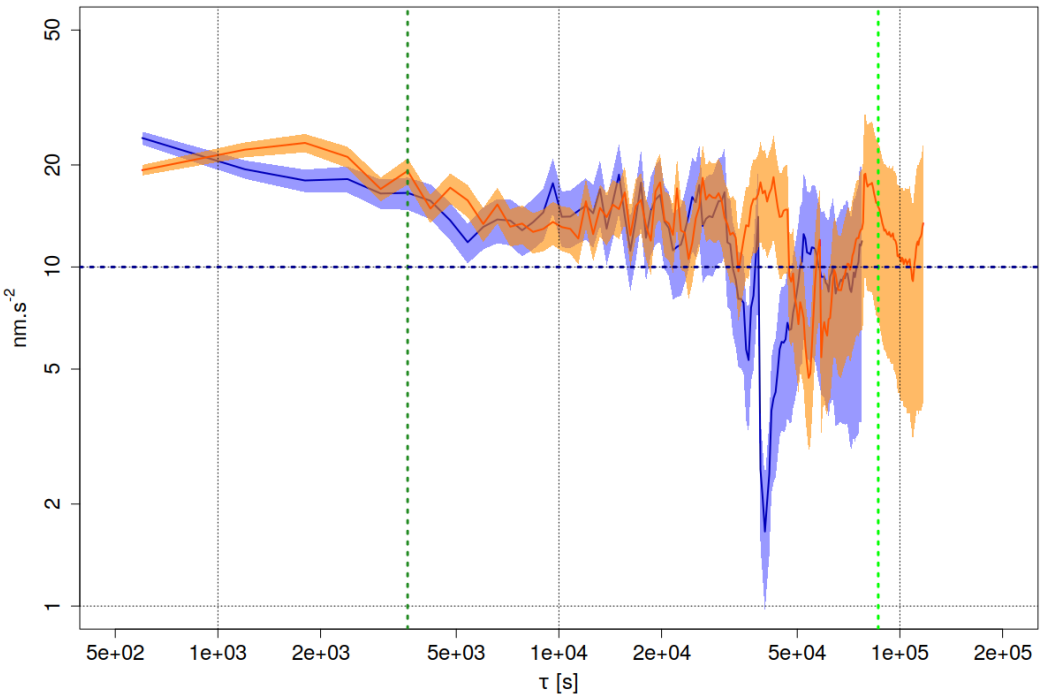

Figure 3.10: Allan deviation at night (blue) and day (orange). AQG-A01 at GEK (Larzac) 12/12/2018 - 08/01/2019.

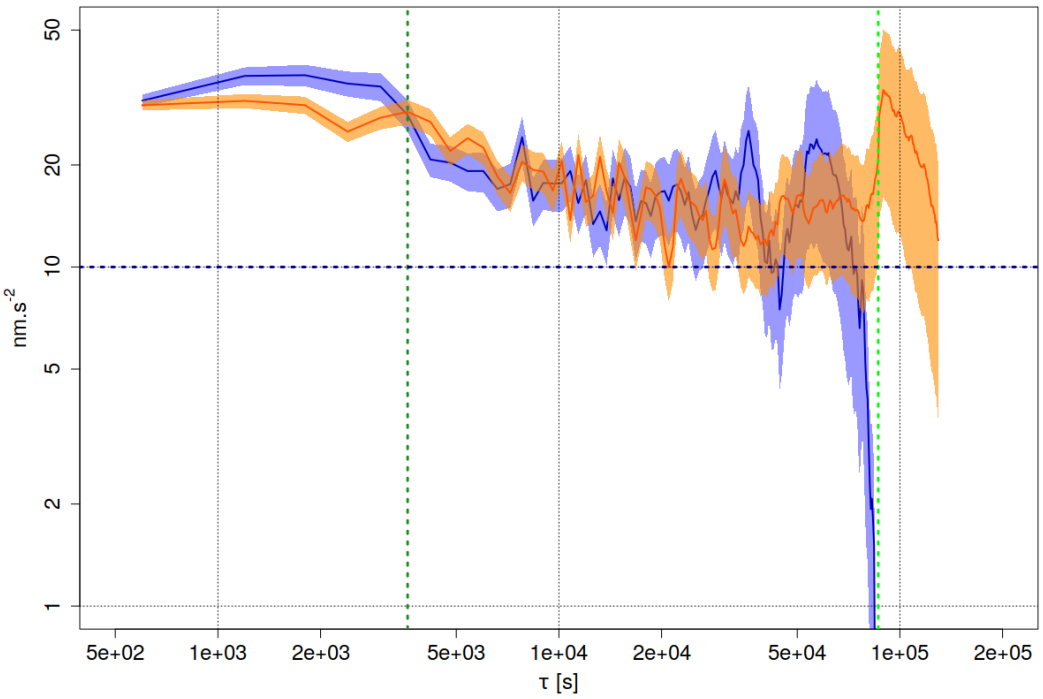

Figure 3.11: Allan deviation at night (blue) and day (orange). AQG-A01 at Géosciences Montpellier, 25/03 - 24/04/2019.

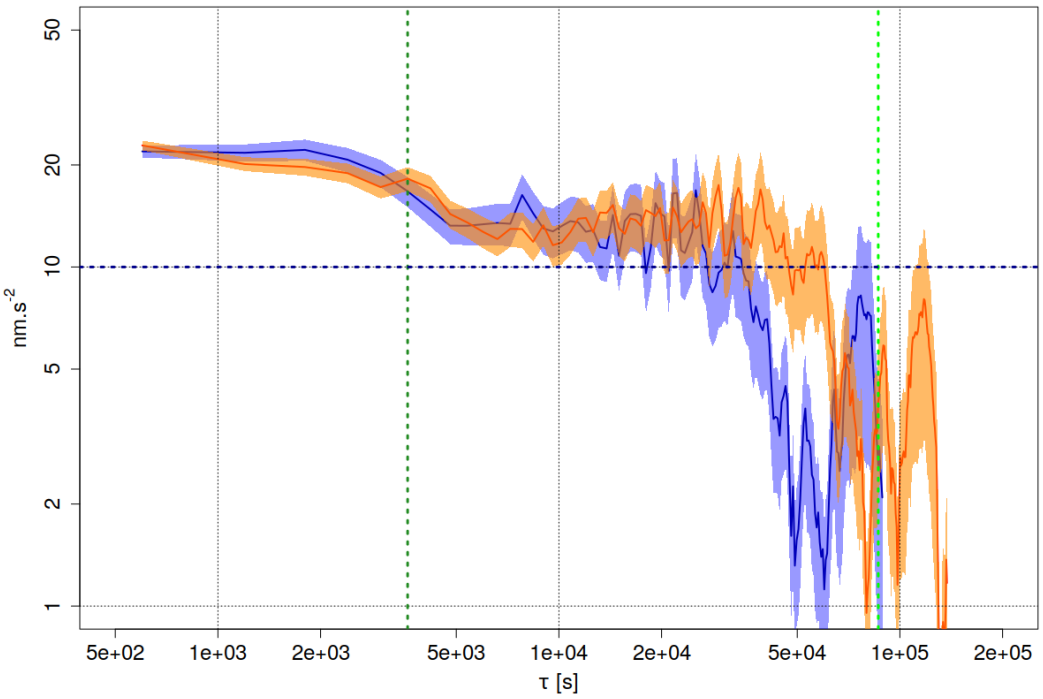

Figure 3.12: Allan deviation at night (blue) and day (orange). AQG-A01 at Trappes 23/07/2019 - 23/08/2019.

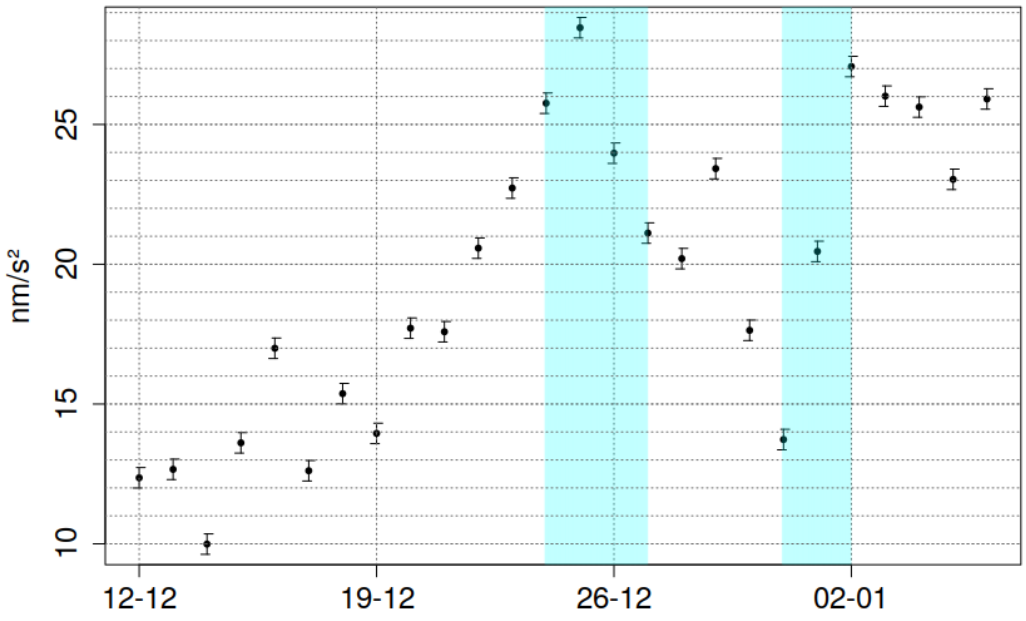

Figure 3.13: Allan deviation after 1 h of integration duration, calculated for each acquisition day. AQG-A01 at GEK (Larzac) 12/12/2018 - 08/01/2019. Public holidays are marked in light blue.

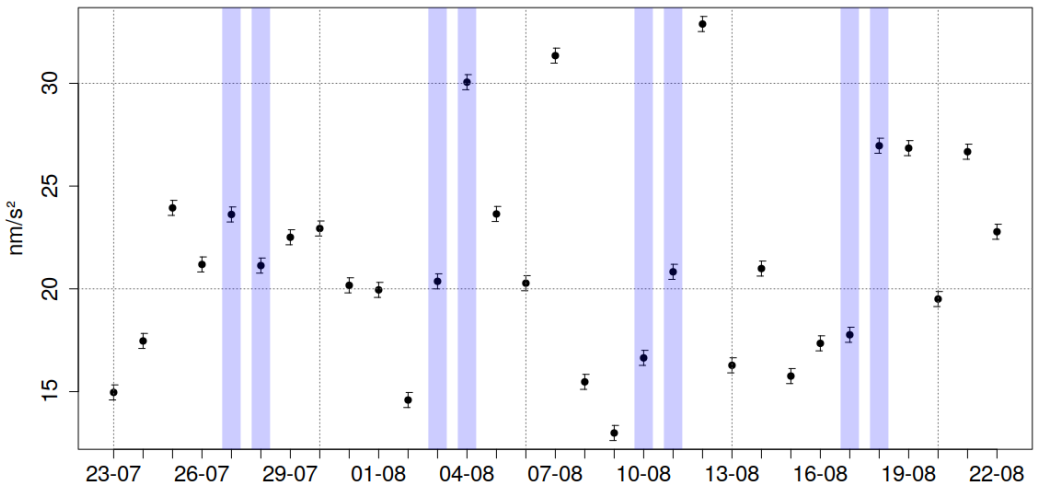

Figure 3.14: Allan deviation after 1 h of integration duration, calculated for each acquisition day. AQG-A01 at Trappes 23/07/2019 - 23/08/2019. Weekends are marked in light purple.

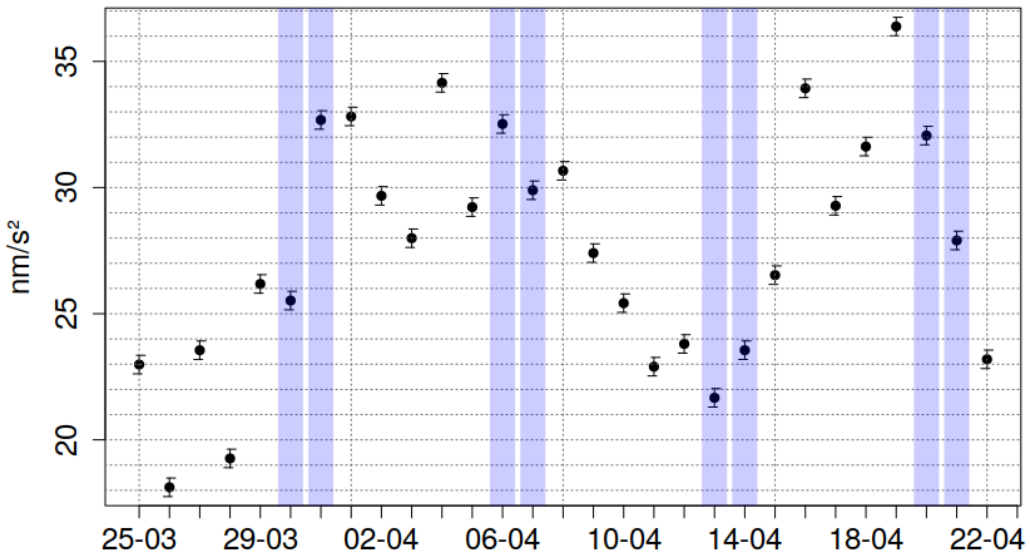

Figure 3.15: Allan deviation in $nm.s^{-2}$ after 1 h of integration duration, calculated for each acquisition day. AQG-A01 at Géosciences Montpellier on 25/03-24/04/2019. Weekends are marked in light purple.

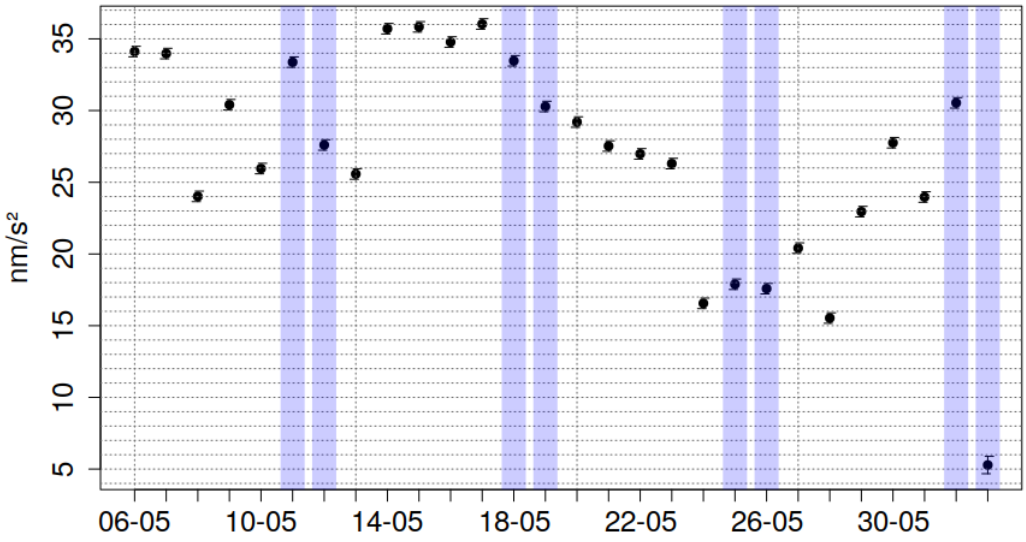

Figure 3.16: Allan deviation in nm.s^{-2} after 1 h of integration duration, calculated for each acquisition day. AQG-A01 at Géosciences Montpellier on 06/05-03/06/2019. Weekends are marked in light purple.

3.4.0.1 Sub-daily variations

The earlier described decrease in sensitivity for data averaging periods of a few hours (Figure 3.8) are also visible in oscillations at sub-daily time intervals. Hourly averaged data show variations of $\sim$ 100 nm·s^{-2}, as shown for Trappes (Figure 3.19), Montpellier (Figure 3.18) and the Larzac (Figure 3.17). A larger scatter is visible in the series obtained in Montpellier and Trappes than for the Larzac site.

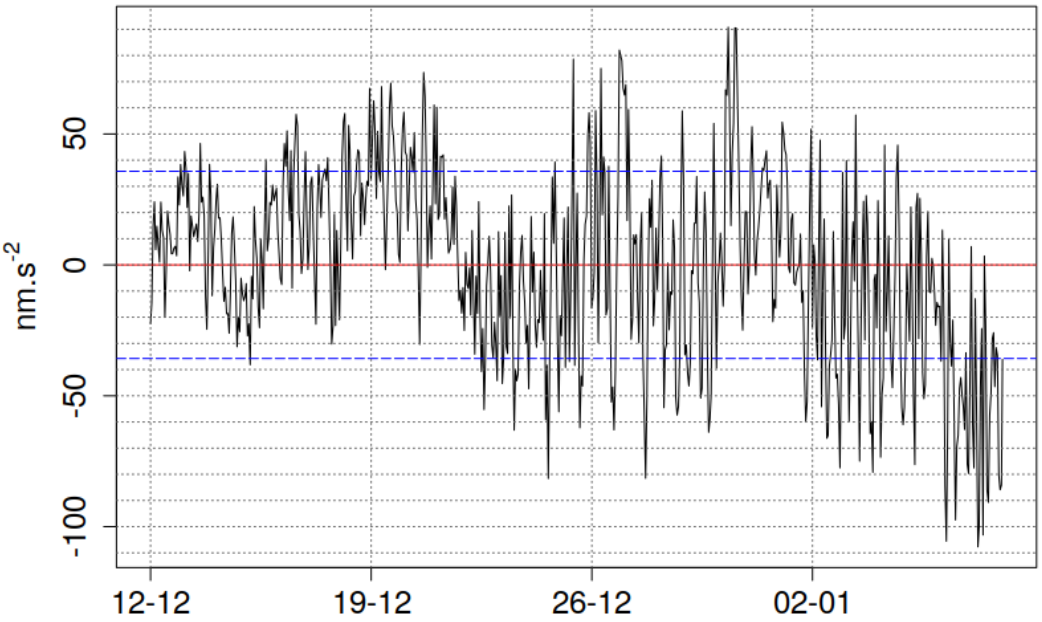

Figure 3.17: AQG-A01 hourly corrected gravity residuals (of the mean) in nm.s^{-2} at the Larzac observatory, 12/12/2018 - 08/01/2019. Mean (red) and standard deviation over the whole series (dashed blue line).

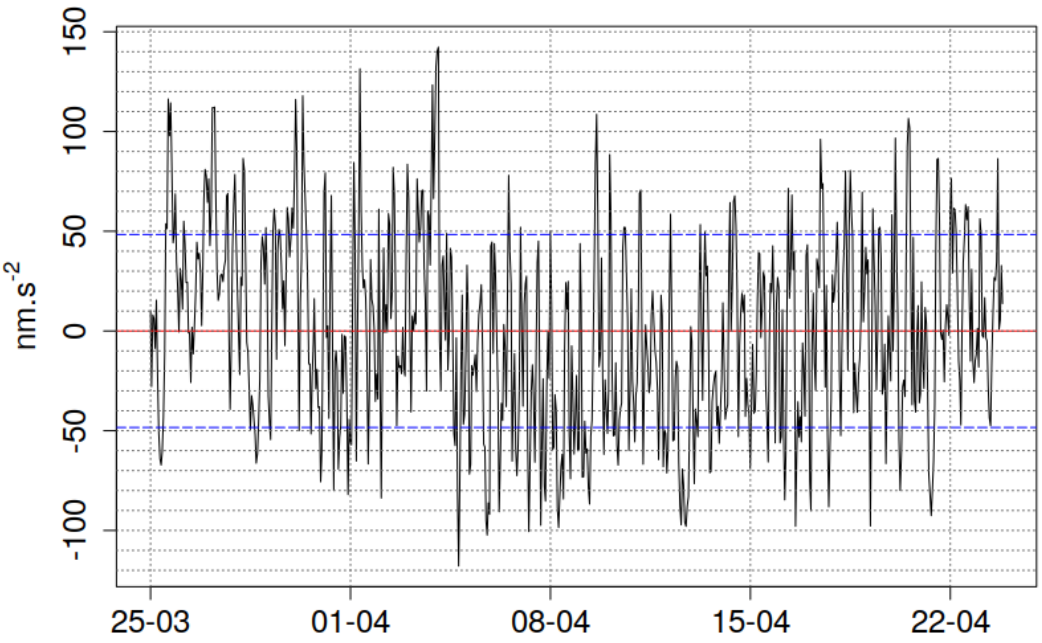

Figure 3.18: AQG-A01 hourly averaged gravity residuals (of the mean) in nm.s^{-2}, obtained with the AQG-A01 at Géosciences Montpellier, 25/03 - 24/04/2019. Mean (red) and standard deviation over the whole series (dashed blue line).

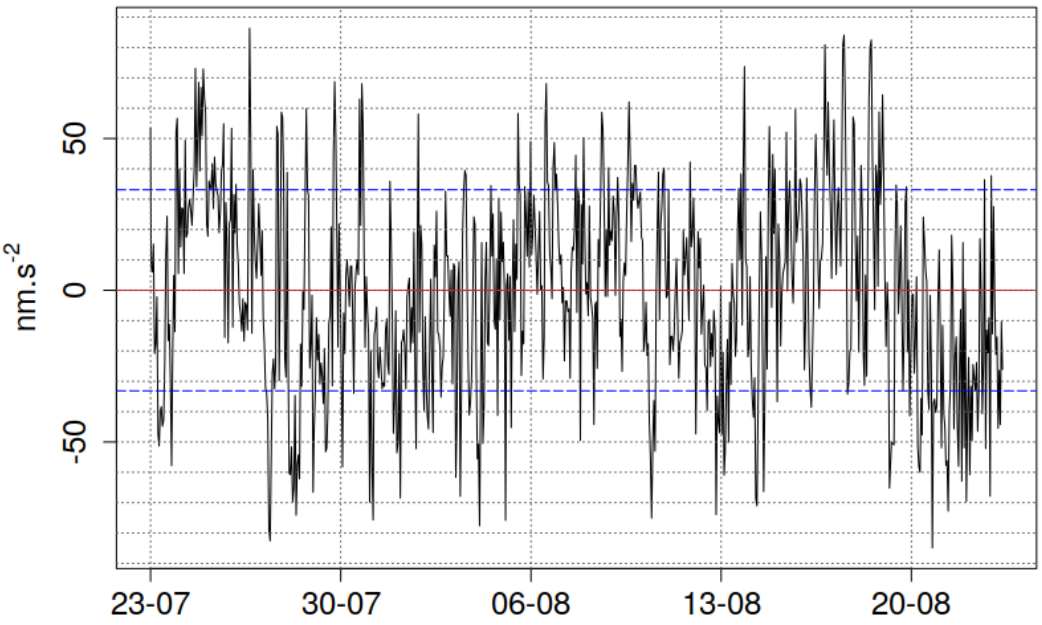

Figure 3.19: AQG-A01 hourly gravity residuals from the mean in nm.s^{-2} obtained with the AQG-A01 at LNE (Trappes), 23/07 - 23/08/2019. Mean (red) and standard deviation over the whole series (dashed blue line).

The temporal structure of the sub-daily oscillations is assessed by calculating the auto-correlation of the gravity time series, which was carried out for time lags in hourly steps for a total window of 48 h. These analyses show that the three sites show different noise structures. At the Larzac observatory (Figure 3.20) a maximum positive correlation of 0.4 at a time lag of 24 h is

observed. Two further peaks between 7 and 8 h as well as between 15 and 16 h, respectively, show a positive correlation of approximately 0.3. The iGrav#002 gravity residuals have been analysed for possible auto-correlated structure and did not show significant signals.

At Géosciences Montpellier a similar auto-correlated signal at 24 h is observed. Figure 3.21 shows a maximum correlation of 0.4, the survey in May/June (Figure 3.22) behaves similarly. The series obtained in Montpellier does not include the auto-correlated signals observed at the Larzac, but show a second peak at the 12 h time lag with a positive correlation of approximately 0.2. At Trappes, a weaker but significant auto-correlation of 0.2 around the 24h time lag has been identified (Figure 3.23).

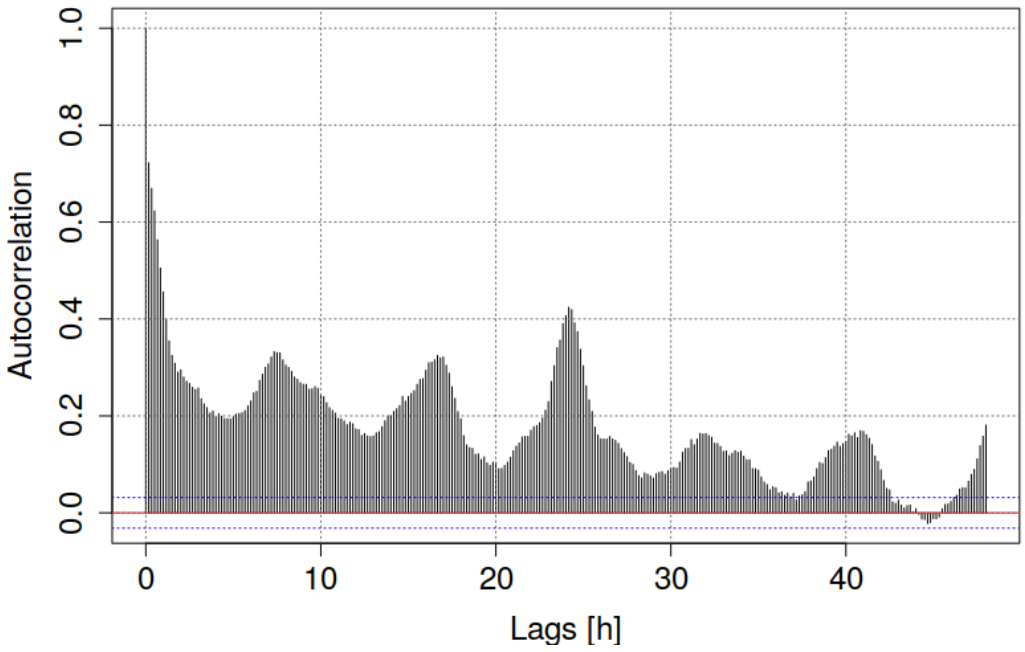

Figure 3.20: Auto-correlation of gravity residuals for a 48 h window. AQG-A01 at GEK (Larzac) 12/12/2018 - 08/01/2019.

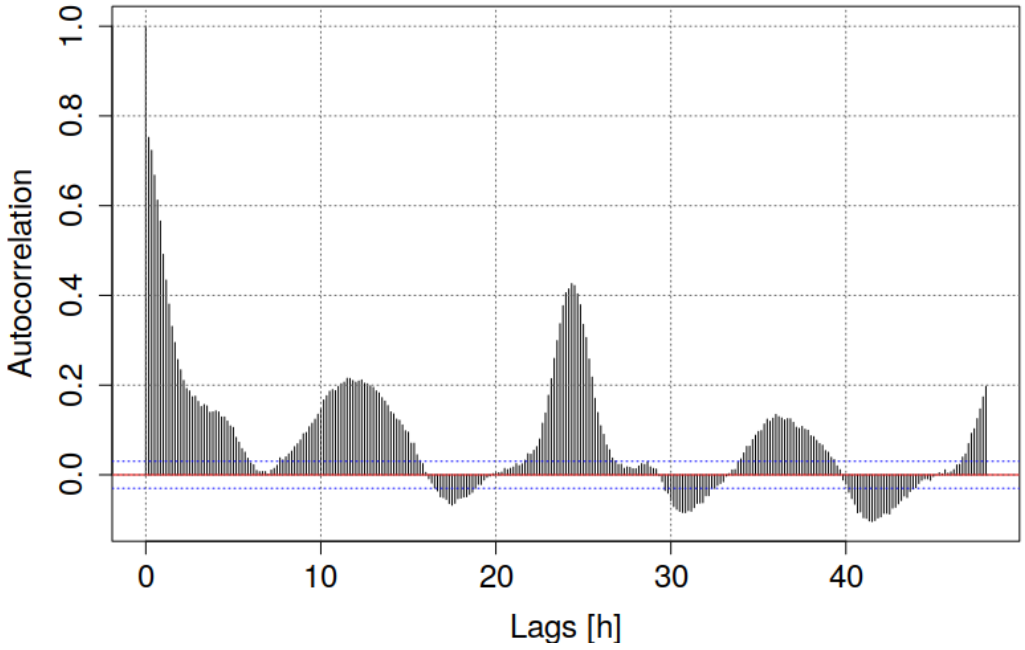

Figure 3.21: Auto-correlation of gravity residuals for a 48 h window. AQG-A01 at Géosciences Montpellier during 25/03 - 24/04/2019

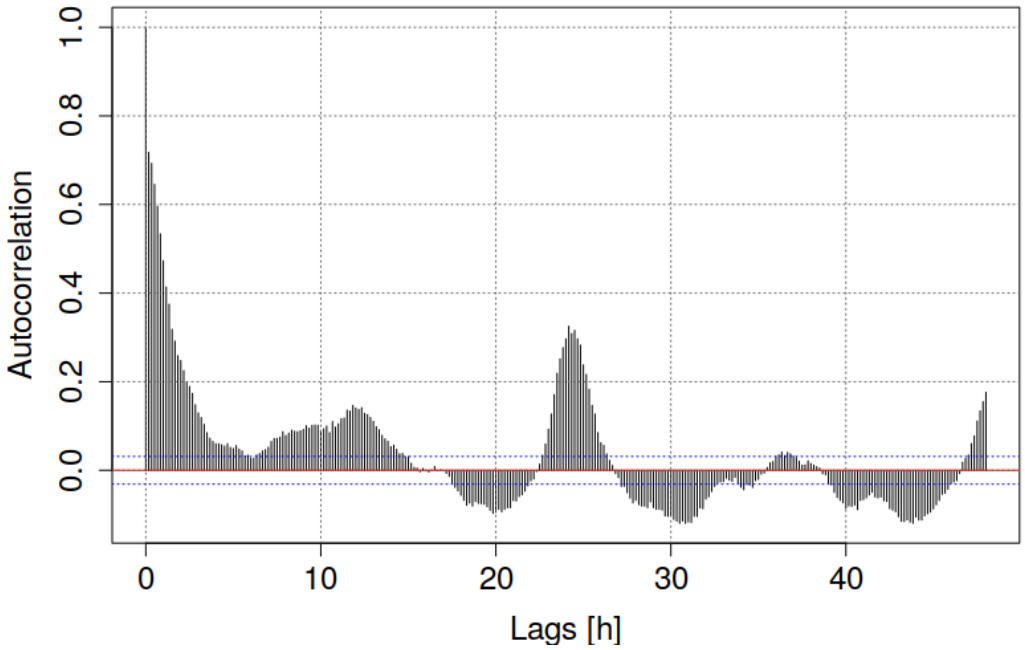

Figure 3.22: Auto-correlation of gravity residuals for a 48 h window. AQG-A01 at Géosciences Montpellier during 06/05 - 03/06/2019

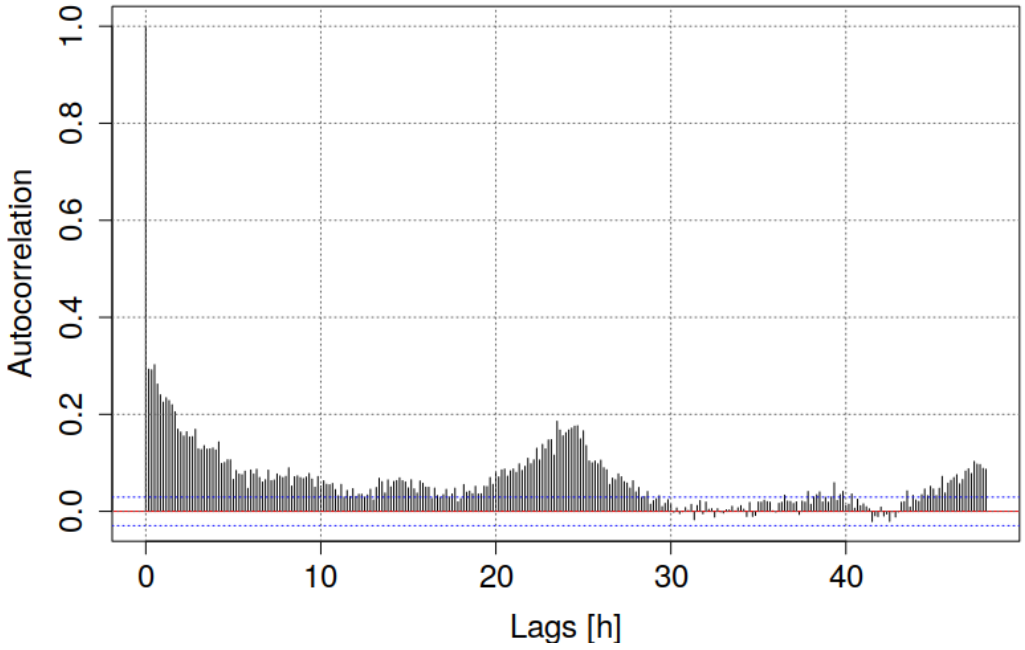

Figure 3.23: Auto-correlation of gravity residuals for a 48 h window. AQG-A01 at LNE (Trappes) 23/07 - 23/08/2019

Oscillations of sub-daily periods are visible in the gravity residuals for all sites. The structure of the noise at these intervals is not clear and their frequency and auto-correlation signals are not reproducible from one site to another. All sites show positively, significantly auto-correlated time lags of roughly 24 hours, respectively, which can easily be explained by anthropogenic noise. The Montpellier site also shows a 12 hour time lag. The auto-correlation of the gravity residuals obtained at the Larzac site shows significant positively correlated signals that can be seen for seven to eight and 15 - 16 hour time lags.

3.4.0.1.1 Additional environmental effects

Seismic noise

Seismic data at the Larzac was used to investigate the oscillations at these specific time lags. Data recorded by a STS-2 seismometer installed on the Larzac site is made available by RESIF. Seismic velocities of North and vertical direction, respectively at 1, 20, and 200 Hz was treated using the *R* software package 'eseis - Environmental Seismology Toolbox' (Dietze (2018)). Deconvolution was performed given the sensor details (STS-2 broadband triaxial sensor by Streckeisen). The auto-correlation function was applied to all frequencies and directions (six in total) for a 24h window. The 20 Hz data had been cut into weekly chunks to reduce computational load. The seismic velocities in a horizontal and upward direction at a frequency of one Hz and at 200 Hz show at the most weakly auto-correlated signal (Figure 3.24). The power spectral density (PSD) characterises the power distribution of a signal as a function of frequency. The PSD

of the vertical velocities as 20 Hz (Figures 3.27 and 3.28; Haned and Champollion, personal communication) show a weak pattern every 24 h, that reduces further during the Christmas holidays. However, for 20 Hz velocities for both directions negatively correlated time lags of about two hours and positively correlated time lags of five to six hours (Figure 3.25) appeared to dominant.

In order to focus on the residual noise, the seismic data was filtered for frequencies smaller than 1/60 Hz, using the function 'ffilter' from the R-package 'seewave' (Sueur, Aubin, and Simonis (2008)) which first applies a Fourier transform before a user-chosen frequency range is filtered out. After filtering the 20 Hz time series for frequencies below 1/60 Hz, the auto-correlation was recalculated and yielded no significant auto-correlation. The comparison of the auto-correlation of the gravity residuals obtained on the Larzac site in December 2018 to January 2019 using the data obtained from the on-site STS2 seismometer did not find similarity in frequencies. It cannot be ruled out conclusively that the observed oscillations are related to incomplete correction of ground vibrations, but our analysis shows that it is not very likely. We do not have an external explanation for the seven to eight or 15 - 16 h oscillations visible only for the AQG#A01 series for the Larzac site.

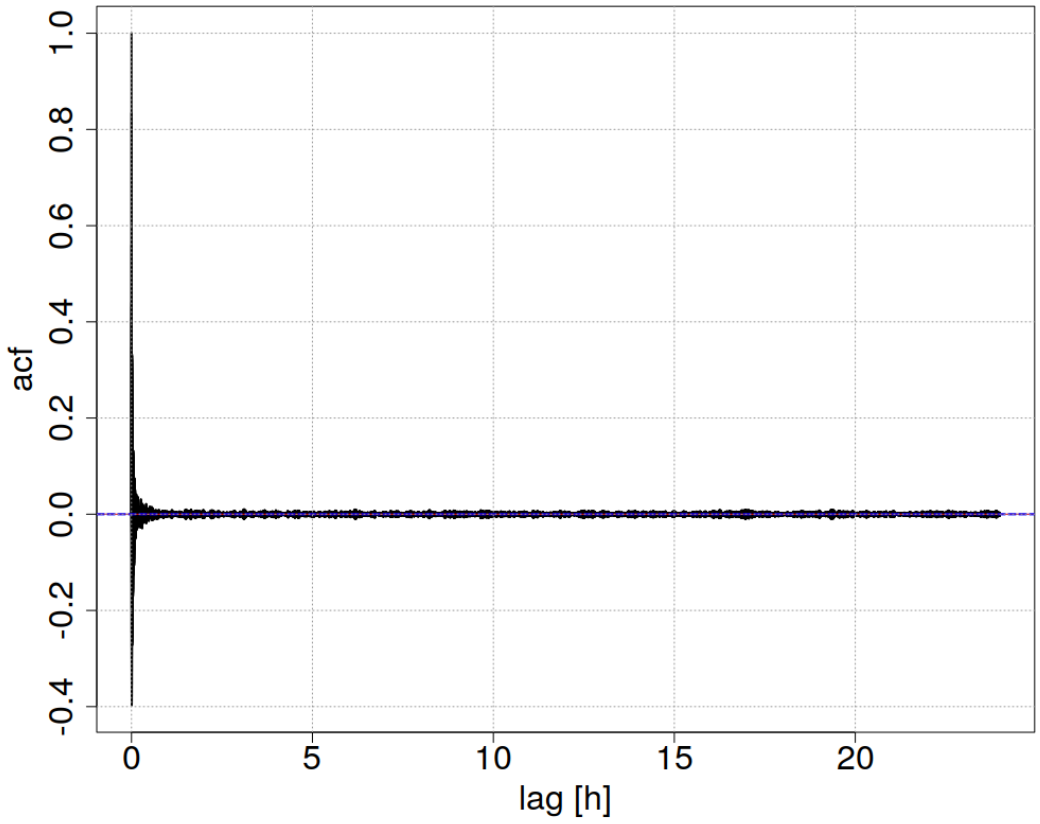

Figure 3.24: Auto-correlation of seismic velocities in Northern direction at one Hz obtained from the STS-2 seismometer installed on the Larzac observatory site (RESIF). Time lags in hours. 12/2018 - 01/2019

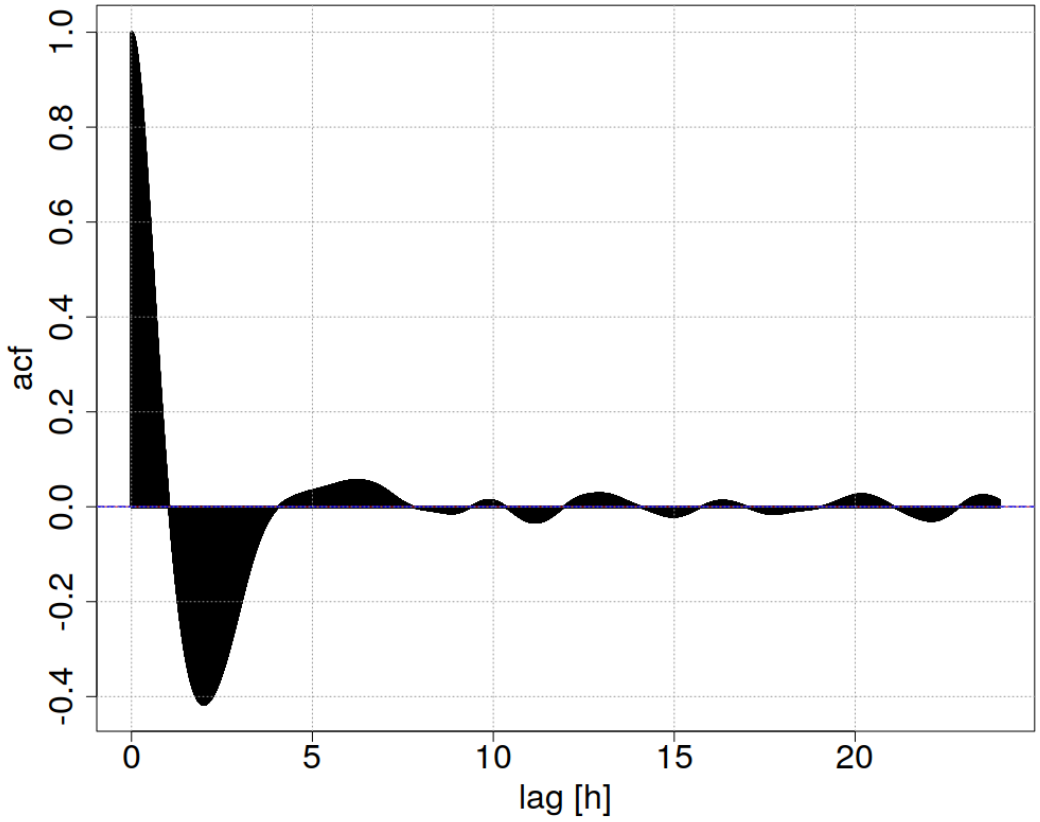

Figure 3.25: Auto-correlation of vertical seismic velocities at 20 Hz obtained from the STS-2 seismometer installed on the Larzac observatory site (RESIF). Time lags in hours. 12/2018 - 01/2019

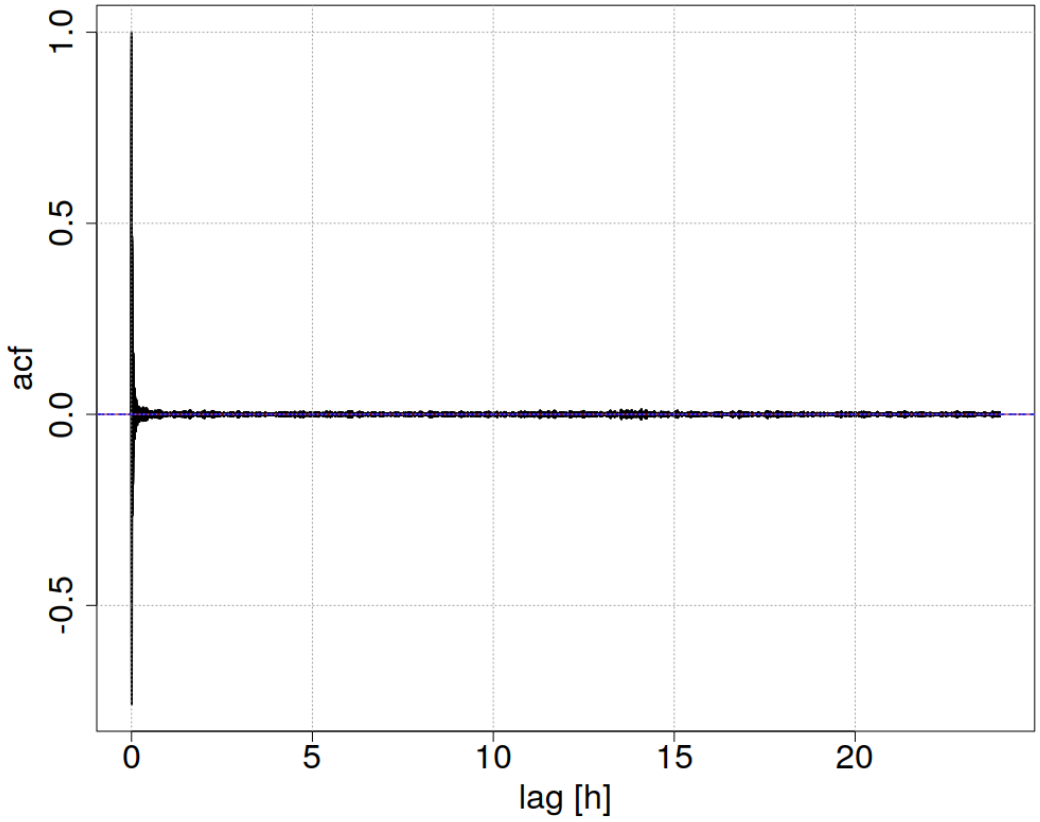

Figure 3.26: Auto-correlation of vertical vertical seismic velocities at 20 Hz filtred for frequencies lower than 1/60 Hz obtained from the STS-2 seismometer installed on the Larzac observatory site (RESIF). Time lags in hours. 12/2018 - 01/2019

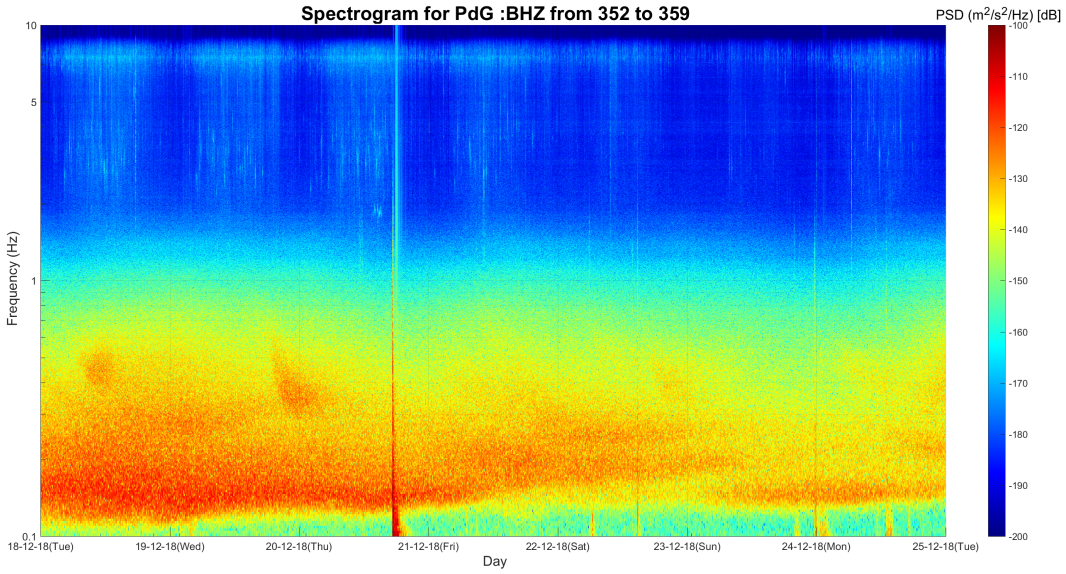

Figure 3.27: Power spectral density plot of vertical seismic velocities at 20 Hz obtained from the STS-2 seismometer installed on the Larzac observatory site (RESIF). Frequency in Hz. 12/12/2018 - 25/12/2019. Haned and Champollion, personal communication.

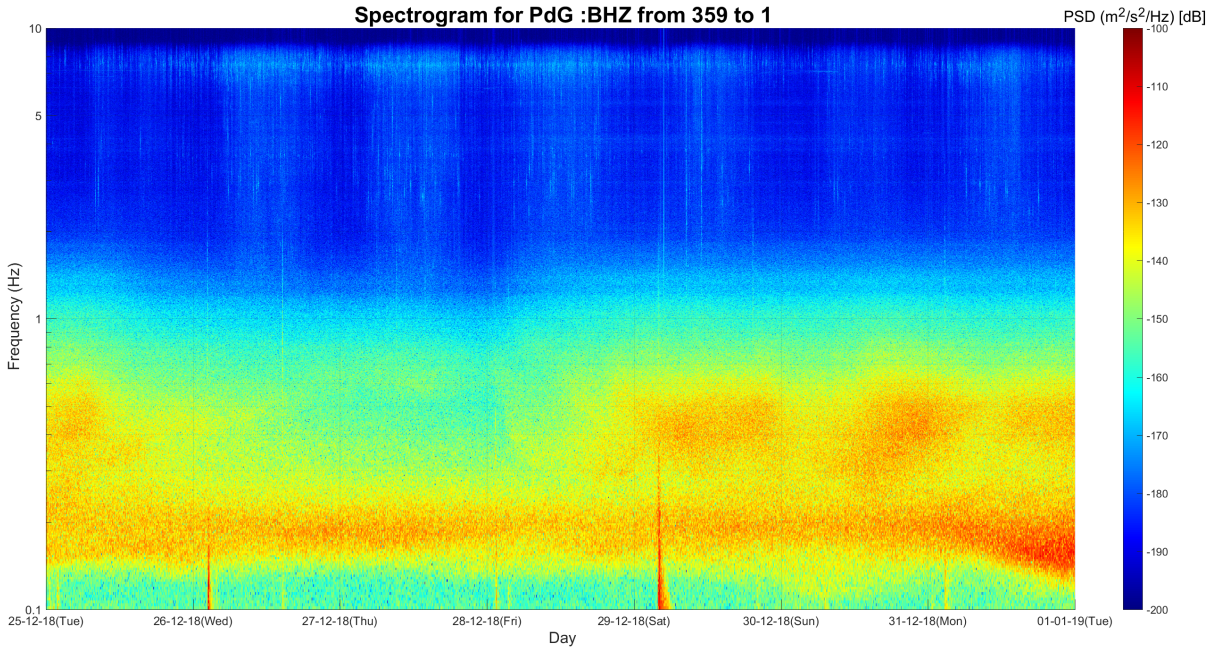

Figure 3.28: Power spectral density plot of vertical seismic velocities at 20 Hz obtained from the STS-2 seismometer installed on the Larzac observatory site (RESIF). Frequency in Hz. 25/12/2018 - 01/01/2019, Haned and Champollion, personal communication.

3.4.0.1.2 Cross-correlation

The cross-correlation between the observed sub-daily oscillations in the gravity residuals and the environmental and instrumental variables recorded by the AQG#A01 was evaluated. Correlation matrices based on the entire time series were calculated for each data set. Correlations of > 0.2 between gravity residuals are discussed and compared between sites and acquisition periods.

Larzac

The correlation matrix for the Larzac series in December 2018 (Figure 3.29) shows positive correlations between 0.3 and 0.35 for the laser properties and temperature variables. The gravity residuals and temperature residuals are not continuously correlated throughout the time series (Figure 3.30).

The correlation matrix for the series obtained in February 2019 (Figure 3.31) gives a different picture: Only two laser properties (ϕ_{cooler} and $\phi_{repumper}$) are correlated with the measurements of g and to a lesser extent than in December 2018.

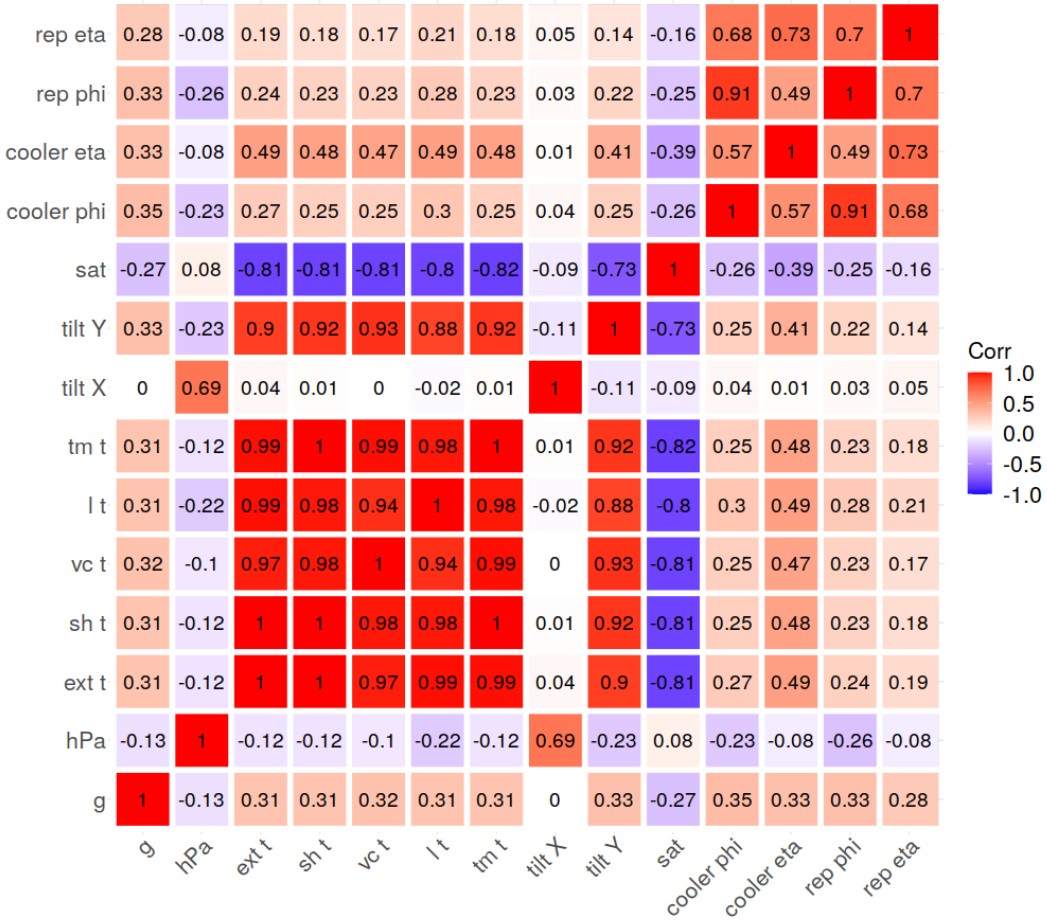

Figure 3.29: Correlogram of gravity residuals ('g') and acquistion variables. Gravity residuals averaged over 10 minutes. AQG-A01 at GEK (Larzac) 12/12/2018 - 08/01/2019. Variables: 'hPa' : atmospheric pressure, 'ext t': external temperature, 'sh t' : sensor head temp., 'vc t': vacuum chamber temp., 'l t': laser temp., 'tm t' : tiltmeter temp., tilt X, tilt Y, 'sat' : correction frequency offset of the saturated absorption spectroscopy, Laser polarisation angles phi and eta (rad) of the two lasers: cooler laser and repumper.

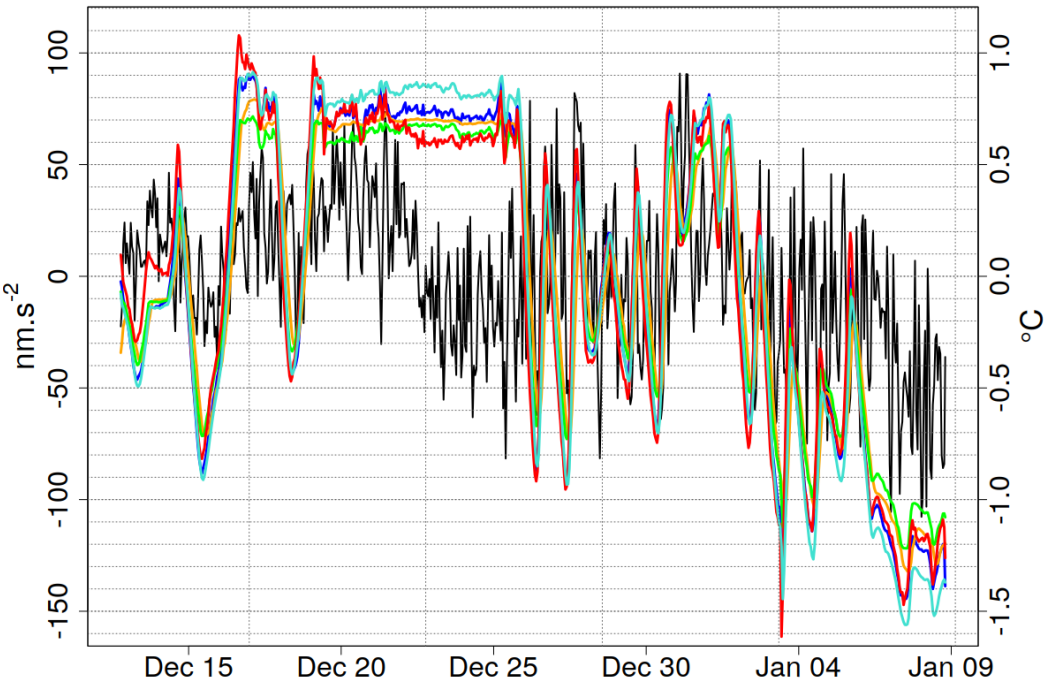

Figure 3.30: AQG-A01 at GEK (Larzac) 12/12/2018 - 08/01/2019. 10 minute gravity residuals from the mean in nm.s^{-2}. Temperature residuals in °C from the mean: External (blue), laser (red), sensor head (green), vacuum chamber (orange) and tiltmeter (turquoise).

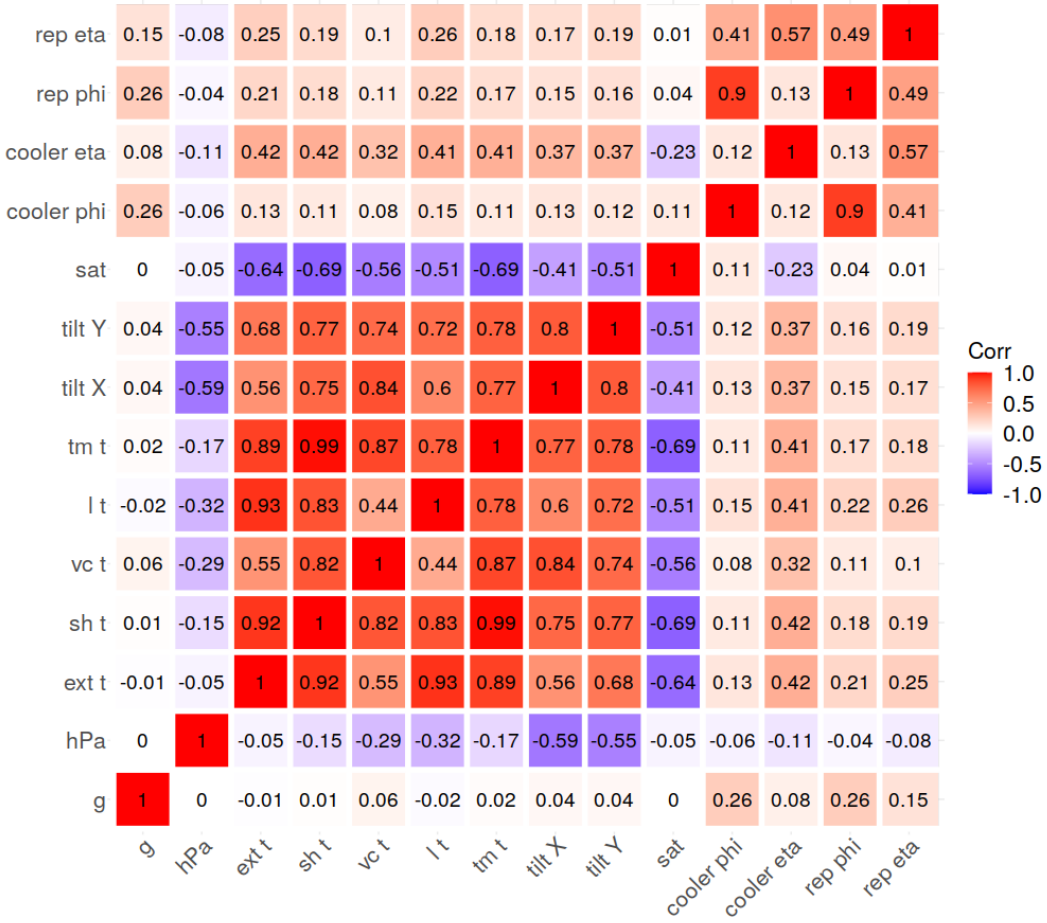

Figure 3.31: Correlogram of gravity residuals ('g') and acquistion variables. Gravity residuals averaged over 10 minutes. AQG-A01 at GEK (Larzac) 26/02 - 06/03/2019. Variables: 'hPa' : atmospheric pressure, 'ext t': external temperature, 'sh t' : sensor head temp., 'vc t': vacuum chamber temp., 'l t': laser temp., 'tm t' : tiltmeter temp., tilt X, tilt Y, 'sat' : correction frequency offset of the saturated absorption spectroscopy, Laser polarisation angles phi and eta (rad) of the two lasers: cooler laser and repumper.

Montpellier

For the first series acquired at Géosciences Montpellier (25/03 - 24/04/2019), gravity residuals are positively correlated with tilts y-direction (0.59) and negatively with tilts in x-direction (-0.8) (Figure 3.32). In the second series (06/05 - 03/06/2019), only ϕ_{cooler} and $\phi_{repumper}$ show a positive correlation of more than 0.2 with the gravity residuals.

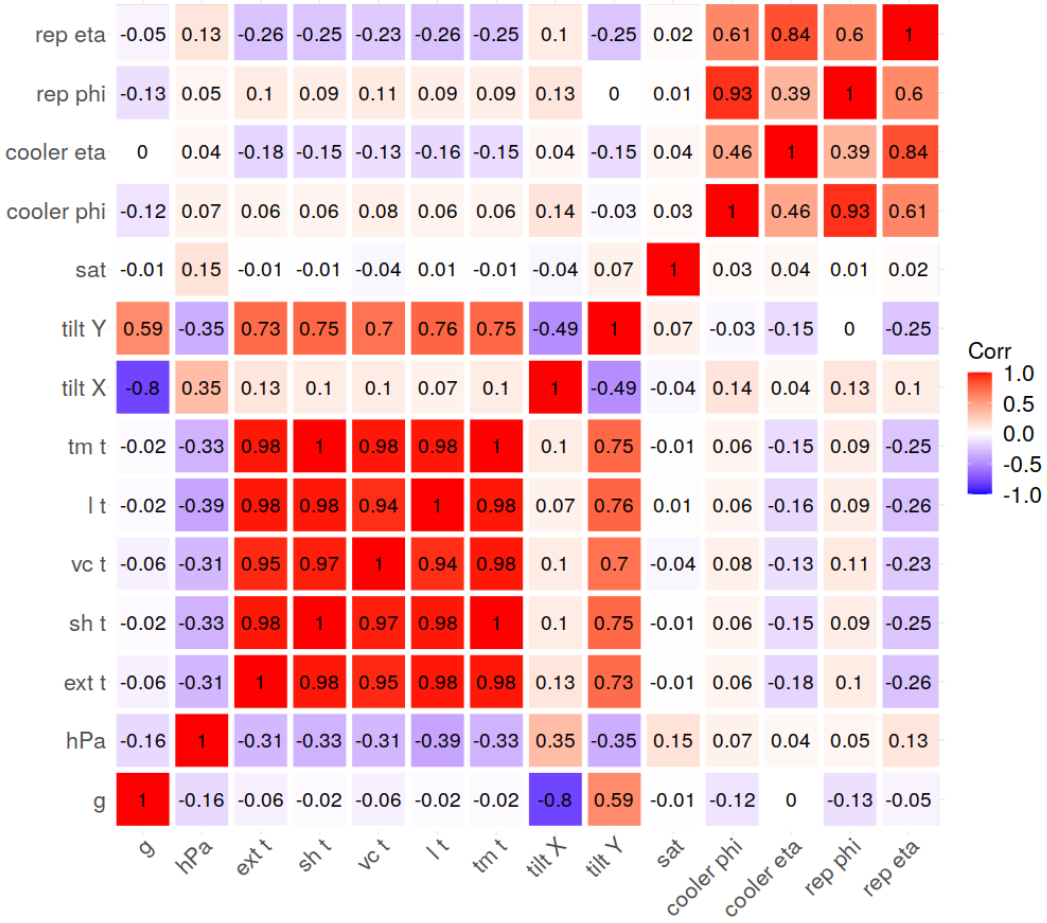

Figure 3.32: Correlogram of gravity residuals ('g') and acquistion variables. Gravity residuals averaged over 10 minutes. AQG-A01 at Géosciences Montpellier 25/03 - 24/04/2019. Variables: 'hPa' : atmospheric pressure, 'ext t': external temperature, 'sh t' : sensor head temp., 'vc t': vacuum chamber temp., 'l t': laser temp., 'tm t' : tiltmeter temp., tilt X, tilt Y, 'sat' : correction frequency offset of the saturated absorption spectroscopy, Laser polarisation angles phi and eta (rad) of the two lasers: cooler laser and repumper.

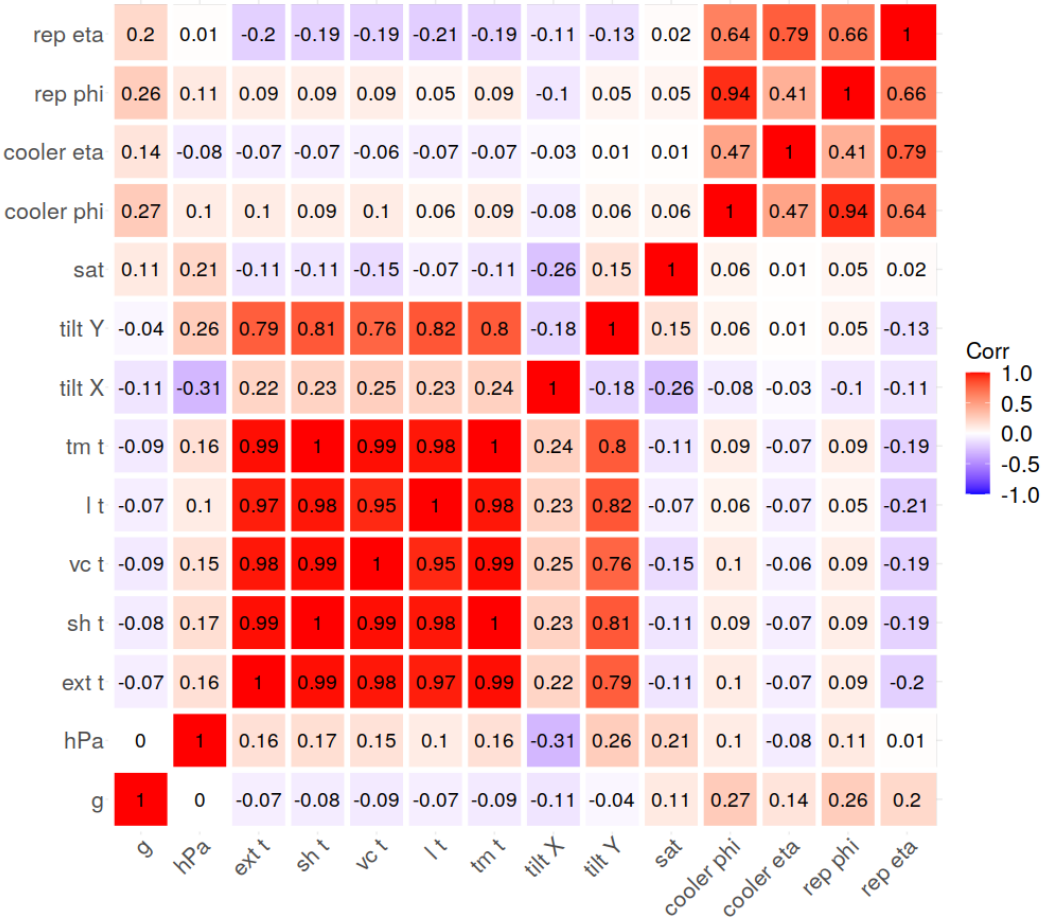

Figure 3.33: Correlogram of gravity residuals ('g') and acquistion variables. Gravity residuals averaged over 10 minutes. AQG-A01 at Géosciences Montpellier 06/05 - 03/06/2019. Variables: 'hPa' : atmospheric pressure, 'ext t': external temperature, 'sh t' : sensor head temp., 'vc t': vacuum chamber temp., 'l t': laser temp., 'tm t' : tiltmeter temp., tilt X, tilt Y, 'sat' : correction frequency offset of the saturated absorption spectroscopy, Laser polarisation angles phi and eta (rad) of the two lasers: cooler laser and repumper.

Trappes

The Trappes series also yields positive correlations between gravity residuals and ϕ_{cooler} and $\phi_{repumper}$ of 0.36. These correlations are stronger than in Montpellier or Larzac. Moreover, $\eta_{repumper}$ is weakly correlated with gravity (0.24).

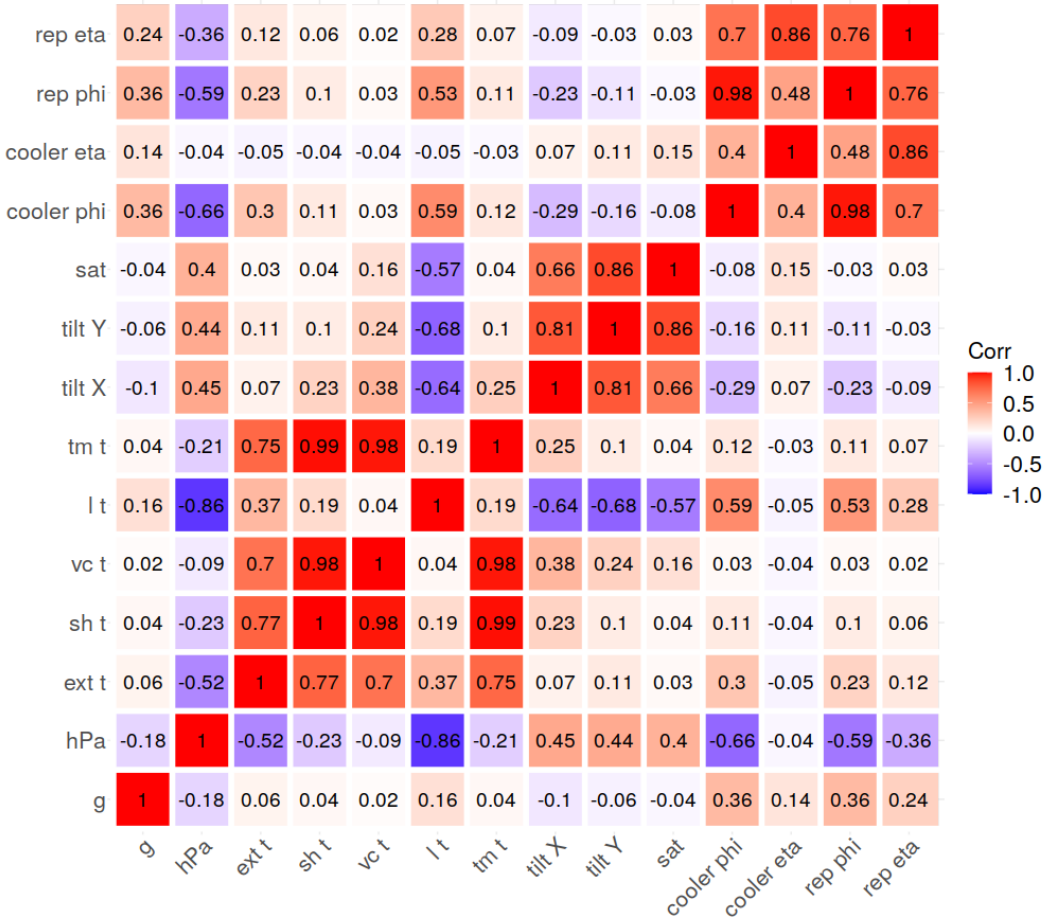

Figure 3.34: Correlogram of gravity residuals ('g') and acquistion variables. Gravity residuals averaged over 10 minutes. AQG-A01 at LNE Trappes 23/07/2019 - 23/08/2019. Variables: 'hPa' : atmospheric pressure, 'ext t': external temperature, 'sh t' : sensor head temp., 'vc t': vacuum chamber temp., 'l t': laser temp., 'tm t' : tiltmeter temp., tilt X, tilt Y, 'sat' : correction frequency offset of the saturated absorption spectroscopy, Laser polarisation angles phi and eta (rad) of the two lasers: cooler laser and repumper.

3.5 Intermediate conclusion

In conclusion, the presented studies of the AQG#A01's sensitivity and stability show a high variability that is not systematically relatable to internal or external variables, site conditions, or temporal patterns. Cross-correlation analysis of the gravity residual series and recorded instrumental and environmental variables suggests the sub-daily variations to be related to laser properties. The strengths of the cross-correlations vary between sites and acquisitions and do not show a clear picture. In one series (Larzac, 12/12/2018 - 08/01/2019), the vacuum temperature appears to be significantly cross-correlated. The correlation with temperature became only apparent in the Larzac gravity series, probably due to the lower noises level at the site that allowed for these correlations to be detectable. A further observation is that correlations within

groups of related variables, in particular temperature variables and the laser properties, vary between series.

This fact limited the scope of experiments conducted with the AQG#A01, as also described in the following section (3.6), and made it necessary to wait for an updated instrument. In order to reduce susceptibility to sub-daily variations, improved temperature control is an important step forward in instrumental development. These requirements gave rise to the improvements realised in the AQG#B01 (section 3.7).

Auto-correlated signals of 24 h periods for the Montpellier and Trappes sites could potentially be related to ambient noise caused by anthropogenic activity. The power spectral density of seismic noise in Montpellier obtained in April and May 2020 during the operation of the AQG#B01 are shown in Figures 3.35 and 3.36. A relatively clear diurnal pattern at various frequencies is visible.

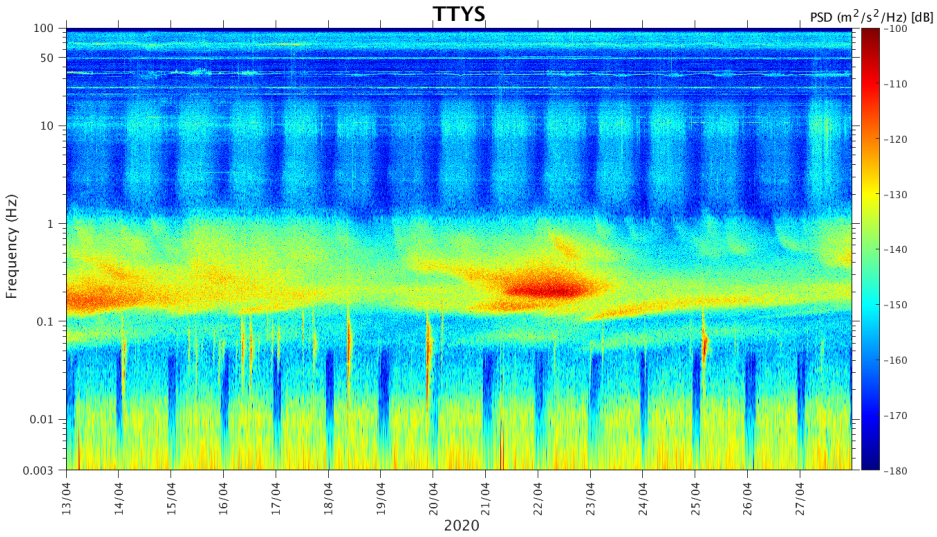

Figure 3.35: Power spectral density plot of seismic velocities at 200 Hz obtained at Géosciences Montpellier. Frequency in Hz. 13/04 - 27/04/2020. Haned and Champollion, personal communication

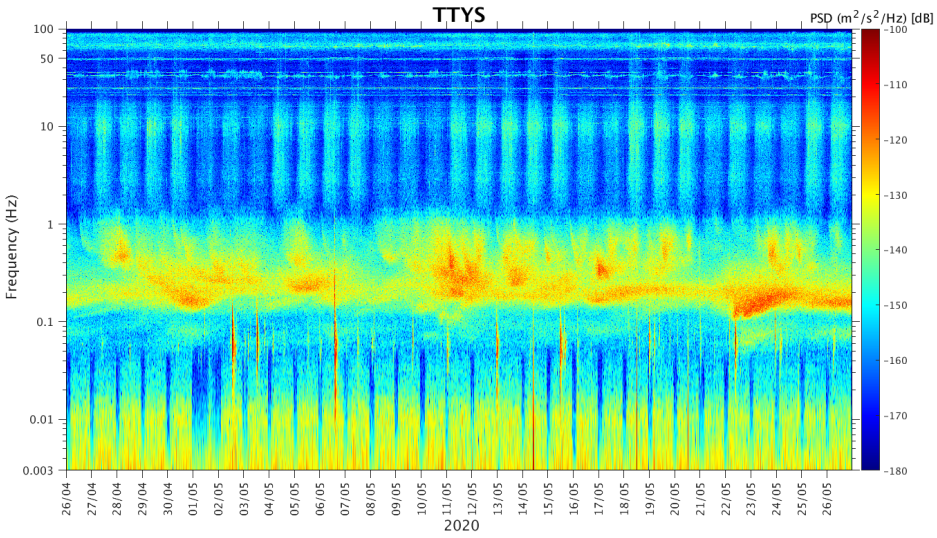

Figure 3.36: Power spectral density plot of seismic velocities at 200 Hz obtained at Géosciences Montpellier. Frequency in Hz. 26/04 - 26/05/2020. Haned and Champollion, personal communication

To complement the analysis for the AQG#A01, seismic data of 2019 needs to be compared to the gravity residuals, both for Montpellier and Trappes. Another aspect that has not been analysed in detail yet, is meteorology. The influence of storms, characterised by wind speed, needs to be investigated as a possible noise source. Therefore, the cross-correlation between gravity residuals and wind speed data obtained from the flux-tower and weather station at the Larzac site needs to be investigated.

3.6 Vertical gravity gradient (VGG) estimation

The vertical gravity gradient (VGG) is the gravitational acceleration's first derivative in z-direction, expressed in the unit of Eotvos ($1E = 10^{-9}s^{-2}$). The vertical gravity gradient on the surface of the Earth is in the order of 3.086 kE. Regional gravity gradient grids can be obtained from satellite data (GOCE mission, e.g. Bouman et al. (2016)). The motivation for a rigorous, local vertical gravity gradient estimation stems from the necessity of defining a reference height during gravimeter inter-comparisons. As instrument sensors are located at different heights and require a height transfer in order to accurately compare the measurements. The local vertical gravity gradient is usually estimated based on the difference δg between measurements obtained on two tripods of different height, usually obtained with relative gravimeter due to their mobility. VGG estimation has been done for the well-characterised Trappes laboratory by Merlet et al. (2008) with a Scintrex-CG5. VGG estimation with an absolute gravimeter offers several advantages over relative gravimeter studies. Temporal drift correction of relative gravimeters usually requires repeated survey loops and comparison with a reference instrument, leading to uncertainty in the final estimation. These repetitions are not necessary for absolute gravimeters. Unlike other absolute gravimeters, the AQG#A01 can relatively easily be moved between tripods. This section investigates the quality of VGG estimation based on AQG#A01 measurements. AQG#A01 measurements were carried out on two heights of 67.2 cm difference (base tripod and base tripod plus additional tripod) on 01/10/2019 at the LNE Trappes observatory.

After one hour of data integration, the AQG#A01 shows a sensitivity of approximately 20 nm·s^{-2} as obtained from the gravity time series's Allan deviation (Figure 3.37). Given this sensitivity, the expected uncertainty on the vertical gravity gradient estimation can be obtained from the square root of the sum of the squared chosen gravity precision values (Table 3.1) (variance) divided by 67.2 cm. As can be seen in Table 3.1, gravimeter data with an uncertainty of 20 nm·s^{-2} would yield 40 E uncertainty regarding the estimated VGG based on this gravity data. These estimates are based on the 67.2 cm height difference (base tripod and base tripod plus additional tripod), assuming a negligible error on the height measurement.

The AQG#A01 measured gravity on the base tripod and on the additional tripod for a protocol that allowed to exploit a VGG estimate based on a one- and two-hour measurement, respectively, as displayed in the protocol in Figure 3.38 and 3.1. From this, six VGG estimations were obtained. VGG_1 and VGG_2 were based on two h measurements each, VGG_3, and VGG_4 are subsets of one hour of these and VGG_5 and VGG_6 were based on one-hour measurements later in the day.

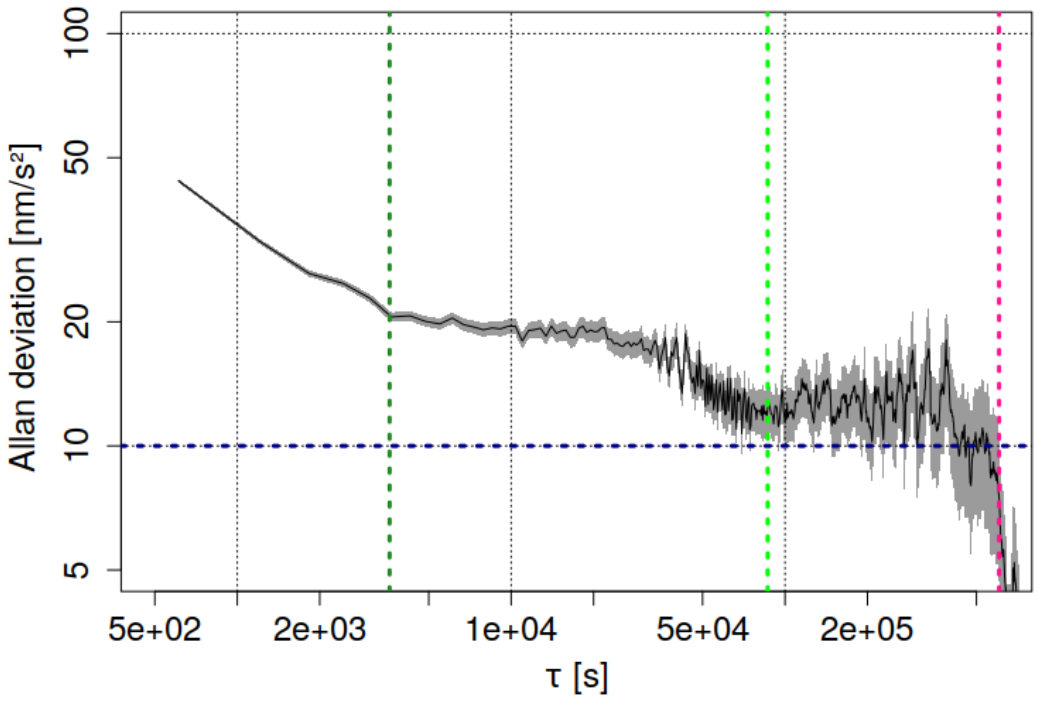

Figure 3.37: Allan deviation for 10-minute data obtained with the AQG-A01 in nms^{-2} obtained at LNE (Trappes), 23/07-23/08/2019. The horizontal blue dashed line shows the sensitivity benchmark of 10 nms^{-2}, the dark green vertical dashed line signifies the integration period of 1 h, the light green one that of 24 h, pink refers to 7 days.

Gravity precision [nms^{-2}]	precision vertical gradient [E]
10	20.41
20	41.46
30	62.51
50	104.60
100	209.82

Table 3.1: Theoretically estimated precision on the vertical gravity gradient, given a height difference of 67.2 cm.

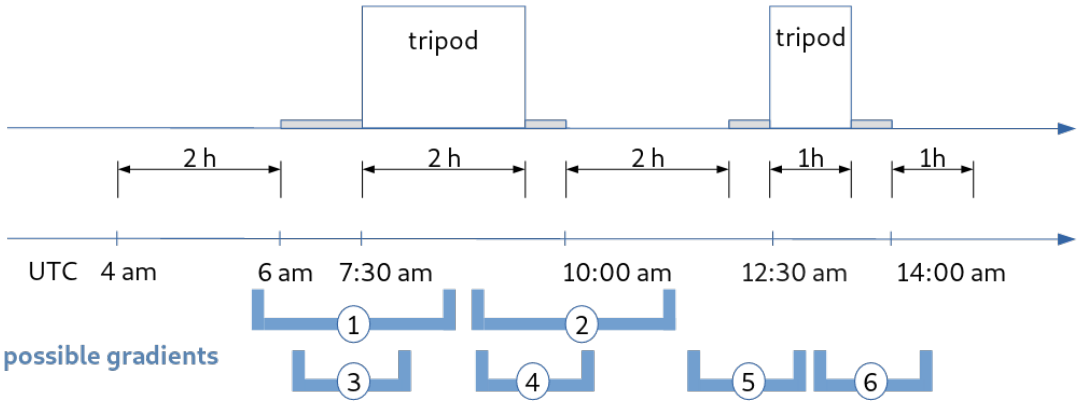

Figure 3.38: Acquisition protocol of VGG survey conducted with AQG-A01 on 67.2 cm tripod in LNE, Trappes, on 01/10/2019. The protocol allows for the assessment of several VGG throughout the day; including a comparison between a VGG based on 1 h measurement duration per height, respectively, and a 2h duration. The numbering of the gradients is shown at the specific result section.

An additional survey to estimate the VGG with the Scintrex CG6#120 relative gravimeter has been carried out on the same day on another measurement point in the same laboratory room for one hour. Each measurement consisted of an integration time of 120 seconds, two measurements per height were carried out. The CG6#120 measurements took place on three tripods (25.25, 75.35, and 125.35 cm) additionally to the base tripod and the CG6#120 sensor height (6.58 cm), applying a randomised, alternating acquisition protocol between heights.

3.6.1 VGG results and discussion

The AQG#A01 VGG estimation yielded on average -3.12 $\pm$ 0.078 kE. The average standard deviation for each VGG estimation was 217 E (Figure 3.40). In comparison, the VGG estimated based on the CG6#120 survey conducted in the afternoon yielded -3.0573 $\pm$ 0.0193 kE. As a comparison, previous studies by Merlet et al. (2008) found an uncertainty of 17 E for loop-based VGG estimations using a CG5; for stationary VGG estimations as low as 10 E. Construction works on the LNE campus in Trappes in October 2019 with a distinct break around noon and their impact on the noise level has to be considered. The noise level was visible on the iGrav and a CG6 that were operating at the same time as the AQG#A01. However, the AQG raw data standard deviation was much higher than that of the CG6#120, suggesting non-environmental noise sources.

The sub-daily variations as observed in other AQG#A01 series before and high noise level reduced the quality of the vertical gravity gradient estimation carried out with the AQG#A01. This is visible in a jump of approximately 200 nm·s^{-2} at around 3 p.m. (Figure 3.39), which

cannot be easily explained.

During the first part of the CG6 survey around midday, tares occurred (not shown here) in the CG6 data and were identified as outliers. The latter part of the survey was used for VGG estimation and shows a higher precision than the VGG estimated based on AQG#A01 data. However, frequent displacements and the necessary repetitions make the relative gravimeter survey less convenient and more time-consuming for the operator. Additionally, drift correction and identification of tares in post-processing requires more effort than the analysis of AQG#A01 data. The AQG#A01 offers the possibility to achieve a VGG estimate with fewer displacements and loops than with a relative gravimeter, and thus offers time gained. However, the precision of the VGG estimation using the described protocol is lower. A higher VGG sensitivity comparable to that of a CG6 could be achieved for longer integration times. Allowing for an integration time of 24 h compensates for the potential gain in time. In general, these results also characterize the repeatability of the measurements depending on the duration of the measurements.

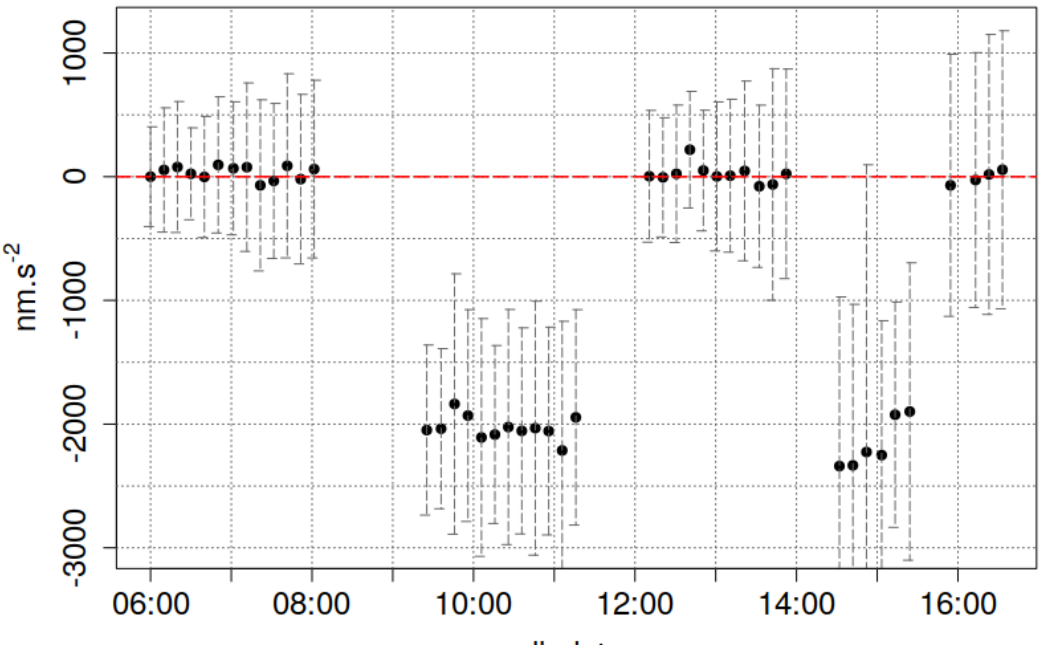

Figure 3.39: Gravity residuals relative to the mean of the measurements at height zero (base tripod) (red dashed line). Measurements on an additional tripod (67.2 cm height difference). Data obtained with the AQG-A01 at LNE (Trappes) on 01/10/2019

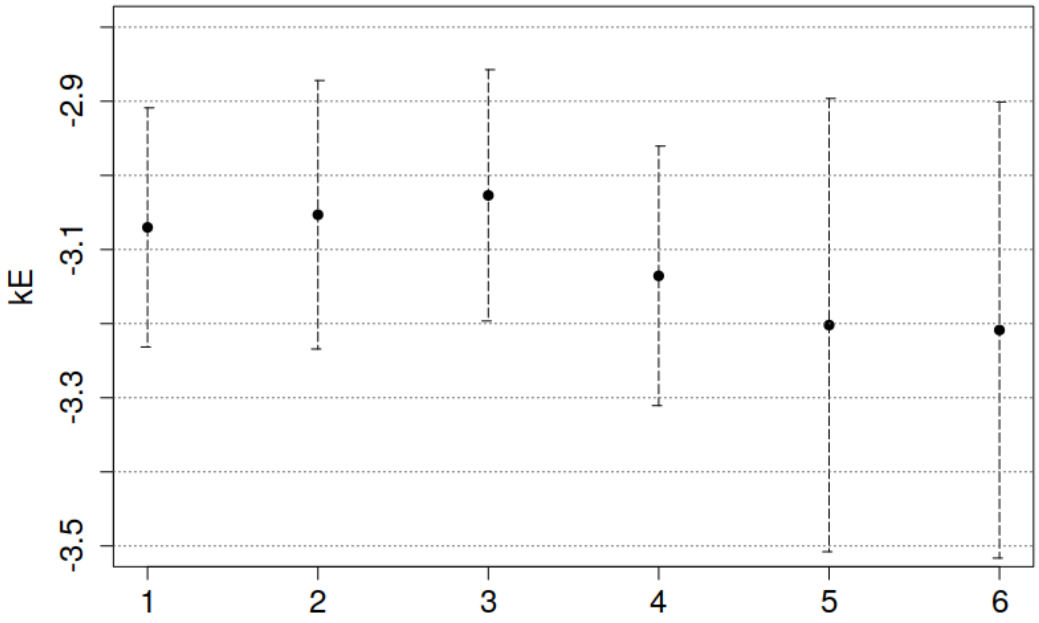

Figure 3.40: Vertical gravity gradients (VGG) in kE for 67.2 cm height difference obtained with the AQG-A01 at LNE (Trappes) on 01/10/2019. Gradient numbers refer to VGG estimated from gravity measurements based on one hour acquisition on each height (VGG nr. 1,2) or two hours (VGG nr. 3-6) (Figure 2.28, Table 2.2)

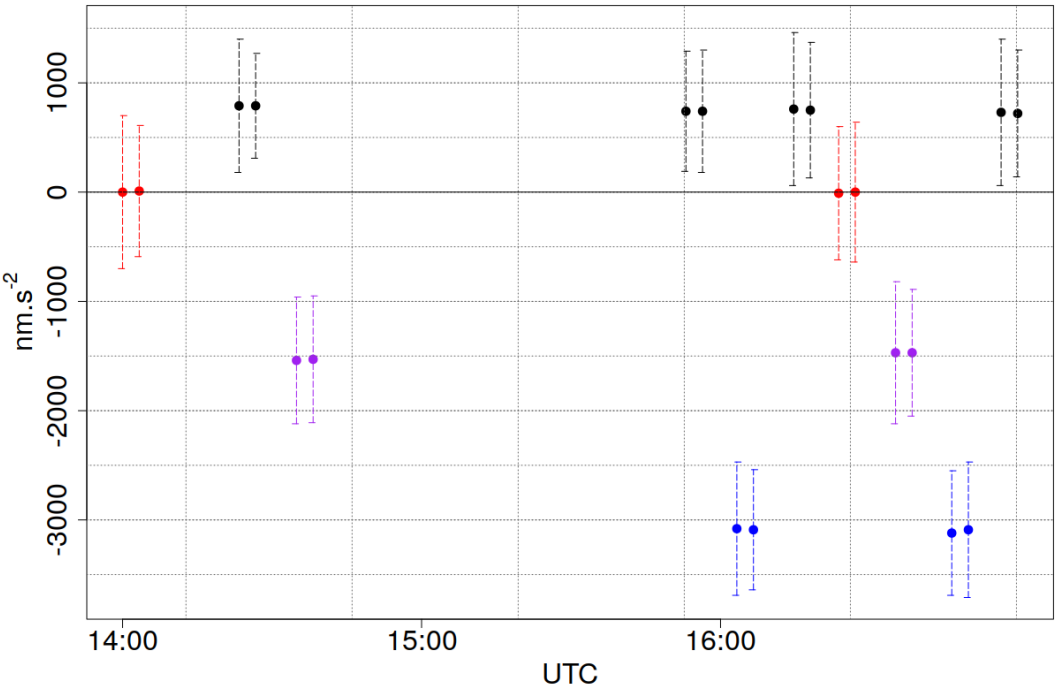

Figure 3.41: CG6-120 gravity residuals for vertical gravity gradient estimation. Gravity residuals in nm.s^{-2}, corrected for tidal effects and drift, obtained at at LNE (Trappes) on 01/10/2019. Colours indicate tripod height: h_0 (black), h_1(red), h_2 (purple), h3 (blue).

3.7 AQG-B01

The AQG#B01 device is the field-version follow-up of the AQG#A01. The earlier mentioned performance measures and procedures carried out for the AQG#A01 were repeated for the AQG#B01 (stability, sensitivity, accuracy, small and large-scale repeatability), while also relying on absolute gravity data obtained with the Micro-g LaCoste FG5#228 as reference. The conducted tests focus on the device's applicability in the context of geophysical monitoring and results were furthermore interpreted regarding the detectability of hydrogeological phenomena. In order to evaluate the performance under outdoor conditions, tests in locations with controlled and uncontrolled external temperatures have been carried out as well as experiments aiming at a potential combined tilt and temperature off-sets. First tests involving sensor axis rotation have been carried out. The procedures and results are discussed in the publication "Evaluation of the capacities of a field absolute quantum gravimeter (AQG#B01)", currently in review for the EGU journal "Geoscientific Instrumentation, Methods and Data Systems".

Figure 3.42: The AQG-B01 during operation in a garage in Montpellier 02/06/2020 - 17/06/2020. Photo: Cooke

3.8 Publication in review : "Evaluation of the capacities of a field absolute quantum gravimeter (AQG#B01)"

https://doi.org/10.5194/gi-2020-22
Preprint. Discussion started: 21 August 2020

Geoscientific Instrumentation Methods and Data Systems Discussions

Evaluation of the capacities of a field absolute quantum gravimeter (AQG#B01)

Anne-Karin Cooke[1], Cédric Champollion[1], and Nicolas Le Moigne[1]
[1]Géosciences Montpellier, Univ. Montpellier, CNRS, Univ. des Antilles, Montpellier, France
Correspondence: Anne-Karin Cooke (annekacooke@gmail.com)

Abstract. Quantum gravimeters are a promising new development allowing for continuous, high-frequency absolute gravity monitoring while remaining user-friendly and transportable. In this study, we present experiments carried out to assess the capacity of the AQG#B01 in view of future deployment as a field gravimeter for hydro-geophysical applications. The AQG#B01 is the field version follow-up of the AQG#A01 portable absolute quantum gravimeter developed by Muquans. We assess the instrument's performance in terms of stability (absence of instrumental drift), sensitivity in relation to other gravimeters, and hydrogeological mass changes. We discuss the observations concerning the accuracy of the AQG#B01 in comparison with a state-of-the-art absolute gravimeter (Micro-g-LaCoste, FG5#228). Repeatability is tested by instrument displacement between close-by measurement positions. We report the repeatability to be better than 50 $nm.s^{-2}$. No significant instrumental drift was observed over several weeks of measurement. This study furthermore investigates whether changes of instrument tilt and external temperature and combination of both, which are likely to occur during field campaigns, influence the measurement of gravitational attraction. We repeatedly tested external temperatures between 20 and 30 °C and did not find any significant effect. As an example of a geophysical signal, a 100 $nm.s^{-2}$ gravity change is detected with the AQG#B01 after a rainfall event at the Larzac geodetic observatory (Southern France). The data agreed with the gravity changes measured with a superconducting relative gravimeter (GWR, iGrav#002) and the expected gravity change simulated as an infinite Bouguer slab approximation. We close with operational recommendations for potential users and discuss specific possible future field applications. While not claiming completeness, we nevertheless present the first characterisation of a quantum gravimeter carried out by future users. Crucial criteria for the assessment of its suitability in field applications have been investigated and are complemented with a discussion of further necessary experiments.

1 Introduction

Gravimetry studies the spatial and temporal variations of the Earth's gravity field which can be linked to changes in mass distribution studied in various disciplines of the Earth sciences. Applications include geodesy and large-scale geodynamics such as tectonics and slow subsidence (Camp et al. (2011); Hwang et al. (2010)) as well as crust deformation and glacial isostatic uplift (Mazzotti et al. (2011); Olsson et al. (2019)). Gravimetry has furthermore proved to be a tool in natural hazard assessment such as monitoring of volcanic activity (Bonvalot et al. (1998), Carbone et al. (2017)) or mapping of underground

https://doi.org/10.5194/gi-2020-22
Preprint. Discussion started: 21 August 2020

Geoscientific Instrumentation Methods and Data Systems Discussions

voids or the study of earthquakes (Imanishi (2004)). Applications in energy and resources comprise geothermal fields (Pearson-Grant et al. (2018)), CO2 storage reservoirs (Sugihara et al. (2017)), or artificial groundwater recharge facilities (Kennedy et al. (2016)). Gravimetric methods find furthermore application in the context of oil and mineral exploration and prospecting (e.g. Ferguson et al. (2007); Hinze et al. (2013)). In hydrology gravity measurement provide possibilities to monitor storage dynamics of local and landscape-scale groundwater resources (e.g. Creutzfeldt et al. (2008); Creutzfeldt et al. (2010); Jacob et al. (2010); Hector et al. (2014); Hector et al. (2015); Fores et al. (2016a); Güntner et al. (2017)) and even evapotranspiration rates (Van Camp et al. (2016)). Applications and active gravity research fields have been extensively reviewed by Crossley et al. (2013) and Van Camp et al. (2017).

Gravimeters are devices that measure the gravitational attraction g on the Earth's surface. Nowadays gravimeters based on different measurement principles exist for various applications. Gravimeters can be characterised by their measurement performance: the repeatability of a measurement refers to the agreement between repeated measurements and is usually assessed by carrying out several repeated location changes in between measurements. The sensitivity (or precision) of a gravimeter is a relative uncertainty and refers to the smallest change in gravitational acceleration that the gravimeter is able to detect. We refer to stability as the absence of a significant instrumental drift in time or correlated noise. The accuracy of a gravity measurement describes to which extent it can be considered as correct in absolute terms and refers to the uncertainty of a measurement relative to an absolute standard (Niebauer (2015)).

Relative gravimeters sense the gravitational attraction indirectly by measuring the force needed to counteract gravitation by stabilizing a test mass and are used to monitor relative gravity changes. These devices show drifts that can become important within days (spring gravimeters) or months (superconducting gravimeters) (Van Camp et al. (2017)). Relative gravimeters require regular calibration with absolute gravimeters as reference stations and repeated looped or absolute measurements to eliminate drifts in field surveys (Hector and Hinderer (2016); Kennedy and Ferré (2015)) and can be sensitive to temperature changes (for example with a relative spring gravimeter as in Fores et al. (2016b)). The most sensitive relative gravimeters are superconducting gravimeters and achieve a high precision of about 0.1 $nm.s^{-2}$ while measuring continuously at a sampling rate of 1 Hz. They are based on magnetic levitation instead of a mechanical spring (Hinderer et al. (2015)).

Absolute gravimeters estimate the norm of the gravitational acceleration g during vertical free fall in vacuum (Niebauer et al. (1995)). Absolute gravimeters are mostly based on a free-fall corner-cube retro-reflector in a vacuum chamber with an instrumental uncertainty in the order of a few tens of $nm.s^{-2}$ (Niebauer (2015)). Currently available absolute gravimeters are not suitable for continuous monitoring due to mechanical parts with a limited lifespan. This limits the number of free fall experiments and requires frequent instrument repairs. Their operation usually requires a high technical skill level and they can not be operated by a non-specialist.

Quantum sensing offers new possibilities for measuring inertia and the development of quantum absolute gravimeters. The general measurement principle of an absolute quantum gravimeter (AQG) is that of matter-wave interferometry ((Peters et al. (2001)); Merlet et al. (2010)). The atoms can be exploited as test masses as well as a tool to measure the travelled path in order to sense gravity (Peters et al. (2001)). A laboratory realisation, the Cold Atom Gravimeter (CAG) developed at LNE-SYRTE in the context of the Kibble balance has demonstrated unprecedented performances both in sensitivity and accuracy. It has

https://doi.org/10.5194/gi-2020-22
Preprint. Discussion started: 21 August 2020


Geoscientific Instrumentation Methods and Data Systems Discussions

since participated at International Comparisons of Absolute Gravimeters (ICAG) showing a better short-term sensitivity than absolute gravimeters and a well quantified accuracy budget (Jiang et al. (2012); Francis et al. (2013); Gillot et al. (2014)). Numerous research institutions and private companies work on different realisations of cold atom gravimeters (Geiger et al. (2020)) such as GAIN (Germany; Hauth et al. (2013)) or WAG-H5-1 (China; Huang et al. (2019)).

Robust atom manipulation, as a crucial step towards the realisation of a field instrument, was achieved by atom trapping and detection without the necessity to align several optical components. This has been realised thanks to a single hollow pyramidal reflector, allowing operation with a single optical beam, and leading to a compact implementation (after Bodart et al. (2010)). An exhaustive review on the state-of-the-art of cold-atom gravity-inertial sensors, different sensor types, applications, and differences in performance has been provided by Geiger et al. (2020). The first commercially available gravimeter (AQG#A) based on this technology has been developed by Muquans. The compact design enabled a mobile instrument that does not require special training in operation. Advances in on-the-fly correction of external effects have contributed to a compact and stable instrument of high sensitivity measuring at 2 Hz sampling rate. A stability better than 10 $nm.s^{-2}$ during one month of operation was observed, and the instrument's repeatability was preliminary quantified to be in the same order of magnitude (Ménoret et al. (2018)) for 24 h of averaging.

The main aims of this study are to assess the stability and repeatability of the first field absolute quantum gravimeter (Muquans, AQG#B01) in view of future deployment as a field gravimeter for hydro-geophysical applications. The assessment is done during continuous measurements and experiments (impact of orientation or transportation) in comparison to absolute and relative gravimeters. The sensitivity to tilt and temperature changes as well as the interaction between both are of crucial importance to assess the suitability of the AQG#B01 as a field instrument. Its sensitivity to ambient temperature changes is evaluated by conducting tests in a controlled environment. Finally, recommendations are presented for the future use of the AQG#B01 in field experiments.

2 Site and instrumental set-up

The field site allows for the monitoring of gravity with complementary instruments and of environmental variables to link gravity variations to mass changes occurring in the surroundings of the study site. Instrument tests and monitoring from December 2019 to April 2020 were carried out at the Larzac Observatory, which is part of the French National Research Infrastructure OZCAR (Gaillardet et al. (2018); OZCAR-RI H+ Larzac - France) and the European long-term environmental monitoring network ELTER (Mollenhauer et al. (2018)). The Larzac Observatory is located on the La Jasse site in L'hospitalet-du-Larzac in Southern France. The observatory is highly instrumented with hydro-meteorological monitoring (eddy co-variance flux tower, rain gauges) and well suited for hydrogeophysical studies (Fores et al. (2018)). It is also part of the French seismological and geodetic network RESIF (Volcke et al. (2014)). The Larzac site further serves as a site for gravimeter testing, for instance in a study on the AQG#A01 or gPhoneX (Micro-g LaCoste; Fores et al. (2019)). A superconducting gravimeter on the site (GWR, iGrav#002) has been monitoring gravity variations for almost a decade. Residual gravity changes caused by hydrological mass changes of less than 100 $nm.s^{-2}$ have been identified (Fores et al. (2016a)). An absolute free-fall gravimeter

https://doi.org/10.5194/gi-2020-22
Preprint. Discussion started: 21 August 2020


Geoscientific Instrumentation Methods and Data Systems Discussions

(Micro-g-LaCoste, FG5#228) has been transported to and operated at the site. During the International Key Comparison of Absolute Gravimeters in 2017 (CCM.G-K2.2017), the FG5#228 showed a degree of equivalence of 3 $nm.s^{-2}$ with the 12 other absolute gravimeters and 55 $nm.s^{-2}$ uncertainty within 95% confidence (Wu et al. (2020)). In this study, the FG5#228 serves as a reference. In the Larzac observatory, the AQG#B01 and FG5#228 were operated on the same concrete pillar with approximately one meter distance between both instruments.

The AQG#B01 is the field version follow-on of the AQG#A01 described in Ménoret et al. (2018). It is based on the same measurement specifications and overall architecture but underwent a complete system redesign in order to meet outdoor operation requirements and to increase the stability of the measurement. The laser module and sensor head have been provided with an active thermal stabilization, allowing for a potential operation temperature range between 0°C and 40°C. Power consumption has been reduced to less than 500 Watt and battery operation is possible for field experiments. Improvement in ease of use and transportability has been achieved with each element weighing 40 kg or less. The enclosure for the lasers and the sensor head has been made water- and airtight. Connectors and cables are suitable for field conditions and a reduction in the number of connectors further facilitates fast and efficient field set-up. As an example, shifting the AQG#B01 in the Larzac observatory from one pillar to another takes around 5 minutes for one person.

In late April 2020, additional AQG#B01 and FG5#228 measurements and tests were continued in the facilities of the laboratory Géosciences Montpellier in the cellar, about 100 kilometers southwest of the Larzac site. The laboratory is in an urban area on the Montpellier University campus. Previous FG5#228 measurements show small gravity changes (less than 50 $nm.s^{-2}$ over one year) (Jacob et al. (2008)) for a close-by site on campus. Environmental noise is monitored with a large band seismometer. Due to the Covid-19 lockdown, the environmental noise is largely reduced: less difference in noise level is seen between workdays, weekends, and public holidays.

3 Methods and experiments

The experiment timeline and data availability are displayed in Figure 1. The iGrav#002 data are available continuously. Software malfunctioning or updates and seismic events caused data gaps in the AQG#B01 series. In late January a seismic event made a restart necessary and caused no damage to the instrument. Improvements to avoid loss of measurements caused by these incidents are in progress. An instrument test was conducted remotely by the developer on March 23rd. Apart from those, an offset of 100 $nm.s^{-2}$ was observed to emerge in the AQG#B01 gravity time series before the second temperature test on 10/02/2020. The cause is still under investigation and the authors are in contact with the instrument developer. Additional monitoring variables registered during operation are being investigated. Up to this point, the main hypothesis is mechanical stress in the sensor head, acquired in-between temperature tests.

https://doi.org/10.5194/gi-2020-22
Preprint. Discussion started: 21 August 2020

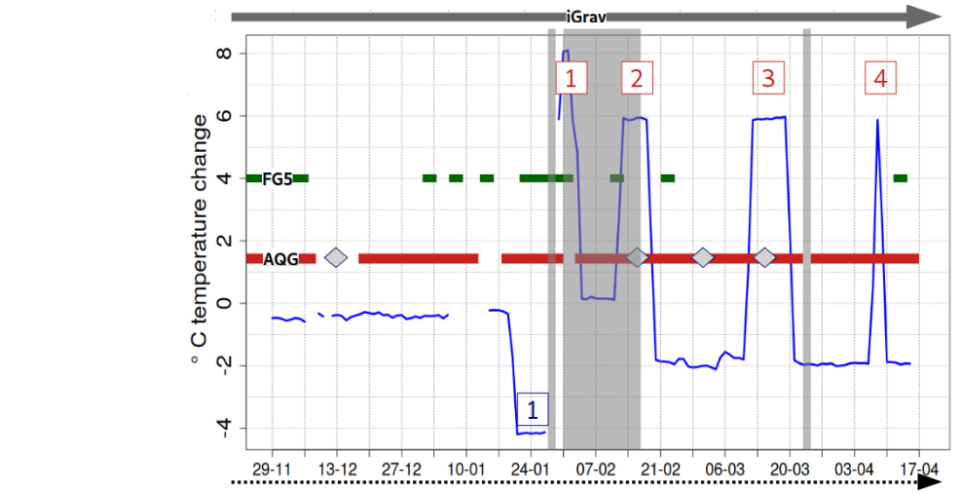

Figure 1. Timeline and data availability for the campaigns at Larzac observatory December 2019-April 2020. The AQG-B01 data series are marked in red, the FG5-228 measurements are marked in dark green. The iGrav-002 measured continously (marked in darkgrey). AQG-B01 data at dates marked in gray in later Janaury, early Feburary and late March were not considered in the analysis, due to inconsistencies during the experiments, as explained in section 4.4.2. The thin blue line represents the residuals from the mean observatory temperature to illustrate the temperature tests. One test has been carried out at reduced temperatures and four at increased temperatures. Grey diamonds during the AQG-B01 series mark the dates of tilt tests carried out on the AQG-B01.

3.1 Drift, accuracy and sensitivity

The sensitivity is assessed by calculating the Allan deviation (Allan (1966)) as a measure of frequency stability over the gravity data series. The Allan deviation is calculated for the three gravimeters (FG5#228, AQG#B01, and iGrav#002) after classical post-processing: calibration and drift correction of the iGrav#002 data set, correction for solid Earth and ocean loading tides using Tsoft (Camp and Vauterin (2005)), atmospheric pressure and polar motion for all data sets. Polar coordinates were obtained from the International Earth rotation and Reference systems Service. Site-specific combined ocean and solid Earth tidal parameters had been estimated with ETERNA (Wenzel (1996)) software based on long-term iGrav#002 time series (Fores et al. (2016a)). Gravity residuals refer hereafter to the processed gravity data set.

The influence of global, non-local hydrological and atmospheric gravity effects on the Larzac site was estimated using the EOST loading service (Boy and Hinderer (2006); Boy and Lyard (2008); Boy et al. (2009)) applying the model GLDAS/Noah (v2.1) (Rodell et al. (2004)). Gravity residuals obtained from AQG#B01 and iGrav#002 were related to local cumulative precipitation obtained from on-site rain gauges to assess the detectability of small hydrogeological mass changes. A 1D hydrological model using rainfall as input describes the gravity changes due to hydrological mass changes adequately (Fores et al. (2016a)),

https://doi.org/10.5194/gi-2020-22
Preprint. Discussion started: 21 August 2020


Geoscientific Instrumentation Methods and Data Systems Discussions

hence to display the gravity changes caused by rainfall an infinite homogeneous Bouguer anomaly was assumed. The Bouguer plate was calculated according to:

$$\delta g_B = 2\pi\rho GH. \tag{1}$$

G refers to the gravitational constant, ρ to the density of water and the plate thickness H refers to the cumulative rainfall. The Bouguer plate equivalent was corrected for the estimated averaged daily deep percolation discharge of one mm per day (Fores et al. (2018)). The investigated precipitation event took place during the winter months, evapotranspiration was thus not considered. The FG5#228 measurements provide absolute reference points to assess any drift with time in the AQG#B01 time series. The period between the 28/11/2020 and 25/01/2020 was used for drift assessment, as numerous tests (tilt, temperature) were conducted afterwards. Daily averaged residuals are compared in order to assess the accuracy of the AQG#B01.

The difference of effective measurement height requires a correction for the vertical gravity gradient when the accuracy of the AQG#B01 is estimated. For this set-up, the AQG#B01 effective measurement height was at 65.1 cm, the FG5#228 at 121.77 cm. The horizontal gravity differences between the FG5#228 and AQG#B01 measurement locations in Larzac and Montpellier have been estimated with a relative Scintrex CG5 and CG6 gravimeter, at 1.2 m height difference. Estimated vertical gravity gradients at the Montpellier site were found to be approximately -2.9 kE (1 kE = 10 $nm.s^{-2}cm^{-1}$). In the Larzac observatory estimated vertical gravity gradients on pillar 1 (FG5) and 2 (AQG) are -3.225 and -3.220 kE, respectively, averaged over one year of monthly measurements (Cooke et al., in preparation). AQG#B01 and FG5#228 gravity residuals were thus transferred to the same height by correcting for a vertical gravity gradient of -3.22 and -3.225 kE in the Larzac Observatory and for -2.86 and -2.89 kE in the laboratory in Montpellier, respectively.

3.2 Adjustment of ambient temperature in the observatory

The observatory is kept at relatively stable 24°C in the weeks before and in between the experiments. The AQG#B01 was operated during five periods of modified ambient temperature with periods of standard temperature in between (Figure 1). The temperature in the observatory was changed by adjusting the air conditioning device. The first temperature test comprised a reduced temperature, followed by four tests of higher temperatures, relative to the 24°C default temperature listed in Table 1. During the first period of increased temperature, an elevated noise level and interruption due to the seismic event were observed by both the iGrav#002 and the AQG#B01 and these periods were therefore not considered in the analysis.

3.3 Tilt calibration under adjusted ambient temperatures

Instrument tilt variations are monitored by a tiltmeter located at the top of the sensor head. This allows for a constant monitoring and in-line post-correction of g values according to the effective tilt experienced by the instrument. Mechanical alignment between the vertical measurement axis and the tiltmeter reference is susceptible to drifts. Uncorrected tilts lead to the measurement of a projection of g as compared to a well-aligned, vertical measurement. The tiltmeter reference offset can be assessed using gravity measurements and directly used for gravity correction in the AQG acquisition software. For this calibration, several measurements (~20) are performed for various x and y tilt values, up to one mrad from the initial position. The in-

https://doi.org/10.5194/gi-2020-22
Preprint. Discussion started: 21 August 2020

Geoscientific Instrumentation Methods and Data Systems Discussions
Open Access
EGU

Table 1. Temperature test periods in the Larzac observatory

#	Start date	End date	Temperature °C
cooling			
1	20/01/2020	28/01/2020	20
heating			
1	28/01/2020	03/02/2020	30
2	12/02/2020	19/02/2020	30
3	11/03/2020	21/03/2020	30
4	07/04/2020	09/04/2020	30

strument's tilts in x and y are adjusted manually to reach a certain angle θ and the raw gravity data are then adjusted along a function of $\frac{1}{\cos(\theta-\theta_0)}$, in order to evaluate θ_0, corresponding to the real vertical axis. The offset coefficient has been tested in the Muquans facilities in Talence (France) and has since been redone twice at the Larzac observatory. Furthermore, it was investigated whether the obtained offset coefficient had changed over time or had shown any response to temperature changes. The offset calibration test on 19/02/2020 was carried out in the GEK at an increased temperature of 28°C and 05/03/2020 at 22°C.

3.4 Manual tilt deregulation under adjusted ambient temperatures

Temperature changes or temperature gradients may influence mechanical parts and tilt the instrument. To investigate possible interactions between temperature and tilt and to ensure reliable application of their corrections, manual tilt deregulation was carried out during phases of modified ambient temperature. Between 09/12/2019 and 13/12/2019, manual tilt deregulation in x and y during room temperature was tested. On March 11th the room temperature was modified from 22 to 30°C and on the same day, the tilt in x-direction was manually set to 0.5 mrad.

3.5 Repeatability

On April 17th, 2020 the AQG#B01 was transported to the facilities of the laboratory Géosciences Montpellier on University campus and operated in the basement of the building. The distance between the Larzac observatory and Montpellier is about 100 km and there is 640 m difference in altitude. The transport to Montpellier was the second displacement of the AQG#B01 after its first delivery to the Larzac observatory in November 2019. This implies the turn-off, deconnection, displacement and cold restart of the instrument. The data were compared to FG5#228 measurements at both sites. Small-scale repeatability was assessed using repeated gravity measurements on the same position in the gravity lab in the basement of Géosciences Montpellier. Vertical gravity gradients were additionally estimated with a relative gravimeter (Scintrex CG6).

https://doi.org/10.5194/gi-2020-22
Preprint. Discussion started: 21 August 2020


Geoscientific Instrumentation Methods and Data Systems Discussions

3.6 Coriolis effect

Gravimeters are sensitive to a Coriolis shift, the Sagnac effect caused by the Earth's rotation. This effect can generate an additional bias in quantum interferometers. The horizontal atomic velocity component generates an additional Coriolis acceleration depending on the E-W direction. This leads to a possible gravity bias (Peters et al. (2001), Louchet-Chauvet et al. (2011)). By symmetrical construction (hollow pyramidal reflector and location of the detection photo-diodes), horizontal atomic velocities are reduced and the AQG#B01 should not be sensitive to the Coriolis effect. We assess the potential residual Coriolis effect in the AQG#B01. By rotating the device by 180°measurements, two opposite orientations are obtained, hence a change in sign of the Coriolis acceleration is expected. As in Louchet-Chauvet et al. (2011), the tests were carried out under the assumption that parameters do not change between the measurements. The same set-up was thus kept constant to rule out other systematic effects. Coriolis AQG#B01 measurements last at least 24 hours to reduce the effect of residuals after tidal correction.

4 Results and discussion

4.1 Sensitivity

The sensitivity of the AQG#B01 is firstly evaluated by statistical time series analysis in comparison with other gravimeters and secondly by direct monitoring of natural gravity changes. It was calculated for the first week of December 2019 using 10 minute AQG#B01 data and one-minute iGrav#002 data (Figure 2). The first week in December 2019 shows no rainfall and no instrument tests were performed. At an integration interval of one hour, the sensitivity of the AQG#B01 reached 10 $nm.s^{-2}$, the iGrav#002 shows a higher sensitivity at short time scale, but an increase at long time due to environmental noise and tides residuals. At 24h the AQG#B01 approaches the sensitivity of the iGrav, and averages around 5 $nm.s^{-2}$ for this time span.

https://doi.org/10.5194/gi-2020-22
Preprint. Discussion started: 21 August 2020

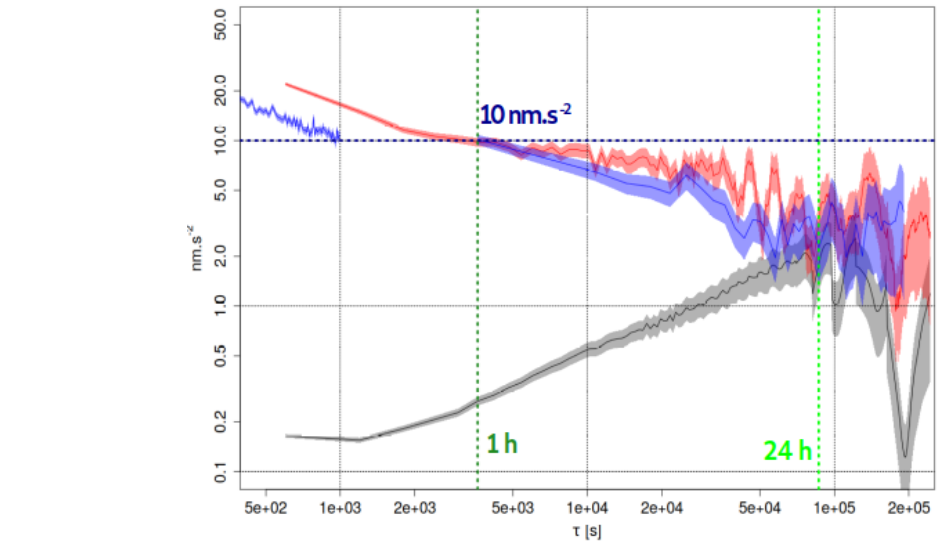

Figure 2. Allan deviation in $nm.s^{-2}$ for the first week of December 2019 at the Larzac site. One-minute series were used for the iGrav-002 (grey), 10-minute data for the AQB-01 (red). The irregular sampling frequency of the FG5-228 (100 drops every 10 seconds, then 2600 s break) was taken into account by plotting the short-term Allan deviation (< 1000s for 10 s data) and the long-term (1 h data) separately (both blue). The horizontal blue dashed line shows the sensitivity benchmark of 10 $nm.s^{-2}$, the dark green vertical dashed line signifies the integration period of 1 h, the light green one that of 24 h.

The analysis of the Allan deviation showed that for averaging periods of a few hours the iGrav#002 is the more sensitive instrument for this data set. The AQG#B01 and the iGrav#002 converge to show similar sensitivity of clearly better than 10 $nm.s^{-2}$ at a 24 h averaging period. For shorter integration intervals the sensitivities of the FG5#228 and AQG#B01 are comparable and lower than that of the iGrav. The AQG#B01 does not achieve the sensitivity of laboratory quantum gravimeters that have achieved 2 $nm.s^{-2}$ in less than 2000 s (CAG; Gillot et al. (2014)) or a mobile quantum gravimeter for which 0.5 $nm.s^{-2}$ after one day have been reported (GAIN; Freier et al. (2016)).

For measurements longer than one day, the AQG#B01 is likely to be equally sensitive as the iGrav#002. To obtain values closer to the possible highest sensitivity, a prolonged measurement of several weeks during a low noise period of stable weather conditions and little human interventions is required, as it would be possible for example during summer months in the Larzac observatory. The Allan deviation of the AQG#B01 data recorded in Montpellier showed a sensitivity of approximately 20 $nm.s^{-2}$ after one h, after 24h it was below 10 $nm.s^{-2}$. This decrease in sensitivity for the urban site compared to the Larzac observatory can be explained by the higher level of environmental noise in the university building.

A sensitivity of 10 $nm.s^{-2}$ is achieved in one hour in a naturally low noise environment and a sensitivity of 20 $nm.s^{-2}$ in an urban environment. In the context of characterising the AQG#B's sensitivity, the use of rubber pads below the tripod feet

https://doi.org/10.5194/gi-2020-22
Preprint. Discussion started: 21 August 2020

Geoscientific Instrumentation Methods and Data Systems Discussions
Open Access
EGU

to reduce the effect of ground vibrations was assessed for future field experiments. Figure 3 shows that the Allan deviation is reduced for measurements of less than an hour. At one hour duration, there is no significant difference, for longer integration times there is likely no major improvement. This needs to be reassessed for longer series and at periods of higher environmental noise as the activity at the university was reduced during the COVID19-lockdown.

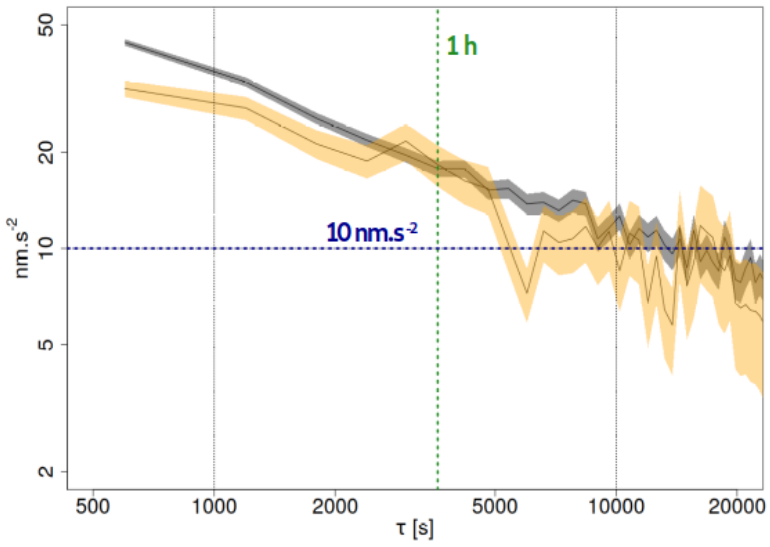

Figure 3. Comparison of sensitivity with (orange) and without (grey) placing the AQG-B01 tripod on rubber pads. The measurement without rubber pads were conducted on 23-26/04/2020, without pads on 28/04/2020.

4.2 Sensitivity to hydrogeological gravity changes

A significant increase in g of $\sim$ 80 $nm.s^{-2}$ between the 13/12/2020 and the 27/12/2020 has been detected by the three gravimeters. As can be seen on Figure 4 (panel (a)) daily gravity residuals of all of them show high resemblance in their temporal variations and differ within their error margins.

Figure 4 panel (b) shows the series of rainfall events in 2019. All three gravimeter signals follow the increase in gravity caused by the rise in soil water content in the aftermath of the rainfall events. The gravity time series continues to increase even after rainfall stops. This is expected since the infiltrating water moves further into the gravimeter's spatial sensitivity which can be described as two flat cones above and below with the instrument in the centre.

The measured change in g is comparable to the expected increase caused by the corresponding Bouguer plate equivalent of the rainfall event. Panel (c) shows the Bouguer plate equivalent in $nm.s^{-2}$ adjusted for deep discharge. Differences between the gravimeters' responses to the rainfall event can partly be explained by their position within the observatory building and the heterogeneity of rock properties. Local gravity measurements are impacted by the building due to shielding from precipitation,

https://doi.org/10.5194/gi-2020-22
Preprint. Discussion started: 21 August 2020


Geoscientific Instrumentation Methods and Data Systems Discussions
Open Access
EGU

commonly referred to as the "umbrella effect" (e.g. Creutzfeldt et al. (2008); Deville et al. (2012); Hector et al. (2014); Fores et al. (2016a); Reich et al. (2019)). The AQG#B01 is operated on pillar 2 in one corner of the building and hence more exposed to the area outside the building. The umbrella effect admittance can be calculated for sensor height and the specific measurement location within the building (Deville et al. (2012); Fores et al. (2016a)).

An umbrella effect of the Larzac observatory e.g. of 80% difference in the gravity of a given Bouguer plate measured on the central pillar (iGrav) inside the building has been observed by Fores et al. (2016a) and decreases once the infiltration front moves further in-depth. For the given Bouguer plate equivalent of 80 $nm.s^{-2}$, up to 64 $nm.s^{-2}$ difference in g can be expected for the iGrav. For the AQG#B01 pillar an umbrella admittance of 46 % has been estimated from a truncated Bouguer plate. Umbrella effect related differences between AQG#B01 and iGrav#002 could hence be up to several tens of $nm.s^{-2}$. As the umbrella effect depends on the initial conditions and the previous rainfall events, it is difficult to determine the sign of the relative offset between the AQG#B01, FG5#228 and iGrav#002 series without further information.

To summarise, the AQG#B01 clearly measures the gravity increase of less than 100 $nm.s^{-2}$ after the rainfall event in the same range as the iGrav. The gravity changes are coherent with previous studies at the site. The differences between the iGrav#002 and AQG#B01 data can be explained by limits of the sensitivity of the AQG#B01 and the heterogeneity of the hydrogeological context in a Karst area.

https://doi.org/10.5194/gi-2020-22
Preprint. Discussion started: 21 August 2020

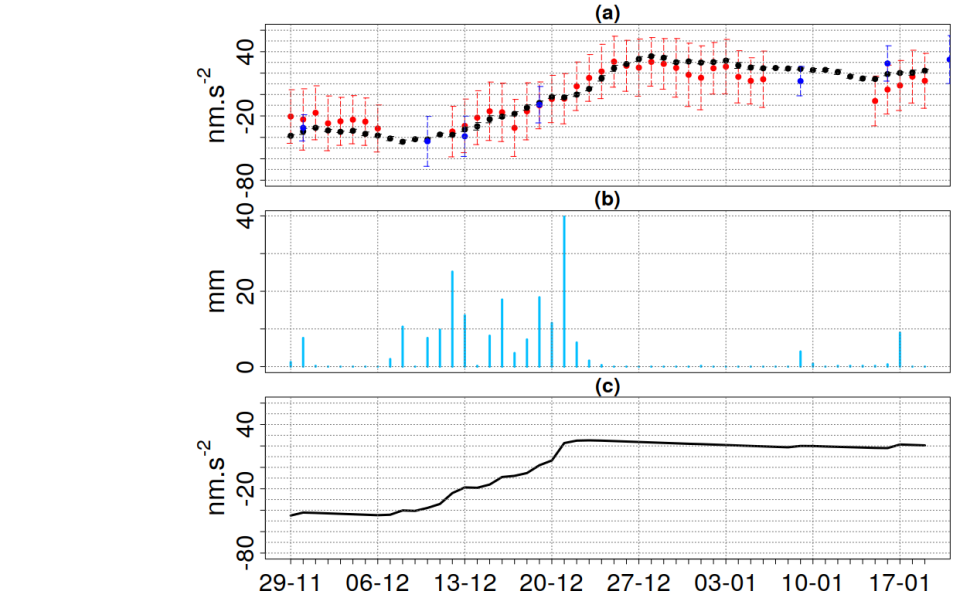

Figure 4. Panel (a): AQG-B01 (red), FG5-228 (blue) and iGrav-002 (black) daily gravity residuals at the Larzac observatory in $nm.s^{-2}$. Residuals of g refer to the mean of the shown measurements, respectively. The error bars refer to the standard deviation of 24 h of measurement. Panel (b): Rainfall series 12/2019–01/2020 on the GEK, LaJasse site, L'hospitalet-du-Larzac. Panel (c): Bouguer plate equivalent (in $nm.s^{-2}$) of precipitation corrected for deep discharge.

4.3 Accuracy, repeatability, and drift

The differences between the AQG#B01 and the FG5#228 during 2 months yielded an estimated, statistically insignificant drift of -0.02 $\pm$ 0.04 $nm.s^{-2}$ per day. A longer measurement is currently in progress to investigate a potential long-term drift. Establishing the complete accuracy budget is a complex task for a new instrument and remains work in progress. A first approximate estimation of the accuracy is done by comparing the AQG measurements with the ballistic gravimeter (FG5#228) in the Larzac observatory. Daily AQG#B01 and FG5#228 gravity residuals show high resemblance in their temporal variations and differ within their error margins (Figure 4). The difference between AQG#B01 and FG5#228 based on 13 measurements (daily averages) between December 2019 and April 2020 in the Larzac observatory is on average 110 $nm.s^{-2}$ with a standard deviation of 31 $nm.s^{-2}$, with the FG5#228 values being smaller than those measured with the AQG#B01. For the Montpellier laboratory, the difference between both instruments is based on 24h averages of ten AQG#B01 measurements between 27/04/2020 and 14/05/2020 and one FG5#228 measurement on 10/06/2020. The difference showed 44 $nm.s^{-2}$ with a standard deviation of 66 $nm.s^{-2}$, with the FG5#228 values being higher than those of the AQG#B01.

https://doi.org/10.5194/gi-2020-22
Preprint. Discussion started: 21 August 2020

Geoscientific Instrumentation Methods and Data Systems Discussions

Table 2. AQG-B01: Small-scale repeatability in Montpellier in 2020. Differences as residuals from the mean of the listed measurements, based on 24h averages. The standard deviation refers to 24 h.

Date	Δg $[nm.s^{-2}]$	SD $[nm.s^{-2}]$
27/04/2020	-43	46
28/04/2020	-5	36
03/05/2020	19	41
08/05/2020	-8	110
13/05/2020	27	66
27/05/2020	-9	60

Absolute comparison between both instruments was not directly possible due to the set-up on different pillars and is impacted by the uncertainty related to the vertical gravity gradient (VGG) correction. An offset in vertical gravity gradient correction between FG5#228 and AQG#B01 of 10 E yields for the difference in height between the two instruments' sensors (δ_{height} = 56.67 cm) 5.7 $nm.s^{-2}$ of uncertainty. The VGG for the pillars in the observatory can be estimated by repeated relative gravimeter measurements on different heights and their uncertainty has been estimated to be around 20 E (Cooke et al., in preparation). Hence, about 11 $nm.s^{-2}$ of uncertainty is due to the fact that the VGG cannot be estimated more precisely up to this point. The possibility of a more precise estimation of the VGG based AQG measurements on tripods is being discussed and in preparation.

Small-scale repeatability tests were only carried out in Montpellier. Table 2 shows an average small-scale repeatability of 3 $nm.s^{-2}$ with a standard deviation of 25 $nm.s^{-2}$ for repeated measurements on the same point and orientation after returning from displacements and other experiments.

AQG#B01 was operated on two measurement points within the same room in the Géosciences laboratory at about one meter distance, of which one serves FG5#228 measurements. At this short distance, no considerable horizontal difference in g is expected. CG6 relative gravity measurements were carried out with two instruments (CG6#120 and CG6#125) on 26/03/2020 on both points and found a negligible difference in g of 2 $\pm$ 6 $nm.s^{-2}$. The difference in g measured with the AQG#B01 between point 1 and point 2 is 15 $\pm$ 48 $nm.s^{-2}$. The measurement on point 2 was carried out using rubber pads under the tripod which added a height of 1.2 cm. This height difference was corrected with 35 $nm.s^{-2}$ based on an estimated vertical gravity gradient obtained from CG6 measurements.

To summarise, these first results show a repeatability better than 50 $nm.s^{-2}$ and no detectable drift over 2 months operation. No impact of transport and displacement such as mechanical relaxation on the gravimeter was observed for small (one m) or large (100 km by car) distances. The complete accuracy budget is still under investigation. Additional location changes between the sites with both the AQG#B01 and the FG5#228 are required to reliably quantify the repeatability. Due to the potential error margin caused by the earlier mentioned uncertainty introduced by the differences in vertical gravity gradient correction and measurements on different pillars, the accuracy in relation to the FG5#228 cannot be estimated completely up to this point.

https://doi.org/10.5194/gi-2020-22
Preprint. Discussion started: 21 August 2020


Geoscientific Instrumentation Methods and Data Systems Discussions
Open Access
EGU

4.4 Temperature and tilt

4.4.1 Tiltmeter calibration

The stability of the tiltmeter offset is important both for long term monitoring and for the repeatability of the measurements after transport by car. Tilts of 5 μrad lie probably within measurement uncertainty. A tilt bias of 50 μrad leads to an error of 12.3 $nm.s^{-2}$ and increases in a quadratic way which leads to 49 $nm.s^{-2}$ for 100 μ rad. The tiltmeter offset calibration changed by 4.7 μrad for x and by 3.8 μrad for y between Talence and the Larzac observatory ($\sim$ 400 km) which is within measurement uncertainty. The tilt calibration obtained from data acquired in the GEK at 30°C on 19/02/2020 yields very similar results to the calibration carried out on 31/10/2019 in Talence at 20°C. On 05/03/2020 a partial test of certain chosen tilts at 22°C was carried out that showed coherent results to the test carried out at 30°C on 19/02/2020. The tiltmeter offset calibration carried out in Talence and in Larzac lie almost four months apart and include the transport of the instrument from Talence to the Larzac site. The obtained offset values showed hence very minor changes over time, after transport or at different external temperatures. The data showed that the tilt calibration is likely to be independent of temperature and to stay stable over time.

4.4.2 Influence of temperature

During the temperature experiment AQG#B01 residuals did not show any statistically significant correlation with external temperature. Gravity residuals, external temperature and tilts are displayed in Figure 5. The AQG#B01 showed no significant shift in the range of 20 to 30°C and neither during episodes of tilt change. The visible variations lie within the earlier observed variations and uncertainty range. Relative offsets between AQG#B01 and iGrav#002 can be linked to the umbrella effect and Karst heterogeneity as discussed in section 4.2. No significant effect of precipitation was observed in the iGrav#002 monitoring. Temperature's impact on the AQG#B01 gravity residuals was difficult to assess considering the first two episodes of elevated temperatures. Experimental conditions varied between the tests, the results were not conclusive. Possibly due to the malfunctioning of the air conditioning, three spikes in temperature occurred during the first test. On 31/01/2020, 01/02/2020, and on 03/02/2020 approximately 35°C were reached for about eight hours each time, before decreasing again to settle at 30°C. During the second temperature test an insulating cover around the sensor head had not been removed resulting in an increase of temperature in the sensor head above nominal operation conditions.

AQG#B01 and iGrav#002 residuals differ less than 50 $nm.s^{-2}$. The reduced temperature test (20°C; January 20-28th) did not yield any significant gravity response to increased external temperatures. In March and April, the tilts stay stable before, during, and after the temperature test and no remarkable shift between the residuals of g obtained with the AQG#B01 compared to those obtained with the iGrav#002 is observed (Figure 5).

https://doi.org/10.5194/gi-2020-22
Preprint. Discussion started: 21 August 2020

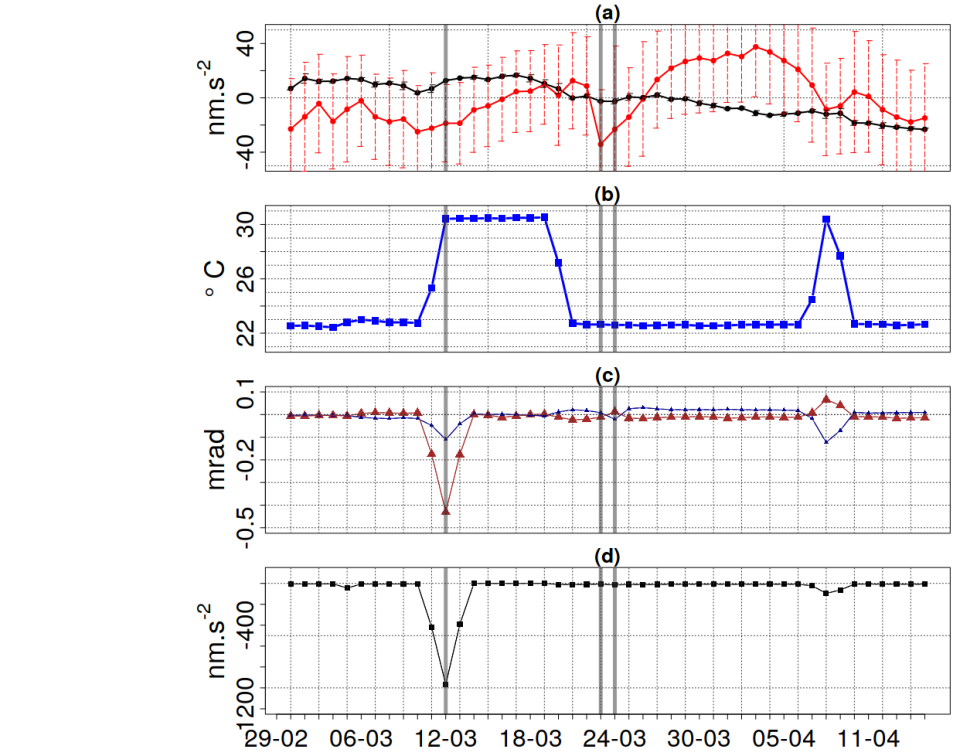

Figure 5. Panel (a): Residuals of g for the iGrav-002 (black) and AQG-B01(red). Panel (b): external temperature (blue). Panel (c): Tilts in x (brown) and y (dark blue) for the tests 3 and 4 in March and April 2020 (see Figure 1 for the timeline). Panel (d): Tilt correction combined for x and y in $nm.s^{-2}$. Dates marked as grey were subject to further instrument tests and adjustments.

4.4.3 Combined tilt and temperature tests

Manually deregulated tilts during temperature changes did not show a visible change in g recorded by the AQG#B01. As can be seen in Figure 5, the tilts showed a minor response during the last temperature test in early April. No impact on the corrected g value (with a tilt correction of $\sim 1000\ nm.s^{-2}$) is observed. Tilts return to values close to zero after a change in temperature.

Simultaneous manual tilt deregulation and room temperature change did not lead to any clear shift of the difference in g between the value of the AQG and that of the iGrav. This result suggests that the measurement of g is not impacted by temperature. It cannot be ruled out that tilts of more than one mrad require a different correction than small tilts. It is thus recommended to keep the sensor head well levelled during operation. The gravity series obtained with the AQG#B01 before, during, and after an elevated temperature of 30°C in March and April 2020 show no impact of these. To reproduce these findings, further temperature experiments and larger ranges should be carried out, potentially exploring also much lower temperatures.

https://doi.org/10.5194/gi-2020-22
Preprint. Discussion started: 21 August 2020

Geoscientific Instrumentation Methods and Data Systems Discussions
Open Access
EGU

4.5 Coriolis effect

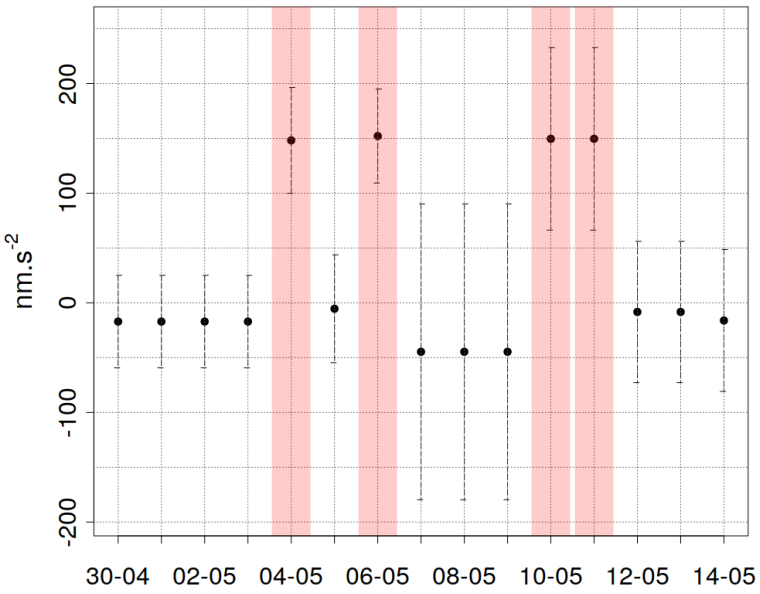

Figure 6. Residual gravity values in $nm.s^{-2}$ obtained with the AQG-B01 during the Coriolis tests at Géosciences Montpellier in 2020: The red bars show a sensor head orientation of 180° compared to the default set-up. Error bars refer to the standard deviation during 24 h. The value of g averaged over 24 h obtained on 10/06/2020 with the FG5-228 was subtracted. Horizontal grid lines show steps of 50 $nm.s^{-2}$.

To assess the potential impact of the Coriolis effect caused by changes in the sensor head's orientation we carried out measurements rotated by 180°compared to the default position. As can be seen in Figure 6, the averaged gravity residuals for the two orientations show a δg of approximately 150 $nm.s^{-2}$ relative to the FG5#228 measurement. These results are much higher than expected, as it has not been observed in other AQG devices (Muquans, 2020, personal communication). These values are higher than the estimation of the Coriolis effect for the CAG (LNE-SYRTE), which yielded 4 $nm.s^{-2}$ uncertainty with peaks of up to 60 $nm.s^{-2}$ as a combination of several uncorrected effects (Louchet-Chauvet et al. (2011)).

The sign of the Coriolis offset on the AQG#B01 as compared to the absolute gravity measurement by the FG5#228 has an important implication for the accuracy assessment and the interpretation of the differences between the two instruments: The FG5 measurement lies between the AQG#B01 values for the two orientations during the tests in Montpellier. FG5#228 measurements were higher than AQG#B01 measurements in the Larzac observatory. The average difference between both instruments hence likely requires to be increased by ~ 75 $nm.s^{-2}$, depending on the orientation of the AQG#B01 sensor head.

https://doi.org/10.5194/gi-2020-22
Preprint. Discussion started: 21 August 2020


Geoscientific Instrumentation Methods and Data Systems Discussions
Open Access
EGU

Repeated and additional orientations (90°and 270°) are work in progress, as well as in comparison with other gravimeters. The authors are in contact with the developer for in-depth instrument tests. Up to this date, the exact source of this change in g has not been identified yet. It is thus recommended to pay attention to sensor head orientation during operation. It will be necessary in the future to evaluate through repeated tests if the impact of Coriolis is stable over time and and whether a Coriolis correction can be established according to the orientation. The Coriolis effect needs to be included in the complete uncertainty budget.

5 Conclusion and perspectives

In this study, we show the results of instrumental tests aimed at the characterization of the AQG#B01 for field applications. The AQG#B01 has proven itself as a reliable instrument in controlled laboratory conditions. Over two months no significant drift was observed and temporal variations are in coherence with the MGL-FG5. Its sensitivity after 24 h of data integration is close to that of the iGrav. In low noise environments, the AQG#B01 showed a sensitivity of 10 $nm.s^{-2}$ after 1 h. AQG#B01 g residuals showed no correlation with manually increased tilts nor increased temperatures. An offset compared to the other gravimeters occurred and its causes are under investigation, as is the accuracy of the AQG#B01.

The obtained results further suggest its suitability for field studies, upon further testing and validation. It is suitable for operation at least within a temperature range between 20 and 30°C over several days and weeks. Larger temperature ranges are possible but have not been systematically tested yet. Tilt correction is likely to be applied correctly even for relatively large tilts and during periods of higher temperatures.

The AQG#B01 detected gravity changes caused by hydrology in the same order of magnitude as the iGrav. The resemblance between AQG#B01 and iGrav#002 residuals concerning their response to a rainfall event demonstrates the AQG#B's capability to detect small transient mass changes. This speaks for the applications of the AQG#B01 in hydrogeophysical studies among others. Mapping and quantification of water storage dynamics as an example for other transient mass changes could be one of many promising applications in this field. Jacob et al. (2010) mapped subsurface water storage heterogeneously distributed in the 100 km^2 Karst catchment in the Larzac using time-lapse micro-gravity. Gravity changes caused by local aquifer re- and discharge dynamics reached up to 220 $nm.s^{-2}$ with a survey precision between 24 and 50 $nm.s^{-2}$. Due to the strong and non-linear drift of relative gravimeters, the analysis of spatial surveys requires a least-squares network adjustment in which spatial and temporal gravity ties between stations within a survey network are considered (Jacob et al. (2010); Hector and Hinderer (2016); Kennedy and Ferré (2015)). The 40 gravity stations were repeatedly visited with a relative spring gravimeter which required absolute FG5#228 measurements as a reference for drift correction. Each of the four surveys yielded over 100 gravity ties as they covered all 40 stations in 12 loops consisting of 5 to 10 stations in each loop. Their study meant seven full days of work for two operators for each survey due to numerous returns to the reference station. Meanwhile, Fores et al. (2016b) showed that relative gravimetry with a CG5 is highly sensitive to temperature. Correcting for temperature induced effects shed new light on apparent spatial gravity differences measured in the field. It is possible that the spatial water storage heterogeneity suggested by Jacob et al. (2010) needs to be re-interpreted in view of remaining, uncorrected effects.

https://doi.org/10.5194/gi-2020-22
Preprint. Discussion started: 21 August 2020


Geoscientific Instrumentation Methods and Data Systems Discussions

The applications in the mentioned studies show the potential gain in precision and time saved provided by the AQG. The AQG#B01 allows to combine two instruments in one. In absence of a detectable drift, regular calibration is not required. In principle, no repeated loops would be necessary, as no gravity ties need to be established. The need for another indoor reference gravimeter becomes obsolete. High precision gravity acquisition is possible with this new movable instrument. It is easy to set-up and use without the need for operation and maintenance by an expert, as for the FG5. The survey time investment and data treatment could be hence reduced remarkably for spatial gravity mapping. The results so far suggest a sensitivity between 10 and 20 $nm.s^{-2}$ after 1 hour. These first results are promising that the AQG#B01 could reach significantly higher precision than relative gravimeters while being transportable. Even if the sensitivity of the AQG#B01 during outdoor operation still needs to be investigated, the results suggest reliable operation in different temperatures, very likely reaching a higher sensitivity than that of relative gravimeters after only one h of measurement. The repeatability has been quantified as better than 50 $nm.s^{-2}$. Our study also revealed important precautions that need to be taken. The first results on the Coriolis effect suggest that for repeated studies the same orientation of the sensor head needs to be kept.

Its time efficient deployment offers new possibilities for natural hazard monitoring and potential early warning systems, some of which are already under investigation with the AQG#A. Joint absolute and relative gravimetry monitoring of volcanic activity are studied at Mt Etna (Carbone et al. (2020)). Another recent project focuses on the AQG on a mobile facility for a hydrological extreme event task force (Reich and Güntner (2020)). The observatory tests under controlled conditions aimed at singling out the effects of ambient conditions, mainly temperature. The next step is clearly to carry out tests outside the building. Repeated displacements between other observatory locations should be carried out to quantify the repeatability of the measurement. The estimation of the vertical gravity gradients by operating the AQG#B01 on two different heights would add another application to the instrument's repertoire.

Data availability. The data are available at https://doi.org/10.5281/zenodo.3978318

Author contributions. Nicolas Le Moigne carried out the instrumental tests. Data analysis was carried out by Anne-Karin Cooke. Planning of experiments and interpretation of results was a joint effort of C.C., N.L.M and A.-K.C.

Competing interests. The study presented in this paper has been carried out in the context of the PhD thesis of Anne-Karin Cooke within the network ITN Enigma (https://enigma-itn.eu/esr-n8-monitoring-water-storage-changes-new-portable-absolute-quantum-gravimeter/). The University of Montpellier (Géosciences) and the company Muquans, the developer of the new absolute quantum gravimeter, have a collaboration for this purpose. During a large part of her PhD, she has been an employee of Muquans. Currently, she is employed by the University of Montpellier.

https://doi.org/10.5194/gi-2020-22
Preprint. Discussion started: 21 August 2020

Geoscientific Instrumentation Methods and Data Systems Discussions
Open Access
EGU

Disclaimer. All measurement presented here are from the Larzac observatory hosted by OSU OREME (http://www.oreme.org) and SNO H+ (http://hplus.ore.fr/). Larzac observatory and instrumentation are mainly funded by the CNRS INSU, ANR, Montpellier University, OZCAR, RESIF and Occitanie region. ENIGMA ITN has received funding from European Union's Horizon 2020 research and innovation programme under the Marie Sklodowska-Curie Grant Agreement N°722028.

Acknowledgements. We would like to thank Pierre Vermeulen and Laura Antoni-Micollier from Muquans for their active support, discussion and feedback. Furthermore, we thank Sébastien Merlet for the discussion and advice.

https://doi.org/10.5194/gi-2020-22
Preprint. Discussion started: 21 August 2020

Geoscientific Instrumentation Methods and Data Systems Discussions

References

Allan, D.: Statistics of atomic frequency standards, Proceedings of the IEEE, 54, 221–230, https://doi.org/10.1109/proc.1966.4634, 1966.

Bodart, Q., Merlet, S., Malossi, N., Santos, F. P. D., Bouyer, P., and Landragin, A.: A cold atom pyramidal gravimeter with a single laser beam, Applied Physics Letters, 96, 134 101, https://doi.org/10.1063/1.3373917, 2010.

Bonvalot, S., Diament, M., and Gabalda, G.: Continuous gravity recording with Scintrex CG-3M meters:a promising tool for monitoring active zones, Geophysical Journal International, 135, 470–494, https://doi.org/10.1046/j.1365-246x.1998.00653.x, 1998.

Boy, J.-P. and Hinderer, J.: Study of the seasonal gravity signal in superconducting gravimeter data, Journal of Geodynamics, 41, 227–233, https://doi.org/10.1016/j.jog.2005.08.035, 2006.

Boy, J. P. and Lyard, F.: High-frequency non-tidal ocean loading effects on surface gravity measurements, Geophysical Journal International, 175, 35–45, https://doi.org/10.1111/j.1365-246x.2008.03895.x, 2008.

Boy, J.-P., Longuevergne, L., Boudin, F., Jacob, T., Lyard, F., Llubes, M., Florsch, N., and Esnoult, M.-F.: Modelling atmospheric and induced non-tidal oceanic loading contributions to surface gravity and tilt measurements, Journal of Geodynamics, 48, 182–188, https://doi.org/10.1016/j.jog.2009.09.022, 2009.

Camp, M. V. and Vauterin, P.: Tsoft: graphical and interactive software for the analysis of time series and Earth tides, Computers & Geosciences, 31, 631–640, https://doi.org/10.1016/j.cageo.2004.11.015, 2005.

Camp, M. V., de Viron, O., Scherneck, H.-G., Hinzen, K.-G., Williams, S. D. P., Lecocq, T., Quinif, Y., and Camelbeeck, T.: Repeated absolute gravity measurements for monitoring slow intraplate vertical deformation in western Europe, Journal of Geophysical Research, 116, https://doi.org/10.1029/2010jb008174, 2011.

Carbone, D., Poland, M. P., Diament, M., and Greco, F.: The added value of time-variable microgravimetry to the understanding of how volcanoes work, Earth-Science Reviews, 169, 146–179, https://doi.org/10.1016/j.earscirev.2017.04.014, 2017.

Carbone, D., Cannavò, F., Greco, F., Messina, A., Contrafatto, D., Siligato, G., Lautier-Gaud, J., Antoni-Micollier, L., Hammond, G., Middlemiss, R., Toland, K., van Zeeuw de Dalfsen, E., Koymans, M., Rivalta, E., Nikkhoo, M., Bonadonna, C., and Frischknecht, C.: The NEWTON-g "gravity imager": a new window into processes involving subsurface fluids, https://doi.org/10.5194/egusphere-egu2020-16329, 2020.

Creutzfeldt, B., Güntner, A., Klügel, T., and Wziontek, H.: Simulating the influence of water storage changes on the superconducting gravimeter of the Geodetic Observatory Wettzell, Germany, GEOPHYSICS, 73, WA95–WA104, https://doi.org/10.1190/1.2992508, 2008.

Creutzfeldt, B., Güntner, A., Thoss, H., Merz, B., and Wziontek, H.: Measuring the effect of local water storage changes on in situ gravity observations: Case study of the Geodetic Observatory Wettzell, Germany, Water Resources Research, 46, https://doi.org/10.1029/2009wr008359, 2010.

Crossley, D., Hinderer, J., and Riccardi, U.: The measurement of surface gravity, Reports on Progress in Physics, 76, 046 101, https://doi.org/10.1088/0034-4885/76/4/046101, 2013.

Deville, S., Jacob, T., Chéry, J., and Champollion, C.: On the impact of topography and building mask on time varying gravity due to local hydrology, Geophysical Journal International, 192, 82–93, https://doi.org/10.1093/gji/ggs007, 2012.

Ferguson, J. F., Chen, T., Brady, J., Aiken, C. L., and Seibert, J.: The 4D microgravity method for waterflood surveillance: Part II — Gravity measurements for the Prudhoe Bay reservoir, Alaska, GEOPHYSICS, 72, I33–I43, https://doi.org/10.1190/1.2435473, 2007.

https://doi.org/10.5194/gi-2020-22
Preprint. Discussion started: 21 August 2020

Geoscientific Instrumentation Methods and Data Systems Discussions

Fores, B., Champollion, C., Moigne, N. L., Bayer, R., and Chéry, J.: Assessing the precision of the iGrav superconducting gravimeter for hydrological models and karstic hydrological process identification, Geophysical Journal International, 208, 269–280, https://doi.org/10.1093/gji/ggw396, 2016a.

Fores, B., Champollion, C., Moigne, N. L., and Chery, J.: Impact of ambient temperature on spring-based relative gravimeter measurements, Journal of Geodesy, 91, 269–277, https://doi.org/10.1007/s00190-016-0961-2, 2016b.

Fores, B., Champollion, C., Mainsant, G., Albaric, J., and Fort, A.: Monitoring Saturation Changes with Ambient Seismic Noise and Gravimetry in a Karst Environment, Vadose Zone Journal, 17, 170 163, https://doi.org/10.2136/vzj2017.09.0163, 2018.

Fores, B., Klein, G., Moigne, N. L., and Francis, O.: Long-Term Stability of Tilt-Controlled gPhoneX Gravimeters, Journal of Geophysical Research: Solid Earth, 124, 12 264–12 276, https://doi.org/10.1029/2019jb018276, 2019.

Francis, O., Baumann, H., Volarik, T., Rothleitner, C., Klein, G., Seil, M., Dando, N., Tracey, R., Ullrich, C., Castelein, S., Hua, H., Kang, W., Chongyang, S., Songbo, X., Hongbo, T., Zhengyuan, L., Pálinkás, V., Kostelecký, J., Mäkinen, J., Näränen, J., Merlet, S., Farah, T., Guerlin, C., Santos, F. P. D., Moigne, N. L., Champollion, C., Deville, S., Timmen, L., Falk, R., Wilmes, H., Iacovone, D., Baccaro, F., Germak, A., Biolcati, E., Krynski, J., Sekowski, M., Olszak, T., Pachuta, A., Agren, J., Engfeldt, A., Reudink, R., Inacio, P., McLaughlin, D., Shannon, G., Eckl, M., Wilkins, T., van Westrum, D., and Billson, R.: The European Comparison of Absolute Gravimeters 2011 (ECAG-2011) in Walferdange, Luxembourg: results and recommendations, Metrologia, 50, 257–268, https://doi.org/10.1088/0026-1394/50/3/257, 2013.

Freier, C., Hauth, M., Schkolnik, V., Leykauf, B., Schilling, M., Wziontek, H., Scherneck, H.-G., Müller, J., and Peters, A.: Mobile quantum gravity sensor with unprecedented stability, Journal of Physics: Conference Series, 723, 012 050, https://doi.org/10.1088/1742-6596/723/1/012050, 2016.

Gaillardet, J., Braud, I., Hankard, F., Anquetin, S., Bour, O., Dorfliger, N., de Dreuzy, J., Galle, S., Galy, C., Gogo, S., Gourcy, L., Habets, F., Laggoun, F., Longuevergne, L., Borgne, T. L., Naaim-Bouvet, F., Nord, G., Simonneaux, V., Six, D., Tallec, T., Valentin, C., Abril, G., Allemand, P., Arènes, A., Arfib, B., Arnaud, L., Arnaud, N., Arnaud, P., Audry, S., Comte, V. B., Batiot, C., Battais, A., Bellot, H., Bernard, E., Bertrand, C., Bessière, H., Binet, S., Bodin, J., Bodin, X., Boithias, L., Bouchez, J., Boudevillain, B., Moussa, I. B., Branger, F., Braun, J. J., Brunet, P., Caceres, B., Calmels, D., Cappelaere, B., Celle-Jeanton, H., Chabaux, F., Chalikakis, K., Champollion, C., Copard, Y., Cotel, C., Davy, P., Deline, P., Delrieu, G., Demarty, J., Dessert, C., Dumont, M., Emblanch, C., Ezzahar, J., Estèves, M., Favier, V., Faucheux, M., Filizola, N., Flammarion, P., Floury, P., Fovet, O., Fournier, M., Francez, A. J., Gandois, L., Gascuel, C., Gayer, E., Genthon, C., Gérard, M. F., Gilbert, D., Gouttevin, I., Grippa, M., Gruau, G., Jardani, A., Jeanneau, L., Join, J. L., Jourde, H., Karbou, F., Labat, D., Lagadeuc, Y., Lajeunesse, E., Lastennet, R., Lavado, W., Lawin, E., Lebel, T., Bouteiller, C. L., Legout, C., Lejeune, Y., Meur, E. L., Moigne, N. L., Lions, J., Lucas, A., Malet, J. P., Marais-Sicre, C., Maréchal, J. C., Marlin, C., Martin, P., Martins, J., Martinez, J. M., Massei, N., Mauclerc, A., Mazzilli, N., Molénat, J., Moreira-Turcq, P., Mougin, E., Morin, S., Ngoupayou, J. N., Panthou, G., Peugeot, C., Picard, G., Pierret, M. C., Porel, G., Probst, A., Probst, J. L., Rabatel, A., Raclot, D., Ravanel, L., Rejiba, F., René, P., Ribolzi, O., Riotte, J., Rivière, A., Robain, H., Ruiz, L., Sanchez-Perez, J. M., Santini, W., Sauvage, S., Schoeneich, P., Seidel, J. L., Sekhar, M., Sengtaheuanghoung, O., Silvera, N., Steinmann, M., Soruco, A., Tallec, G., Thibert, E., Lao, D. V., Vincent, C., Viville, D., Wagnon, P., and Zitouna, R.: OZCAR: The French Network of Critical Zone Observatories, Vadose Zone Journal, 17, 180 067, https://doi.org/10.2136/vzj2018.04.0067, 2018.

Geiger, R., Landragin, A., Merlet, S., and Santos, F. P. D.: High-accuracy inertial measurements with cold-atom sensors, AVS Quantum Science, 2, 024 702, https://doi.org/10.1116/5.0009093, 2020.

Gillot, P., Francis, O., Landragin, A., Santos, F. P. D., and Merlet, S.: Stability comparison of two absolute gravimeters: optical versus atomic interferometers, Metrologia, 51, L15–L17, https://doi.org/10.1088/0026-1394/51/5/l15, 2014.

https://doi.org/10.5194/gi-2020-22
Preprint. Discussion started: 21 August 2020

Geoscientific Instrumentation Methods and Data Systems Discussions
Open Access
EGU

Güntner, A., Reich, M., Mikolaj, M., Creutzfeldt, B., Schroeder, S., and Wziontek, H.: Landscape-scale water balance monitoring with an iGrav superconducting gravimeter in a field enclosure, Hydrology and Earth System Sciences, 21, 3167–3182, https://doi.org/10.5194/hess-21-3167-2017, 2017.

Hauth, M., Freier, C., Schkolnik, V., Senger, A., Schmidt, M., and Peters, A.: First gravity measurements using the mobile atom interferometer GAIN, Applied Physics B, 113, 49–55, https://doi.org/10.1007/s00340-013-5413-6, 2013.

Hector, B. and Hinderer, J.: pyGrav, a Python-based program for handling and processing relative gravity data, Computers & Geosciences, 91, 90–97, https://doi.org/10.1016/j.cageo.2016.03.010, 2016.

Hector, B., Hinderer, J., Séguis, L., Boy, J.-P., Calvo, M., Descloitres, M., Rosat, S., Galle, S., and Riccardi, U.: Hydro-gravimetry in West-Africa: First results from the Djougou (Benin) superconducting gravimeter, Journal of Geodynamics, 80, 34–49, https://doi.org/10.1016/j.jog.2014.04.003, 2014.

Hector, B., Séguis, L., Hinderer, J., Cohard, J.-M., Wubda, M., Descloitres, M., Benarrosh, N., and Boy, J.-P.: Water storage changes as a marker for base flow generation processes in a tropical humid basement catchment (B enin): Insights from hybrid gravimetry, Water Resources Research, 51, 8331–8361, https://doi.org/10.1002/2014wr015773, 2015.

Hinderer, J., Crossley, D., and Warburton, R.: Superconducting Gravimetry, in: Treatise on Geophysics, pp. 59–115, Elsevier, https://doi.org/10.1016/b978-0-444-53802-4.00062-2, 2015.

Hinze, W. J., Von Frese, R. R., and Saad, A. H.: Gravity and magnetic exploration: Principles, practices, and applications, Cambridge University Press, 2013.

Huang, P.-W., Tang, B., Chen, X., Zhong, J.-Q., Xiong, Z.-Y., Zhou, L., Wang, J., and Zhan, M.-S.: Accuracy and stability evaluation of the 85Rb atom gravimeter WAG-H5-1 at the 2017 International Comparison of Absolute Gravimeters, Metrologia, 56, 045 012, https://doi.org/10.1088/1681-7575/ab2f01, 2019.

Hwang, C., Cheng, T.-C., Cheng, C., and Hung, W.: Land subsidence using absolute and relative gravimetry: a case study in central Taiwan, Survey Review, 42, 27–39, https://doi.org/10.1179/003962609x451672, 2010.

Imanishi, Y.: A Network of Superconducting Gravimeters Detects Submicrogal Coseismic Gravity Changes, Science, 306, 476–478, https://doi.org/10.1126/science.1101875, 2004.

Jacob, T., Bayer, R., Chery, J., Jourde, H., Moigne, N. L., Boy, J.-P., Hinderer, J., Luck, B., and Brunet, P.: Absolute gravity monitoring of water storage variation in a karst aquifer on the larzac plateau (Southern France), Journal of Hydrology, 359, 105–117, https://doi.org/10.1016/j.jhydrol.2008.06.020, 2008.

Jacob, T., Bayer, R., Chery, J., and Moigne, N. L.: Time-lapse microgravity surveys reveal water storage heterogeneity of a karst aquifer, Journal of Geophysical Research, 115, https://doi.org/10.1029/2009jb006616, 2010.

Jiang, Z., Pálinkáš, V., Arias, F. E., Liard, J., Merlet, S., Wilmes, H., Vitushkin, L., Robertsson, L., Tisserand, L., Santos, F. P. D., Bodart, Q., Falk, R., Baumann, H., Mizushima, S., Mäkinen, J., Bilker-Koivula, M., Lee, C., Choi, I. M., Karaboce, B., Ji, W., Wu, Q., Ruess, D., Ullrich, C., Kostelecký, J., Schmerge, D., Eckl, M., Timmen, L., Moigne, N. L., Bayer, R., Olszak, T., Ågren, J., Negro, C. D., Greco, F., Diament, M., Deroussi, S., Bonvalot, S., Krynski, J., Sekowski, M., Hu, H., Wang, L. J., Svitlov, S., Germak, A., Francis, O., Becker, M., Inglis, D., and Robinson, I.: The 8th International Comparison of Absolute Gravimeters 2009: the first Key Comparison (CCM.G-K1) in the field of absolute gravimetry, Metrologia, 49, 666–684, https://doi.org/10.1088/0026-1394/49/6/666, 2012.

Kennedy, J., Ferré, T. P. A., and Creutzfeldt, B.: Time-lapse gravity data for monitoring and modeling artificial recharge through a thick unsaturated zone, Water Resources Research, 52, 7244–7261, https://doi.org/10.1002/2016wr018770, 2016.

https://doi.org/10.5194/gi-2020-22
Preprint. Discussion started: 21 August 2020

Geoscientific Instrumentation Methods and Data Systems Discussions
Open Access
EGU

Kennedy, J. R. and Ferré, T. P.: Accounting for time- and space-varying changes in the gravity field to improve the network adjustment of relative-gravity data, Geophysical Journal International, 204, 892–906, https://doi.org/10.1093/gji/ggv493, 2015.

Louchet-Chauvet, A., Farah, T., Bodart, Q., Clairon, A., Landragin, A., Merlet, S., and Santos, F. P. D.: The influence of transverse motion within an atomic gravimeter, New Journal of Physics, 13, 065 025, https://doi.org/10.1088/1367-2630/13/6/065025, 2011.

Mazzotti, S., Lambert, A., Henton, J., James, T. S., and Courtier, N.: Absolute gravity calibration of GPS velocities and glacial isostatic adjustment in mid-continent North America, Geophysical Research Letters, 38, n/a–n/a, https://doi.org/10.1029/2011gl049846, 2011.

Ménoret, V., Vermeulen, P., Moigne, N. L., Bonvalot, S., Bouyer, P., Landragin, A., and Desruelle, B.: Gravity measurements below 10-9 g with a transportable absolute quantum gravimeter, Scientific Reports, 8, https://doi.org/10.1038/s41598-018-30608-1, 2018.

Merlet, S., Bodart, Q., Malossi, N., Landragin, A., Santos, F. P. D., Gitlein, O., and Timmen, L.: Comparison between two mobile absolute gravimeters: optical versus atomic interferometers, Metrologia, 47, L9–L11, https://doi.org/10.1088/0026-1394/47/4/l01, 2010.

Mollenhauer, H., Kasner, M., Haase, P., Peterseil, J., Wohner, C., Frenzel, M., Mirtl, M., Schima, R., Bumberger, J., and Zacharias, S.: Long-term environmental monitoring infrastructures in Europe: observations, measurements, scales, and socio-ecological representativeness, Science of The Total Environment, 624, 968–978, https://doi.org/10.1016/j.scitotenv.2017.12.095, 2018.

Niebauer, T.: Gravimetric Methods – Absolute and Relative Gravity Meter: Instruments Concepts and Implementation, in: Treatise on Geophysics, pp. 37–57, Elsevier, https://doi.org/10.1016/b978-0-444-53802-4.00057-9, 2015.

Niebauer, T. M., Sasagawa, G. S., Faller, J. E., Hilt, R., and Klopping, F.: A new generation of absolute gravimeters, Metrologia, 32, 159–180, https://doi.org/10.1088/0026-1394/32/3/004, 1995.

Olsson, P.-A., Breili, K., Ophaug, V., Steffen, H., Bilker-Koivula, M., Nielsen, E., Oja, T., and Timmen, L.: Postglacial gravity change in Fennoscandia—three decades of repeated absolute gravity observations, Geophysical Journal International, 217, 1141–1156, https://doi.org/10.1093/gji/ggz054, 2019.

Pearson-Grant, S., Franz, P., and Clearwater, J.: Gravity measurements as a calibration tool for geothermal reservoir modelling, Geothermics, 73, 146–157, https://doi.org/10.1016/j.geothermics.2017.06.006, 2018.

Peters, A., Chung, K. Y., and Chu, S.: High-precision gravity measurements using atom interferometry, Metrologia, 38, 25–61, https://doi.org/10.1088/0026-1394/38/1/4, 2001.

Reich, M. and Güntner, A.: A concept of hybrid terrestrial gravimetry and cosmic ray neutron sensing for investigating hydrological extreme events, https://doi.org/10.5194/egusphere-egu2020-13624, 2020.

Reich, M., Mikolaj, M., Blume, T., and Güntner, A.: Reducing gravity data for the influence of water storage variations beneath observatory buildings, GEOPHYSICS, 84, EN15–EN31, https://doi.org/10.1190/geo2018-0301.1, 2019.

Rodell, M., Houser, P. R., Jambor, U., Gottschalck, J., Mitchell, K., Meng, C.-J., Arsenault, K., Cosgrove, B., Radakovich, J., Bosilovich, M., Entin, J. K., Walker, J. P., Lohmann, D., and Toll, D.: The Global Land Data Assimilation System, Bulletin of the American Meteorological Society, 85, 381–394, https://doi.org/10.1175/bams-85-3-381, 2004.

Sugihara, M., Nishi, Y., Ikeda, H., Nawa, K., and Ishido, T.: Monitoring CO2 Injection at the Tomakomai Field Using High-sensitivity Continuous Gravimetry, Energy Procedia, 114, 4020–4027, https://doi.org/10.1016/j.egypro.2017.03.1542, 2017.

Van Camp, M., de Viron, O., Pajot-Métivier, G., Casenave, F., Watlet, A., Dassargues, A., and Vanclooster, M.: Direct measurement of evapotranspiration from a forest using a superconducting gravimeter, Geophysical Research Letters, 43, 10–225, https://doi.org/10.1002/2016GL070534, 2016.

Van Camp, M., de Viron, O., Watlet, A., Meurers, B., Francis, O., and Caudron, C.: Geophysics From Terrestrial Time-Variable Gravity Measurements, Reviews of Geophysics, 55, 938–992, https://doi.org/10.1002/2017rg000566, 2017.

https://doi.org/10.5194/gi-2020-22
Preprint. Discussion started: 21 August 2020

Geoscientific Instrumentation Methods and Data Systems Discussions

Volcke, P., Pequegnat, C., Brichet-Billet, B., Lecointre, A., Wolyniec, D., and Guéguen, P.: RESIF national datacentre: new features and upcoming evolutions, EGU2014-12270, 2014.

Wenzel, H.-G.: The nanogal software: Earth tide data processing package ETERNA 3.30, Bull. Inf. Marées Terrestres, 124, 9425–9439, 1996.

Wu, S., Fend, J., Li, C., Su, D., Wand, Q., Hu, R., Hu, L., Xu, J., Ji, W., Ullrich, C., Pálinkáš, V., Kostelecký, J., Bilker-Koivula, M., Näränen, J., Merlet, S., Moigne, N. L., Mizushima, S., Francis, O., Choi, I.-M., Kim, M.-S., Alotaibi, H. M., Aljuwayr, A., Baumann, H., Priruenrom, T., Woradet, N., KIRBAŞ, C., Coşkun, İ., and Newel, D.: The results of CCM.G-K2.2017 key comparison, Metrologia, 57, 07 002–07 002, https://doi.org/10.1088/0026-1394/57/1a/07002, 2020.

3.8.1 Complementary results and discussion on AQG#B01 experiments

3.8.1.1 Measurements in a garage

As an intermediate step between controlled observatory conditions and open-air measurements, the influence of diurnal temperature changes and anthropogenic noise was assessed by operating the AQG#B01 in a garage. On 02/06/2020 the AQG-B01 was transported from the Géosciences laboratory to a private garage in a residential area in Montpellier (Aiguelongue) (in approximately 3 km distance to Géosciences). The garage was not air-conditioned. The garage is connected to a house inhabited by three people. Initially, the garage doors were kept closed. To allow for a larger amplitude of diurnal temperature change, the doors were opened in the late evening and early morning starting from 08/06/2020. Daily averages of g show a standard deviation of less than 50 nm·s^{-2}, differences between daily averages during the two weeks of operation lie within statistical uncertainty (Figure 3.46, panel a).The sensitivity (Figure 3.48) is reduced compared to the other sites. 26 nm·s^{-2} are reached after one hour of averaging, sensitivity is better than 10 nm·s^{-2} after 24 h of averaging. The Allan deviation decreases linearly within 24h. As a comparison, the daily residuals including standard deviation obtained from the Scintrex CG6#125 relative gravimeter are depicted in Figure 3.47.

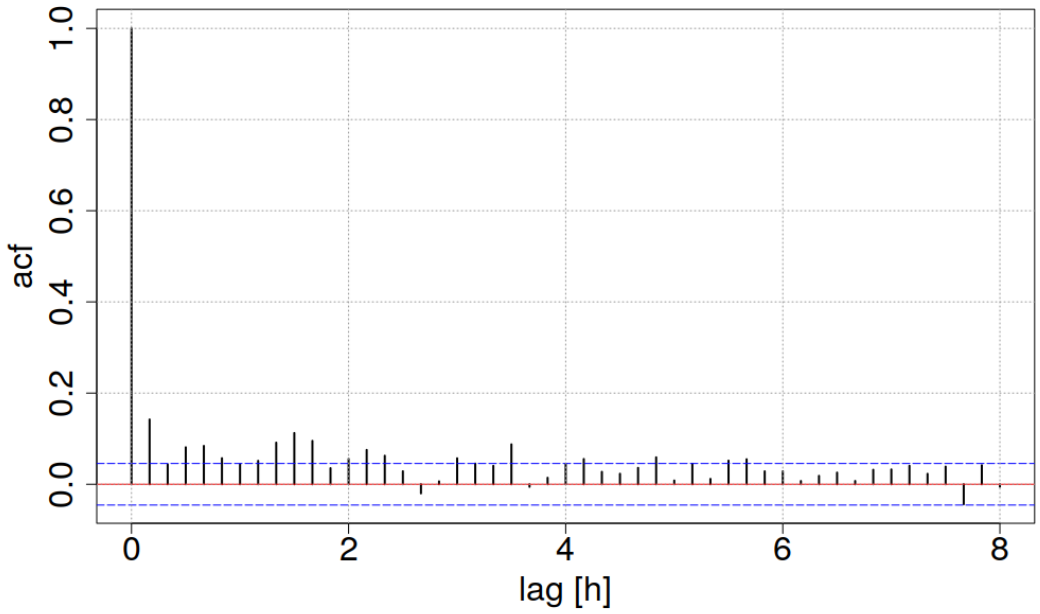

Figure 3.43: Auto-correlation function of AQG-B01 gravity residuals from the mean recorded during operation in a garage in Montpellier 02/06/2020 – 17/06/2020. Time lags in hours.

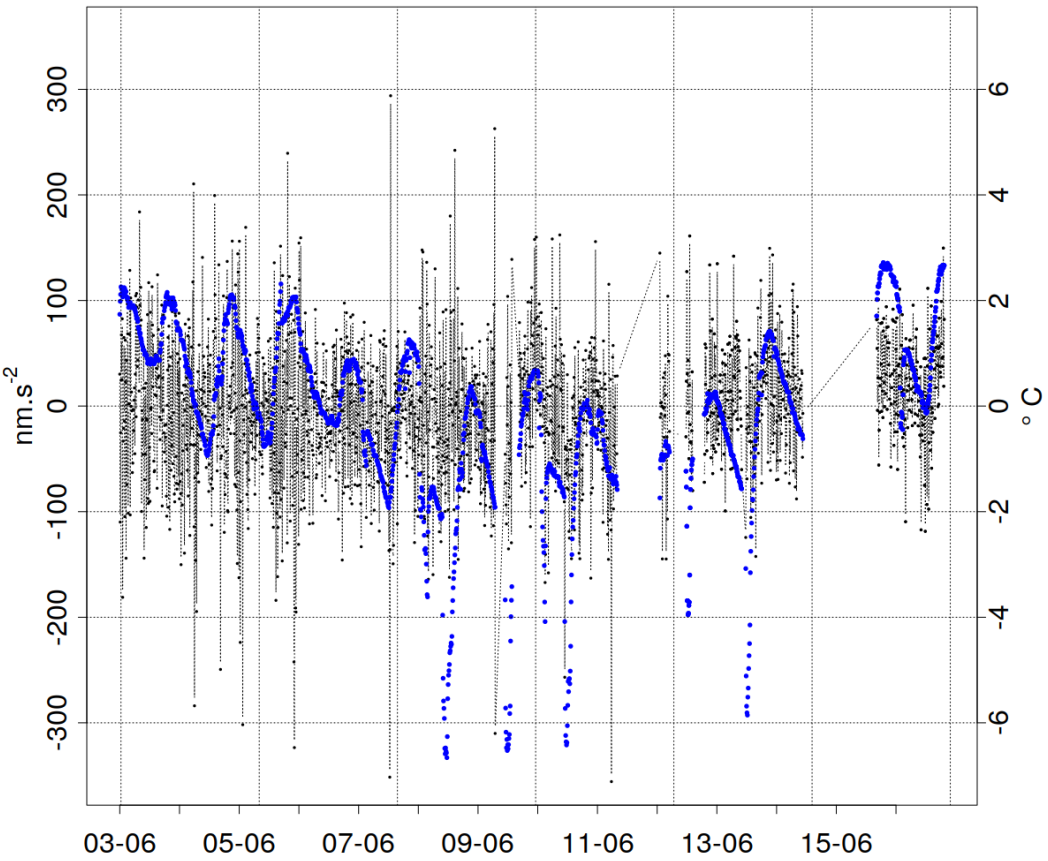

Figure 3.44: AQG-B01 gravity residuals from the mean recorded during operation in a garage in Montpellier 02/06/2020 – 17/06/2020.

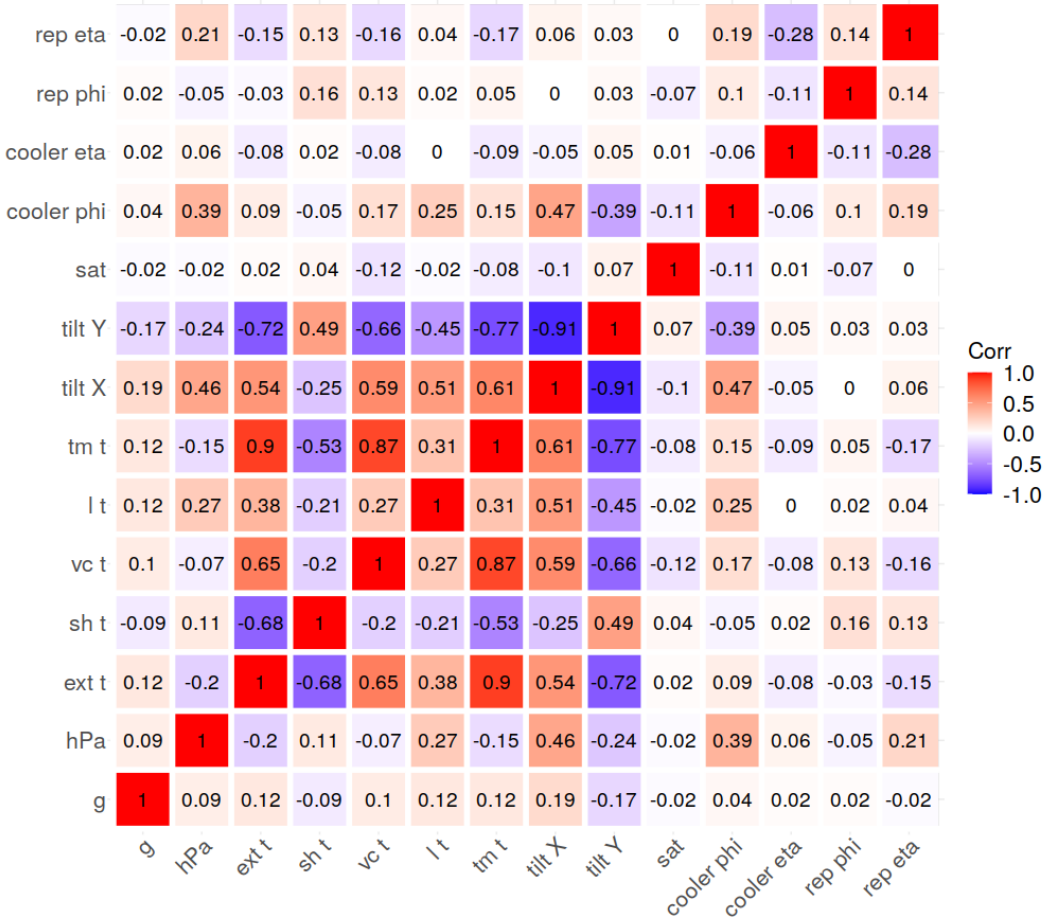

Figure 3.45: Auto-correlation function of AQG-B gravity residuals from the mean recorded during operation. Correlogram of gravity residuals ('g') and acquistion variables. Gravity residuals averaged over 10 minutes, obtained with AQG-B01 in a garage in Montpellier 02/06/2020 – 17/06/2020. Variables: 'hPa' : atmospheric pressure, 'ext t': external temperature, 'sh t' : sensor head temp., 'vc t': vacuum chamber temp., 'l t': laser temp., 'tm t' : tiltmeter temp., tilt X, tilt Y, 'sat' : correction frequency offset of the saturated absorption spectroscopy, Laser polarisation angles phi and eta (rad) of the two lasers: cooler laser and repumper.

As shown in Figure 3.46 (panel b) the achieved temperature range was between 20 and 30° C. No significant correlation between external temperature in the garage and gravity residuals was observed. Gravity and external temperature residuals obtained with the AQG#B01 averaged every 10 minutes are shown in Figure 3.44. Gravity residuals do not show fluctuations as temperature does. The analysis of auto-correlation (Figure 3.43) confirms the absence of temporal patterns. The correlation matrix of the entire time series (Figure 3.45) shows only very weak correlations between gravity residuals and any of the analysed variables. The notably strongest correlations between gravity residuals and tilt in x and y-direction are 0.19 and -0.17, respectively. External and tiltmeter temperatures are strongly correlated (0.9), to a lesser extend also with the tilts. At this point, it needs to be pointed out that the AQG#B01 shows a reduction in correlation

with the recorded external and instrumental variables as compared to the AQG#A01.

As can be seen in Figure 3.46 (panel c), during periods of external temperature a change in sensor head tilts occurs. Tilts returned to values close to zero within hours. Maximal inclinations of about 0.15 mrad were found for tilts in x-direction. Tilts in y-direction stayed more stable and show generally fewer variations. After a manual re-calibration of the tilt after 11/06/2020, tilts move in opposite directions than before, which is likely related to a change in equilibrium after each re-calibration.

During the last days of operation, several acquisition stops occurred that required a manual measurement relaunch and causing data gaps mainly during the night. The causes of these stops have not been identified yet. The residents entered the garage several times throughout the day from the interior door. The opening of the outward garage doors for a temperature change caused increased air circulation in the room. Possible impacts of these winds on tripod levelling and imbalance in temperature of different sides of the tripod cannot be ruled out and need to be investigated.

These results demonstrate the successful deployment of the AQG#B01 in an urban environment. Stable measurements were achieved during two weeks of operation in elevated noise levels and in presence of several environmental effects, in particular, temperature changes of several °C within minutes and air movement when opening the garage doors. Critical aspects are the frequent measurement stops at the end of the series.

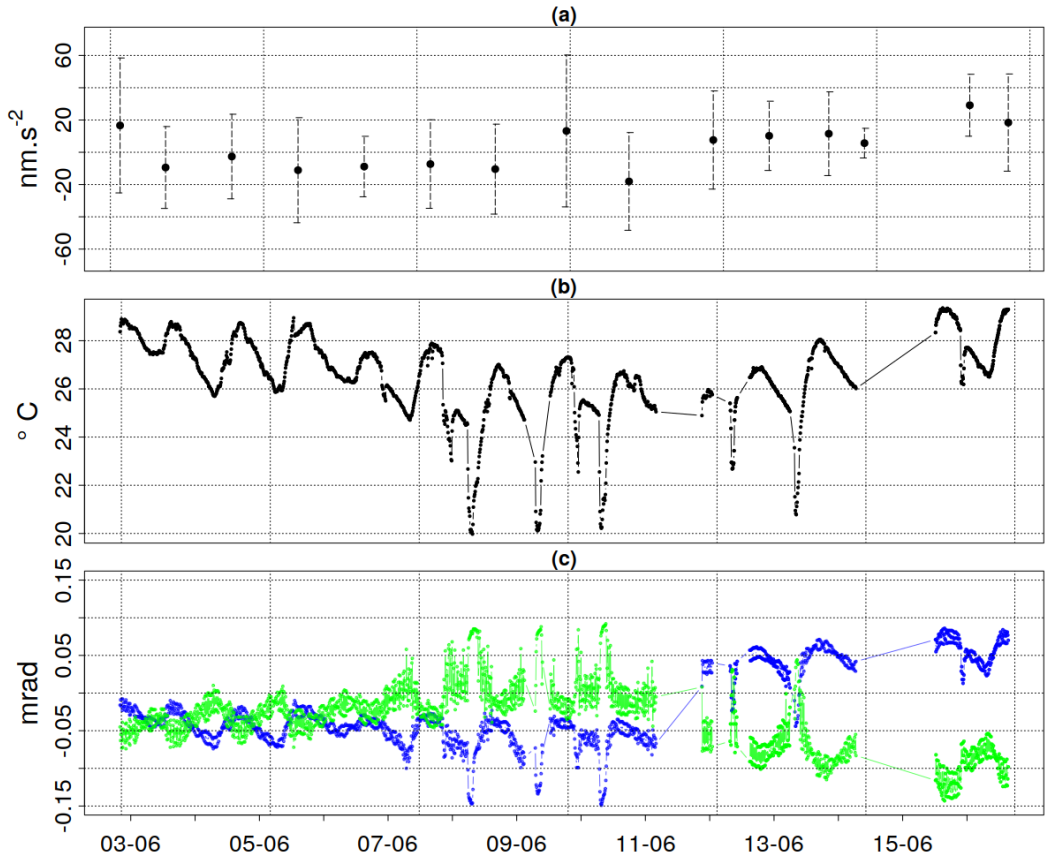

Figure 3.46: Panel a: AQG-B gravity residuals from the mean recorded during operation in a garage in Montpellier 02/06/2020 – 17/06/2020. Panel b: external temperature in the garage recorded by AQG-B01 in °C. Panel c: Sensor head tilts in x (blue) and y (green) given in mrad.

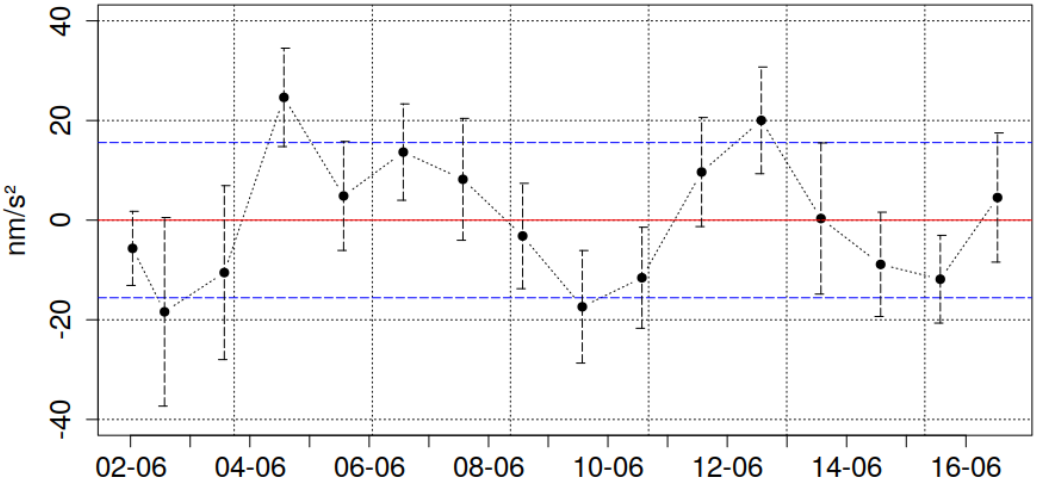

Figure 3.47: Scintrex CG6-125 gravity residuals from the mean recorded during operation in a garage in Montpellier 02/06/2020 – 17/06/2020. One-minute CG6 data was corrected for ocean and solid Earth tides (tidal parameters for Géosciences Montpellier) and a linear drift of -166.483 ± 0.04 $nm.s^{-2}d^{-1}$ subtracted. Mean (red) and standard deviation (blue, dashed line) for the entire series.

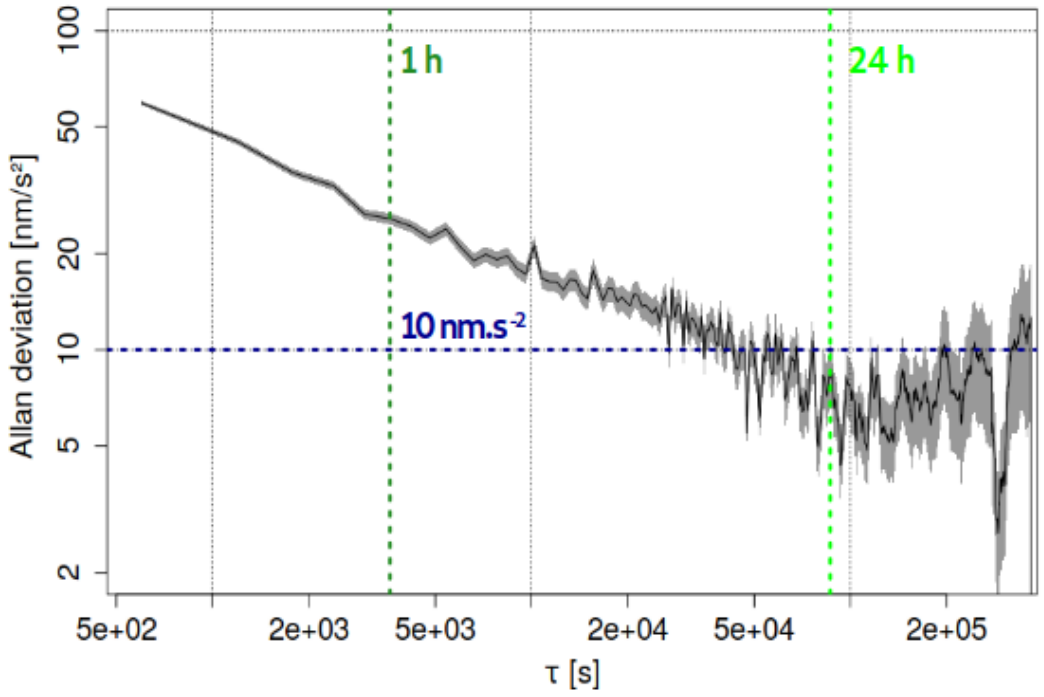

Figure 3.48: Allan deviation of 10 min AQG-B01 data obtained during operation in a garage in Montpellier. The horizontal blue dashed line shows the sensitivity benchmark of 10 nm.s^{-2}, the dark green vertical dashed line signifies the integration period of 1 h, the light green one that of 24 h.

3.8.1.2 Large-scale repeatability

Large-scale repeatability has been estimated from the gravity differences between two distant measurement points. Here we show the comparison of the large-scale repeatability of the different instruments, complementary to the results discussed in the publication "Evaluation of the capacities of a field absolute quantum gravimeter (AQG#B01)".

The results for the AQG#B01 are shown in comparison with the values for Δg measured with the AQG#A01 and the FG5#228 in 2019 in Table 3.2. The Δg between Larzac and Montpellier ($\sim$ 700 m difference in altitude) detected by the AQG#B01 are coherent with a difference of 140 mGal detected with the AQG#A01 and FG5#228 in 2019. The Δg between the two sites differ in the order of 140 nm·s^{-2} between the AQG#B01 and FG5#228. This offset in large-scale repeatability is mainly caused by the gravity difference between the instruments at the Larzac site of 122 nm·s^{-2}. Only one displacement of the AQG#B01 between the Larzac and Montpellier took place since the delivery of the instrument in late 2019. Therefore, repeated measurements and displacements between the sites are required to identify potential systematic effects or errors. The large-scale repeatability study presented here serves for the moment just as a first comparison. Further acquisitions are required to robustly estimate the AQG#B01's large-scale repeatability.

Measurement 1, Measurement 2	FG5-228	AQG-A01	AQG-B01
Larzac (11/01/2019), Montpellier (15/02/2019)	1389606 ± 21	1389506 ± 78	-
Larzac (01/03/2019), Montpellier (04/04/2019) Larzac (04/07/2020)	1389611 ± 21	1389509 ± 82	-
Montpellier (28/05/2020 AQG-B01; 10/06/2020 FG5)	1389594 ± 19	-	1389439 ± 26

Table 3.2: Large-scale repeatability: Δg in nm.s^{-2} between Larzac and Montpellier obtained during surveys in 2019 with the FG5-228 and the AQG-A01 in 2019; AQG-B01 in 2020, respectively

3.9 General discussion on state of AQG devices

The complete uncertainty budget of an instrument requires various repeated tests and inter-comparisons that exceed the scope of this thesis. The discussed instrumental tests conducted with the AQG#A01 and AQG#B01 are not exhaustive and many aspects remain work in progress. Nevertheless, the results obtained from the tests aimed at key performance measures allow to draw conclusions regarding each of the assessed performance criteria. The conducted tests with the AQG#A01 provided valuable insight into the instrument's functioning during operation by scientific users in observatories. Lessons learned from the assessment of the AQG#A01 lead to updated and improved laser polarisation stability in the AQG#B01.

3.9.0.1 Accuracy

The difference between the AQG#B01 and the FG5#228 has been preliminary quantified as on average 110 nm·s^{-2} with a standard deviation of 31 nm·s^{-2} as based on the difference between 13 AQG#B01 and FG5#228 measurements (daily averages) between December 2019 and April 2020 in the Larzac observatory. At Géosciences Montpellier, the difference was 29 nm·s^{-2} with a standard deviation of 67 nm·s^{-2}, with the FG5#228 values being higher than those of the AQG#B01 (based on 24h averages of ten AQG#B01 measurements between 27/04/2020 and 14/05/2020 and one FG5#228 measurement on 10/06/2020).

First tests regarding the potential effect of the sensor head's orientation, the Coriolis effect, on the measurement of g yielded unexpectedly high values. Further tests at different rotation angles, preferably at a low-noise site (Larzac) in comparison with simultaneous FG5 absolute gravity monitoring, are required to investigate this potentially important aspect of the uncertainty budget of the AQG#B01. The accuracy of the AQG#A01 remains work in progress and has not been further detailed in this manuscript. Unpublished instrumental improvements have meanwhile been carried out by Muquans. A detailed, updated assessment of the uncertainty budget of the AQG#A01 is currently carried out at the LNE-SYRTE observatory at Trappes where the AQG#A01 has been operating since mid 2019.

3.9.0.2 Sensitivity

In terms of sensitivity, the results clearly demonstrate the performance improvements obtained with the AQG#B01. The AQG#A01 achieves a sensitivity of better than 10 nm·s^{-2} after 24 h, which the AQG#B01 achieves after only one hour in a calm environment. For noisier environments (Géosciences and garage) the sensitivity after one hour achieved with the AQG#B01 tends to be between 20 and 30 nm·s^{-2}. For the AQG#A01 averaging over 24 h is recommended as its sub-daily oscillations pose limitations. Due to its higher sensitivity, the AQG#B01 allows

for shorter acquisitions than the AQG#A01.

3.9.0.3 Stability

Both AQG devices allow stable measurements of g of several weeks. Significant drifts in time have not been observed. This analysis is limited to data series of about one-month length. Monitoring of ideally at least a few months is required to evaluate long-term stability. A continuous measurement at the Larzac site in 2020 is planned for the AQG#B01 as of the submission date of this manuscript. The experience obtained from the operation in the garage shows that frequent measurement stops required software improvements and modifications in the response to instrumental variables in order to create a robust, continuous measurement system without the necessity of regular human intervention. These software updates have meanwhile been implemented.

3.9.0.4 Repeatability

Both the AQG#A01 and AQG#B01 have been transported and re-installed several times between sites and had been successfully applied in different conditions. Shut-down, disassembly, transport, and full restart did not impact the performance. Additional repeatability tests including the transport to a site with altitude differences are envisaged. The observatory at the Mont Aigoual weather station (Météo France) at 1.567 m peak at about 80 km distance North of Montpellier could serve as a site to be visited, also with FG5 measurements. The AQG#B01's small-scale repeatability has been assessed based on measurements in a relatively noisy environment (Géosciences Montpellier). It could be of interest to repeat these tests on the different concrete pillars at the Larzac site.

3.9.0.5 Potential field operation

The results presented earlier show that the AQG#B01 is on a promising path in view of future field deployment, as it measures g unaffected by temperatures between 20 and 30 °C and tilts of less than 1 mrad. Operation in a garage that potentially includes several sources of uncertainty and noise showed satisfactory stability and expected precision for these conditions. Temperature and tilt tests are possibly of less interest for the AQG#A01 that remains primarily an observatory instrument. The assessment of its uncertainty budget could nevertheless be complemented by the experiments carried out for the AQG#B01, namely tilt sensitivity, temperature manipulation, and combined tilt-temperature experiments. From a practical perspective, the experiences gained during the experiments and displacements carried out with both instruments, confirm the straightforward and user-friendliness of the AQG devices.

As of the date of the submission of this manuscript, the AQG#B01 is ready to be tested in an open-air field campaign.

4 Hydrogravimetry : Vertical gravity gradient monitoring

”Dharmyam yashashyam va vadabhaytoham dakargalam yen jaloplabdhiha
Punsam yathagdeshu shirastathaiva chhitavapi pronnatnimnasanstha.
Ekayna vardayna rasayna chambhyashchyutam namasto vasudha vishayshanta
Nana rastvam bahuvarnatam cha gatam pareekshyam chhititulyamayva.”

”We shall now proceed to treat of the science of undercurrents (dakārgala)
by which man may get at water and observe the duties of life and be happy.
Just in the same way as there are arteries for the circulation
of blood in human bodies, there are water courses running in all directions
above and below within the Earth.”

Varāhamihira, Brihat Samhita, 6th century CE, after Singh et al. (2020))

4.1 Publication in preparation: "On the potential of vertical gravity gradients for soil moisture monitoring" for submission to "Hydrology and Earth System Sciences"

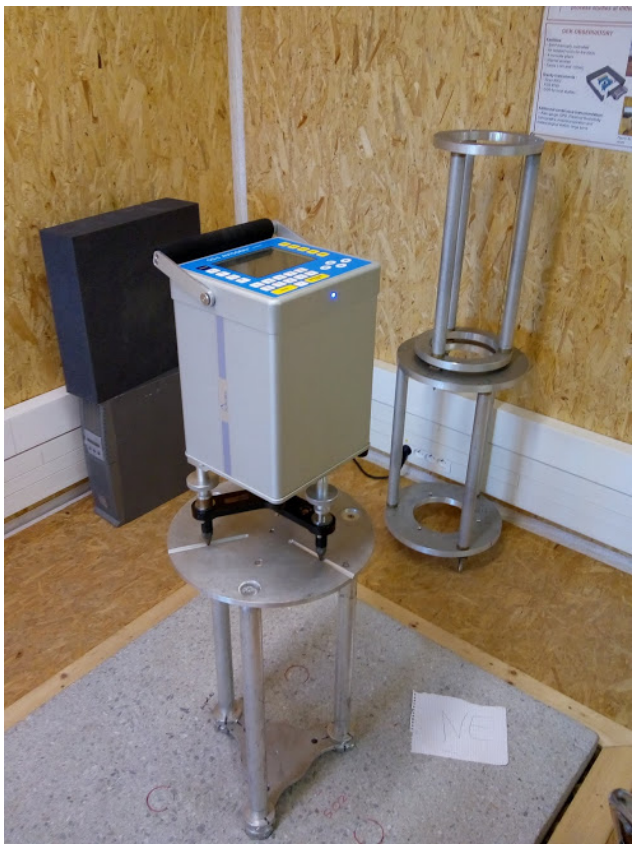

Figure 4.1: Scintrex CG5-1151 relative gravimeter on pillar p_2 on height h_1 in the Larzac observatory in 2018. Photo: Cooke, 2018.

On the potential of vertical gravity gradients for soil moisture monitoring

Anne-Karin Cooke[1], Cédric Champollion[1], Camille Janvier[2], Pierre Vermeulen[2], Nicolas Le Moigne[1], and Sébastien Merlet (not yet confirmed)[3]

[1]Géosciences Montpellier, Univ. Montpellier,CNRS, Univ. des Antilles, Montpellier, France
[2]MuQuans, Talence, France
[3]LNE-SYRTE, Observatoire de Paris, PSL Research University, CNRS, Sorbonne Universités, UPMC, Univ. Paris, France

Correspondence: Anne-Karin Cooke (anne-karin.cooke@umontpellier.fr)

Abstract. Time-lapse ground-based gravimetry is increasingly applied in subsurface hydrology to monitor water storage dynamics as it provides a mass balance constraint. The gravitational effect of water mass changes (e.g. a precipitation event), is usually simplified as a homogeneous, infinite slab (Bouguer plate) of a water column. This assumption may not hold in heterogeneous aquifers (e.g. karsts). The depth-integrative gravity signal does not include information on spatial mass distribution. In contrast to measurements of the gravitational field strength, the vertical gravity gradient (VGG) is sensitive to lateral mass changes. The complementary spatial sensitivities of gravity and VGG can be used to jointly deduct spatial characteristics of mass changes in the subsurface. In this study, we assessed the precision of time-lapse VGG monitoring using relative field gravimeters placed on tripods in a controlled observatory setting and relate our findings to the hydrogeological context of the study site. VGG were estimated from monthly relative gravity surveys on tripods of different heights on three concrete pillars at the Larzac geodetic observatory in Southern France, between December 2017 and November 2018. The repeatability of VGG estimations based on this method has been estimated to be better than 23 $\pm$ 9 E. VGG changes of $\sim$ 80 Eotvos (1 E = 10^{-9} s^{-2}) in one year on one of the measurement locations have been observed. In the absence of other mass changes, the VGG changes were related to possible sources of nearby water storage change. Firstly, the impact of the umbrella effect (shielding of the building from precipitation) was tested as a potential source of VGG changes and found to be limited to a few E. Secondly, possible subsurface porosity distributions were generated in geostatistical stochastic simulation and selected to obey the observed gravity and VGG changes as well as differences between measurement locations. Joint gravity and gravity gradient data reduced the range of simulations consistent with the data. We further discuss the potential of time-lapse VGG measurements as a potential new technique to spatially resolve mass changes in a hydrogeological context.

1 Introduction

Gravimetry measures the Earth's gravitational attraction (referred to as g) and reveals the variability of the gravitational field in space and time. The gravitational attraction g at a given location at a given time is measured with gravimeters which can reach high levels of accuracy and precision of the order of 10^{-9} g. Absolute gravimeters estimate the norm of the gravitational acceleration g during vertical free-fall in a vacuum (Niebauer et al. (1995)). The widely used optical absolute gravimeters show

an instrumental uncertainty of the order of a few tens of nm·s^{-2} (Niebauer (2015)). Recently, quantum absolute gravimeters have achieved comparable performance measures and combine ease of use as well as the possibility of high-frequency, continuous acquisition (Ménoret et al. (2018)).

Relative gravimeters sense the gravitational attraction indirectly by measuring another physical force representing the counteracting force to stabilise a test mass against gravitation. Superconducting relative gravimeters are based on magnetic levitation and reach a precision of ~ 0.1 nm·s^{-2}. They measure continuously at a sampling rate of 1 Hz and tend to be operated stationary at observatories (Hinderer et al. (2015)). Relative spring gravimeters are commonly used for repeated surveys to monitor relative gravity changes due to their transportability, but require regular calibration with absolute reference gravimeters due to their susceptibility to instrumental drifts (Lederer (2009); Christiansen et al. (2011))

Linking the spatial and temporal characteristics of gravity observations to geophysical phenomena and features lies at the core of the discipline. Mapping of spatial gravity anomalies can be used to detect density contrasts of the subsurface as deployed in oil and mineral exploration and prospecting (e.g. Ferguson et al. (2007); Hinze et al. (2013)) or the detection of subsurface depressions (Jacob et al. (2018)). Temporal residuals remain after correcting gravity time series for known effects such as tidal signals and atmospheric pressure variations. These residuals can be attributed to local mass changes (Crossley et al. (2013); Camp et al. (2017)). Gravimetry has delivered valuable contributions to several fields of the Earth sciences. Applications include geodesy and large-scale geodynamics such as tectonics (Camp et al. (2011); Hwang et al. (2010)) and seismology (Imanishi (2004)). This further includes the detection of crust deformation such as glacial isostatic uplift (Mazzotti et al. (2011); Olsson et al. (2019)). Moreover, in civil engineering and natural hazard assessment such as the monitoring of volcanic activity (Bonvalot et al. (1998), Carbone et al. (2017)) and geothermal fields (Pearson-Grant et al. (2018)).

Global and local hydrological gravity effects on gravity observations are caused by crust deformation and Newtonian attraction of water masses (Llubes et al. (2004); Harnisch and Harnisch (2006); Linage et al. (2007); Neumeyer et al. (2008); Longuevergne et al. (2009), Wziontek et al. (2009)). Hydrological signals in ground-based gravity data occur mainly at intermediate time and length scales (hours to years, meters to kilometers). Furthermore, they can be strongly site-dependent and complex to determine (Harnisch and Harnisch (2006)).

Hydrogravimetry as one of the emerging hydrogeophysical exploration methods provides a spatially integrative and non-invasive approach for subsurface imaging. The main characteristic of gravity measurements is their depth-integrative nature that comprises contributions of local as well as distant mass changes. This has found its application in constraining mass balances for total water storage (TWS) estimations. It facilitates the characterisation of subsurface flow in heterogeneous aquifers where classical hydrological point measurements lack representativeness (Binley et al. (2015)). For example, in highly weathered karsts water levels from single boreholes may not be representative of the overall subsurface water content dynamics (Hartmann et al. (2014)). Ground-based gravimetry offers an important tool to sense local mass changes that are too small for large-scale space-borne gravimetry but too far or spatially distributed to be represented in hydrological point measurements, as shown by recent, hydrogravimetrical studies in karst regions (Mazzilli et al. (2012); Mouyen et al. (2019)).

The strength of gravimetry is simultaneously its main drawback due to the non-uniqueness of gravity inversion solutions and the difficulty to resolve the spatial mass distribution such as depth deduction and directional information. Despite these

challenges, signal separation and identification can be achieved by the inclusion of other geophysical, geodetic, or hydrological techniques and the analysis of the temporal signature of the gravity change. This hybrid, time-lapse hydrogravimetry is thus able to constrain and quantify water storage changes (WSC) and to separate contributing areas and involved processes (Naujoks et al. (2007); Naujoks et al. (2010)), such as precipitation (Meurers et al. (2007), Delobbe et al. (2019)), soil moisture (Krause et al. (2009)), evapotranspiration (Van Camp et al. (2016)) and surface runoff and discharge (Lampitelli and Francis (2010); Creutzfeldt et al. (2013), Piccolroaz et al. (2015)), catchment water storage changes (Hasan et al. (2008),Hector et al. (2013), Hector et al. (2014), Hector et al. (2015); Güntner et al. (2017)) or to monitor artificial groundwater recharge facilities (Davis et al. (2008); Kennedy et al. (2016)).

The contributions to a gravity signal can be separated temporally since certain processes show different dynamics. For instance, soil matrix capillarity effects hold water in the root zone and often show other timescales of retention and release than the groundwater table. In arid areas, a fast water table drop at the beginning of the dry season that is followed by a slower decrease and accompanied by a decrease of the root zone storage has been observed by (Pfeffer et al. (2013)). Signal separation can also take into account the opposing effects of surface and subsurface mass changes. For example, the observed gravity signal represents a superposition of a decline in the gravity signal by water mass loss to the atmosphere and an increase in gravity, due to percolating soil water reaching larger depths. During a precipitation event, Krause et al. (2009) observed a decline in gravity residuals at first due to the filling of the interception or canopy storage above the gravimeter, later followed by an increase in gravity once the water masses reached areas below the gravimeter. Evapotranspiration may set in after the precipitation event stops and hence reduces the relative gravity decline.

Additionally to temporal signal separation based on different temporal dynamics, the spatial derivative can be considered. The use of differential gravity measurements has to our knowledge been applied in only a few studies in hydrogeology. Kennedy et al. (2014) deploy two superconducting gravimeters during an aquifer recharge experiment. From the difference in the signal, the velocity of the infiltration front at shallow depth can be resolved and vertical infiltration distinguished from horizontal spreading. Surface-to-Depth (S2D) gravity surveys revealed the storage dynamics of the epikarst layer between surface and caves (Jacob et al. (2009); Champollion et al. (2018)) and facilitated the separation of rainfall signature and groundwater gravity signal (Delobbe et al. (2019)) and in return correct biases in radar-based methods in precipitation observation. However, such cavities are only accessible with gravimeters at a few fortunate sites. These studies show that additional information on the local gravity field provided by "gradients" between gravity measurements can complement and improve water mass balance estimations compared to those obtained from stationary, single-gravimeter monitoring.

The "gradients" in the mentioned studies are averaged over large distances and do not represent the sensitivity of the vertical gradient (VGG) of the terrestrial gravity field at a specific point, as measured by a gradiometer. On larger scales, space-borne gravity gradient data are obtained by GOCE (Gravity field and steady-state Ocean Circulation Explorer), a satellite mission monitoring the Earth's gravity field (Rummel et al. (2011)) or during air-borne gradient surveys for resource prospecting (e.g. Jirigalatu and Ebbing (2019)). Classically, vertical gravity gradients have been interpolated from terrestrial gravity maps or borehole gravity measurements and can deliver constraints on the depth of subsurface geology and through inversion (Rim and Li (2012); Capriotti and Li (2014)). The missing link is therefore small-scale and time-lapse gravity gradient information from

direct measurements. This study investigates the potential of depth deduction from time-lapse gravity gradient monitoring, as a potential technique to spatially resolve mass changes in a hydrogeological context, without the need for large-scale gravimeter displacements. We thus assess the precision of time-lapse VGG monitoring using relative field gravimeters placed on tripods in a controlled observatory setting and relate our findings to the hydrogeological context of the study site. We further discuss the potential of time-lapse VGG measurements for water storage monitoring.

In the following, we introduce the definition of the local vertical gravity gradient and discuss its sensitivity.

2 Vertical gravity gradients

Outside a mass, the gravitational potential satisfies Laplace's equation, leading to five independent directional gradients in 3 dimensions (Blakely (1995)). The diagonal tensor components are often referred to as T_{xx}, T_{yy} and T_{zz}. T_{zz} or the vertical gravity gradient (VGG) is the gravitational acceleration's first derivative in z-direction, expressed in the unit of Eotvos (1 E = 10^{-9}s^{-2}).

Figure 1 panel (a) shows a profile of the sensitivity of a gravimeter, which is calculated based on the gravitational attraction of a point mass defined as (1):

$$g_z = \frac{Gmz}{(z^2 + x^2)^{\frac{3}{2}}}, \tag{1}$$

where G refers to the gravitational constant (6·6740831e^{-11}m^3·kg^{-1}·s^{-2}), m to the mass, x and z refer to the horizontal and vertical distances from the point mass, respectively. As shown in Figure 1 panel (a), the gravimeter located centrally at z = 0 and x = 0 is highly sensitive to mass changes located directly above and below it. The decrease in sensitivity with z^2 of g in contrast to a decrease of the gradient with z^3 explains the gradient's stronger sensitivity to the mass changes in the close environment. As the spatial derivative of g, the sensitivity of a gradiometer decays faster with distance and is also sensitive to mass changes at distance in x-direction (2):

$$T_{zz} = \frac{Gm(x^2 - 2z^2)}{(z^2 + x^2)^{\frac{5}{2}}}, \tag{2}$$

The gradient's lateral lobes of sensitivity (Figure 1 panel (b)) allow for lateral mass detection, which is not possible with the spatial sensitivity of a gravimeter. The spectral power of gravity gradient signals includes higher spatial frequencies, which can thus be used for the detection of edges of structures and their centre of mass.

To our knowledge, time-lapse VGG measuring as a monitoring technique has not been explored much yet. Gravity gradient information tends to be mainly used in the context of mineral and oil exploration. In hydrogeology, gravimeters, especially relative field gravimeters are more commonly used. These instruments enable to create a synthetic gradiometer with a small enough baseline (distance between the gravimeters) to be relevant in a hydrogeophysical context. Therefore, we focus on the approximation of a gradiometer using two gravimeters.

The sensitivities of two gravimeters at a vertical height difference L (Figure 1 panel (c), (3)) may approximate the sensitivity of a gradiometer (Figure 1 panel (b)) as :

$$T_{zz} = g(z + \frac{L}{2}) - g(z - \frac{L}{2}) = Gm \frac{\frac{z+\frac{L}{2}}{((z+\frac{L}{2})^2+x^2)^{\frac{3}{2}}} - \frac{z-\frac{L}{2}}{((z-\frac{L}{2})^2+x^2)^{\frac{3}{2}}}}{L}, \tag{3}$$

at a distance which is large compared to the baseline.

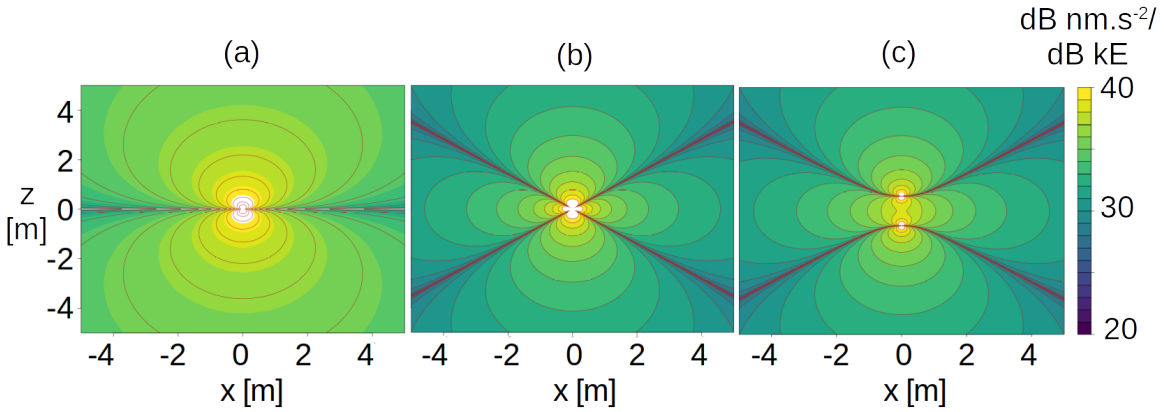

Figure 1. Panel (a): Spatial sensitivity profile of a gravimeter located at zero height in dB nm.s^{-2}. Panel (b): Spatial sensitivity of a gradiometer in dB kE. Panel (c): Combined spatial sensitivity of two gravimeter at 1.2 m vertical distance in db kE. Distances in z and x in m.

On the field scale, direct gravity gradient measuring is rarely done, despite its potential benefits. For instance, numerical studies suggest the increase in resolvability of oil reservoir changes by time-lapse gradiometry and gravimetry (Elliott and Braun (2017); Reitz et al. (2015)). The use of the derivatives of the gravitational field for improved source separation has been shown for high-density fluids, in the case of water the density contrasts are weaker which may limit detectability. In hydro-gravimetrical studies, a homogeneously distributed infiltration front is commonly approximated as a Bouguer plate. The expected change in gravity caused by a water column of height H can be calculated as:

$$\delta g_B = 2\pi\rho G H, \tag{4}$$

with G referring to the gravitational constant and ρ to the density of water. Gravity caused by a Bouguer plate is by definition independent of the measurement position laterally and vertically. On the other hand, even with a Bouguer plate, the gradient will depend on the vertical distance z, but not on the location in x and y. If the water content distribution does not obey the Bouguer plate assumption, g and the VGG do depend on the location in x, y, and z of the corresponding mass. In that case, local vertical gravity gradient changes emerge that provide additional information that can be used to constrain the model of the mass distribution. Time-lapse VGG and gravity measurements can distinguish temporal signatures, as the signal of interest moves in and out of the spatial sensitivity ranges of gravity and its gradient. The complementary sensitivities in space between gravity and the VGG offers the possibility to distinguish between homogeneous and heterogeneous mass distributions, respectively.

3 Methods

3.1 Study site and instruments

Instrument tests and monitoring was carried out at the Larzac observatory, a highly instrumented site for hydro-meteorological and hydrogeophysical monitoring (e.g. Valois (2011); Galibert et al. (2014); Mazzilli et al. (2016), Fores et al. (2016a); Fores et al. (2018)). It is part of the French National Research Infrastructure OZCAR (Gaillardet et al. (2018); OZCAR-RI H+ Larzac - France) and the European long-term environmental monitoring infrastructure network ELTER (Mollenhauer et al. (2018)). It furthermore belongs to the French seismological and geodetic network RESIF (Volcke et al. (2014)). The observatory is located at 708 m a.s.l. on the La Jasse site in L'hospitalet-du-Larzac, France, shown in Figure 2. The site lies in the Durzon catchment on the Larzac, a plateau of middle to upper Jurassic limestones and dolomites. Gravimetry contributed to the understanding of hydrodynamics on different scales, such as identifying the dolomitic epikarst present in the catchment as the main water storage compartment (Pinault et al. (2001); Jacob et al. (2008); Jacob et al. (2009), Jacob et al. (2010)), Deville et al. (2012), Fores et al. (2018)). Rainfall reaching the observatory roof enters a pipe and is left to drain at 100 m distance. Precipitation data can be obtained from an on-site rain gauge and actual evapotranspiration can be estimated based on data provided by an eddy-covariance flux tower. The site is also dedicated to the operation and testing of gravimeters, e.g. gPhoneX (Micro-g LaCoste; Fores et al. (2019)) or new absolute quantum gravimeter studies (Ménoret et al. (2018)) due to low environmental noise.

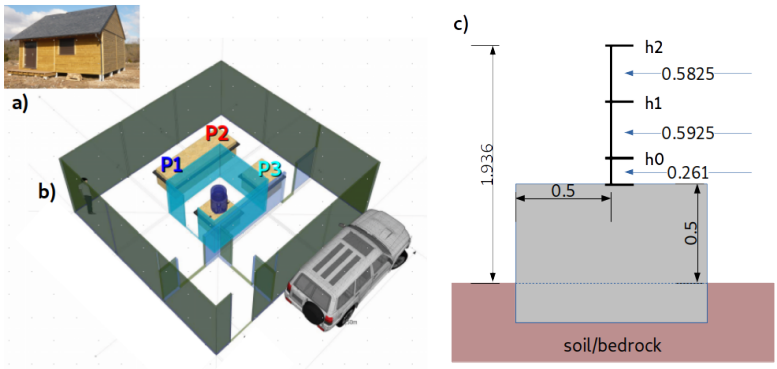

Figure 2. Panel (a): The Larzac geodetic observatory. Panel (b): Vertical gravity gradient surveys were conducted on concrete pillar locations p_1 (blue), p_2 (turquoise), p_3 (red). The central pillar (later referred to as p0) is continuously occupied by the superconducting gravimeter iGrav-002. Panel (c): Measures of pillar and tripod heights h0, h1 and h2 given in m.

To allow for fast instrument displacement between measurement locations the gravimeters of choice are relative spring gravimeters. They are favourable in terms of transportability, ease of use as well as fast measurement launch. This study was conducted mainly using the relative gravimeter Scintrex Autograv CG5 (#1151) (Limited (2014)). Additional surveys

were conducted with a second CG5#1215 (Limited (2014)) and a CG6#120 (Limited (2018)) in parallel with those of the CG5#1151.

A superconducting gravimeter on the site (GWR, iGrav#002) located on the central pillar in the building (p_0, SE of the other pillars, Figure 2) provides continuous relative gravity monitoring of up to 1 nm·s^{-2} precision after 60 s of data integration during low noise level conditions. A drift of 45 $nm.s^{-2}yr^{-1}$ has been reported (Fores et al. (2016b)) until 2016, the drift has been reassessed in 2020 (Champollion, 2020, personal communication) and has been estimated to be 92 $nm.s^{-2}yr^{-1}$.

3.2 VGG estimation

3.2.1 Gravity acquisition and expected VGG sensitivity

CG5 relative gravimeters show a resolution of 10 nm·s^{-2} and a precision better than 50 nm·s^{-2} (Crossley et al. (2013)). Jacob et al. (2008) report a survey error range of 24 to 55 nm·s^{-2} during field campaigns. As the acquisition in this study was conducted under controlled conditions inside a building providing constant temperature and shielding from radiation or wind, we expect the precision to be higher. The expected uncertainty on the VGG can be estimated for the set-up shown in Figure 2. A gravity precision of 24 nm·s^{-2} for a height difference of 0.59 m would lead to an error of 58 E. For a height difference of 1.175 m, the expected error is 29 E.

Gravity surveys were conducted on concrete pillars. The CG5#1151 was placed with its levelling-tripod on top of two light metal tripods of about 60 cm height each. The acquisition starts at height h0 (0.26 m), followed by height h1 (0.85), h2 (1.44 cm), and returns to h0. Five consecutive gravity measurements with an integration time of 90 seconds each have been launched on each position and height, in agreement with Merlet et al. (2008) who recommend 85 seconds. The instrument was thus moved to its next position about every 10 minutes (seven minutes and 30 seconds acquisition plus additional time for placing the instrument and tripods, re-levelling, and launching the measurement). Gravity was measured on position p_1 (NW) and p_2 (NE), both on the large concrete pillar in the North of the building, and p_3 on the smaller concrete pillar in the SW corner. A map of the interior of the observatory including all distances and heights is shown in Figure 2, the protocol is shown in Figure 3. The entire survey provides 60 gravity measurements per pillar. 16 surveys were carried out between 12/2017 and 11/2018. The VGG was approximated from the gravity difference per unit height difference between two gravity measurement points:

$$VGG = \frac{(g_{h_2} - g_{h_0})}{h_2 - h_0}. \tag{5}$$

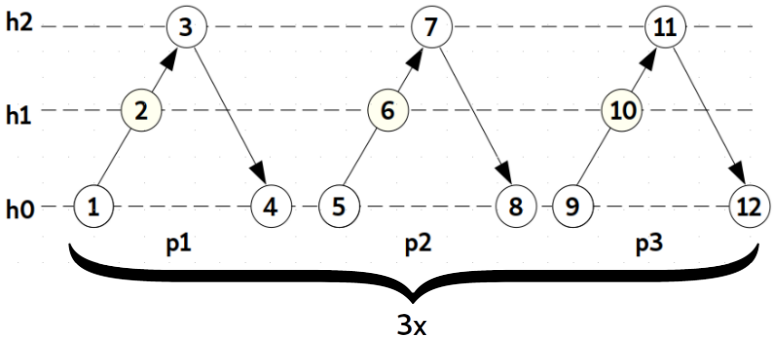

Figure 3. Measurement protocol. On each pillar (p_1-p_3) gravity on each height is measured in three repetition loops.

3.2.2 Post-processing

Post-processing was performed using the software pyGrav (Hector and Hinderer (2016)), a Python code based on Gravprocess (Cattin et al. (2015)) developed for relative gravity survey analysis. It calls the openly available tidal model function PREDICT from the ETERNA program package (Wenzel (1996)) to correct for solid Earth and ocean tide corrections. We used site-specific combined earth and ocean tidal parameters, previously estimated with ETERNA based on long-term iGrav#002 time series (Fores et al. (2016a)). Atmospheric pressure correction was carried out using half-hourly barometric pressure time series with a site-specific pressure admittance factor of -2.71574 $nm.s^{-2}hPa^{-1}$ (Fores et al. (2016a)). PyGrav's temporal drift adjustment executes a least-squares inversion drift estimation (Hwang et al. (2002)). Simple differences between stations, in our case pillars, is inferred from a posteriori covariance matrix in reference to a fixed gravity value, double differences are related to a repeatedly revisited base station and comparison with different loops. Outliers per loop and pillar were manually removed. Vertical gradient estimation was carried out in PyGrav as a linear trend with measurement height. Both previous measurements and simulations of the local gravitational field based on the mass of the concrete pillars revealed a non-linear VGG along this height (gravity curvature), with a stronger VGG closer to the surface of the pillar. To increase the precision of the VGG estimation, the larger distance (h_2-h_0) was chosen. The VGG estimated based on h_1-h_0 are not dealt with here (see supplementary material).

Actual evapotranspiration was estimated using EddyPro software gap-filled with the R-package ReddyProc (Wutzler et al. (2018)), using radiation, humidity and eddy co-variance data provided by the nearby flux tower (data available at OREME). For further detail on the data treatment can be found in Fores et al. (2016a).

3.2.3 Repeatability and instrument comparison

All relative gravity surveys were carried out with the CG5#1151. Estimated VGG based on data from additional surveys obtained with the two CG5 gravimeters (#1151 and #1215) and between the CG5#1151 and the CG6#120 were compared. Repeatability between survey days was assessed through consecutive relative gravity surveys that took place between the

06/06/2018 and the 10/06/2018 with the CG5#1151 and CG5#1215 during stable weather conditions without precipitation. On 30/08/2018, 14 measurement loops with the CG5#1151 and CG6#120 were carried out on the same pillar (p_3) to assess repeatability between consecutive loops.

4 Results and discussion VGG estimations

4.1 Repeatability

Gradient residuals show a repeatability of 23 $\pm$ 9 E averaged for all three pillars, obtained during several consecutive daily surveys during stable weather conditions in June 2018 (Figure 4; Table 1). The VGG during those four days stay relative stable with standard deviations of 7.7 (p_1), 14.5 (p_2), and 9.1 E (p_3), respectively. Coherent, small temporal variations of the VGG on the three pillars are visible. However, they are mostly within the error margin.

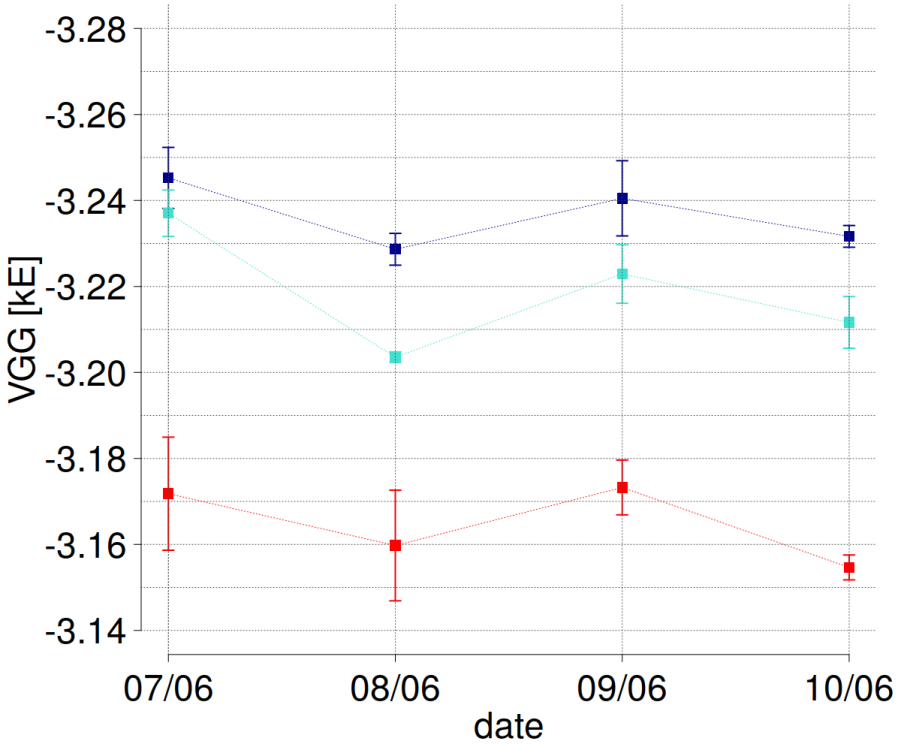

Figure 4. Repeatability study. VGG surveys on consecutive days in June 2018 on pillar p_1 (darkblue), p_2 (turquoise) and p_3 (red), measured with CG5-1151.

4.2 Uncertainty estimation

Another repeatability study on the same pillar (p_3) during one day yielded 21 $\pm$ 13 with the CG5#1151. Further results of repeatability studies as well as differences between instruments (Table 1) tend to be on average less than 20 E.

Table 1 VGG estimation uncertainty analysis.

Comparison	Mean and SD [E]
Repeatability consecutive days (CG5-1151)	23 $\pm$ 9
Repeatability: same pillar (p_3) (CG5-1151)	21 $\pm$ 13
Repeatability: same pillar (p_3) (CG6-120)	4 $\pm$ 5
Differences CG6-120; CG5-1151	15 $\pm$ 13
Differences CG5-1151; CG5-1251	5 $\pm$ 13

4.3 One-year VGG survey

In Figure 5 panel (a) the VGG estimated for the three pillar locations from the relative gravity surveys in 2017 and 2018 are shown. We do not go into further detail regarding the absolute differences between pillars that are related to differences in concrete mass and can be corrected for, but we focus on the apparent change of the relative differences between p_3 and p_1/p_2. The mean estimated VGG for p_1 is -3.226 with a standard deviation over the whole series of 0.022 kE and -3.220 $\pm$ 0.017 kE for p_2, respectively. The mean VGG estimated for p_3 lies at -3.188 $\pm$ 0.026 kE. Gravity residuals measured with the iGrav#002 show an increase of approximately 50 nm·s^{-2} during spring 2018 and start to decrease in summer (Figure 5; panel (b)). The iGrav data for 12/2017 - 01/2018 was omitted due to a residual instrumental drift after a restart. Panel (c) shows the effective daily rainfall at the Larzac site.

Differences between VGG on p_1 and p_2 are not significant and neither show significant trends over the course of one year. Statistical significance of differences between measurements on the three pillars was evaluated using a repeated-measures analysis of variance (ANOVA) (Lawrence (2016)) for the entire gravity data set prior to VGG estimation. The data's normal distribution was tested using Levene's test for normality. As an Ad-hoc test to distinguish the influence of pillars individually, the Tukey-HSD ad-hoc test (R Core Team (2020)) showed that VGG on pillars 1 and 2 do not differ significantly from each other.

However, p_3 has been found to differ significantly from p_1 and p_2. Furthermore, after April 27th, 2018, VGG on p_3 appear to diverge from those of p_1 and p_2 and increase by 80 E in November 2018 compared to December 2017. Trends were assessed using the Mann-Kendall non-parametric trend test for time-series and Sen-slope test (McLeod (2011); Pohlert (2020)). The start of the trend in late April 2018 was confirmed with the Petitt test (Pohlert (2020)), which identifies the moment of change in a series. Gravity residuals measured with the iGrav#002 and VGG on p_3 appear to be negatively correlated (Figure 5). During a relative gravity increase, the VGG on p_3 decrease. However, regression did not yield a clear linear relationship between both.

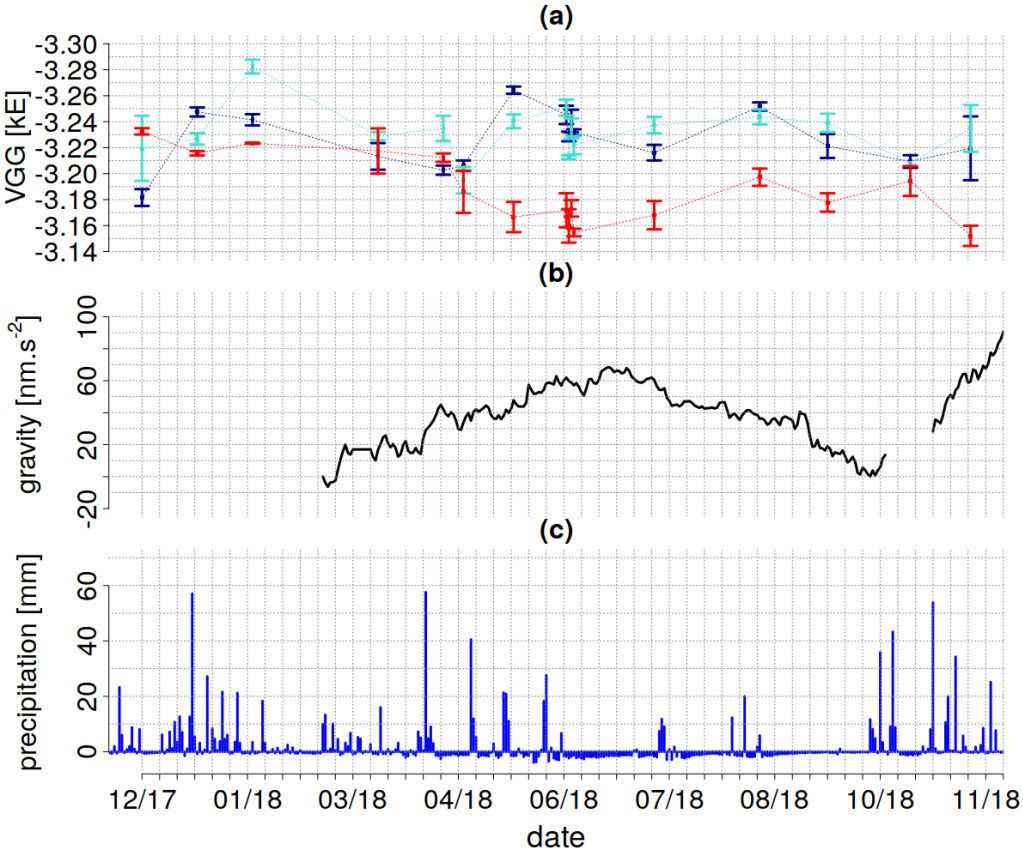

Figure 5. Panel (a): Vertical gravity gradients in kE estimated for the three pillar locations p_1 (blue), p_2 (turquoise), p_3 (red), measured at the Larzac observatory in 2017-2018. Panel (b): Gravity residuals in nm.s^{-2} obtained with iGrav-002. Panel (c): Effective rainfall in mm.

The observed VGG variations over several months on p_3 exceed the assessed repeatability. Assuming that the observed gradient changes are caused by a mass signal, possible sources of mass change are investigated. Significant anthropogenic mass changes (construction work or erosion) near the building were not observed. We base this study on the assumption of soil water redistribution processes being the main contributing factor to detectable VGG variations.

5 Origin of gravity gradient changes

The general approach is the forward-modelling of potential effects and the comparison with the observations. In the following sections, 3D-hydro-gravimetrical modelling is applied to assess the influence of local heterogeneous distribution of soil mois-

ture due to topography and to the observatory building ('umbrella effect'). Subsequently, the influence of deeper subsurface heterogeneity and the variably saturated zone are assessed. These investigations are guided by the observed constraints of negligible differences in VGG between pillars p_1 and p_2 and $\pm$ 40 E between them and pillar p_3.

5.1 Topography

Firstly, we investigated the potential lateral effects of varying water content in the surrounding topography. We calculated the effect of topography with a prismatic gravity forward-calculation of the digital elevation model of a horizontal of 200 x 200 m at one meter horizontal and 0.1 m vertical resolution with the GEK building in its centre. We compared a dry and a saturated case assuming 20 % porosity and found the effect to be less than one E and thus negligible for our analysis.

5.2 Building umbrella effect

Gravity measurements are impacted by the surrounding building due to shielding from precipitation, commonly referred to as the "umbrella effect" (e.g. Deville et al. (2012), Creutzfeldt et al. (2010)). The umbrella effect produces a local water mass anomaly whose shape changes with time and depends on the relative location of the pillars within the building. The gradients on the three pillars could be thus influenced by this mass anomaly. The admittance factor correcting for the umbrella effect depends on the measurement location in the building and sensor height as well as on the state of progression of the infiltration front (Güntner et al. (2017); Fores et al. (2016a)). The interaction between the temporal pattern of rainfall at sealed sites and soil water redistribution processes cause a non-linear gravity response. The relative impact of the umbrella effect on the gravity measurement changes with increasing depth. As shown by Fores et al. (2016a), the strength of the umbrella effect depends on previous rainfall events and thus the state of soil water saturation before the rainfall. Up to 40% reduction of the Bouguer plate were observed for the FG5, operated on pillar p_1 at a height of about 1.20 m, whereas up to 80 % for the iGrav at 0.35 m sensor height on p0, closer to the centre of the building.

The gravity anomaly below the building can be approximated as a gap in the Bouguer plate with a 3D prismatic gravity forward calculation (Okabe (1979)), and consequently, the corresponding VGG on the pillars can be calculated. For instance, an umbrella effect causing 80% reduction in the corresponding Bouguer plate for a given rainfall event has been observed (Fores et al. (2016a)). Assuming a soil porosity of 10 %, the order of magnitude of the different soil water content between inside and outside this volume is approximately 10 %. A 10 mm rainfall could thus lead to 1 Eotvos change in VGG, a 100 mm rainfall to 10 Eotvos. Differences in VGG between the pillars are less than 1 E. The calculation was based on the infiltration front being close to the surface.

From this first approximation, we can assume that the expected "umbrella effect noise" on vertical gravity gradients is likely to be of the order of a few Eotvos maximum. However, the calculation is overly simplified in terms of location and geometrical shape of the "umbrella volume". We investigate the generation of the umbrella effect in a 3D-hydrological model. This allows us to further examine the potential temporal dynamics of the simulated VGG on the pillars. In the following, we describe the specifications of the physically-based model approach.

5.2.1 Conceptual model

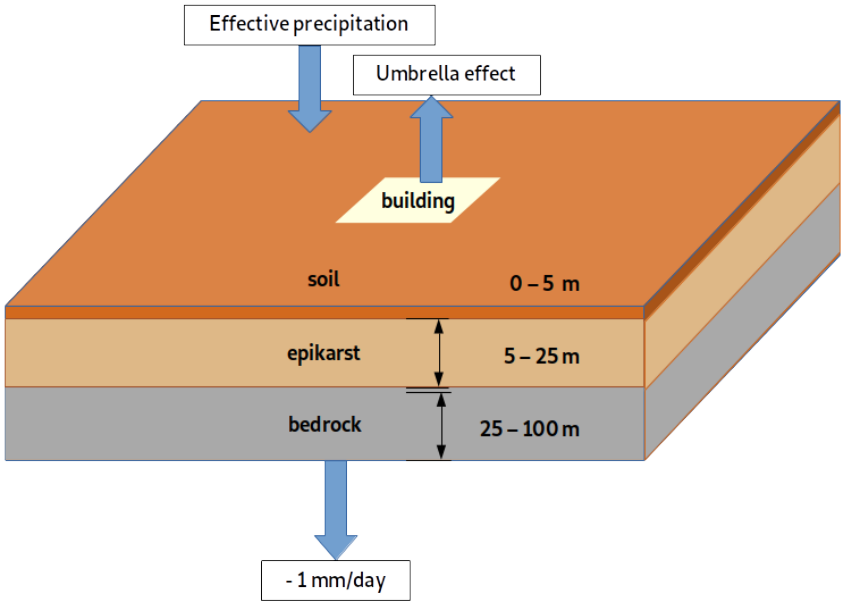

Figure 6. Conceptual model (chart not to scale) with observatory in its centre.

A 3D numerical hydrological model was set up based on PFLOTRAN, an open-source, parallel subsurface flow, and reactive transport finite elements code (Hammond et al. (2014)). Figure 6 depicts the conceptual model (not to scale). The model was defined as a uniform rectangular domain of 1 km^2 area and 100 m depth, corresponding to the depth of the underground cave gallery located below the observatory. A 7.6 x 7.6 m square area in the centre of the model domain on the surface layer was defined as the area of the GEK building. A radially refined cell discretisation allows for smaller cell sizes close to the area of interest in the centre of the model domain, ranging from 0.1 m at the top centre to 15 m at the edges horizontally and from 0.1 to 4 m vertically, respectively. Site topography is little pronounced (< 2 m variation in the 250 m² around the building) and a flat surface was assumed. Soil properties were assumed to be horizontally homogeneous. Fores et al. (2016a) found gravity variations within 100 m of the observatory to not exceed 32 nm·s^{-2}, relative to the measurements taken in the building. Vertical layering into soil, epikarst, and bedrock represents the only inserted heterogeneity of subsurface properties.

5.2.2 Parameters

Subsurface water flow was computed in PFLOTRAN's RICHARDS MODE, meant for "single phase, variably saturated, isothermal systems" (PFLOTRAN documentation). The code solves the 3D Richards equation (Richards (1931)) numerically.

The Richards equation is given (here in 2D) as:

$$\frac{\partial \theta}{\partial t} = \frac{\partial}{\partial x}\left[K(x,z,\theta)\frac{\partial \psi}{\partial x}\right] + \frac{\partial}{\partial z}\left[K(x,z,\theta)\frac{\partial \psi}{\partial z} + K(x,z\theta)\right], \tag{6}$$

with the volumetric water content θ, pressure head ψ, and x and z as horizontal and vertical coordinates, respectively. K is the hydraulic conductivity and dependent on saturation. The water retention function relates water content and head through the effective saturation S_e as:

$$S_e = \frac{\theta - \theta_r}{\theta_s - \theta r} = [1 + (\alpha|\psi|)^n]^m, \tag{7}$$

where θ_s and θ_r stand for saturated and residual volumetric water content, respectively. The empirical parameters α, n and m depend on soil type and are connected by:

$$m = 1 - \frac{1}{n}. \tag{8}$$

The resulting hydraulic conductivity K is a function of the saturated hydraulic conductivity K_s and effective saturation, as given by:

$$K = K_s S_e^{\frac{1}{2}}[1 - (1 - S_e^{\frac{1}{m}})^m]^2 \tag{9}$$

(van Genuchten (1980)).

Model parameter choices are shown in Table 2, which have been found by Fores et al. (2018) using Hydrus-1D by Šimůnek et al. (2016).

Table 2 Model parameter choices, based on ranges found by (Fores at al., 2018)

Parameter	soil (0 - 5 m)	epikarst (5 - 25 m)	bedrock (25 - 100 m)
Porosity [%]	20	15	10
Tortuosity [-]	0.55	0.55	0.55
Van Genuchten parameter m [-]	0.33	0.33	0.33
Van Genuchten parameter $\alpha[Pa^{-1}]$	$1.5e^{-5}$	$1.5e^{-5}$	$1.5e^{-5}$
Permeability $[m^2]$	10^{-11}	10^{-11}	10^{-11}
Residual saturation [%]	5	5	5

5.2.3 Initial and boundary conditions

The side boundaries were assigned a Neumann boundary condition of no flow. The lower boundary was assigned a constant outflow of one mm per day based on validated estimations (Fores et al. (2016a)). Effective daily rainfall was introduced as a surface boundary condition except for the area under the building, where both precipitation and evapotranspiration were set to zero. As an initial condition, a hydrostatic pressure of 90325 Pa was assigned to the bottom boundary. The simulation was run with effective rainfall data from the site from 26/10/2012 to 31/12/2018, comprising 2258 days.

3D gravity effects can be accurately calculated as the sum of storage change in hydrological model cells represented as the gravity of a prism (Leirião et al. (2009)). The PFLOTRAN source code was coupled with a FORTRAN-based gravity forward routine based on Okabe (1979). Gravity caused by water saturation was calculated for the three pillar locations and their corresponding VGG were obtained from the linear regression of gravity and height.

5.2.4 Results and discussion on building umbrella effect

Figure 7 panel (a) shows simulated gravity in nm·s^{-2} in the observatory and iGrav gravity residuals for pillar p0. The model reproduces the observed gravity residuals within a root mean square error (RMSE) of 13.78 nm·s^{-2}.

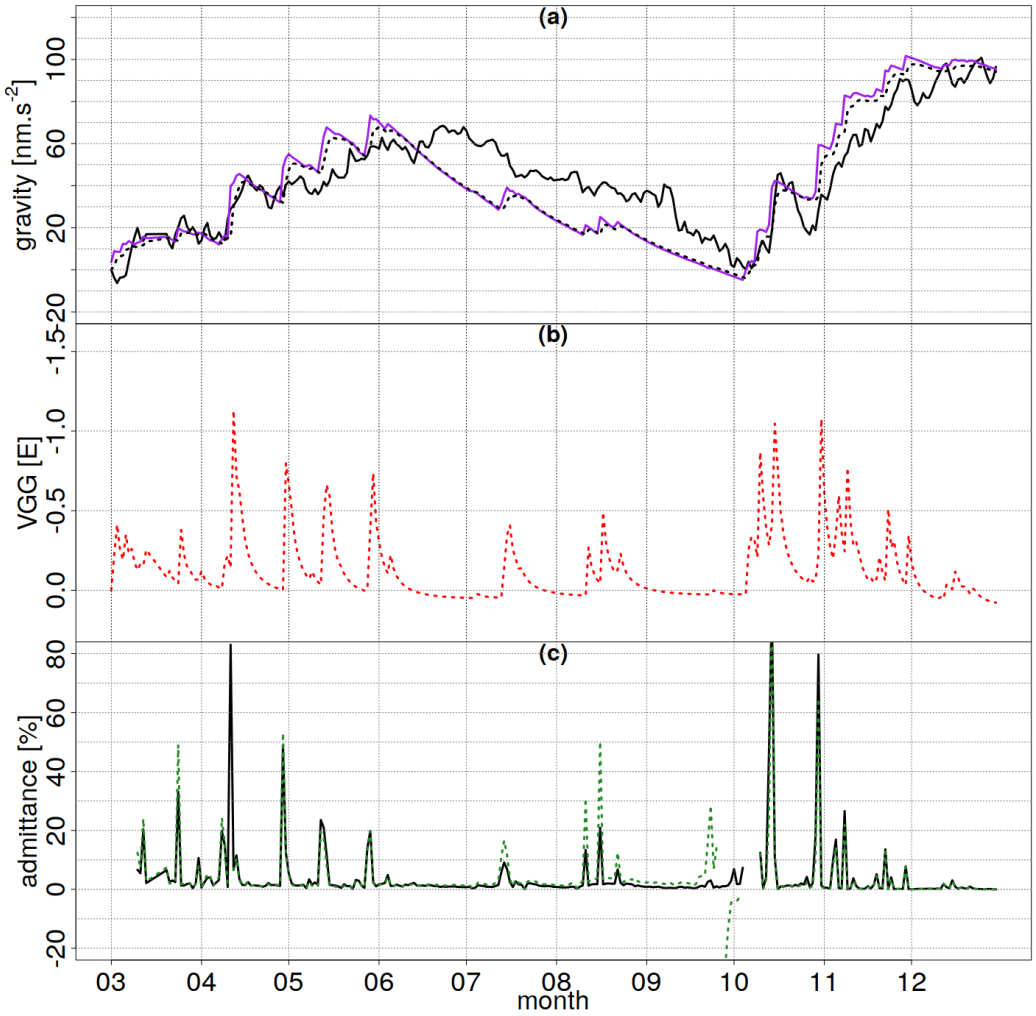

Figure 7. Panel (a): Simulated gravity residuals (black, dashed line), gravity residuals measured with iGrav-002 (black, continuous) and Bouguer plate equivalent (purple) for 2018, all in nm.s^{-2}. Panel (b): Simulated vertical gravity gradient residuals in E for pillar p_3. Panel (c): Umbrella effect admittance calculated from the Bouguer plate equivalent and iGrav gravity data (black) and for the simulated gravity residuals (green, dashed line).

In panel (b), simulated VGG for p_3 do not exceed a few E. The simulated VGG for p_1 and p_2 yielded values close to those of p_1, differences are at the level of a fraction of one E and are hence not depicted here. Model runs with a different choice

of soil permeability and soil porosities were carried out that are not shown here. Simulated VGG were in the same order of magnitude.

In order to evaluate whether the observed umbrella effect was simulated correctly, we compare the gravity reduction relative to a Bouguer plate, also referred to as umbrella admittance. This is obtained from the difference between the expected gravity signal (Bouguer slab equivalent of daily rainfall) and simulated one the one hand and observed gravity on the other hand. For most of the time series, the simulated admittance agrees well with the measured admittance (Figure 7; panel (c)). Small misfits between observed and simulated umbrella effect could be explained by the uncertainty regarding the amount of rainfall (rain gauge malfunctioning and uncertainty of actual evapotranspiration estimation and gap-filling procedures). Another possibility is the uncertainty introduced by the decision to not include evapotranspiration for the shielded (but not sealed) area below the building. Soil moisture retention is possibly higher beneath the building than in the surrounding soil surface due to shading and reduced evapotranspiration. However, moisture losses are still likely to occur due to the lack of sealing.

To summarise, the model reproduces observed gravity changes and the umbrella effect. However, the simulated VGG are not of the order of magnitude of the observed trends in p_3 (several tens of Eotvos). This agrees with the previous, simplified estimation of the impact of the umbrella effect modelled as a truncated plate. From these results, it can be argued that the umbrella effect is not the main contribution to the observed VGG variations. In the next step, we examine other causes of heterogeneous soil water content distributions.

5.3 Geostatistical stochastic simulation

Geophysical studies suggest natural karst heterogeneity at the plot scale on the Larzac site. Weathered corridors and sinkholes were identified in about 100 m distance to the observatory building. Time-lapse electrical and seismic refraction tomography showed a change in epikarst properties after rainfall. Seismic velocity variations of 25 to 35% have been observed and related to saturation changes (Valois (2011)). In lack of subsurface imaging data, the range of possible VGG changes is explored using simulation based on realistic estimates of subsurface properties. We, therefore, used stochastic geostatistical simulation (Lantuéjoul (2002)) to generate multiple, plausible alternative realisations of 3D porosity distributions of the same probability. In an inversion approach, simulated realisations were searched that obey the conditions of causing VGG signals that are detectable given the instrumental set-up in the Larzac observatory while keeping the corresponding gravity signal relatively small.

Spatial simulations were based on the variogram method which requires specifying the magnitude of change of the variable (partial sill) and the correlation length in space, the corresponding model parameter choices are listed in Table 3. The partial sill specifies the magnitude of change of the variable and has been set to 15% and refers to the simulated porosity range (5-20 %), based on borehole logs (Fores (2016)). The partial range is the length or distance at which values are correlated. After visual examination of ERT survey inversions (Champollion, 2019, personal communication) , test ranges of 10, 20, and 50 m were chosen. Soil moisture saturation was defined as 10 % of the porosity.

Simulations were based on three of the most commonly used variogram model types (exponential, spherical, and gaussian) and carried out using the R-package $gstat$ (Pebesma (2004)). Gravity and VGG were calculated for the three pillar locations

in the observatory on height h0 and h2 based on the water saturation of each grid cell at a discretisation of 5 m. This grid size was chosen based on the expected VGG changes caused by spatial mass heterogeneity with a characteristic length of 5 m. The expected change in VGG was modelled for a simplified model of alternating, regular cubes of 5 m edge length and 200 $kg \cdot m^{-3}$ density contrast. VGG were calculated along transects above the surface of the cube pattern (based on the tripod heights used in the experimental study). For these parameters, VGG changes of more than 20 E require a cube size of 5 m.

Table 3 Variogram model parameters

Variogram model	Exponential, Spherical, Gaussian
Correlation length (range) [m]	10, 20, 50
Partial sill %	15
Model extensions [m]	250 x 250, 100 depth
discretisation [m]	5
N simulation runs per combination	1000

5.3.1 Results and discussion on geostatistical simulation

The simulated subsurface realisations were selected according to the detection limit derived from the uncertainty assessment of the used VGG estimation method. The VGG and gravity values were standardised relative to the mean of all realisations. We limit the selection of model realisations to the condition of relatively small gravity changes, negligible VGG differences between p_1 and p_2 and differences above detection limit between either p_1 and p_2, respectively, and p_3. 76 realisations obey the criterion of detectable (> 20 E) difference between p_1/p_2 and p_3 (Table 4) of which especially short-range spherical models stick out. Eight realisations remain after selecting for a gravity difference of less than $\pm$ 100 $nm \cdot s^{-2}$ and VGG differences between p_1, p_2 and p_3 of at least 40 E, while showing less than 20 E difference between the VGG on p_1 and p_2 (Figure 8).

Surface views and W-E profiles of two of the eight realisations are shown, one based on a spherical model given a correlation length of 20 m (Figures 9 and 10), the second based on a gaussian model of 50 m correlation length (Figures 11 and 12). The spherical model shows emerging patterns of lower and higher porosity with an anomaly close to the building. In the gaussian model, a larger area of higher porosity at the surface emerges around the observatory building. The remaining selected realisations are animated for the surface view, vertical W-E profiles and vertical N-S profiles).

Table 4 Number of selected simulations obeying the criterion of $\Delta VGG_{p_1,p_2-p_3}$ >20 E, and $\Delta VGG_{p_1-p_2}$ < 20 E.

Variogram model	Exponential	Spherical	Gaussian
Correlation length			
10 m	11	14	6
20 m	9	20	4
50 m	2	4	6

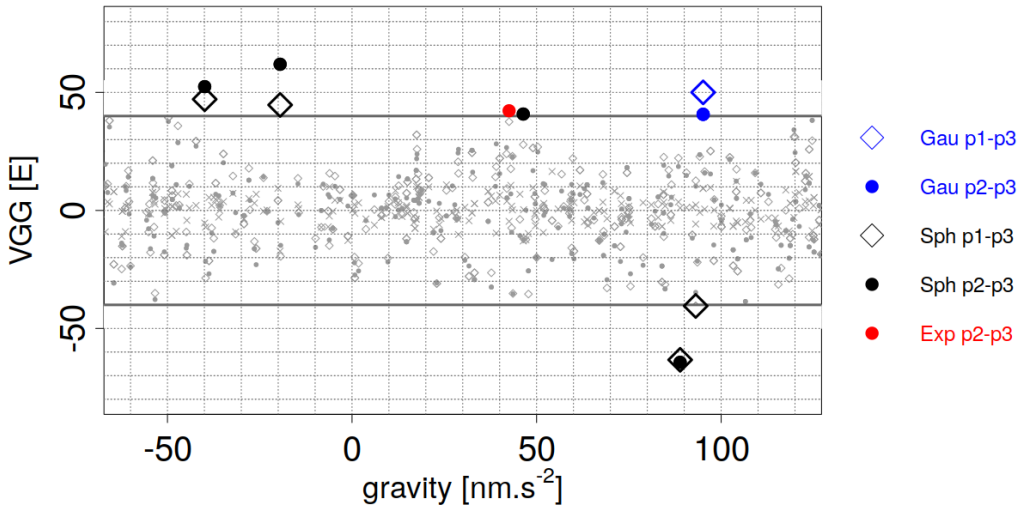

Figure 8. Selection of simulated realisations according to the defined constraints of > 40 E and < 100 nm.s^{-2}. Diamonds refer to differences in VGG in E between p_1-p_3, dots refer to p_2-p_3. Colors refer to the variogram models: Exponential (red), spherical (black), Gaussian (blue). Realisations not exceeding the 40 E criterion are marked in grey.

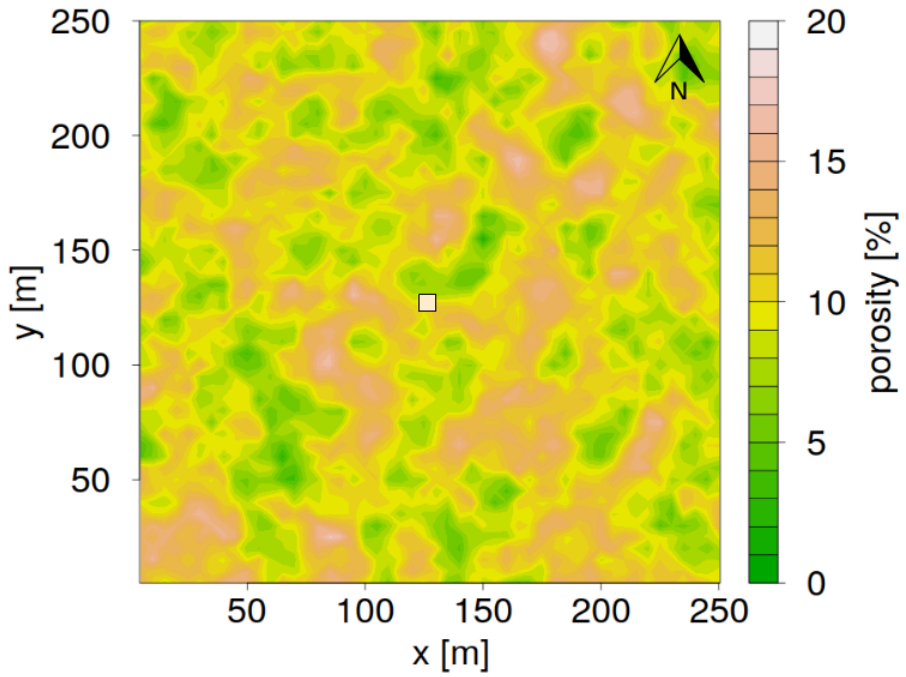

Figure 9. Surface topview of the spherical model (20 m predefined correlation length). Larzac observatory building in centre. Scale in percent porosity. Distances in m. This realisation yielded 40 E difference between p_1 and p_3, between 35 p_2 and p_3, 93 nm.s^{-2} gravity change on p_1 compared to the mean of all realisations.

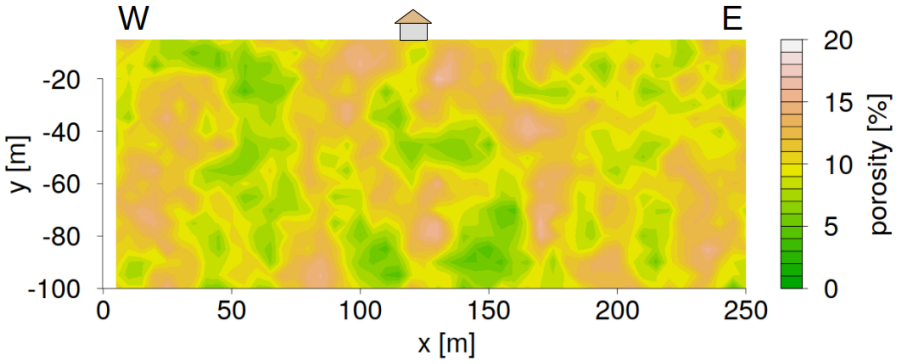

Figure 10. W-E profile of the spherical model (20 m predefined correlation length). Larzac observatory building in centre. Scale in percent porosity. Distances in m.

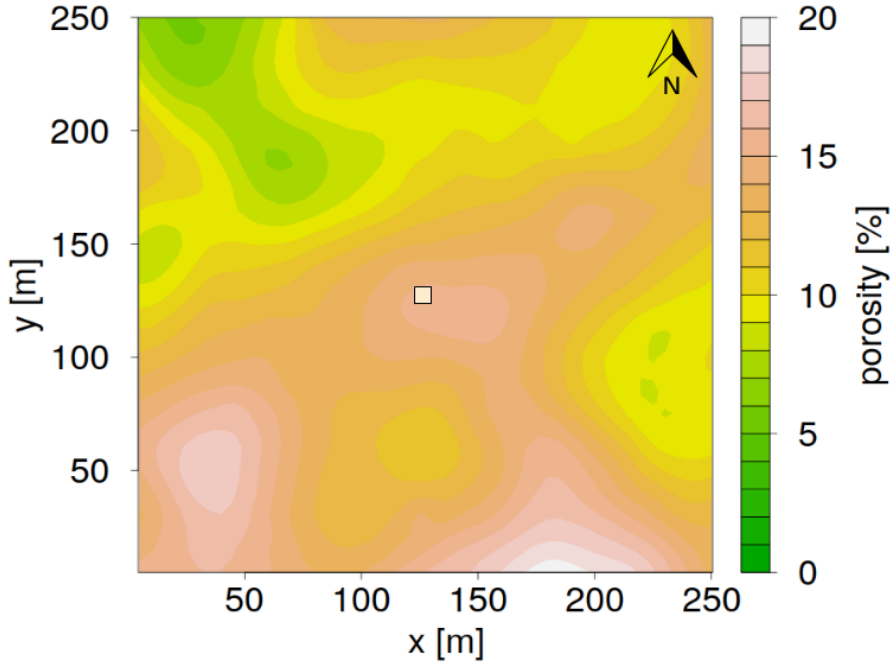

Figure 11. Surface topview of the gaussian model (50 m predefined correlation length). Larzac observatory building in centre. Scale in percent porosity. Distances in m. This realisation yielded 50 E difference between p_1 and p_3, between 41 p_2 and p_3, 95 nm.s^{-2} gravity change on p_1 compared to the mean of all realisations

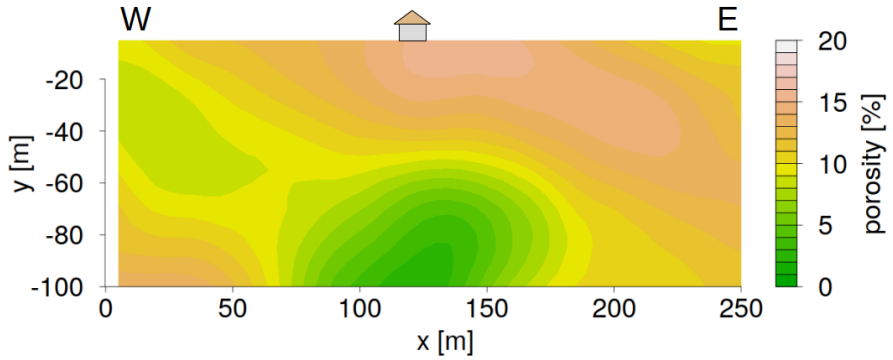

Figure 12. W-E profile of the gaussian model (50 m predefined correlation length). Larzac observatory building in centre. Scale in percent porosity. Distances in m.

The simulated subsurface distributions are based on the assumption of isotropy. The selected realisations were characterised regarding the possible emergence of spatial patterns. Various fracture network orientations in the Durzon karst system have been identified (Gerbaux (2009): Deville (2013)) such as the N0E – N20E, associated with open fractures. Weathered corridors oriented N150E - N160E are relatively frequent and were also found in seismic and electric resistivity studies (Valois (2011)). Other orientations occurring in the Durzon karst system (N040E – N050E and N120E) are less represented at the Larzac observatory site. Directional variograms of the selected, simulated 3D porosity distributions were calculated testing various orientations and particularly taking into account the reported fracture orientations for the surface top view and two vertical profiles (W-E and N-S) with the laboratory building in the centre.

Directional variogram analysis of surface and profile distribution of the eight cases showed that the fitted variogram obtained a range close to the original predefined correlation length which means that for most cases no new structures of longer correlation length emerged and no significant directional anisotropy was identified. An exemption is one realisation based on a Gaussian model of 50 m wavelength with a distinct anisotropic structure. A surface orientation of $\sim$ N30E is visible in Figure 11, as well as a subsiding structure in the vertical profile (Figure 12). Comparisons with mapped cavities at the site were not conclusive (Karst3D Team (2019)). All eight realisations show a partial sill between 5 and 6 % porosity.

To summarise, no significant common directional anisotropy of the eight realisations was identified. Models generating short-wavelength patterns that appear close to the observatory building and thus creating local heterogeneity as well as models of larger wavelength and thus larger structures emerged from the simulations. As a conclusion, already relatively small porosity differences could be responsible for detectable VGG changes. In order to choose the best model between large scale and small scale structures, further subsurface information close to the building is required.

The combination of VGG estimates and gravity data shows that by setting selection criteria of detectable VGG changes and negligible gravity changes, the initially large number of simulated realisations (9000) is greatly reduced (76). In a second step, the selection was further narrowed down to eight by the condition of the order of magnitude of the differences between close-by pillars. This points at the potential of "differential VGG monitoring". The differences between VGG measurements on nearby pillars contribute to resolving specific mass distributions.

6 Closing discussion and perspectives

The vertical gravity gradient estimation based on repeated loops carried out with a relative spring gravimeter on tripods is a time-consuming method that does not allow for a high temporal resolution. The measurement takes about one work day and thorough post-processing is required for adequate correction of drifts and other effects. We quantified the repeatability of VGG estimates as better than 23 $\pm$ 9 E. For the 117.5 cm height difference between measurements, 20 E refer to 23.5 nm·s^{-2} error.

The carried out geostatistical stochastic simulations show possible spatial distributions of subsurface properties that would lead to VGG differences between pillars of several tens of E while limiting gravity variations within a few tens of nm·s^{-2}. We assumed a porosity range in coherence with borehole logs and inversion results of previous hydro-geophysical studies. This study showed that VGG monitoring can hint at local subsurface heterogeneity that would otherwise not be visible in the

gravity series alone. Gravity gradients allow accessing surface heterogeneity and location of mass changes. In contrast to single gravity measurements that represent depth-integrative measurements, gravity gradients give access to information beyond the limitations of the classically used Bouguer plate approximation in hydrogravimetry.

Hydro-gravimetrical simulations show that the umbrella effect causes much smaller VGG variations than the observed VGG variations of several tens of E. Stochastic geostatistical simulations generated various realisations of heterogeneous subsurface porosity distributions of which some reproduce potentially detectable VGG differences between pillar p_3 and p_1,p_2. Spatial "soil noise" in the gradient signal adds uncertainty and limits the resolvability and detectability of subsurface objects during mapping surveys, as modelled by Boddice et al. (2019). We claim that time-lapse soil noise caused by soil water content changes could require consideration depending on the application. We examined time-lapse gradient noise caused by the umbrella effect and found it to be of a few E maximally for the given soil model parameters, building size, and rainfall series at the Larzac site. Analogous to the procedure presented by Reich et al. (2019), depending on building size, soil properties, and availability of data, a procedure for umbrella effect estimation for the VGG should be developed.

We recommend, however, to first refine the simulation parameters based on the earlier mentioned possibility of directional variogram fitting and joint inversion with data provided by further geophysical imaging methods. In order to gain a better understanding of the subsurface processes at the Larzac site that potentially show a detectable influence on VGG estimations, we suggest a joint approach of additional soil water content monitoring, refined stochastic simulations, and hydrological model development. Repeated electric resistivity tomography surveys would add information on the seasonal saturation changes from which furthermore directional variogram models could be fitted which would constrain the geostatistical simulations and increase hydrogeological realism. Karst water storage dynamics and porosity distribution has been resolved by long-term ERT monitoring (Watlet et al. (2018)). Additional ERT profiles at different angles to the building could aid in identifying local anisotropy applying directional variogram fitting (as e.g. done in karsts by Carrière et al. (2013)).

6.1 Time-lapse soil noise in the context of high precision gravimetry and gradiometry

If the observatory building is not surrounded by a sealed area but exposed to natural soil moisture dynamics, hydrological changes as a source of "VGG noise" should possibly be taken into account for these kinds of observatories. The Larzac observatory serves as a controlled environment of low noise level for gravimeter tests and instrument comparisons. Knowledge of the local VGG is required to correct gravity residuals for different gravity sensor heights. Geodetic observatories located at sites likely to be exposed to subsurface water mass changes might benefit from a dedicated time-variable VGG correction for gravity time series. The varying amplitude of the umbrella effect has already been shown to add significant differences between gravimeters operated on different pillars inside the observatory. We claim that natural soil heterogeneity adds another factor that may limit the repeatability of absolute gravity comparisons due to variability in vertical gravity gradient correction. Quantifying the effect of vertical gravity variability may facilitate signal separation of local and larger hydrological effects. After crust deformation and Newtonian effects on gravity measurements caused by hydrology (Llubes et al. (2004)), a third effect, the local water mass induced influence on vertical gradient variability and the corresponding modification of the vertical gravity correction emerges. This might influence repeatability and comparability between high precision instruments. A difference in

VGG of 20 E between two instruments operated on two heights of 60 cm difference (e.g. quantum gravimeter and FG5) would add 12 nm·s^{-2} of error. VGG are often estimated before gravimeter comparison and consequently assumed as constant, to our knowledge this assumption is rarely challenged.

Recently, a special focus lies on quantum technology in gravimetry (Geiger et al. (2020)). High precision gravimetry and gradiometry can both be influenced by temporal gravity gradient fluctuations and at the same time offer unprecedented potential to study them as the signal of interest. Especially absolute quantum gravimeters (Ménoret et al. (2018)) offer possibilities for VGG surveys as they are easier and faster to transport and set-up than reference absolute gravimeters. The cumbersome VGG estimation with relative gravimetry could already be simplified and more data could be acquired in less time as absolute gravimeters do not require repeated loops for drift correction. Commercially available quantum differential gravimeters are currently in development and allow for the simultaneous measurement of g and Δg from minutes to months without drift with a reported precision of a few E and a few tens of nm·s^{-2} for less than half an hour of averaging (Janvier et al. (2020)). In order to assess the sensitivity of a continuously measuring gradiometer at the Eotvos level, it would become necessary to correctly quantify time-lapse gradient noise as an error source. On the contrary, time-lapse gradient monitoring could be used to potentially identify subsurface properties such as e.g. infiltration processes, at high temporal resolution. The development of high precision instruments requires simultaneous progress in the development of new conceptual and computational frameworks to correct for and to make use of vertical gravity gradient time series for hydrogeophysical applications.

Author contributions. Execution of relative gravity surveys, post-processing and analysis have been carried out by A.-K.C. in close discussion with C.C., C.J. and N.L.M. Planning of the measurements and interpretation of the results were a joint effort of A.-K.C., C.C., C.J., P.V. and S.M. Planning and execution of hydro-gravimetrical modelling and interpretation of results has been carried out by A.-K.C. and C.C. in close discussion with C.J. Treatment of iGrav data: C.C. and N.L.M. Treatment of hydro-meteorological data: A.-K.C.

Competing interests. The study presented in this paper has been carried out in the context of the PhD thesis of Anne-Karin Cooke within the network ITN Enigma (https://enigma-itn.eu/esr-n8-monitoring-water-storage-changes-new-portable-absolute-quantum-gravimeter/). The University of Montpellier (Géosciences) and the company Muquans, the developer of absolute quantum gravimeters, have a collaboration for this purpose. During a large part of her PhD, she has been an employee of Muquans. Currently, she is employed by the University of Montpellier. Pierre Vermeulen is an employee of Muquans. Camille Janvier develops a quantum differential gravimeter at Muquans.

Disclaimer. All measurement presented here are from the Larzac observatory hosted by OSU OREME (http://www.oreme.org) and SNO H+ (http://hplus.ore.fr/). Larzac observatory and instrumentation are mainly funded by the CNRS INSU, ANR, Montpellier University, OZCAR, RESIF and Occitanie region. ENIGMA ITN has received funding from European Union's Horizon 2020 research and innovation programme under the Marie Sklodowska-Curie Grant Agreement N°722028.

Acknowledgements. We would like to thank Bruno Desruelle, Séverin Pistre, Jean Chèry, Benoit Ildefonse, Kamini Singha, Bridget Scanlon and all fellows of the ITN Enigma, their supervisors as well as associate industrial and scientific partners of the network for the numerous, fruitful discussions. Special thanks to Olivier Francis for instrumental support and interesting discussions. We would like to also thank Philippe Vernant for the cave topography.

References

Binley, A., Hubbard, S. S., Huisman, J. A., Revil, A., Robinson, D. A., Singha, K., and Slater, L. D.: The emergence of hydrogeophysics for improved understanding of subsurface processes over multiple scales, Water Resources Research, 51, 3837–3866, https://doi.org/10.1002/2015wr017016, 2015.

Blakely, R.: Potential theory in gravity and magnetic applications, Cambridge University Press, Cambridge, United Kingdom, 1995.

Boddice, D., Metje, N., and Tuckwell, G.: Quantifying the effects of near surface density variation on quantum technology gravity and gravity gradient instruments, Journal of Applied Geophysics, 164, 160–178, https://doi.org/10.1016/j.jappgeo.2019.03.012, 2019.

Bonvalot, S., Diament, M., and Gabalda, G.: Continuous gravity recording with Scintrex CG-3M meters:a promising tool for monitoring active zones, Geophysical Journal International, 135, 470–494, https://doi.org/10.1046/j.1365-246x.1998.00653.x, 1998.

Camp, M. V., de Viron, O., Scherneck, H.-G., Hinzen, K.-G., Williams, S. D. P., Lecocq, T., Quinif, Y., and Camelbeeck, T.: Repeated absolute gravity measurements for monitoring slow intraplate vertical deformation in western Europe, Journal of Geophysical Research, 116, https://doi.org/10.1029/2010jb008174, 2011.

Camp, M. V., de Viron, O., Watlet, A., Meurers, B., Francis, O., and Caudron, C.: Geophysics From Terrestrial Time-Variable Gravity Measurements, Reviews of Geophysics, 55, 938–992, https://doi.org/10.1002/2017rg000566, 2017.

Capriotti, J. and Li, Y.: Gravity and gravity gradient data: Understanding their information content through joint inversions, in: SEG Technical Program Expanded Abstracts 2014, Society of Exploration Geophysicists, https://doi.org/10.1190/segam2014-1581.1, 2014.

Carbone, D., Poland, M. P., Diament, M., and Greco, F.: The added value of time-variable microgravimetry to the understanding of how volcanoes work, Earth-Science Reviews, 169, 146–179, https://doi.org/10.1016/j.earscirev.2017.04.014, 2017.

Carrière, S. D., Chalikakis, K., Sénéchal, G., Danquigny, C., and Emblanch, C.: Combining Electrical Resistivity Tomography and Ground Penetrating Radar to study geological structuring of karst Unsaturated Zone, Journal of Applied Geophysics, 94, 31–41, https://doi.org/10.1016/j.jappgeo.2013.03.014, 2013.

Cattin, R., Mazzotti, S., and Baratin, L.-M.: GravProcess: An easy-to-use MATLAB software to process campaign gravity data and evaluate the associated uncertainties, Computers & Geosciences, 81, 20–27, https://doi.org/10.1016/j.cageo.2015.04.005, 2015.

Champollion, C., Deville, S., Chéry, J., Doerflinger, E., Moigne, N. L., Bayer, R., Vernant, P., and Mazzilli, N.: Estimating epikarst water storage by time-lapse surface-to-depth gravity measurements, Hydrology and Earth System Sciences, 22, 3825–3839, https://doi.org/10.5194/hess-22-3825-2018, 2018.

Christiansen, L., Lund, S., Andersen, O. B., Binning, P. J., Rosbjerg, D., and Bauer-Gottwein, P.: Measuring gravity change caused by water storage variations: Performance assessment under controlled conditions, Journal of Hydrology, 402, 60–70, https://doi.org/10.1016/j.jhydrol.2011.03.004, 2011.

Creutzfeldt, B., Güntner, A., Thoss, H., Merz, B., and Wziontek, H.: Measuring the effect of local water storage changes on in situ gravity observations: Case study of the Geodetic Observatory Wettzell, Germany, Water Resources Research, 46, https://doi.org/10.1029/2009wr008359, 2010.

Creutzfeldt, B., Troch, P. A., Güntner, A., Ferré, T. P. A., Graeff, T., and Merz, B.: Storage-discharge relationships at different catchment scales based on local high-precision gravimetry, Hydrological Processes, 28, 1465–1475, https://doi.org/10.1002/hyp.9689, 2013.

Crossley, D., Hinderer, J., and Riccardi, U.: The measurement of surface gravity, Reports on Progress in Physics, 76, 046 101, https://doi.org/10.1088/0034-4885/76/4/046101, 2013.

Davis, K., Li, Y., and Batzle, M.: Time-lapse gravity monitoring: A systematic 4D approach with application to aquifer storage and recovery, GEOPHYSICS, 73, WA61–WA69, https://doi.org/10.1190/1.2987376, 2008.

Delobbe, L., Watlet, A., Wilfert, S., and Camp, M. V.: Exploring the use of underground gravity monitoring to evaluate radar estimates of heavy rainfall, Hydrology and Earth System Sciences, 23, 93–105, https://doi.org/10.5194/hess-23-93-2019, 2019.

Deville, S.: Caractérisation de la zone non saturée des karsts par la gravimétrie et l'hydrogéologie, Ph.D. thesis, https://tel.archives-ouvertes.fr/tel-00829346, 2013.

Deville, S., Jacob, T., Chéry, J., and Champollion, C.: On the impact of topography and building mask on time varying gravity due to local hydrology, Geophysical Journal International, 192, 82–93, https://doi.org/10.1093/gji/ggs007, 2012.

Elliott, E. J. and Braun, A.: On the Resolvability of Steam Assisted Gravity Drainage Reservoirs Using Time-Lapse Gravity Gradiometry, Pure and Applied Geophysics, 174, 4119–4136, https://doi.org/10.1007/s00024-017-1636-5, 2017.

Ferguson, J. F., Chen, T., Brady, J., Aiken, C. L., and Seibert, J.: The 4D microgravity method for waterflood surveillance: Part II — Gravity measurements for the Prudhoe Bay reservoir, Alaska, GEOPHYSICS, 72, I33–I43, https://doi.org/10.1190/1.2435473, 2007.

Fores, B.: Gravimétrie et surveillance sismique pour la modélisation hydrologique en milieu karstique: application au bassin du Durzon (Larzac, France), Ph.D. thesis, https://tel.archives-ouvertes.fr/tel-01649606, 2016.

Fores, B., Champollion, C., Moigne, N. L., Bayer, R., and Chéry, J.: Assessing the precision of the iGrav superconducting gravimeter for hydrological models and karstic hydrological process identification, Geophysical Journal International, 208, 269–280, https://doi.org/10.1093/gji/ggw396, 2016a.

Fores, B., Champollion, C., Moigne, N. L., and Chery, J.: Impact of ambient temperature on spring-based relative gravimeter measurements, Journal of Geodesy, 91, 269–277, https://doi.org/10.1007/s00190-016-0961-2, 2016b.

Fores, B., Champollion, C., Mainsant, G., Albaric, J., and Fort, A.: Monitoring Saturation Changes with Ambient Seismic Noise and Gravimetry in a Karst Environment, Vadose Zone Journal, 17, 170 163, https://doi.org/10.2136/vzj2017.09.0163, 2018.

Fores, B., Klein, G., Moigne, N. L., and Francis, O.: Long-Term Stability of Tilt-Controlled gPhoneX Gravimeters, Journal of Geophysical Research: Solid Earth, 124, 12 264–12 276, https://doi.org/10.1029/2019jb018276, 2019.

Gaillardet, J., Braud, I., Hankard, F., Anquetin, S., Bour, O., Dorfliger, N., de Dreuzy, J., Galle, S., Galy, C., Gogo, S., Gourcy, L., Habets, F., Laggoun, F., Longuevergne, L., Borgne, T. L., Naaim-Bouvet, F., Nord, G., Simonneaux, V., Six, D., Tallec, T., Valentin, C., Abril, G., Allemand, P., Arènes, A., Arfib, B., Arnaud, L., Arnaud, N., Arnaud, P., Audry, S., Comte, V. B., Batiot, C., Battais, A., Bellot, H., Bernard, E., Bertrand, C., Bessière, H., Binet, S., Bodin, J., Bodin, X., Boithias, L., Bouchez, J., Boudevillain, B., Moussa, I. B., Branger, F., Braun, J. J., Brunet, P., Caceres, B., Calmels, D., Cappelaere, B., Celle-Jeanton, H., Chabaux, F., Chalikakis, K., Champollion, C., Copard, Y., Cotel, C., Davy, P., Deline, P., Delrieu, G., Demarty, J., Dessert, C., Dumont, M., Emblanch, C., Ezzahar, J., Estèves, M., Favier, V., Faucheux, M., Filizola, N., Flammarion, P., Floury, P., Fovet, O., Fournier, M., Francez, A. J., Gandois, L., Gascuel, C., Gayer, E., Genthon, C., Gérard, M. F., Gilbert, D., Gouttevin, I., Grippa, M., Gruau, G., Jardani, A., Jeanneau, L., Join, J. L., Jourde, H., Karbou, F., Labat, D., Lagadeuc, Y., Lajeunesse, E., Lastennet, R., Lavado, W., Lawin, E., Lebel, T., Bouteiller, C. L., Legout, C., Lejeune, Y., Meur, E. L., Moigne, N. L., Lions, J., Lucas, A., Malet, J. P., Marais-Sicre, C., Maréchal, J. C., Marlin, C., Martin, P., Martins, J., Martinez, J. M., Massei, N., Mauclerc, A., Mazzilli, N., Molénat, J., Moreira-Turcq, P., Mougin, E., Morin, S., Ngoupayou, J. N., Panthou, G., Peugeot, C., Picard, G., Pierret, M. C., Porel, G., Probst, A., Probst, J. L., Rabatel, A., Raclot, D., Ravanel, L., Rejiba, F., René, P., Ribolzi, O., Riotte, J., Rivière, A., Robain, H., Ruiz, L., Sanchez-Perez, J. M., Santini, W., Sauvage, S., Schoeneich, P., Seidel, J. L., Sekhar, M., Sengtaheuanghoung, O., Silvera, N., Steinmann, M., Soruco, A., Tallec, G., Thibert, E., Lao, D. V., Vincent, C.,

Viville, D., Wagnon, P., and Zitouna, R.: OZCAR: The French Network of Critical Zone Observatories, Vadose Zone Journal, 17, 180 067, https://doi.org/10.2136/vzj2018.04.0067, 2018.

Galibert, P.-Y., Valois, R., Mendes, M., and Guérin, R.: Seismic study of the low-permeability volume in southern France karst systems, GEOPHYSICS, 79, EN1–EN13, https://doi.org/10.1190/geo2013-0120.1, 2014.

Geiger, R., Landragin, A., Merlet, S., and Santos, F. P. D.: High-accuracy inertial measurements with cold-atom sensors, AVS Quantum Science, 2, 024 702, https://doi.org/10.1116/5.0009093, 2020.

Gerbaux, G.: Impact de la fracturation et de la karstification sur la dynamique des eaux souterraines dans le Larzac. Stage de fin d'étude Master 2, Université Montpellier 2, 2009.

Güntner, A., Reich, M., Mikolaj, M., Creutzfeldt, B., Schroeder, S., and Wziontek, H.: Landscape-scale water balance monitoring with an iGrav superconducting gravimeter in a field enclosure, Hydrology and Earth System Sciences, 21, 3167–3182, https://doi.org/10.5194/hess-21-3167-2017, 2017.

Hammond, G. E., Lichtner, P. C., and Mills, R. T.: Evaluating the performance of parallel subsurface simulators: An illustrative example with PFLOTRAN, Water Resources Research, 50, 208–228, https://doi.org/10.1002/2012wr013483, 2014.

Harnisch, G. and Harnisch, M.: Hydrological influences in long gravimetric data series, Journal of Geodynamics, 41, 276–287, https://doi.org/10.1016/j.jog.2005.08.018, 2006.

Hartmann, A., Goldscheider, N., Wagener, T., Lange, J., and Weiler, M.: Karst water resources in a changing world: Review of hydrological modeling approaches, Reviews of Geophysics, 52, 218–242, https://doi.org/10.1002/2013rg000443, 2014.

Hasan, S., Troch, P. A., Bogaart, P. W., and Kroner, C.: Evaluating catchment-scale hydrological modeling by means of terrestrial gravity observations, Water Resources Research, 44, https://doi.org/10.1029/2007wr006321, 2008.

Hector, B. and Hinderer, J.: pyGrav, a Python-based program for handling and processing relative gravity data, Computers & Geosciences, 91, 90–97, https://doi.org/10.1016/j.cageo.2016.03.010, 2016.

Hector, B., Séguis, L., Hinderer, J., Descloitres, M., Vouillamoz, J.-M., Wubda, M., Boy, J.-P., Luck, B., and Moigne, N. L.: Gravity effect of water storage changes in a weathered hard-rock aquifer in West Africa: results from joint absolute gravity, hydrological monitoring and geophysical prospection, Geophysical Journal International, 194, 737–750, https://doi.org/10.1093/gji/ggt146, 2013.

Hector, B., Hinderer, J., Séguis, L., Boy, J.-P., Calvo, M., Descloitres, M., Rosat, S., Galle, S., and Riccardi, U.: Hydro-gravimetry in West-Africa: First results from the Djougou (Benin) superconducting gravimeter, Journal of Geodynamics, 80, 34–49, https://doi.org/10.1016/j.jog.2014.04.003, 2014.

Hector, B., Séguis, L., Hinderer, J., Cohard, J.-M., Wubda, M., Descloitres, M., Benarrosh, N., and Boy, J.-P.: Water storage changes as a marker for base flow generation processes in a tropical humid basement catchment (B enin): Insights from hybrid gravimetry, Water Resources Research, 51, 8331–8361, https://doi.org/10.1002/2014wr015773, 2015.

Hinderer, J., Crossley, D., and Warburton, R.: Superconducting Gravimetry, in: Treatise on Geophysics, pp. 59–115, Elsevier, https://doi.org/10.1016/b978-0-444-53802-4.00062-2, 2015.

Hinze, W. J., Von Frese, R. R., and Saad, A. H.: Gravity and magnetic exploration: Principles, practices, and applications, Cambridge University Press, 2013.

Hwang, C., Wang, C.-G., and Lee, L.-H.: Adjustment of relative gravity measurements using weighted and datum-free constraints, Computers & Geosciences, 28, 1005–1015, https://doi.org/10.1016/s0098-3004(02)00005-5, 2002.

Hwang, C., Cheng, T.-C., Cheng, C., and Hung, W.: Land subsidence using absolute and relative gravimetry: a case study in central Taiwan, Survey Review, 42, 27–39, https://doi.org/10.1179/003962609x451672, 2010.

Imanishi, Y.: A Network of Superconducting Gravimeters Detects Submicrogal Coseismic Gravity Changes, Science, 306, 476–478, https://doi.org/10.1126/science.1101875, 2004.

Jacob, T., Bayer, R., Chery, J., Jourde, H., Moigne, N. L., Boy, J.-P., Hinderer, J., Luck, B., and Brunet, P.: Absolute gravity monitoring of water storage variation in a karst aquifer on the larzac plateau (Southern France), Journal of Hydrology, 359, 105–117, https://doi.org/10.1016/j.jhydrol.2008.06.020, 2008.

Jacob, T., Chery, J., Bayer, R., Moigne, N. L., Boy, J.-P., Vernant, P., and Boudin, F.: Time-lapse surface to depth gravity measurements on a karst system reveal the dominant role of the epikarst as a water storage entity, Geophysical Journal International, 177, 347–360, https://doi.org/10.1111/j.1365-246x.2009.04118.x, 2009.

Jacob, T., Bayer, R., Chery, J., and Moigne, N. L.: Time-lapse microgravity surveys reveal water storage heterogeneity of a karst aquifer, Journal of Geophysical Research, 115, https://doi.org/10.1029/2009jb006616, 2010.

Jacob, T., Samyn, K., Bitri, A., Quesnel, F., Dewez, T., Pannet, P., and Meire, B.: Mapping sand and clay-filled depressions on a coastal chalk clifftop using gravity and seismic tomography refraction for landslide hazard assessment, in Normandy, France, Engineering Geology, 246, 262–276, https://doi.org/10.1016/j.enggeo.2018.10.007, 2018.

Janvier, C., Ménoret, V., Lautier, J., Desruelle, B., Merlet, S., dos Santos, F. P., and Landragin, A.: Operating an industry-grade quantum differential gravimeter, https://doi.org/10.5194/egusphere-egu2020-9185, 2020.

Jirigalatu, J. and Ebbing: A fast equivalent source method for airborne gravity gradient data, GEOPHYSICS, 84, G75–G82, https://doi.org/10.1190/geo2018-0366.1, 2019.

Karst3D Team: Karst3D, https://doi.org/10.15148/940C2882-49F1-49DB-A97E-12303CACE752, 2019.

Kennedy, J., Ferré, T. P. A., Güntner, A., Abe, M., and Creutzfeldt, B.: Direct measurement of subsurface mass change using the variable baseline gravity gradient method, Geophysical Research Letters, 41, 2827–2834, https://doi.org/10.1002/2014gl059673, 2014.

Kennedy, J., Ferré, T. P. A., and Creutzfeldt, B.: Time-lapse gravity data for monitoring and modeling artificial recharge through a thick unsaturated zone, Water Resources Research, 52, 7244–7261, https://doi.org/10.1002/2016wr018770, 2016.

Krause, P., Naujoks, M., Fink, M., and Kroner, C.: The impact of soil moisture changes on gravity residuals obtained with a superconducting gravimeter, Journal of Hydrology, 373, 151–163, https://doi.org/10.1016/j.jhydrol.2009.04.019, 2009.

Lampitelli, C. and Francis, O.: Hydrological effects on gravity and correlations between gravitational variations and level of the Alzette River at the station of Walferdange, Luxembourg, Journal of Geodynamics, 49, 31–38, https://doi.org/10.1016/j.jog.2009.08.003, 2010.

Lantuéjoul, C.: Geostatistical Simulation, Springer Berlin Heidelberg, https://doi.org/10.1007/978-3-662-04808-5, 2002.

Lawrence, M. A.: ez: Easy Analysis and Visualization of Factorial Experiments, https://CRAN.R-project.org/package=ez, r package version 4.4-0, 2016.

Lederer, M.: Accuracy of the relative gravity measurement, Acta Geodyn. Geomater, 6, 155, 2009.

Leirião, S., He, X., Christiansen, L., Andersen, O. B., and Bauer-Gottwein, P.: Calculation of the temporal gravity variation from spatially variable water storage change in soils and aquifers, Journal of Hydrology, 365, 302–309, https://doi.org/10.1016/j.jhydrol.2008.11.040, 2009.

Limited, S.: CG-5 Scintrex Autograv TM System Operation Manual, Scintrex Limited, 222 Snidercroft Road, Concord, Ontario, Canada, L4K 2K1, https://scintrexltd.com, 2014.

Limited, S.: CG-6 Scintrex Autograv TM System Operation Manual, Scintrex Limited, 222 Snidercroft Road, Concord, Ontario, Canada, L4K 2K1, https://scintrexltd.com, 2018.

Linage, C. D., Hinderer, J., and Rogister, Y.: A search for the ratio between gravity variation and vertical displacement due to a surface load, Geophysical Journal International, 171, 986–994, https://doi.org/10.1111/j.1365-246x.2007.03613.x, 2007.

Llubes, M., Florsch, N., Hinderer, J., Longuevergne, L., and Amalvict, M.: Local hydrology, the Global Geodynamics Project and CHAMP/GRACE perspective: some case studies, Journal of Geodynamics, 38, 355–374, https://doi.org/10.1016/j.jog.2004.07.015, 2004.

Longuevergne, L., Boy, J., Florsch, N., Viville, D., Ferhat, G., Ulrich, P., Luck, B., and Hinderer, J.: Local and global hydrological contributions to gravity variations observed in Strasbourg, Journal of Geodynamics, 48, 189–194, https://doi.org/10.1016/j.jog.2009.09.008, 2009.

Mazzilli, N., Jourde, H., Jacob, T., Guinot, V., Moigne, N. L., Boucher, M., Chalikakis, K., Guyard, H., and Legtchenko, A.: On the inclusion of ground-based gravity measurements to the calibration process of a global rainfall-discharge reservoir model: case of the Durzon karst system (Larzac, southern France), Environmental Earth Sciences, 68, 1631–1646, https://doi.org/10.1007/s12665-012-1856-z, 2012.

Mazzilli, N., Boucher, M., Chalikakis, K., Legchenko, A., Jourde, H., and Champollion, C.: Contribution of magnetic resonance soundings for characterizing water storage in the unsaturated zone of karst aquifers, GEOPHYSICS, 81, WB49–WB61, https://doi.org/10.1190/geo2015-0411.1, 2016.

Mazzotti, S., Lambert, A., Henton, J., James, T. S., and Courtier, N.: Absolute gravity calibration of GPS velocities and glacial isostatic adjustment in mid-continent North America, Geophysical Research Letters, 38, n/a–n/a, https://doi.org/10.1029/2011gl049846, 2011.

McLeod, A.: Kendall: Kendall rank correlation and Mann-Kendall trend test, https://CRAN.R-project.org/package=Kendall, r package version 2.2, 2011.

Ménoret, V., Vermeulen, P., Moigne, N. L., Bonvalot, S., Bouyer, P., Landragin, A., and Desruelle, B.: Gravity measurements below 10-9 g with a transportable absolute quantum gravimeter, Scientific Reports, 8, https://doi.org/10.1038/s41598-018-30608-1, 2018.

Merlet, S., Kopaev, A., Diament, M., Geneves, G., Landragin, A., and Santos, F. P. D.: Micro-gravity investigations for the LNE watt balance project, Metrologia, 45, 265–274, https://doi.org/10.1088/0026-1394/45/3/002, 2008.

Meurers, B., Camp, M. V., and Petermans, T.: Correcting superconducting gravity time-series using rainfall modelling at the Vienna and Membach stations and application to Earth tide analysis, Journal of Geodesy, 81, 703–712, https://doi.org/10.1007/s00190-007-0137-1, 2007.

Mollenhauer, H., Kasner, M., Haase, P., Peterseil, J., Wohner, C., Frenzel, M., Mirtl, M., Schima, R., Bumberger, J., and Zacharias, S.: Long-term environmental monitoring infrastructures in Europe: observations, measurements, scales, and socio-ecological representativeness, vol. 624, pp. 968–978, Elsevier BV, https://doi.org/10.1016/j.scitotenv.2017.12.095, 2018.

Mouyen, M., Longuevergne, L., Chalikakis, K., Mazzilli, N., Ollivier, C., Rosat, S., Hinderer, J., and Champollion, C.: Monitoring of groundwater redistribution in a karst aquifer using a superconducting gravimeter, E3S Web of Conferences, 88, 03 001, https://doi.org/10.1051/e3sconf/20198803001, 2019.

Naujoks, M., Weise, A., Kroner, C., and Jahr, T.: Detection of small hydrological variations in gravity by repeated observations with relative gravimeters, Journal of Geodesy, 82, 543–553, https://doi.org/10.1007/s00190-007-0202-9, 2007.

Naujoks, M., Kroner, C., Weise, A., Jahr, T., Krause, P., and Eisner, S.: Evaluating local hydrological modelling by temporal gravity observations and a gravimetric three-dimensional model, Geophysical Journal International, pp. no–no, https://doi.org/10.1111/j.1365-246x.2010.04615.x, 2010.

Neumeyer, J., Barthelmes, F., Kroner, C., Petrovic, S., Schmidt, R., Virtanen, H., and Wilmes, H.: Analysis of gravity field variations derived from Superconducting Gravimeter recordings, the GRACE satellite and hydrological models at selected European sites, Earth, Planets and Space, 60, 505–518, https://doi.org/10.1186/bf03352817, 2008.

Niebauer, T.: Gravimetric Methods – Absolute and Relative Gravity Meter: Instruments Concepts and Implementation, in: Treatise on Geophysics, pp. 37–57, Elsevier, https://doi.org/10.1016/b978-0-444-53802-4.00057-9, 2015.

Niebauer, T. M., Sasagawa, G. S., Faller, J. E., Hilt, R., and Klopping, F.: A new generation of absolute gravimeters, Metrologia, 32, 159–180, https://doi.org/10.1088/0026-1394/32/3/004, 1995.

Okabe, M.: Analytical expressions for gravity anomalies due to homogeneous polyhedral bodies and translations into magnetic anomalies, GEOPHYSICS, 44, 730–741, https://doi.org/10.1190/1.1440973, 1979.

Olsson, P.-A., Breili, K., Ophaug, V., Steffen, H., Bilker-Koivula, M., Nielsen, E., Oja, T., and Timmen, L.: Postglacial gravity change in Fennoscandia—three decades of repeated absolute gravity observations, Geophysical Journal International, 217, 1141–1156, https://doi.org/10.1093/gji/ggz054, 2019.

Pearson-Grant, S., Franz, P., and Clearwater, J.: Gravity measurements as a calibration tool for geothermal reservoir modelling, Geothermics, 73, 146–157, https://doi.org/10.1016/j.geothermics.2017.06.006, 2018.

Pebesma, E. J.: Multivariable geostatistics in S: the gstat package, Computers & Geosciences, 30, 683–691, https://doi.org/10.1016/j.cageo.2004.03.012, 2004.

Pfeffer, J., Champollion, C., Favreau, G., Cappelaere, B., Hinderer, J., Boucher, M., Nazoumou, Y., Oï, M., Mouyen, M., Henri, C., Moigne, N. L., Deroussi, S., Demarty, J., Boulain, N., Benarrosh, N., and Robert, O.: Evaluating surface and subsurface water storage variations at small time and space scales from relative gravity measurements in semiarid Niger, Water Resources Research, 49, 3276–3291, https://doi.org/10.1002/wrcr.20235, 2013.

Piccolroaz, S., Majone, B., Palmieri, F., Cassiani, G., and Bellin, A.: On the use of spatially distributed, time-lapse microgravity surveys to inform hydrological modeling, Water Resources Research, 51, 7270–7288, https://doi.org/10.1002/2015wr016994, 2015.

Pinault, J.-L., Plagnes, V., Aquilina, L., and Bakalowicz, M.: Inverse modeling of the hydrological and the hydrochemical behavior of hydrosystems: Characterization of Karst System Functioning, Water Resources Research, 37, 2191–2204, https://doi.org/10.1029/2001wr900018, 2001.

Pohlert, T.: trend: Non-Parametric Trend Tests and Change-Point Detection, https://CRAN.R-project.org/package=trend, r package version 1.1.2, 2020.

R Core Team: R: A Language and Environment for Statistical Computing, R Foundation for Statistical Computing, Vienna, Austria, https://www.R-project.org/, 2020.

Reich, M., Mikolaj, M., Blume, T., and Güntner, A.: Reducing gravity data for the influence of water storage variations beneath observatory buildings, GEOPHYSICS, 84, EN15–EN31, https://doi.org/10.1190/geo2018-0301.1, 2019.

Reitz, A., Krahenbuhl, R., and Li, Y.: Feasibility of time-lapse gravity and gravity gradiometry monitoring for steam-assisted gravity drainage reservoirs, GEOPHYSICS, 80, WA99–WA111, https://doi.org/10.1190/geo2014-0217.1, 2015.

Richards, L. A.: CAPILLARY CONDUCTION OF LIQUIDS THROUGH POROUS MEDIUMS, Physics, 1, 318–333, https://doi.org/10.1063/1.1745010, 1931.

Rim, H. and Li, Y.: Single-hole imaging using borehole gravity gradiometry, GEOPHYSICS, 77, G67–G76, https://doi.org/10.1190/geo2012-0003.1, 2012.

Rummel, R., Yi, W., and Stummer, C.: GOCE gravitational gradiometry, Journal of Geodesy, 85, 777–790, https://doi.org/10.1007/s00190-011-0500-0, 2011.

Šimůnek, J., van Genuchten, M. T., and Šejna, M.: Recent Developments and Applications of the HYDRUS Computer Software Packages, Vadose Zone Journal, 15, vzj2016.04.0033, https://doi.org/10.2136/vzj2016.04.0033, 2016.

Valois, R.: Caractérisation structurale de morphologies karstiques superficielles et suivi temporel de l'infiltration à l'aide des méthodes électriques et sismiques, Ph.D. thesis, https://tel.archives-ouvertes.fr/tel-00659289, 2011.

Van Camp, M., de Viron, O., Pajot-Métivier, G., Casenave, F., Watlet, A., Dassargues, A., and Vanclooster, M.: Direct measurement of evapotranspiration from a forest using a superconducting gravimeter, Geophysical Research Letters, 43, 10–225, https://doi.org/10.1002/2016GL070534, 2016.

van Genuchten, M. T.: A Closed-form Equation for Predicting the Hydraulic Conductivity of Unsaturated Soils, Soil Science Society of America Journal, 44, 892–898, https://doi.org/10.2136/sssaj1980.03615995004400050002x, 1980.

Volcke, P., Pequegnat, C., Brichet-Billet, B., Lecointre, A., Wolyniec, D., and Guéguen, P.: RESIF national datacentre: new features and upcoming evolutions, EGU General Assembly, 2014.

Watlet, A., Kaufmann, O., Triantafyllou, A., Poulain, A., Chambers, J. E., Meldrum, P. I., Wilkinson, P. B., Hallet, V., Quinif, Y., Ruymbeke, M. V., and Camp, M. V.: Imaging groundwater infiltration dynamics in the karst vadose zone with long-term ERT monitoring, Hydrology and Earth System Sciences, 22, 1563–1592, https://doi.org/10.5194/hess-22-1563-2018, 2018.

Wenzel, H.-G.: The nanogal software: Earth tide data processing package ETERNA 3.30, Bull. Inf. Marées Terrestres, 124, 9425–9439, 1996.

Wutzler, T., Lucas-Moffat, A., Migliavacca, M., Knauer, J., Sickel, K., Šigut, L., Menzer, O., and Reichstein, M.: Basic and extensible post-processing of eddy covariance flux data with REddyProc, Biogeosciences, 15, 5015–5030, https://doi.org/10.5194/bg-15-5015-2018, 2018.

Wziontek, H., Wilmes, H., Wolf, P., Werth, S., and Güntner, A.: Time series of superconducting gravimeters and water storage variations from the global hydrology model WGHM, Journal of Geodynamics, 48, 166–171, https://doi.org/10.1016/j.jog.2009.09.036, 2009.

4.2 Complementary results and discussion

This section provides additional simulation results and discusses several sources of spatial heterogeneity and temporal variations of gravity and its vertical gradient.

Firstly, the following sections investigate masses in the observatory building that potentially influence the local gravity field at the Larzac observatory. The gravitational effects are simulated and their influence on the gravity and vertical gravity gradient measurements is discussed. In particular, the influence of the mass of the operator is examined. Most importantly, the masses of the concrete pillars inside the observatory building and their signature in the measured gravity and VGG data are modelled with special focus on differences between pillars at different measurement heights.

Secondly, general considerations on the sensitivity of VGG measurements and the consequent deduction of spatial characteristics of mass anomalies are given. The results of the geostatistical stochastic simulations previously presented in the publication in preparation are discussed in this context. Moreover, mapped geological structures at the site are taken into account. Lastly, an additional geostatistical stochastic simulation focuses on the potential influence of local soil water storage in the reach of three boreholes near the building.

4.2.1 VGG estimation from relative gravimetry

4.2.2 Simulated gravity field in the observatory building

4.2.2.1 Influence of operator

The error caused by the mass of the operator on the VGG estimated between height h_0 (0.261 m) and h_2 (1.436 m) was simulated using the simplified shape of a rectangular prism of 1.64 m height and 0.2 m depth and width, respectively. A mass of 65 kg and density 985 $\mathrm{kg \cdot m^{-3}}$ of the human body was chosen. Figure 4.2 shows that distances larger than 0.6 m the influence of the presence of the operator next to the measurement decreases to less than 20 E. During gravity acquisition, the operator distanced herself from the gravimeter and stayed several meters away towards the opposing wall of the building. This potential error source has therefore been ruled out as negligible.

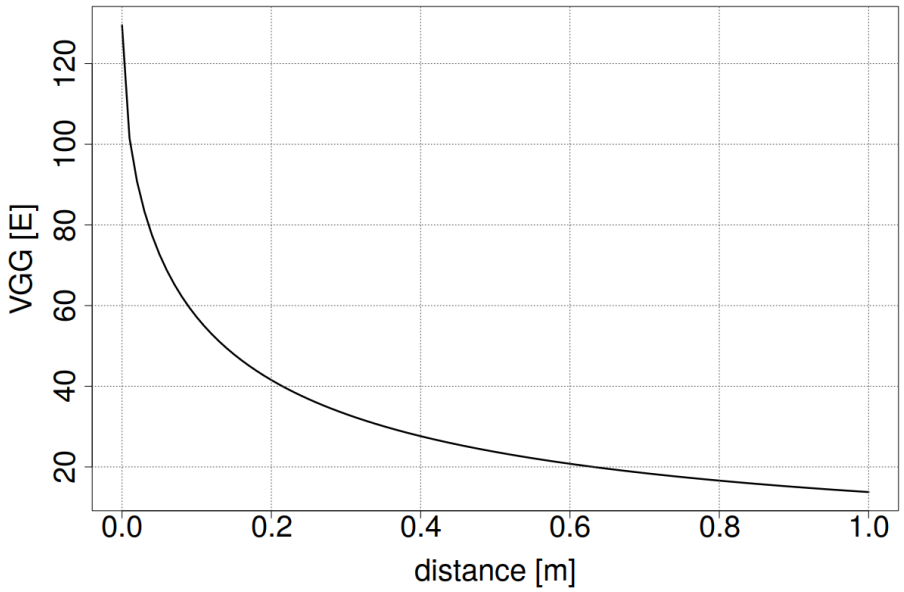

Figure 4.2: Modelled influence in E of the body mass of the operator on the vertical gravity gradient measurement as a function of distance in meters.

4.2.2.2 Simulated influence of concrete pillars

The requirement of stable and robust measurement locations makes it necessary to construct concrete pillars at gravity observatories. Due to the typically high density of concrete, the influence of these compact structures on the local gravitational field can be important. Therefore, simulated gravity and VGG calculated based on geometries of the four pillars (Figure 4.3 is shown for the surface areas of the pillars p_1/p_2 and p_3.

Figure 4.3: Larzac observatory concrete pillars during construction in 2011 (Photo: Le Moigne, 2011)

A density $\rho_{concrete}$ of 2400 kg·m^{-3} was assumed. Pillars stick 0.5 m out of the ground. Their entire height is 0.7 m. The remaining 0.2 m were not considered due to the negligible density contrast between concrete and surrounding bedrock. Secondly, gravity of the area of the corresponding pillar at the height of measurement on tripods is shown relative to the mean gravity on the pillar's surface. Figures 4.4, 4.5 and 4.6 display the gravity surface of the pillar $p_{1,2}$ at height h_0 (0.261 m), h_1 (0.85 m) and h_2 (1.436 m), which are coherent with the heights used for the relative gravimetry surveys.

4.2.2.2.1 Simulated gravity

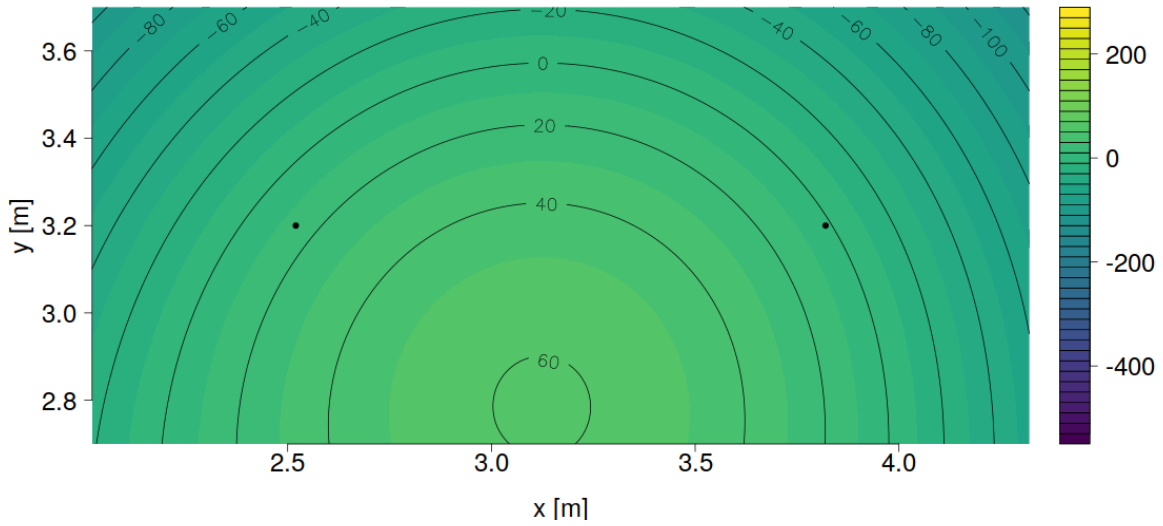

Figure 4.4: Gravity on surface of concrete pillar 1/2 at h_0 (0.261 m). Gravity residuals in nm.s^{-2} relative to mean gravity on the surface of $p_{1,2}$. Gravity field caused by the mass of the pillars 0-4. Centres of gravimeter measurement locations are marked as points.

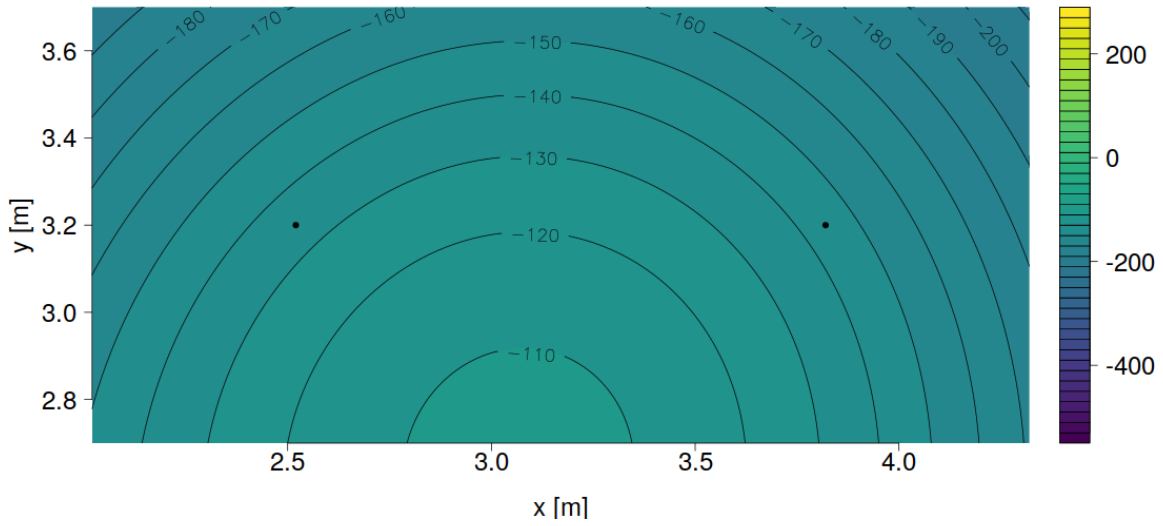

Figure 4.5: Gravity on surface of concrete pillar 1/2 at h_1(0.85 m). Gravity residuals in nm.s^{-2} relative to mean gravity on the surface of $p_{1,2}$. Gravity field caused by the mass of the pillars 0-4. Centres of gravimeter measurement locations are marked as points.

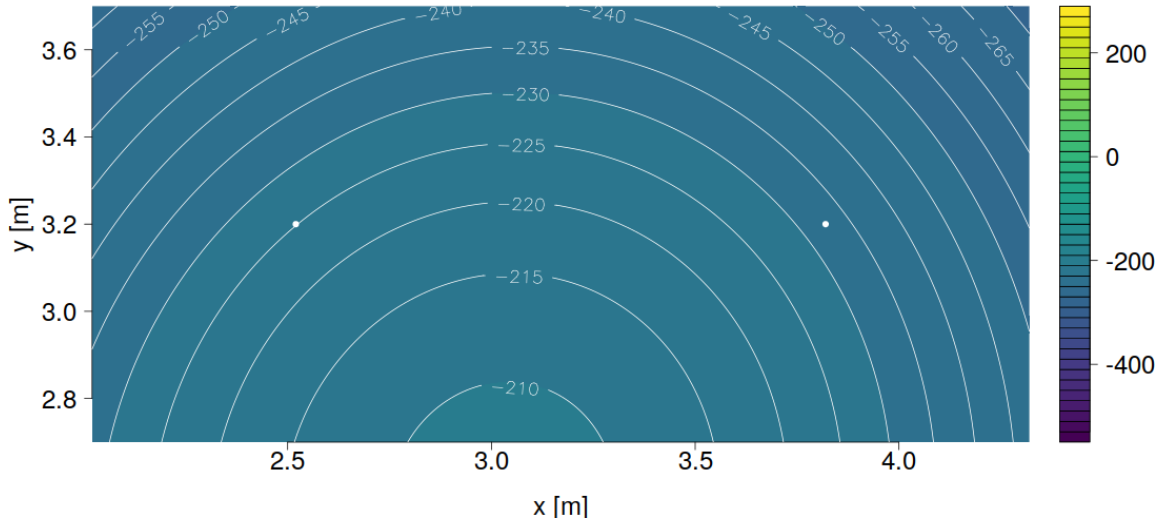

Figure 4.6: Gravity on surface of concrete pillar 1/2 at h_2 (1.436 m). Gravity residuals in nm.s^{-2} relative to mean gravity on the surface pf $p_{1,2}$. Gravity field caused by the mass of the pillars 0-4. Centres of gravimeter measurement locations are marked as points.

Equivalently, this is shown for pillar p_3 in Figures 4.7, 4.8 and 4.9. Centres of gravimeter measurement locations are marked as points. As expected, the gravity highest values are not in the centre of each pillar, but shifted towards the centre of gravity of all four pillars.

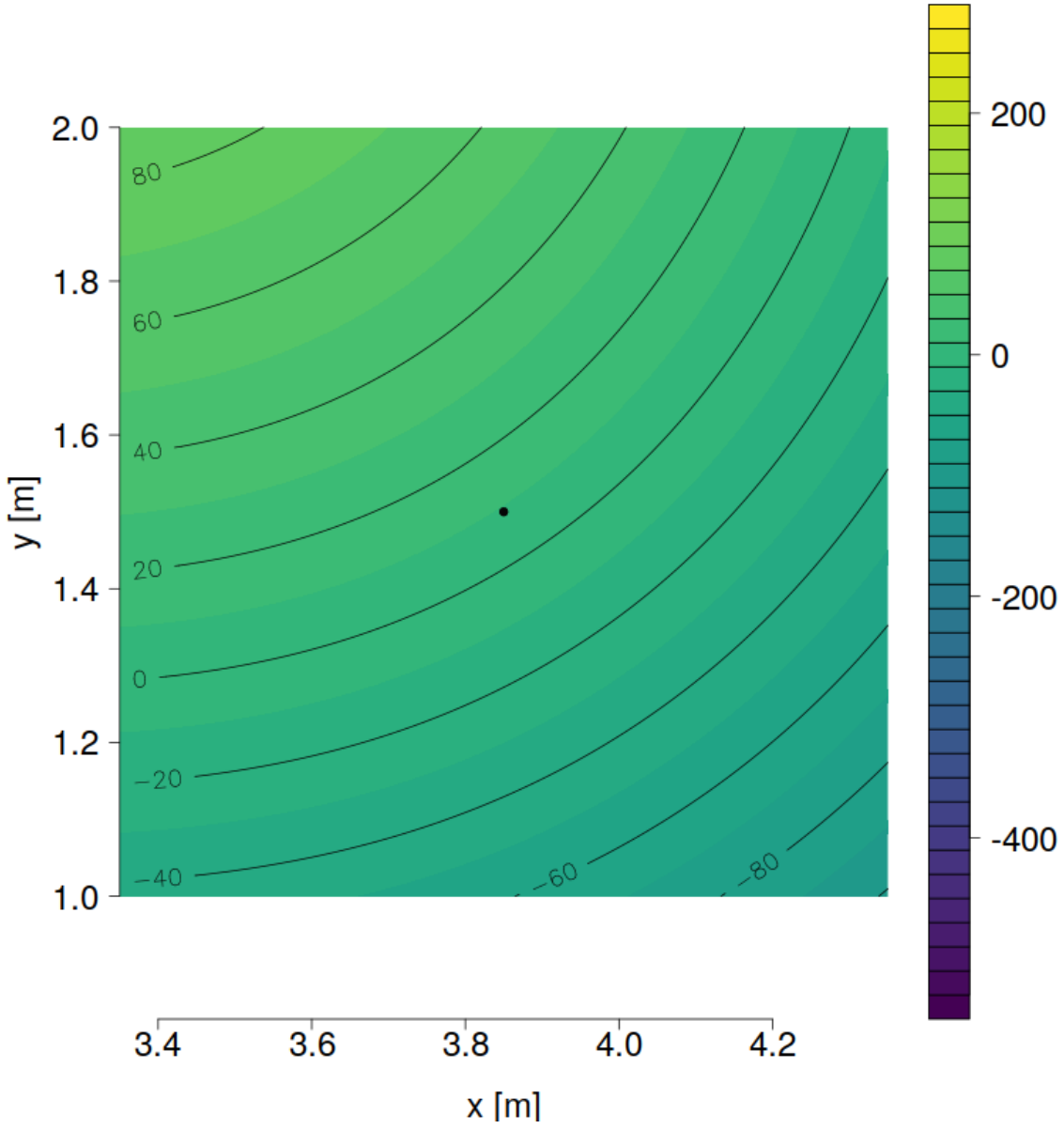

Figure 4.7: Gravity on surface of concrete pillar 3 at h_0 (0.261 m). Gravity residuals in nm.s^{-2} relative to mean gravity on the surface of p_3. Gravity field caused by the mass of the pillars 0-4. Centres of gravimeter measurement locations are marked as points.

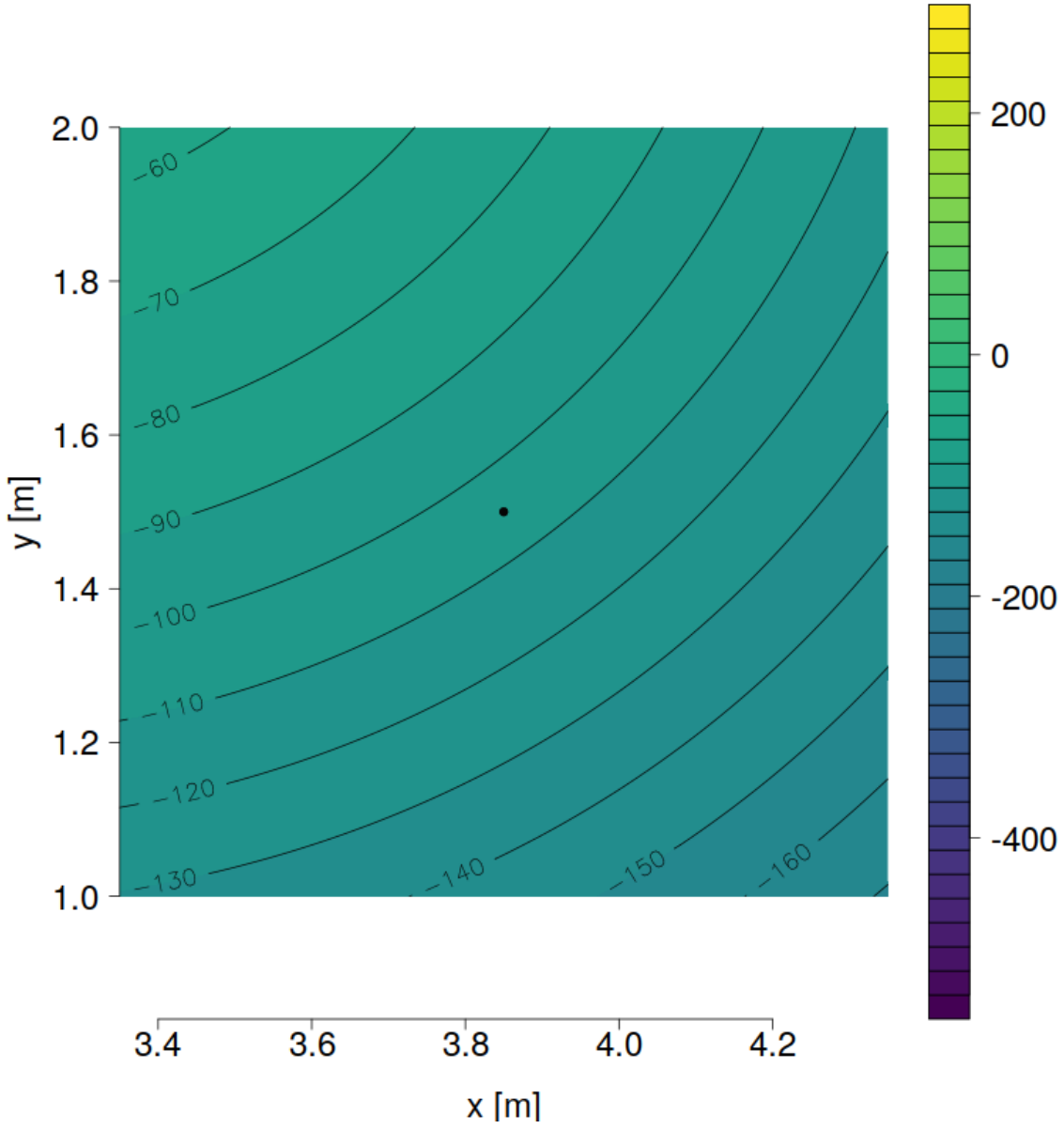

Figure 4.8: Gravity on surface of concrete pillar 3 at h_1(0.85 m). Gravity residuals in nm.s^{-2} relative to mean gravity on the surface of p_3. Gravity field caused by the mass of the pillars 0-4. Centres of gravimeter measurement locations are marked as points.

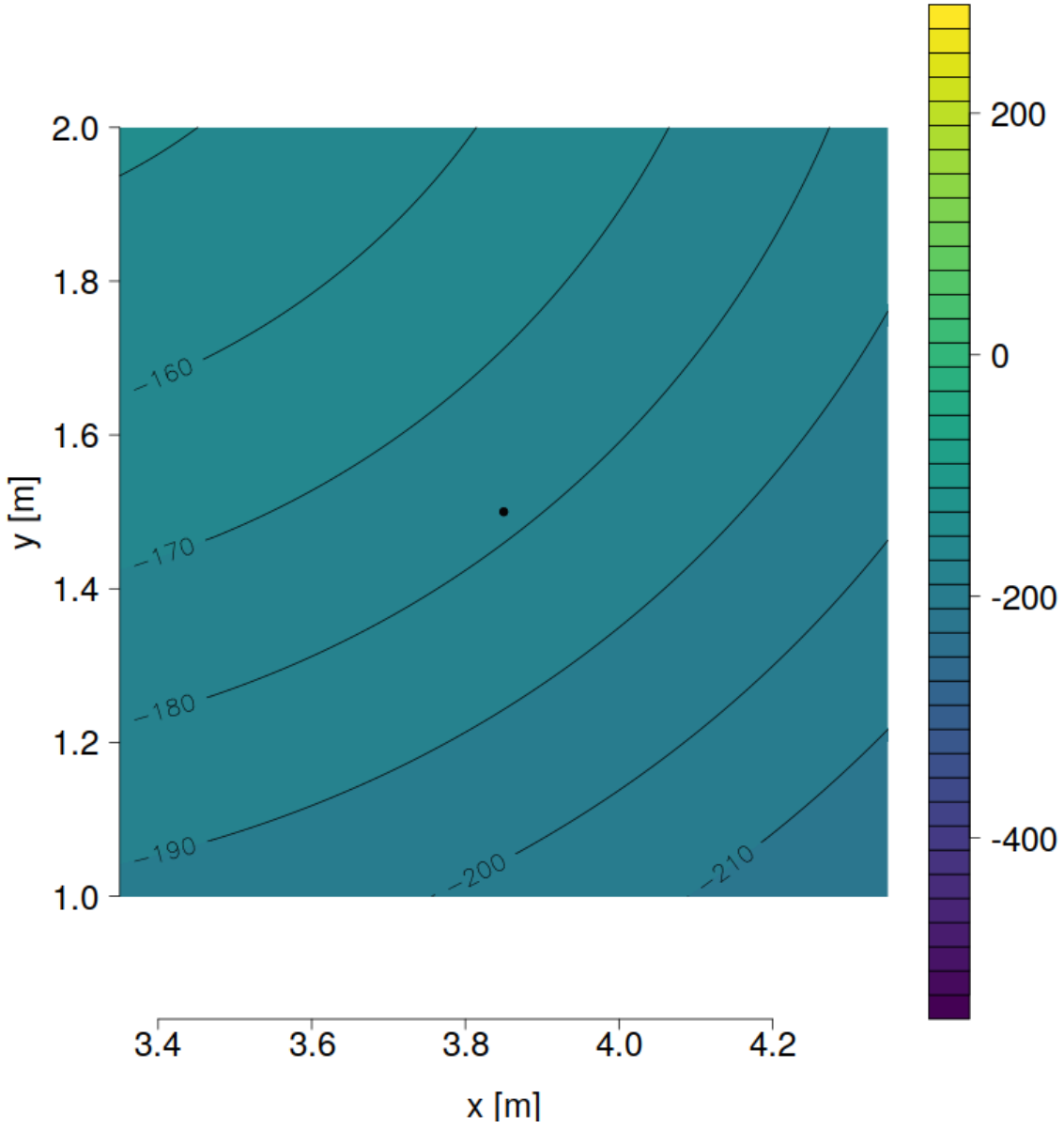

Figure 4.9: Gravity on surface of concrete pillar 3 at h_2 (1.436 m). Gravity residuals in nm.s^{-2} relative to mean gravity on the surface of p_3. Gravity field caused by the mass of the pillars 0-4. Centres of gravimeter measurement locations are marked as points.

Gravity at h_0 is highest for p_1, followed by p_2 and p_3. Simulated gravity varies by several tens of nm·s^{-2} across the pillar surface pf $p_{1,2}$. At height h_0 this results in a 12.3 nm·s^{-2} larger gravity value on measurement locations p_1 than on p_2. This difference declines with further height to 10 nm·s^{-2} at h_1 and 7.4 nm·s^{-2} on h_2. Differences between p_1 and p_3 reach 75.6 nm·s^{-2} at height h_0 and 63.3 nm·s^{-2}, respectively, between p_2 and also decline with height (Table 4.1). The expected gravity values at each measurement location and height, are summarised in Figure 4.11.

4.2.2.2.2 Comparison with measured gravity

The simulated horizontal gravity differences between pillars shown in Table 4.1 show negligible

Pillar	height	difference [nm.s^{-2}]
p_1 - p_2	h_0	12.3
p_1 - p_2	h_1	10.0
p_1 - p_2	h_2	7.2
p_1 - p_3	h_0	75.6
p_1 - p_3	h_1	41.0
p_1 - p_3	h_2	23.6
p_2 - p_3	h_0	63.3
p_2 - p_3	h_1	30.9
p_2 - p_3	h_2	16.2

Table 4.1: Differences in gravity between measurement locations on pillars p_1, p_2, p_3 at heights h_0, h_1, h_2.

differences between pillars p_1 and p_2 and stronger differences to p_3. Comparisons between gravity residuals measured with the AQG#A01 in September 2017 on the three pillars (Figure 4.10, Ménoret et al. (2018)) did not find significant differences between p_1 and p_2, gravity on p_3 is of the order of $\sim$ 115 nm·s^{-2} less than on p_1 and p_2. Based on all surveys obtained with the CG5#1151, the differences between pillars h_0 cannot be resolved due to the large scatter. The average difference $\Delta g_{p_{1,2,obs}}$ between pillar p_1 and p_2 at h_0 are 37 nm·s^{-2} with a standard deviation of 242 nm·s^{-2}. $\Delta g_{p_{1,3,obs}}$ is 20 $\pm$ 288 nm·s^{-2} and $\Delta g_{p_{2,3,obs}}$ -56 $\pm$ 186 nm·s^{-2}.

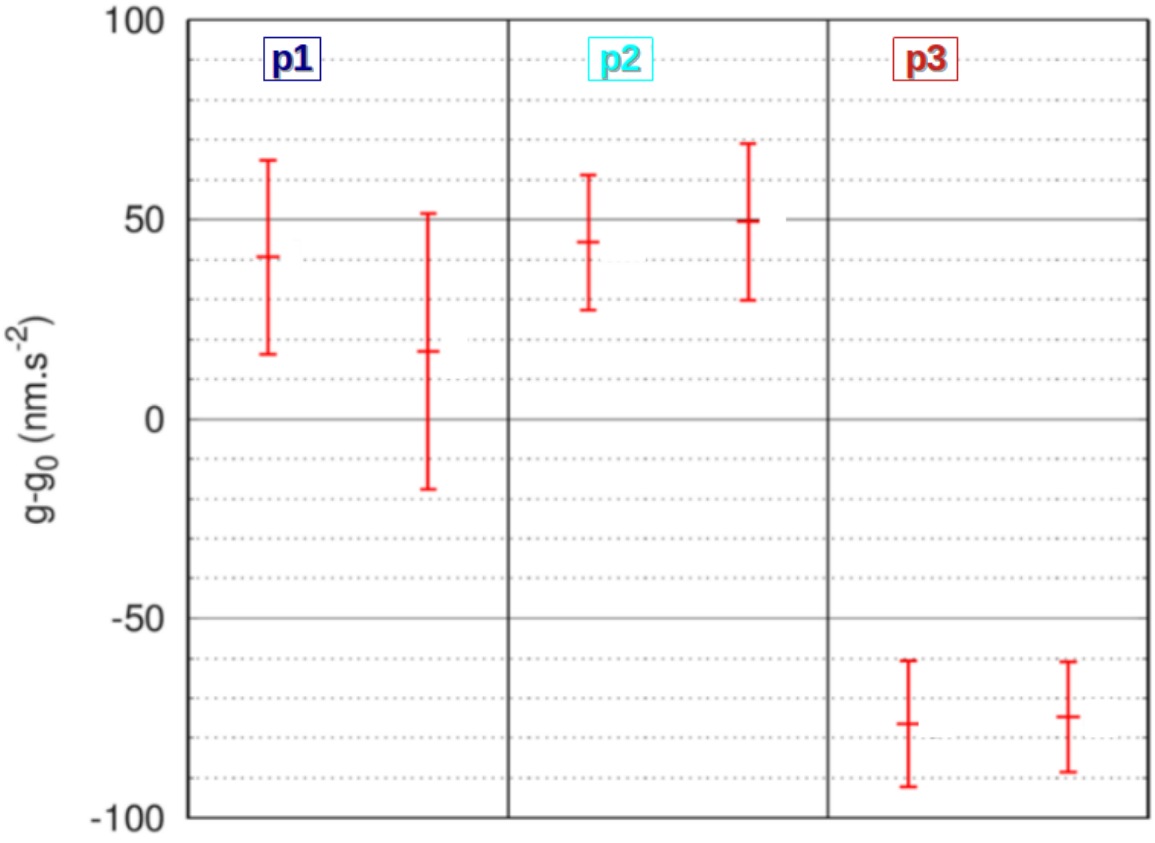

Figure 4.10: Gravity residuals in nm.s^{-2}, relative to the average g_0 of the six repeated measurements obtained in September 2017. Adapted, after Ménoret et al., 2018, p. 8.

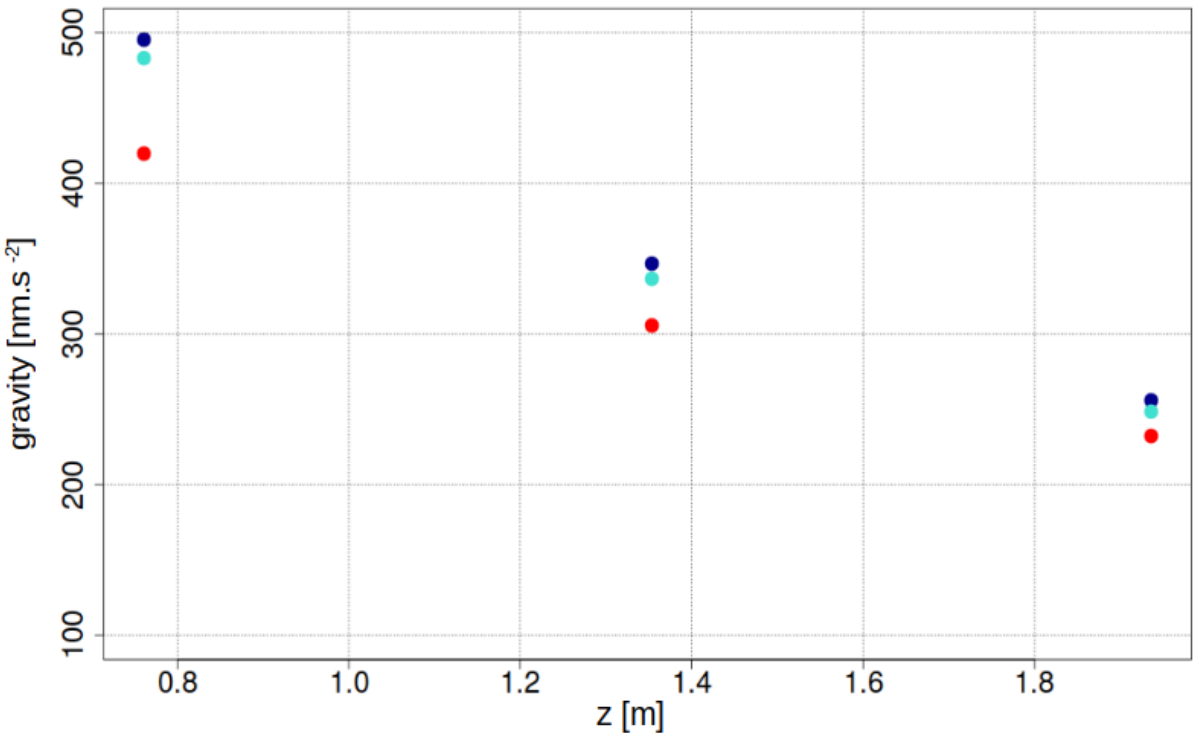

Figure 4.11: Expected gravity in nm.s^{-2} caused by the mass of the pillars at exact measurement locations for pillar p_1 (darkblue), p_2 (turquoise) and p_3 (red).

4.2.2.2.3 Simulated VGG

Based on the simulated gravity values per height, the corresponding VGG was calculated for the difference in gravity between h_1 - h_0, for the second part of the height difference h_2 - h_1 and for the entire length (h_2 - h_0). Additionally, the terrestrial gradient estimated for this site (-3.0895 kE) was added to the simulated VGG and plotted with estimated VGG measured on 19/04/2018 (Figure 4.12).

Comparison with VGG observations

The simulated VGG agree with the estimated VGG based on relative gravimetry for the $VGG_{h_2-h_0}$ based on the height difference h_2 - h_0. As can be noticed in Figure 4.11, the simulated gravity gradient between h_1 - h_0 is stronger than between h_2 - h_1. The concrete pillars cause a nonlinearity of the VGG with height, which can also be referred to as gravity curvature. While simulated gravity curvature differs negligibly between pillars p_1 and p_2, p_3 shows a different behaviour relatively to $p_{1,2}$.

Moreover, the measured VGG show a stronger curvature for the three pillars in both surveys. The model based on only the concrete pillar masses $VGG_{h_1-h_0,sim}$ is smaller than $VGG_{h_1-h_0,obs}$ and $VGG_{h_2-h_1,sim}$ larger than $VGG_{h_1-h_0,obs}$. Both offsets appear to compensate each other, as simulated and measured $VGG_{h_2-h_0}$ show negligible differences.

Based on these simulations, the curvature on both p_1 and p_2 between h_0 and h_{FG5} is -0.5 $E.cm^{-1}$ and -0.35 $E.cm^{-1}$ on p_3. As shown earlier in the comparison between measured and simulated VGG at different height segments (Figures 4.12), the observed VGG show that $VGG_{h_1-h_0,obs}$ could be several tens of E stronger than simulated. However, the experimental determination of the gravity curvature is restricted by the uncertainty of the relative gravimetry measurements.

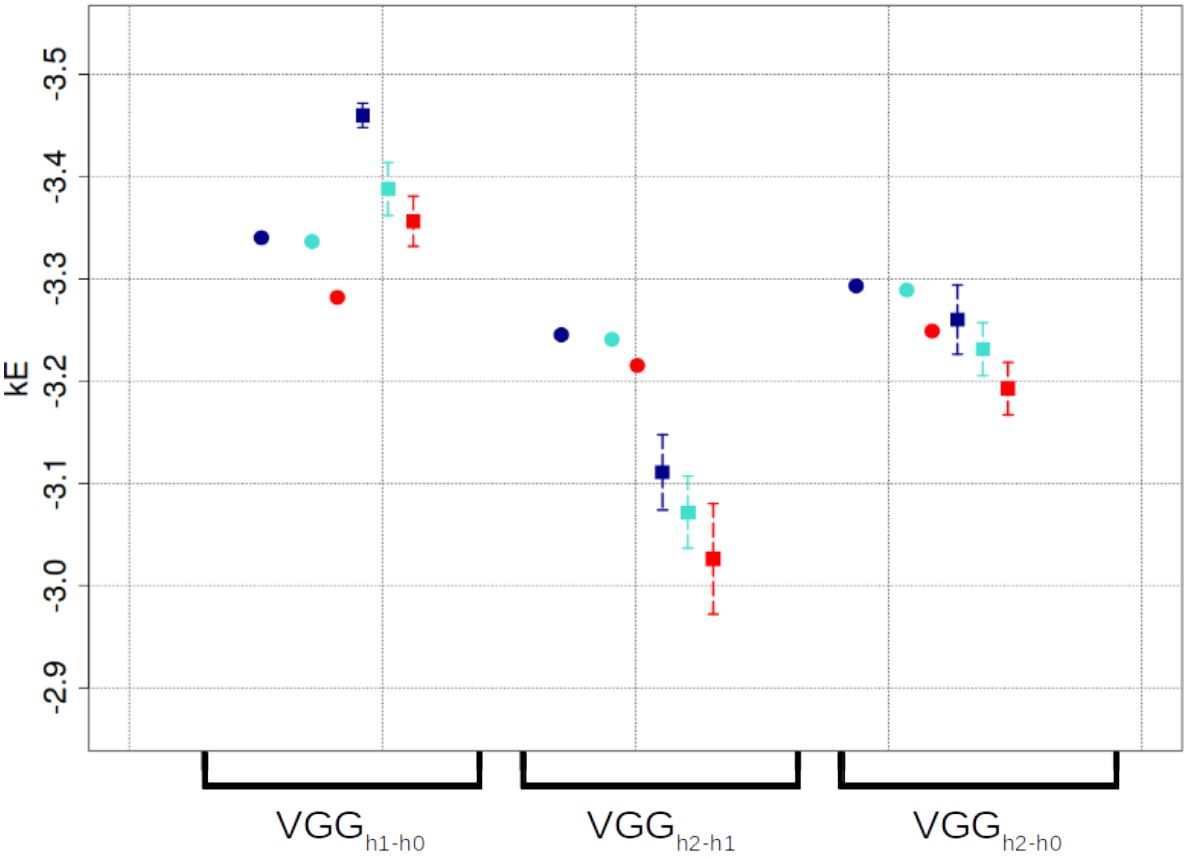

Figure 4.12: Dots: Expected VGG in kE caused by the mass of the pillars and terrestrial gravity gradient (-3.0895 kE) at exact measurement locations for pillars p_1 (darkblue), p_2 (turquoise) and p_3 (red). Squares: Estimated VGG based on measurements obtained on 19/04/2018 for for pillar p_1 (darkblue), p_2 (turquoise) and p_3 (red). Error bars refer to the standard deviation of the three measurement loops, before drift correction.

4.2.3 Impact of local gravitational field on VGG corrections during instrument intercomparison

The impact of the nonlinearity of the local gravitational field caused by the geometry of the pillar set-up in the observatory has implications for the VGG correction applied to gravimeters operating at different heights. If an instrument with a measurement height 60 cm is corrected for the VGG obtained from the difference between h_0 and h_2 ($VGG_{h_2-h_0}$) compared to the VGG obtained between h_0 and h_1 ($VGG_{h_1-h_0}$) several tens of nm·s^{-2} difference occurs. In Table 4.2 the gradient correction based on the VGG estimates on the two different height differences

Pillar	Δg corrected for $VGG_{h_1-h_0}$ [nm.s^{-2}]	Δg corrected for $VGG_{h_2-h_0}$ [nm.s^{-2}]
p_1	-148.6	-120.7
p_2	-146.3	-118.2
p_3	-114.0	-94.4

Table 4.2: Differences in gravity between measurement locations on pillars p_1, p_2, p_3 at heights h_0, h_1, h_2.

are shown for the three pillars. It shows that for pillar p_1, the gravity value corrected for $VGG_{h_1-h_0}$ would be 27.9 nm·s^{-2} higher than when corrected for $VGG_{h_2-h_0}$. For pillar p_2 and p_3, the difference would be 28.1 and 19.5 nm·s^{-2}, respectively. The assumption of a linear vertical gradient over the distance Δh_{0-2} would thus lead to an insufficient VGG correction and therefore to an underestimation of the measured gravity value. This underestimation varies between pillars. For gravimeters measuring at the same height of 60 cm height, a relatively small offset of 0.22 nm·s^{-2} is expected between pillars p_1 and p_2. The differences between p_1 and p_3 due to the difference in VGG correction error would be 8.3 nm·s^{-2} and 8.6 nm·s^{-2} between p_2 and p_3.

The gravity differences between pillars $p_{1,2}$ and p_3 resulting from the concrete pillars masses earlier shown in Table 4.1 would have to be reduced by the mentioned off-sets of the applied VGG corrections.

4.2.3.1 Considerations for the comparison between AQG#A01, AQG#B01, and FG5#228

The earlier discussed heights h_0, h_1 and h_2 were defined by the available tripods and the measurement height of the relative gravimeters. In the following, the simulated gravitational field caused by the four concrete pillars is analysed at the measurement heights and locations used for the AQG#B01 and FG5#228. The observed differences between FG5#228 and AQG#B01 have been found to be on average 110 $\pm$ 30 nm·s^{-2} (Cooke, Champollion, and Moigne (2020)). How does the simulated nonlinearity of the gravitational field relate to the measurements?

In the context of the gravimeter characterisation the FG5#228 was operated at a measurement height of $\sim$ 121.7 m (h_{FG5}) on pillar p_1, the AQG#B01 at $\sim$ 0.65 m (h_{AQG-B}) on pillar p_2.

The FG5#228 and AQG#B01 measurement points differ thus by their location on the pillar and by their height. Simulated gravity at location p_1 at h_{FG5} is lower than on p_2 at h_{AQG_B}. The net difference between simulated gravity on p_2 at h_{AQG_A} and simulated gravity on p_1 at h_{FG5} is 94.2 nm·s^{-2}.

Firstly, the horizontal difference at height h_{AQG_B} between pillar location p_1 and p_2 can be

corrected for, namely by 12.5 nm·s^{-2}. Secondly, the vertical gravity gradient correction is applied. There are the two options of either correcting for a VGG adequate for the measurement height ($VGG_{h_{AQG_B}-h_0,sim}$) or for the VGG averaged over the height of the second instrument ($VGG_{h_{FG5}-h_0,sim}$), respectively. When using $VGG_{h_{FG5}-h_0}$ an off-set of 40.2 nm·s^{-2} remains, the gravity value is underestimated due to an insufficient VGG correction. In contrast, $VGG_{h_{AQG_B}-h_0,sim}$ leads to a complete correction of the off-set.

This means that the error for gravity on p_2 at h_{AQG_B} caused by neglecting the curvature and applying the same VGG correction ($VGG_{h_{FG5}-h_0,sim}$) to both locations and heights, is 40.2 nm·s^{-2}. Additionally, the simulated horizontal difference in gravity between p_1 and p_2 at h_{AQG_B} is 12.5 nm·s^{-2}. When relating these simulated results to the practical measurements one can conclude that gravity observations on p_2 at h_{AQG_B} would appear by 52.7 nm·s^{-2} smaller than observations on p_1 at h_{FG5}, as a combined effect of the vertical and horizontal off-sets.

4.2.3.2 Conclusion

The calculations presented in this section aim at giving an order of magnitude of the error introduced by the nonlinearity of the gravitational field caused by the size, location, and mass of the concrete pillars. Pillar geometry was measured at cm precision and the density distribution of the concrete was assumed to be homogeneous. Smaller, lightweight pillars in a cylinder shape at the outer edges of the building were not considered in this analysis. The simulated VGG and gravity curvature only take into account the masses of the four concrete pillars. The influence of the surrounding bedrock heterogeneity may add uncertainty. The suggested corrections are therefore not exhaustive and require to be refined once more frequent, higher precision VGG measurements are available in order to map the observatory's gravity field thoroughly. The results highlight the necessity to adequately characterise and map the gravity gradients in the building prior to instrument comparison. In observatories where concrete pillars are integrated into the surrounding bedrock or building foundation, the density contrast between concrete and surrounding is negligible and the gravity field would be expected to be more homogeneous.

4.2.4 VGG sensitivity and simulations

The results of the geostatistical simulations show that a vast range of gravity and vertical gravity gradients can emerge from subsurface heterogeneity. We examined a limited amount of realisations that fulfill the aim of the simulations to generate subsurface porosity distributions that could be responsible for detectable vertical gravity gradient changes and differences between pillars.

Generally speaking, the resolution of a mass anomaly deductible from VGG observations is

defined by the interaction of the variables

- height of the tripod used for VGG estimation
- distance between measurement locations (distance between the concrete pillars)
- distance between observation and the heterogeneity of interest
- characteristics of the heterogeneity (spatial extension, shape, density contrast at the borders, mass difference)

Ultimately, the resolution of the VGG is furthermore limited by the uncertainty of the method and the sensitivity of the instruments in use.

Gravity caused by a Bouguer plate is by definition independent of the measurement position laterally and vertically. The VGG above a Bouguer plate is dependent on the vertical distance z and independent of the location in x and y. In the following, two scenarios are discussed that do not obey the Bouguer plate assumption. Firstly, the simplest aberration of a Bouguer slab, a truncated or semi-infinite Bouguer slab is investigated. The expected gravity, VGG, and the difference between VGG at a horizontal distance (differential VGG) of a semi-infinite Bouguer slab are evaluated. Subsequently, a 3D-heterogeneity pattern is simplified based on cube-shaped areas of varying soil saturation. Equivalently, these mass distributions are analysed regarding the expected gravity, VGG, and differential VGG.

4.2.4.0.1 Semi-infinite Bouguer slab

A 10 m and a 50 m thick water-saturated layers of 20 % porosity are modelled as a semi-infinite Bouguer slab. The expected change in gravity caused by an semi-infinite Bouguer slab of a water column of a thickness H can be calculated as:

$$\delta g_{B_{semi-infinite}} = 2\rho GH(\frac{\pi}{2} + \tan^{-1}(\frac{x}{z})), \tag{33}$$

with G referring to the gravitational constant, ρ to the density of water, z is the vertical and x the horizontal distance from the beginning of the slab at $x = 0$ in direction of positive x (Telford, Geldart, and Sheriff (1990)). Vertical gravity gradients were calculated linearly from gravity simulated on two measurement heights (0.5 and 1.675 m), which were chosen in reference to the measurement heights on the concrete pillars in the Larzac observatory. Furthermore, the difference between VGG at horizontal distance Δx_{p2-p3} (1.7 m, distances in Figure 4.16) was added to the plot. Figure 4.13 shows the change in gravity as a function of horizontal distance for a slab of (1) 10 m and (2) 50 m (2) thickness. A strong increase in gravity is expected at the edge of the semi-infinite slab.

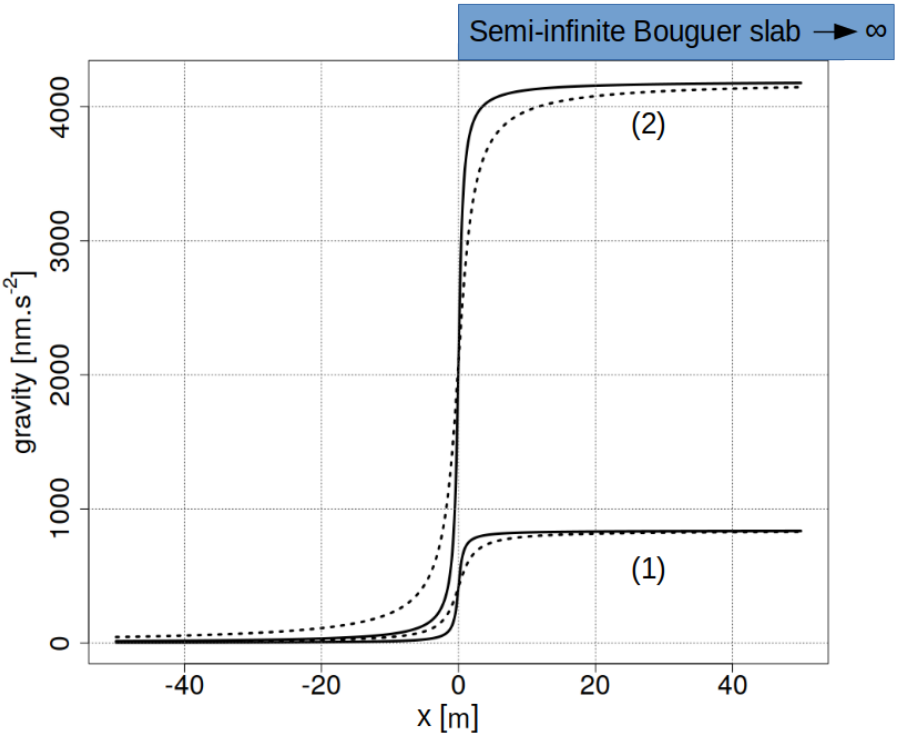

Figure 4.13: Simulated gravity of a semi-infinite Bouguer slab in nm.s^{-2} on 0.5 m (black, dashed) and 1.675 m height (black, continuous). (1) Slab of 10 m thickness. (2) Slab of 50 m thickness. Distance in meter from slab starting at x = 0 m. Density: 200 kg.m^{-3}.

Figures 4.14 and 4.15 show the corresponding vertical gravity gradients (red line) between 0.5 m and 1.675 m height for a 10 m and a 50 m thick slab, respectively. Moreover, the difference between VGG at 1.7 m horizontal distance ($VGG_{\Delta x=1.7m}$, light blue line) is shown. VGG and $VGG_{\Delta x=1.7m}$ changes around x = 0 m show a large amplitude and changes in sign.

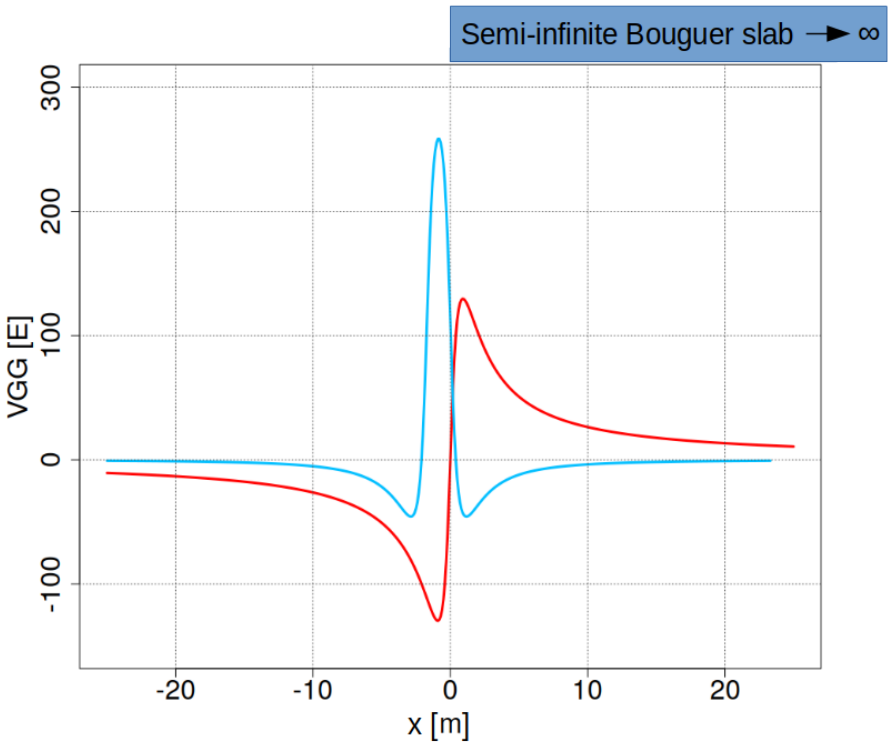

Figure 4.14: Simulated vertical gravity gradient of a semi-infinite Bouguer slab in nm.s^{-2} between 0.5 m and 1.675 m height (red). Difference in E between VGG at 1.7 m horizontal distance (light blue). Slab of 10 m thickness. Distance in meter from slab starting at x = 0 m. Density: 200 kg.m^{-3}.

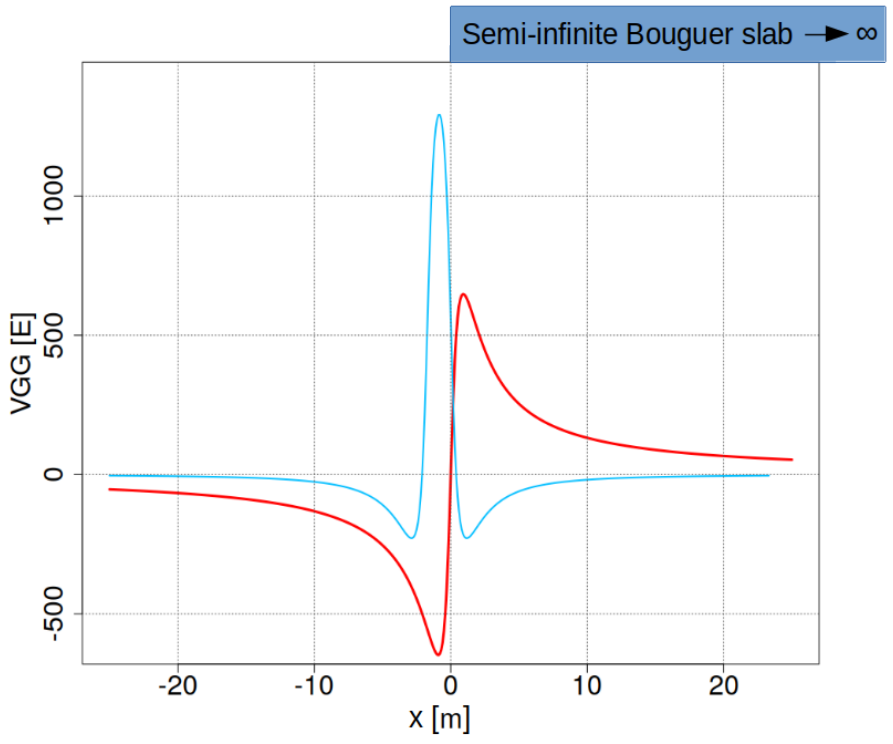

Figure 4.15: Simulated vertical gravity gradient of a semi-infinite Bouguer slab in nm.s^{-2} between 0.5 m and 1.675 m height (red). Difference in E between VGG at 1.7 m horizontal distance (light blue). Slab of 50 m thickness. Distance in meter from slab starting at x = 0 m. Density: 200 kg.m^{-3}.

4.2.4.0.2 Heterogeneity pattern

To illustrate the change of gravity and VGG with distance to a density heterogeneity, this relation is simulated as calculating gravity and VGG along a transect above a simplified cube pattern. The two directions are shown in Figure 4.17. Panel (a) depicts a straight and panel (b) a diagonal transect. As before, vertical gravity gradients were calculated linearly from gravity simulated on two measurement heights (0.5 and 1.675 m). The density contrast is set to 200 $kg \cdot m^{-3}$, which simulates water saturated cubes of 20 % porosity for every alternating cube, the empty cubes are set to zero water content. In the following, this is shown for 10 and 50 m cube sizes, each for straight and diagonal transects, respectively. For both cube sizes, the whole model domain has a an surface area of 500 × 500 m and is 50 m deep. This leads to 100 cubes of 50 m edge length and 12500 cubes of 10 m edge length.

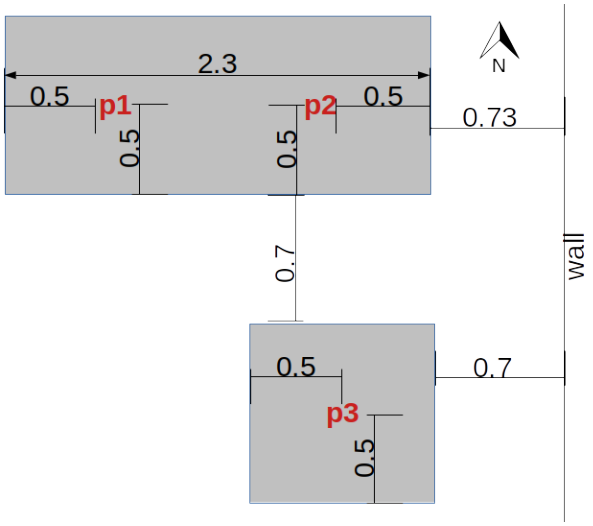

Figure 4.16: Horizontal distances between pillar measurement locations p_1, p_2 and p_3 (red). Distances in m. $x_{p1-p2} = 1.3$ m, $x_{p1-p3} = 2.158$ m, $x_{p2-p3} = 1.7$ m

A heterogeneity pattern of 10 m resolution probed along the centre of the surface squares (Figure 4.18) shows the highest gravity amplitudes in the centres and switches signs at the transition between cubes, as does the VGG signal. A diagonal transect yields a maximum of gravity and VGG at the centre of the square surface area and reduces to zero at the point of transition between areas, due to compensation of positive and negative anomalies in the symmetrical set-up (Figure 4.19). Maximal gravity signals of 90 $nm \cdot s^{-2}$ at 0.5 m height appear in the centres. The relative change in gravity and gradients can provide information on the distance to the heterogeneity. As can be seen in Figure 4.18, still relative small gravity changes accompanied by a change in VGG would be characteristic for a gravity and VGG monitoring approaching and crossing a density contrast edge. These patterns can also be interpreted from the view of a spatially stationary gravity and VGG measurement and moving mass heterogeneity around it,

as infiltration in heterogeneous media or a pumping experiment.

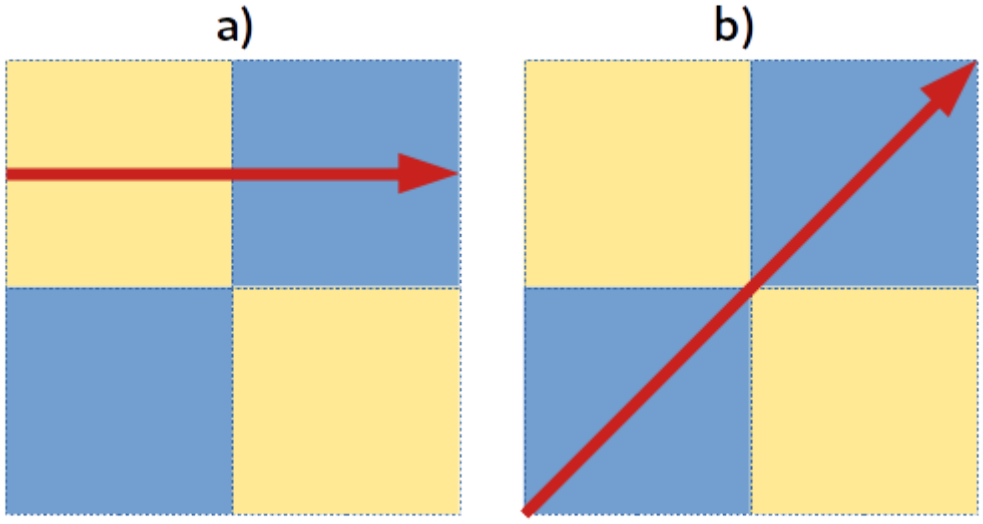

Figure 4.17: Panel (a): Transect crossing through the centre of each surface square of a 3D cubic heterogeneity. Panel (b): Diagonal transect.

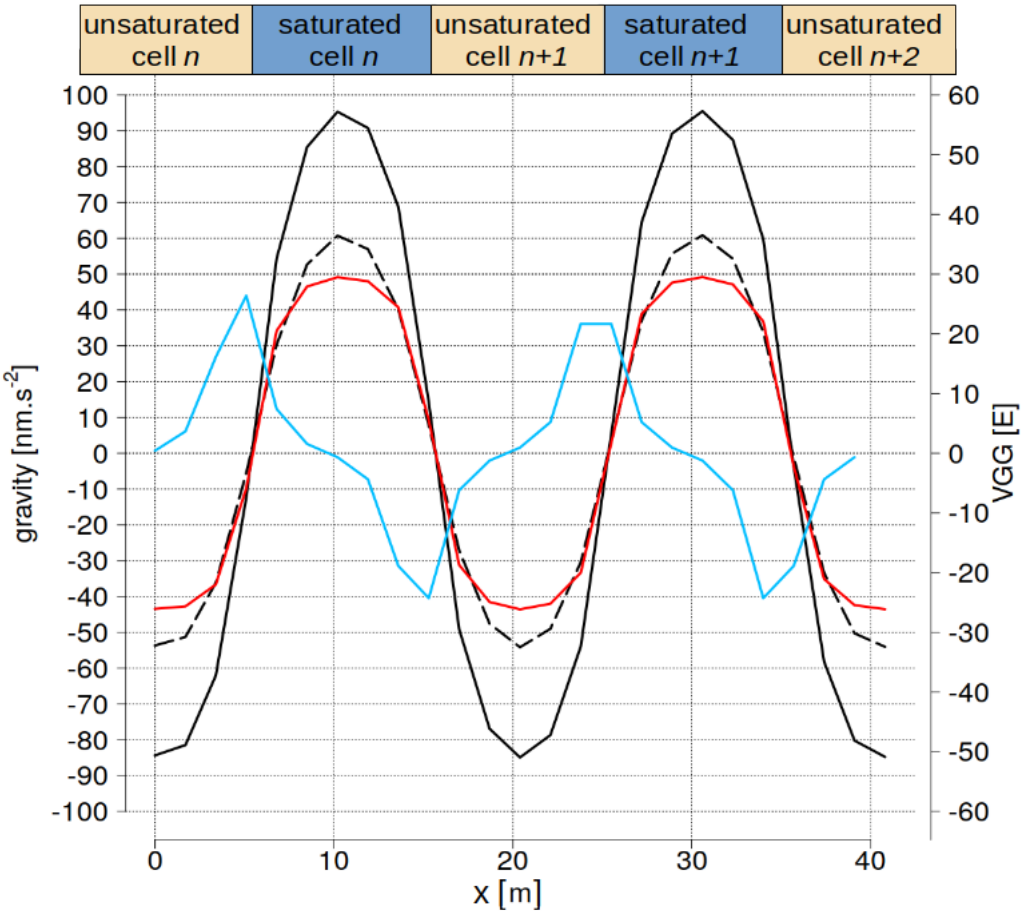

Figure 4.18: Simulation of a 3D cubic heterogeneity pattern of 10 m edge length, respectively, with 200 kg.m^{-3} density. Gravity in nm.s^{-2} on 0.5 m (black, dashed) and 1.675 m height (black, continuous). Vertical gravity gradient as the difference between both heights in E (red). Difference in E between VGG at 1.7 m horizontal distance (light blue). Gravity and VGG along a transect crossing through the centre of each surface square. Calculations at 1.7 m intervals.

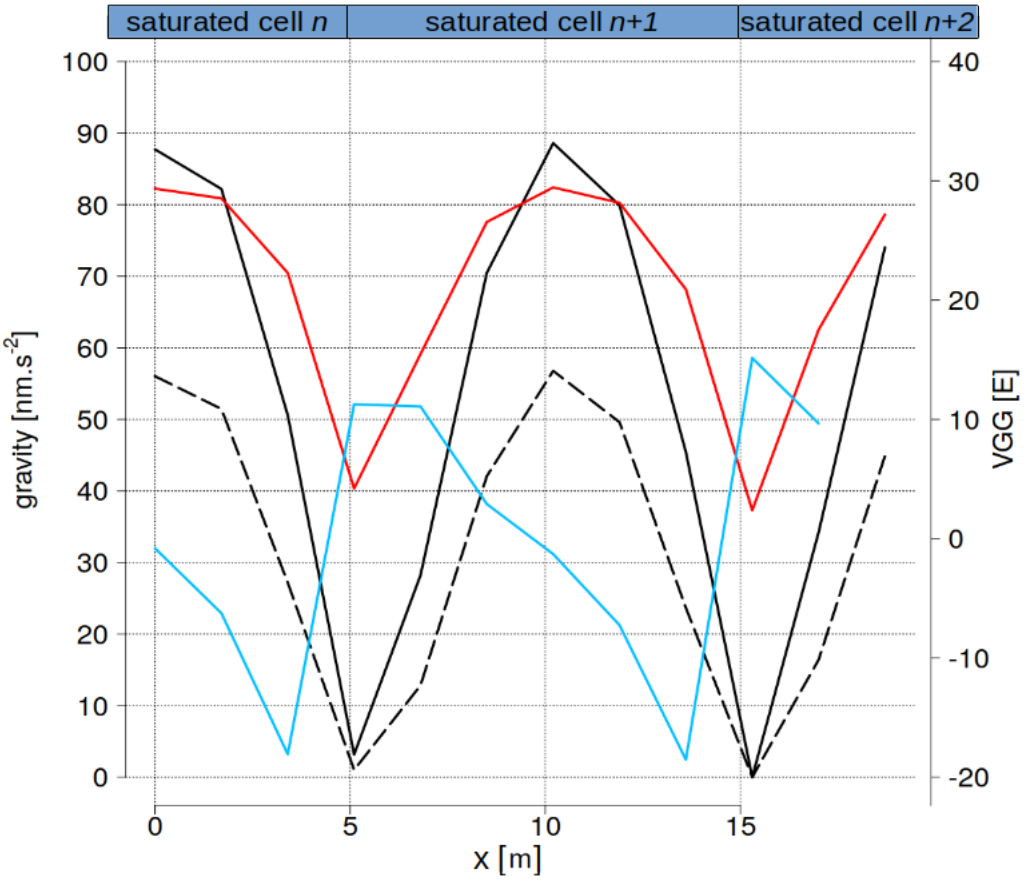

Figure 4.19: Simulation of a 3D cubic heterogeneity pattern of 10 m edge length, respectively, with 200 kg.m^{-3} density. Gravity in nm.s^{-2} on 0.5 m (black, dashed) and 1.675 m height (black, continuous). Vertical gravity gradient as the difference between both heights in E (red). Difference in E between VGG at 1.7 m horizontal distance (light blue). Gravity and VGG along a transect crossing the surface pattern diagonally. Calculations at 1.7 m intervals.

A corresponding change of sign dependent on the distance to the cube edges is visible for heterogeneity patterns of 50 m in Figures 4.20 and 4.21. Larger structures (Figures 4.20 and 4.21) lead to a stronger change in gravity. In the centres gravity increases by more than 500 nm·s^{-2} compared to the edges. VGG measurements at several locations close to the centre of the anomaly would show relatively small differences, as the change in VGG decreases and forms a stable plateau (especially visible in Figure 4.21). Gravity changes decrease towards the centres of the anomaly. However, their order of magnitude stays measurable. For example between 10 to 20 m (Figure 4.21) distance from the edge of the anomaly, the expected gravity change is $\sim$ 200 nm·s^{-2} for a 50 m structure, whereas VGG change within the detection limit ($<$ 20 E). $\delta VGG_{\Delta x=1.7m}$ of the structures of 10 and 50 m characteristic length, respectively, show an amplitude of 20 to 30 E for the two transect probing directions.

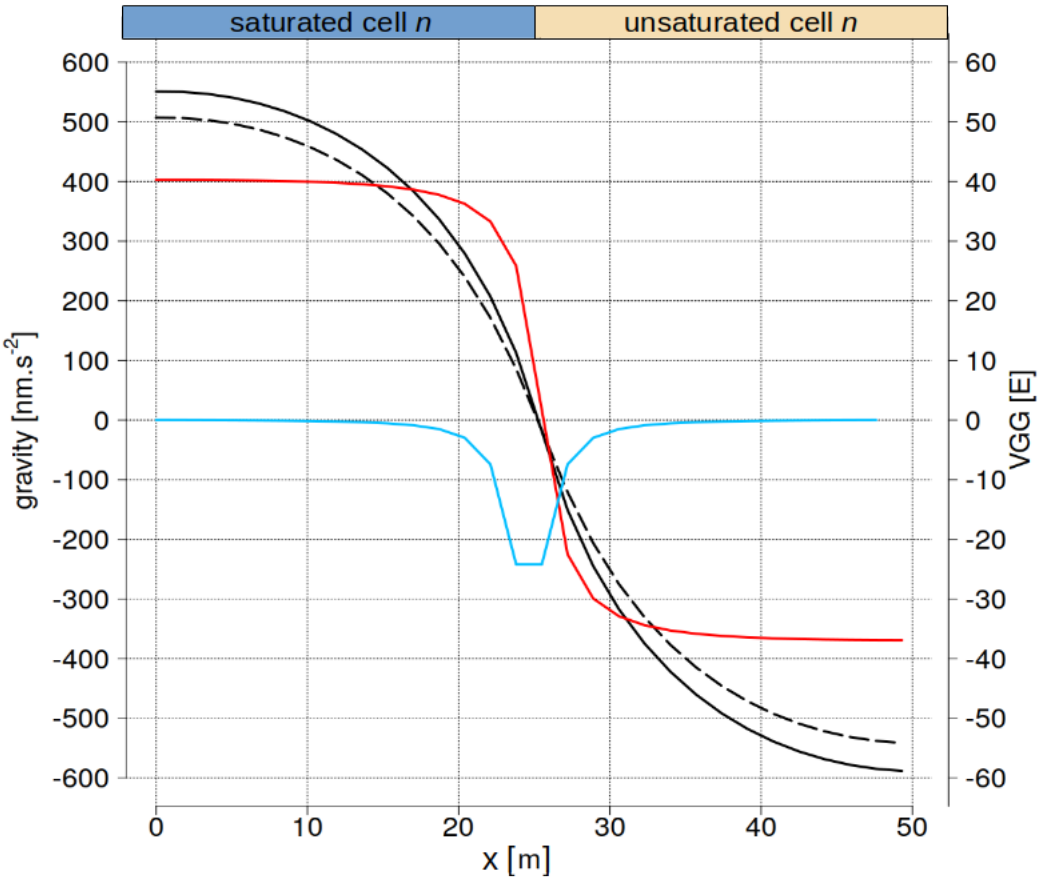

Figure 4.20: Simulation of a 3D cubic heterogeneity pattern of 50 m edge length, respectively, with 200 kg.m^{-3} density. Gravity in nm.s^{-2} on 0.5 m (black, dashed) and 1.675 m height (black, continuous). Vertical gravity gradient as the difference between both heights in E (red). Difference in E between VGG at 1.7 m horizontal distance (light blue). Gravity and VGG along a transect crossing through the centre of each surface square.

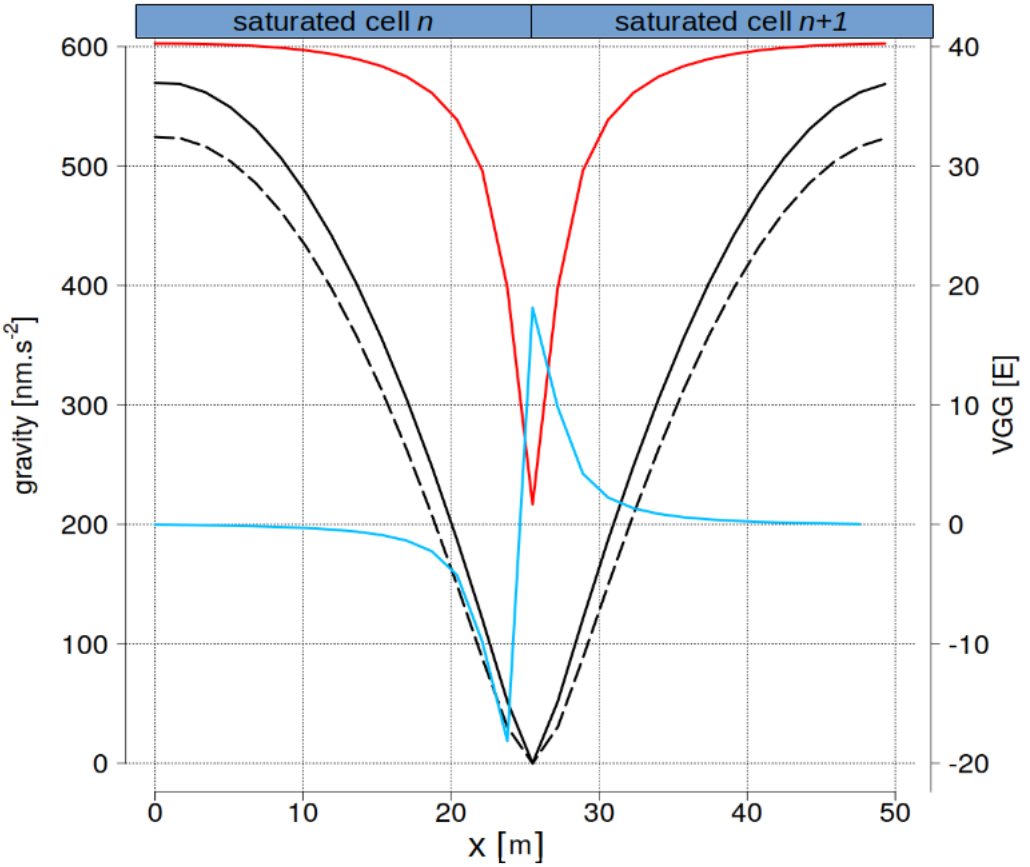

Figure 4.21: Simulation of a 3D cubic heterogeneity pattern of 50 m edge length, respectively, with 200 kg.m^{-3} density. Gravity in nm.s^{-2} on 0.5 m (black, dashed) and 1.675 m height (black, continuous). Vertical gravity gradient as the difference between both heights in E (red). Difference in E between VGG at 1.7 m horizontal distance (light blue). Gravity and VGG along a transect crossing the surface pattern diagonally.

4.2.4.0.3 Intermediate conclusion

For the given choice of porosity, saturation, and characteristic lengths, the simulated semi-infinite slab and the local heterogeneity pattern can be distinguished based on the larger amplitudes of VGG and gravity change. At the edge of the slab, the change in sign of the VGG change (also visible in $VGG_{\Delta x=1.7m}$) does not occur in this way at the edge of the saturated cubes. The semi-infinite slab is characterised by an absence of VGG or gravity change a greater horizontal distances. In view of the differential VGG observations ($\sim$ 40 E difference between $VGG_{p_{1,2}}$ and VGG_{p_3}), the heterogeneity pattern produces similar values close to the edge of a heterogeneity. VGG observations at additional locations in x-direction are required to constrain the subsurface model even further.

4.2.4.1 Fractures and cavities

Most of the simulations that emerged from the geostatistical stochastic simulation presented in the publication in preparation and that show detectable VGG differences between pillars (>

20 E) were based on models of 10 m and 20 m correlation length. Spatial heterogeneities of 10 m characteristic length are less limited by the criterion of small gravity changes, whereas larger structures only show small gravity but important VGG changes at a smaller range of possible distances from the measurement location. At the Larzac site, several features show characteristic lengths between 10 and 50 m. Three boreholes at approximately 20 m distance from the building at 20 and 50 m depth, respectively. The impact of water content changes at these locations is investigated in section 4.2.5. Only one of the final eight simulated realisation is based on 50 m correlation length (Gaussian). This case was investigated for any relation to known geological structures.

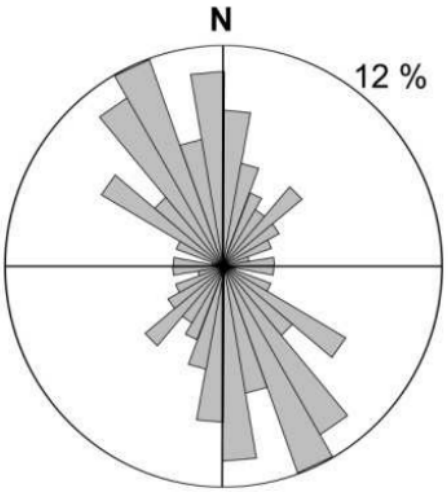

Figure 4.22: Rosette of fracture directions at the Larzac observatory site (Deville, 2013, adapted from Gerbaux, 2009).

Figure 4.22 shows the anisotropy at the Larzac site expressed in fracture direction distribution. Fracture orientation was assessed from surface observations (Gerbaux (2009)). Karst cavities tend to be aligned with fracturation observable on the surface (e.g. Chalikakis et al. (2011)). A cavity ('Cavité aven des dolines', Karst3D Team (2019)) of about 100 m maximal depth and one km length is located beneath the site and is accessible from the surface at $\sim$ 50 m SE of the observatory building. The 3D map of the cavity has been compared to the eight selected simulation realisations and did not show spatial resemblance.

The simulation based on a Gaussian variogram model with 50 m correlation length is depicted with the 2D-geometry of the cave system, both on the surface (Figure 4.23) and at 100 m depth (Figure 4.24). However, as the spatial sensitivity of the VGG is greatly reduced, the configuration at 100 m depth in Figure 4.24 is not constraint by VGG information. The cavity and the porosity pattern on the surface show comparable orientation angles at least at some segments, especially at the centre of the plot. Also, the forking of the cavity aligns with changes in porosity on the surface. However, other, more dominant orientations are visible that are

orthogonal to the direction of the cavity.

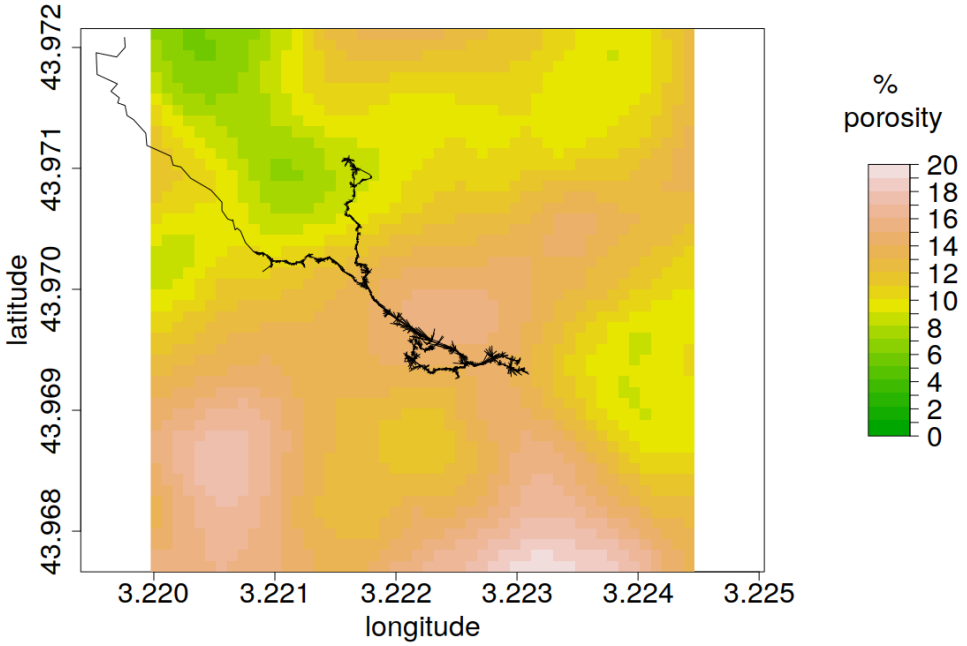

Figure 4.23: Simulation Gaussian (50 m) nr. 251 surface. Cavity 'Cavité aven des dolines' (Karst3D, 2019)

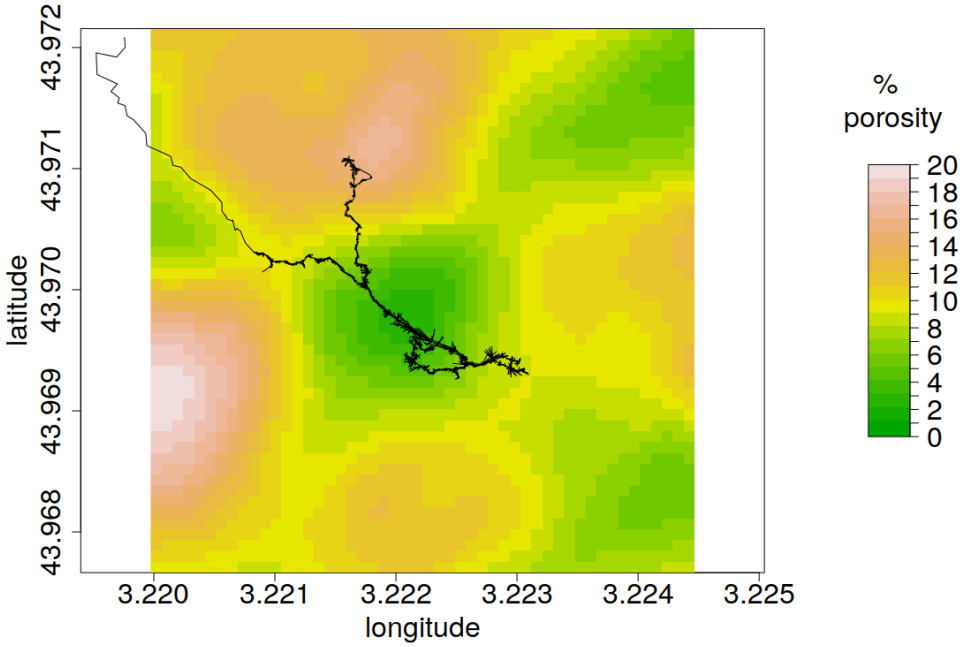

Figure 4.24: Simulation Gaussian (50 m) nr. 251 at 100 m depth. Cavity 'Cavité aven des dolines' (Karst3D, 2019)

Apparent spatial correlation at a greater distance from the observatory is likely to have emerged randomly as they are less constrained by gravity and VGG residuals. Surface depressions on the

Larzac plateau can hint at weathered areas of thus higher porosity than the bedrock. This for example the case in the area of the sinkhole that serves as an entrance to the cavity (at $\sim$ 50 m SE of the building). Topography (Figure 4.25) and simulated surface porosity distribution do not show resemblance.

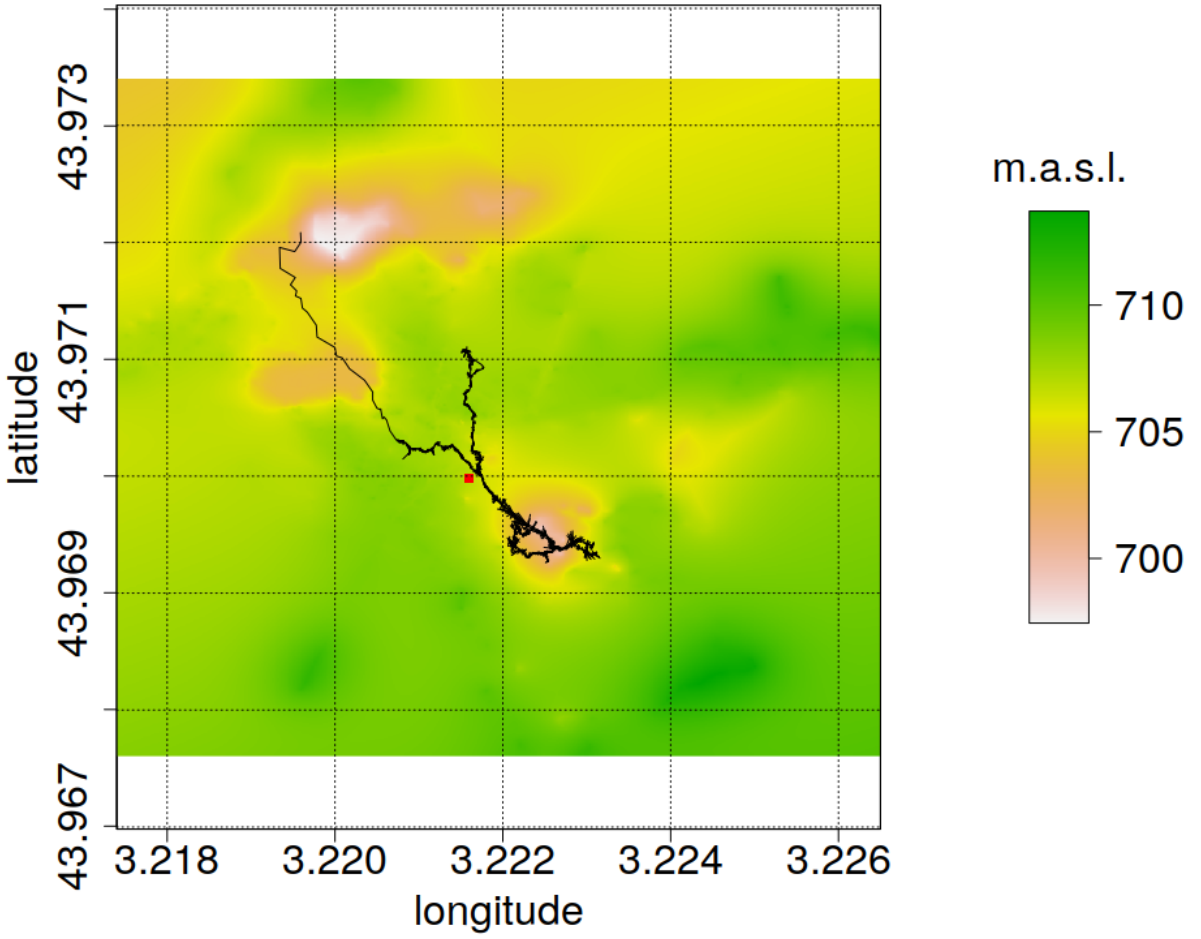

Figure 4.25: Topography surrounding the Larzac observatory building (red square) in m.a.s.l. The 2D-geometry of the cavity is laid upon the map (black).

4.2.5 Local storage near boreholes

Closer to the observatory, three boreholes within 20 m distance, two at 20 m (SD1, SD2), and one at 50 m depth (SC1) show several meters of yearly water level variations. Figure 4.26 shows the residuals between VGG on p_3 and the annual mean of the VGG on p_1 and p_2 as well water levels for the boreholes SD1, SD2 at 20 m depth, and SC1 at 50 m depth. Water levels for SC1 can vary almost 20 m during one year, SD1 and SD2 show variations of up to 10 m. Water level peaks in SC1 arrive later than for the two shallower wells. For a given point in time, low water levels in SC1 and high levels in SD1/SD2 can occur and vice versa. In spring 2018 (Figure 4.26) water levels in SD2 decline at a faster rate than in SD1. SD2 falls dry in July, SC1 starts to decline later.

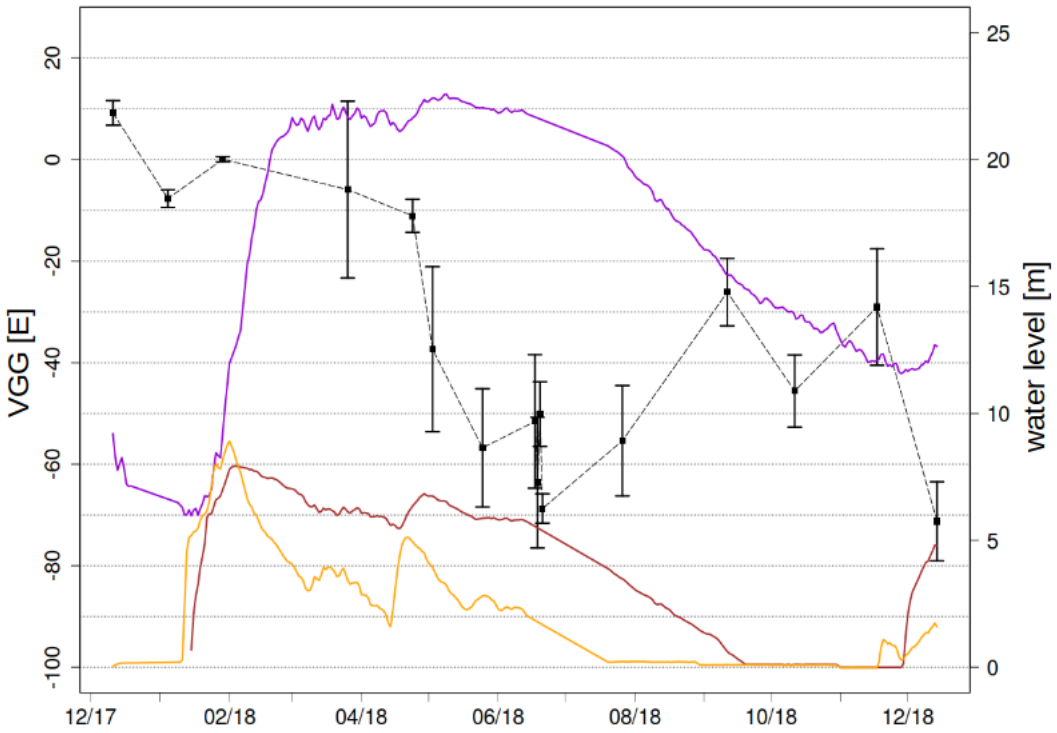

Figure 4.26: Residuals between the estimated vertical gravity gradients (VGG) in E for pillar p_3 (black) and the annual mean of the estimated VGG on pillars p_1 and p_2. Water level time series in m for boreholes SD1 (brown), SD2 (orange) and SC1 (purple) the Larzac observatory, 2017-2019.

The cause for the observed shifted temporal dynamics of the storage supplying the boreholes and their degree of connectivity is under investigation. Fores (2016) discuss the possibility of cross-cutting fractures that connect different storages. Despite their proximity, a slug test suggests that a direct hydraulic connection between SC1 and SD1 (H. Jourde, personal communication) is unlikely, which could suggest independent small storage entities, as shown in Figure 4.27.

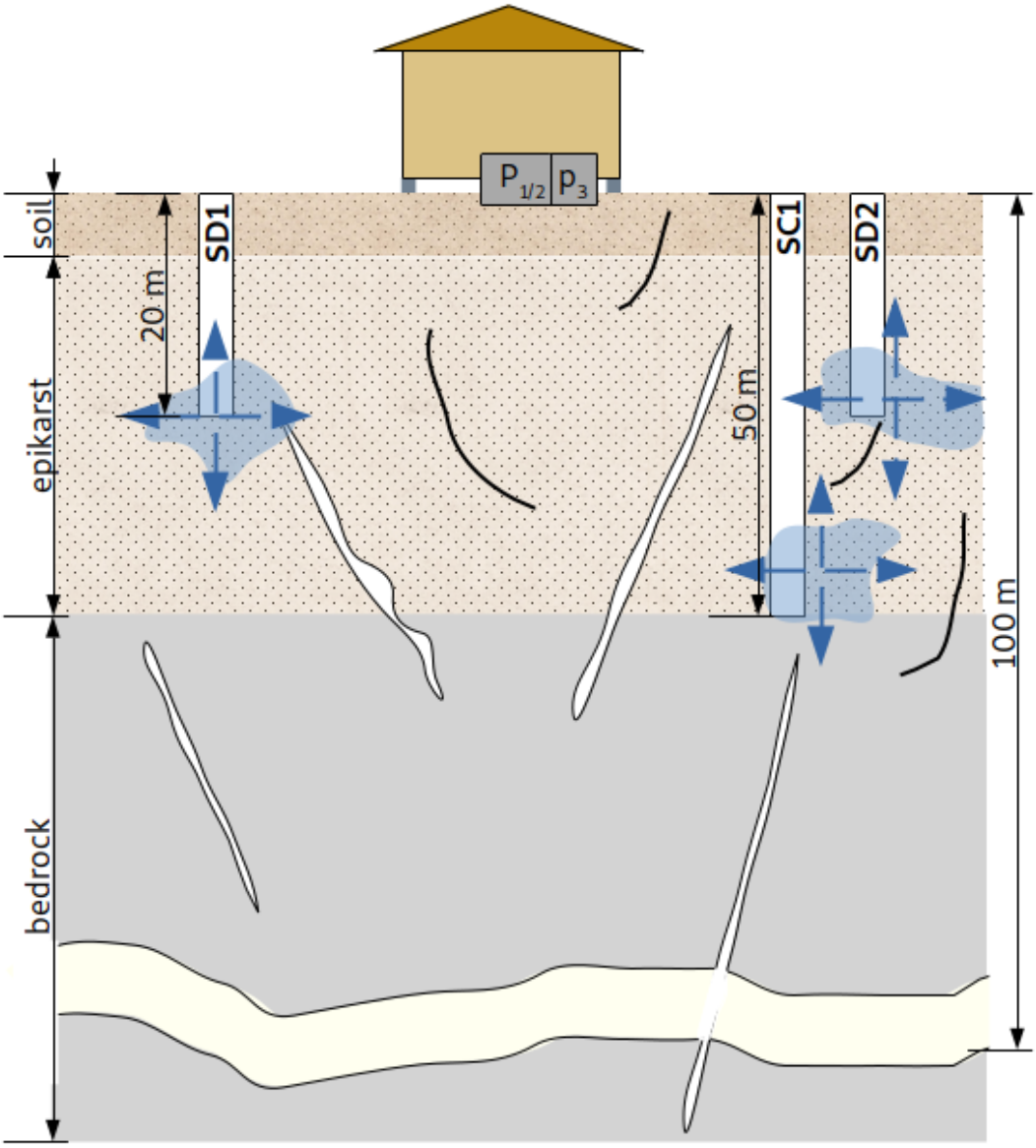

Figure 4.27: Conceptual model chart of observatory and potential local heterogenous soil water storages that supply the boreholes SC1 at 50 m, and SD1/SD2 at 20 m depth. Pillar $p_{1,2}$ is behind p_3

The relative VGG variations on p_3 suggest a negative correlation between borehole water levels and gravity gradient changes, as discussed in the publication in preparation. The cross-correlations calculated between the borehole water height time series for SD2, SD1, and SC1 and the estimated VGG on pillars 1 to 3 are shown in Figure 4.28. VGG on p_1 and p_2 show insignificant or at most weak cross-correlations with water levels in SD1, SD2, and SC1. However, VGG on p_2 show a cross-correlation of -0.32 for 3 days lag for SD1. VGG on p_3 show a stronger cross-correlation of 0.46 with SD1 for -6 days time lag, -0.38 with SD2 for three days lag and -0.29 with SC1 for two days lag. This analysis remains exploratory as the number of estimated VGG data points is too small for a robust analysis of cross-correlation.

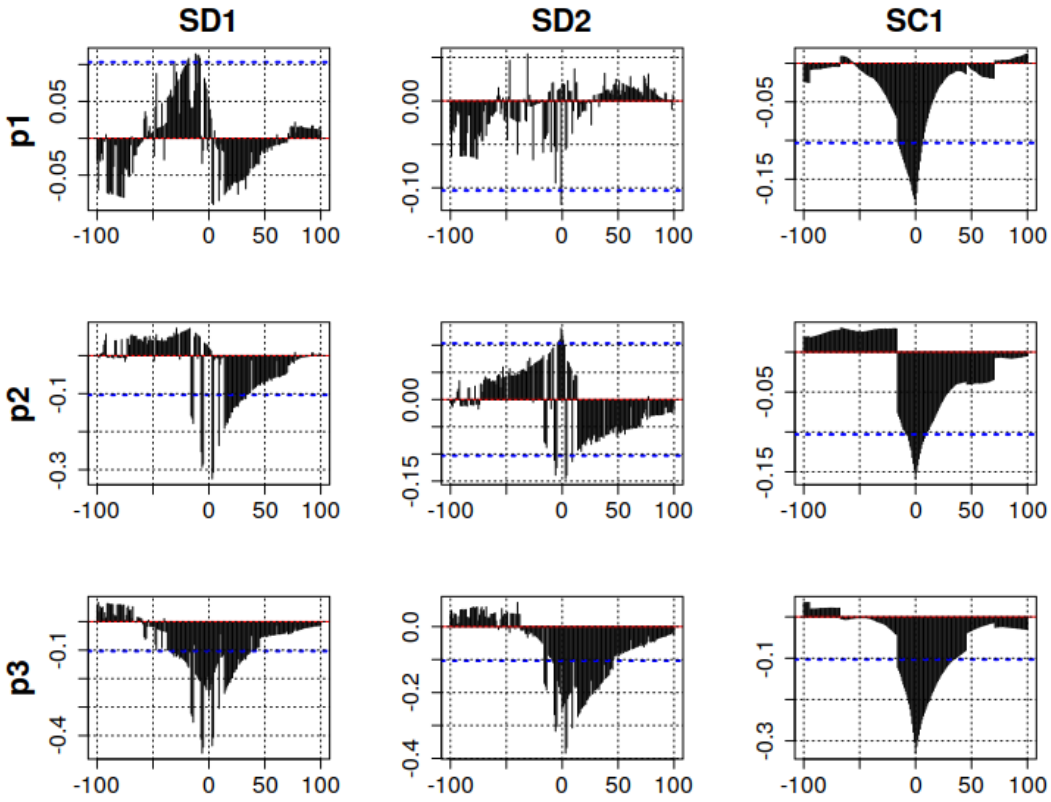

Figure 4.28: Cross-correlation between water level time series for borehole SD2 and estimated VGG on pillars p_1, p_2 and p_3. Blue dashed line: significance limit.

These findings raise the question of whether the change in VGG could hint at a change in a specific storage location that is within the VGG's range of sensitivity. Subsequently, the potential impact of the filling and emptying of storage volumes at the borehole locations on the VGG measured in the observatory building was investigated using hydro-gravimetrical forward-modelling. A gravity forward routine Okabe (1979) for a rectangular prism has been used to simulate multiple realizations of saturated areas of a simple prismatic shape. For simplification, the wells were assumed at the centre of these saturated "patches" as shown in Figure 4.27. These areas were assigned a maximal saturation of 15 %, surrounding areas were set to 0 %. A simplified, homogeneous model domain of 100 x 100 m and 50 m with 5 m cell discretisation depth without vertical layer properties or further heterogeneity other than the borehole areas was set-up. Ranges of vertical and horizontal extents are shown in Table 4.3. All combinations of these parameters (> 8000 realisations) were simulated. Gravity and VGG expected at the three pillar locations in the observatory were calculated for each simulation.

4.2.5.1 Results and discussion: Local storage near boreholes

The distribution of simulated gravity and VGG for the three pillars following the multiple realisations of the local borehole storages are shown in Figure 4.29. Mean simulated gravity

Parameter	Range [m]
Extent in x-direction	10, 20, 30
Extent in y-direction	10, 20, 30
Water level SD1, SD2	5, 10

Table 4.3: Simulation parameter ranges borehole extents

of p_1 is 225 nm·s^{-2}, 239 nm·s^{-2} for p_2 and 249 for p_3. Mean simulated VGG are 7.95 for p_1, 10.54 E for p_2, and 11.06 E for p_3. Larger VGG values occur for larger gravity values, as VGG of more than 60 E occur and gravity values of approximately 500 nm·s^{-2} for pillar p_3. The simulated gravity signals that are correlated with higher VGG of more than 40 E, are of the order of magnitude of the observed residuals in the iGrav data series in 2018, showing increase of approximately 600 nm·s^{-2} during the year.

The distribution of differences between the VGG simulated on the three pillars is shown in Figure 4.30. Differences between pillars stay within a range of a few E; up to 10 E between p_1 and p_3 are found for some combinations. Differences in VGG between pillars can only be caused by a difference in relative location to the water storage volumes, as no further assumptions regarding the VGG locations were introduced into the simulation.

The results show that water storage at 20 and 50 m depth, respectively, produce potentially observable VGG changes. The gravity changes are of several hundreds of nm·s^{-2}. If one assumes that the water height dynamics of the storages that the boreholes SC1, SD1, and SD2 have access to, generally represent the mass balance measurable with a gravimeter at the plot scale of the Larzac site, gravity and VGG observations may be strongly influenced by the filling and emptying of these storages. Potentially, the combined gravity-VGG monitoring could allow for depth deduction of the observed mass changes. Saturation in greater depth, as represented by water level data obtained from borehole SC1, shows a similar annual dynamic as iGrav gravity residuals. Analogous, mass redistribution processes at shallower depth as represented by water level changes in boreholes SD1 and SD2, may become visible in VGG observations. Gravity changes without VGG changes would hint at percolation processes at depth.

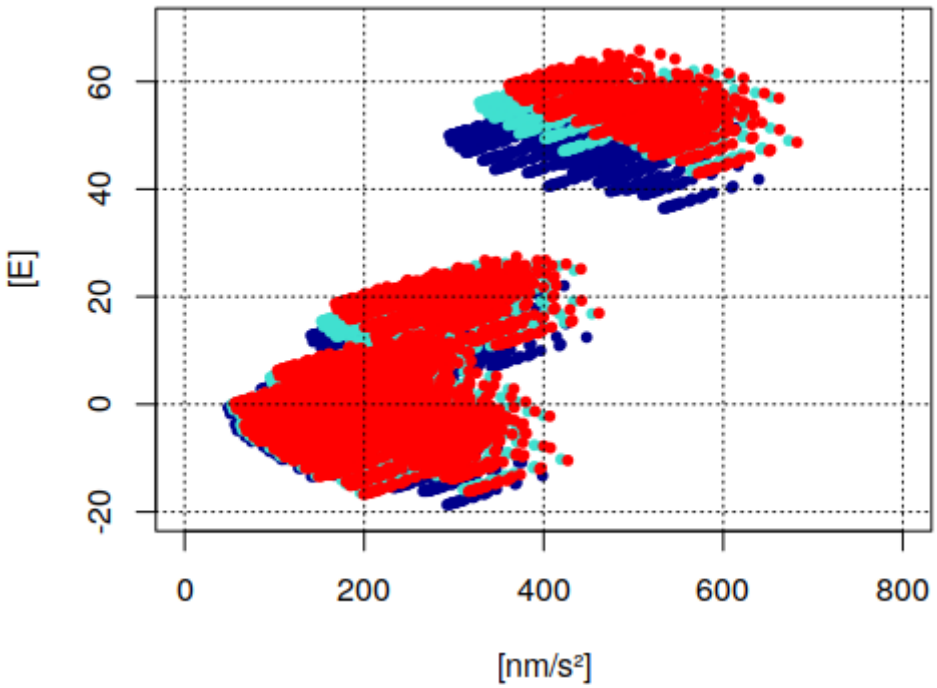

Figure 4.29: Simulated gravity in nm.s^{-2} and VGG in E for pillars p_1 (darkblue), p_2 turquoise), p_3 (red).

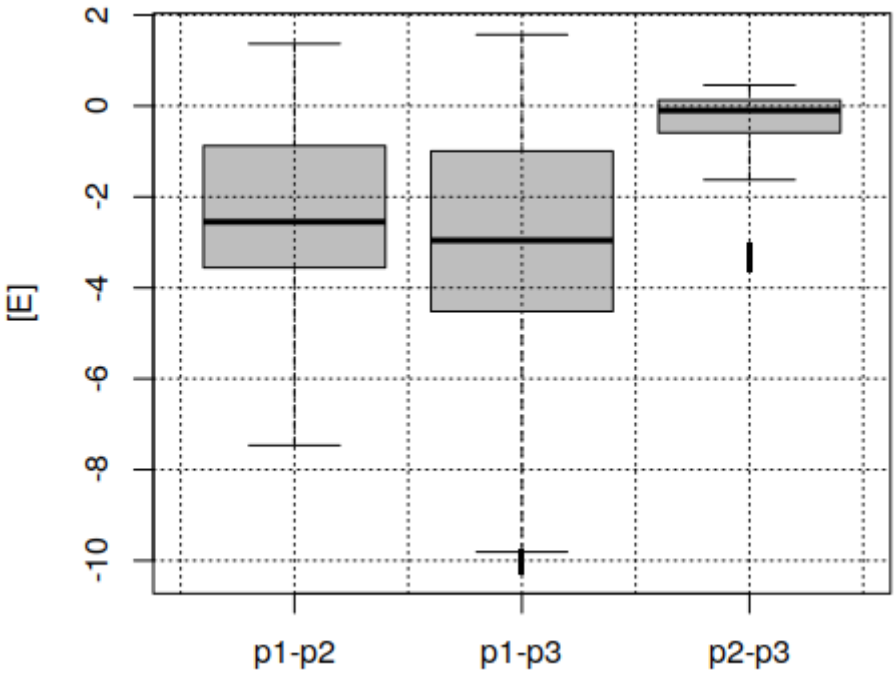

Figure 4.30: Differences in E between the VGG simulated on the pillars.

The simulation did not produce considerable differences in VGG between pillars. The chosen model parameter ranges may be limited and the results only show a selection of possible VGG caused by the borehole "patches". The volume contributing to the water level in the boreholes as well as the spatial soil saturation differences require refined constraints on their extends and

shapes.

In contrast to the measurements, that show a decline in VGG on p_3 during an increase in gravity in the iGrav series, the simulations produce a positive correlation between VGG and gravity residuals. VGG decline on p_3 correlates temporally with declines in shallow borehole water levels (SD1 and SD2), whereas gravity residuals, as well as water levels in the deeper borehole (SC1), show a delayed response. It is possible that the storage contributing to SC1 is of a larger horizontal extent than the modelled prism shapes. Declining of shallow storages would lead to declining VGG. The decline in gravity caused by the emptying of shallower storages might be compensated by the filling of deeper and possibly larger storages. Consequently, declining water storage in shallow depth can be accompanied by increasing gravity due to the filling of deeper storages that are located inside the gravimeter's flat cone of sensitivity.

4.3 Conclusion and synthesis

4.3.1 Observation of unexplained VGG changes exceeding the estimated repeatability

Vertical gravity gradient (VGG) monitoring was conducted by repeated relative gravity surveys on three tripod heights on three pillars inside the Larzac geodetic observatory. VGG estimates based on the difference between gravity on the base tripod and the highest tripod ($\Delta h = 1.117$ m) showed a repeatability of better than 23 ± 9 E. VGG monitoring was carried out between December 2017 and November 2018. During that year, VGG changes of ~ 80 E were observed on the measurement location on concrete pillar p_3, while VGG differences on the pillars p_1 and p_2 were considered to be below the detection limit of this method.

4.3.2 Umbrella effect of the observatory building likely to cause only minor VGG changes

The VGG changes were assumed to be related to water storage changes as other mass changes in the surroundings of the observatory building were not reported. For water mass changes to become visible in VGG measurements, a heterogeneous spatial distribution is required, unlike the commonly applied assumption of a Boguer plate equivalent of a homogeneous water column. The search for an explanation of the observed VGG changes was therefore focused on processes causing spatially distributed, 3D mass anomalies in the proximity of the measurement locations. The ground shielding effect of the building area changes the local soil water content, which in hydrogravimetry is commonly referred to as the 'umbrella effect'. The assessment was carried out using 3D hydro-gravimetrical modelling. In conclusion, the impact of the umbrella effect was found to be limited to a few E.

However, assumptions concerning on the model input variables, such as the use of daily effective rainfall series, might have to be challenged. This simplification ignores near-surface soil wetting and drying patterns and local, actual evapotranspiration. Despite not being totally sealed off, evapotranspiration beneath the building in the model was assumed to be neglected due to shading. With data from the above-mentioned sources, this assumption could be tested and refined.

4.3.3 Differential VGG monitoring as a constraint in hydrogravimetrical inversion

Subsurface porosity distributions were generated in a geostatistical stochastic simulation and selected to obey the observed gravity and VGG changes as well as differences between measurement locations. Joint gravity and gravity gradient data effectively reduced the range of simulations consistent with the data. The distance between the measurement locations on the three pillars provided an additional constraint. The selection of fitting simulation results was further narrowed down by the explicit use of these differential VGG observations. Time-lapse, differential VGG measurements show potential as a new technique to spatially resolve mass changes in a hydrogeological context. In the case of the Larzac site, a clear conclusion regarding the relationship between the simulated porosity distribution and existing cavities and fracture orientation or the surface topography are not easily drawn. It was concluded that the models are not sufficiently constrained, especially at a larger distance from the observatory building. Potentially also a larger number of simulations would be required to sample the probability space more thoroughly.

The gravitational effect of the change in water height in water storage entities covered by three boreholes within $\sim$ 20 m distance to the observatory building has been simulated using a simplified prism shape and a saturation difference of 15 %. Up to 60 E VGG change and approximately 500 nm$\cdot$s^{-2} change in gravity can be seen for p_3. These values are of the order of magnitude of the VGG and gravity observations but require refined model parameters.

In general, the simulated subsurface saturation differences were based on a spatially variable porosity distribution assuming a constant saturated percentage. The next step would be to investigate saturation distributions that emerge generically from dynamic forcing (e.g. temporal pattern of rainfall input) and the interaction with the subsurface properties.

4.3.4 More soil moisture constraints required

As proposed earlier, a directional variogram analysis of survey data acquired in electric resistivity or seismic refraction tomography campaigns is required to adequately describe the anisotropy of the subsurface. Furthermore, saturation estimates especially at shallow depths would be required

to successfully disentangle mass effects at different depth in the gravity and VGG signal. For this reason, high-precision, long-term geodetic observatories (e.g. Wettzell (Creutzfeldt et al. (2010)), Moxa (Kroner (2001)) or Membach (M. V. Camp et al. (2006))) are equipped with soil moisture monitoring corresponding to the requirements of the site. Due to the shallow soil depth and the surfacing lime-stone bedrock, the advantage of e.g. an array of time-domain reflectory probes (TDR) at the Larzac is limited and not representative. A promising technology for soil moisture monitoring is Cosmic-ray neutron sensing (CRNS). These sensors are envisaged to be installed at Larzac site in the near future. The horizontal footprints of a ground-based gravimeter, an eddy-covariance flux-tower, and the terrestrial Cosmic Neutron Ray Soil moisture sensing (with a soil penetration depth of less than one meter) (Zreda et al. (2008)) lie all in the range of less than one km diameter. Combined CRNS and gravity measurements have been shown to yield improvements in the depth-resolution of hydrological storage changes (Reich and Güntner (2020)). The temporal dynamics of the umbrella effect could be simulated in higher resolution with access to topsoil moisture.

4.3.5 Impact of VGG 'noise' in the context of gravimeter validation

The time-invariable effects of nonlinearity of the observatory's gravitational field have been evaluated. The effects of the masses of the concrete pillars and their specific spatial set-up inside the building VGG on gravity and VGG measurements have been assessed. Correcting for these systematic effects reduces uncertainty in gravimeter comparison. Site-specific spatial gravity differences remain.

The effect of time-variable VGG on gravimeter operation at different heights is likely to be negligible, as VGG on p_1 and p_2 stay relatively stable. However, the repeatability of gravimeter measurements on pillar p_3 could be impacted. For instance, given the measurement height of the AQG#B01 (0.65 m), a VGG change of 60 E would lead to an error of 39 nm·s^{-2}.

If VGG changes are large enough, a constant VGG correction term leads to errors in the gravity measurements. In the inversion process applied in the geostatistical study, the objective functions or criteria for gravity and VGG were dealt with as independent. Ideally, both terms need to be considered as coupled. The earlier mentioned surface saturation monitoring using additional methods could provide additional constraints to distinguish between the two effects.

As a conclusion, the important question that arises from the work conducted in this thesis is:

How do mass redistribution on the one hand and the corresponding change in VGG correction on the other hand contribute to observed spatio-temporal gravity variations?

4.3.6 Improved VGG monitoring

Finally, the expected improvements of VGG measurements carried out with the AQG#B01 are discussed. Potentially, the deployment of an AQG#B01 would greatly increase the VGG acquisition frequency. Unlike relative spring gravimeters, the AQG#B01 is not susceptible to sudden spring tares causing nonlinear behaviour or strong instrumental drifts. This reduces the necessity of time-consuming, repeated loops, and minimizes post-processing.

The AQG#B01's repeatability has been assessed and quantified as 3 ± 25 nm·s^{-2}. Its accuracy in absolute terms is still under investigation. However, for differential gravity measurements, as required for VGG estimation, the repeatability and precision are of main concern.

The AQG#B01's sensitivity after one hour of data integration has been quantified as 10 nm·s^{-2} in a calm environment (Larzac observatory). The tripod currently available for the AQG devices has a height of 0.672 m. These measures would lead to a VGG sensitivity of 21 E with a repeatability of 6.3 ± 53 E. To increase the sensitivity to better than 10 E, a height difference of at least 1.42 m would be necessary. These considerations are restricted by the height of the building's ceiling and practicability regarding shifting the instrument onto the higher tripod. It could be envisaged to develop an automated, moving platform (potentially combined with automated tilt levelling). This would further reduce the need for human intervention and deliver VGG monitoring of high temporal resolution.

The main improvements stem from the reduction in time investment compared to the use of a relative spring gravimeter and the increase in the temporal resolution of VGG monitoring. VGG measurements of higher acquisition frequency would allow for a more robust analysis of temporal cross-correlation with hydro-meteorological time series acquired at the site. This could allow for advanced temporal separation of water mass movements at different depths.

Furthermore, the promising results of the temperature tests suggest the possibility to obtain VGG measurements outside the observatory building, given a suitable location on the bedrock or the installation of a new concrete pillar. Before this is possible, any potential influence of winds and radiation on the measurement of g with the AQG#B01 has to be assessed. VGG measurements outside the observatory would provide the possibility of horizontal spacing larger than the distances between concrete pillars.

5 General conclusion

The main objective of this thesis was the assessment of high precision performance measures of absolute quantum gravimeters in comparison with high precision absolute and relative gravimeters and additional geophysical and environmental data. This was carried out in controlled conditions and experiments in view of future deployment in field conditions.

Two absolute quantum gravimeters, the Muquans AQG#A01, and AQG#B01, have been evaluated focusing on important performance measures: accuracy, sensitivity, stability, and repeatability. Measurements of several weeks have been carried out at three different locations: The Larzac observatory, Géosciences Montpellier, and Trappes (near Paris). From the experience from these displacements, the following can be concluded:

- Successful shut-down, disassembling, transport and full restart was achieved with both instruments during several relocations
- Drift-free measurement of g over several weeks with both AQG devices

5.1 AQG-A01

Complementary to the study by Ménoret et al. (2018), the following additional results have been obtained for the AQG#A01:

- In a low-noise environment (Larzac), the AQG-A01 achieves a sensitivity of less than 10 $\mathrm{nm{\cdot}s^{-2}}$ after 24 h of data integration
- Sensitivity and stability show a high variability due to sub-daily oscillations
- Oscillations likely to be related to laser instability, but correlation not systematically reproducible at all study sites
- Vertical gravity gradient estimation based on measurements on tripods of two different heights with the AQG-A01 less precise than VGG estimation with a CG6 relative gravimeter

5.2 AQG-B01

Based on the experience gained from the AQG#A01, the follow-up field version (AQG#B01) includes considerable improvements in sensitivity and stability. The characterization of the AQG#B01 for field applications was focused on potential terrain conditions impacting temperature, sensor head tilt, and orientation.

The key findings are the following:

- In low noise environments (Larzac observatory), the AQG-B01 showed a sensitivity of 10 nm·s^{-2} after 1 h
- Sensitivity after 24 h of data integration is close to that of the iGrav-002 at the Larzac observatory
- In noisy environments (Montpellier), the sensitivity is between 20 and 30 nm·s^{-2} after 1 h
- Repeatability has been quantified as 3 with a standard deviation of 25 nm·s^{-2}
- Monitoring of hydrological mass changes: Agreement between gravity residuals measured with the iGrav and AQG-B01
- Reliable operation in controlled conditions with an external temperature range between 20 and 30 °C over several weeks
- No effect of a potential interaction between temperature and sensor head tilt on the measurement of g observed
- Reliable operation during two weeks in a garage, no observed impact of fast temperature changes, increased noise levels or air movement during opening of garage doors
- Montpellier: Δg between AQG-B01 and FG5-228 was 44 nm·s^{-2} with a standard deviation of 66 nm·s^{-2} ($g_{AQG-B} < g_{FG5}$)
- Larzac: Δg between AQG-B01 and FG5-228 was 110 nm·s^{-2} with a standard deviation of 31 nm·s^{-2} ($g_{AQG-B} > g_{FG5}$)

Proposed next steps

Practical insights could be gained from the instrument characterisation presented in this thesis. However, the study is not exhaustive, as the assessment of the uncertainty budget of a gravimeter remains a complex task. In the near future, the following tests are of importance:

- The impact of sensor head orientation (Coriolis effect) on the measurement of g needs to be further investigated
- Long-term monitoring of several months to evaluate stability
- Repeatability and transportability need to be repeated. Additional displacements between Montpellier and the Larzac (and other locations)

Potential applied studies

The potential gain in precision and time saved makes the AQG#B01 a promising instrument for e.g. large-scale gravity mapping. Such studies were formerly only feasible using a relative

gravimeter that requires repeated acquisition loops and a reference absolute gravimeter for drift corrections. The AQG#B01 can be used without a reference instrument: It provides stable, repeatable measurements of absolute gravity while being transportable and user-friendly. Time-lapse monitoring of mass changes, e.g. hydrogeophysical signals, at other sites is envisioned. Continuous monitoring at high precision allows for studies of high temporal resolution at different scales. The AQG#B01 would especially be suited for the monitoring of transient mass changes at durations (e.g. a few weeks) that are too short to justify the effort of installing a stationary, superconducting gravimeter. To reliably detect transient phenomena, a drift-free and repeatable determination of g is required for which e.g. spring gravimeters are not suitable. The absolute gravimeter FG5 is not suitable for continuous monitoring.

Impact of vertical gravity gradient on gravimeter comparison

The Larzac observatory provides favourable conditions for gravity monitoring due to the low-noise environment, controlled temperature, and additional hydrogeophysical monitoring at the site. However, its suitability for gravimeter comparison in terms of accuracy is limited by spatial and temporal variability of the local gravitational field. The concrete pillars protrude 0.5 m from the soil surface, causing nonlinear vertical gravity gradients (curvature) within the first two meters above the pillar surface. Differences between observed and simulated curvature caused by the concrete pillars suggest the impact of additional subsurface heterogeneity. Precise mapping of the curvature is limited by the sensitivity of the available VGG estimation method. It is recommended to conduct gravimeter comparisons at observatories where pillars are ideally embedded in a larger, flat concrete plate. Measurements with several displacements between pillars in the Larzac observatory are recommended. Additionally, the Larzac observatory is exposed to soil moisture changes in the surrounding unsaturated zone. Their impact on gravity measurements due to uncertainty related to the VGG-correction can potentially be important. In a nutshell, the VGG monitoring can be summarised in the following points.

Observed temporal VGG variations

- One year of monthly gravity surveys conducted with a CG5 relative gravimeter on three different heights on three pillars
- Repeatability of VGG estimation quantified as better than 23 ± 9 E
- 80 E observed change on measurement location pillar p3
- VGG on pillars p1 and p2 do not show significant trends
- Several tens of E of time-lapse VGG noise can lead to non-trivial gravity offsets

5.3 Differential VGG monitoring as a hydrogeophysical method

The observed VGG changes have been investigated in search of the corresponding mass change.

- Simulated impact of the umbrella effect (building area shielding subsurface from precipitation) on the VGG in the order of a few E
- Impact of subsurface heterogeneity was investigated using geostatistical stochastic simulation
- Combined gravity and differential VGG data significantly reduced the number of suitable simulated subsurface realisations
- No significant correlation between simulated subsurface properties and existing geological structures (cavity, fracture orientation)
- Effect of local topography on VGG estimated as negligible
- Simplified simulations regarding the water storage variations at the locations of two boreholes at 20 m depth show gravity and VGG changes in the order of magnitude of the observed changes

Next steps

- Refined simulations with better-constrained anisotropy parameters, based on additional saturation measurements
- Further investigations on the impact of the temporal dynamics of subsurface storages
- Potential of VGG estimation with AQG-B: more efficient monitoring, expected sensitivity 21 E and repeatability of 6.3 $\pm$ 53 E

Another objective of this thesis was the development of new methods in gravimetry in the context of hydrology. In this thesis, time-lapse VGG monitoring was tested using available relative gravimeters. The expected precision and limitations of the method were evaluated. The study suggests the influence of heterogeneous soil saturation patterns on VGG. The results discussed in this thesis hint at the potential of differential VGG monitoring in resolving spatial mass distributions in hydrogeology. Upon further refinement, Combined VGG and gravity monitoring in hydrogeology could be developed into a promising tool for hydrogeophysical subsurface imaging. Possible paths are presented in the perspectives hereafter.

6 Perspectives: Applications for quantum hydrogravimetry in aquifer property estimation

This last chapter aims at building a bridge to the challenge of quantifying total water storage and its dynamics at different spatial and temporal scales. These perspectives discuss how gravimetry and gradiometry could complement and compete with classical hydraulic methods. The long-term objective is to further enhance the development of promising methods in the young discipline of hydrogeophysics. In order to establish the state-of-the-art and to introduce the ideas, a short excursus into groundwater hydrology is given.

6.1 Hydraulic methods for hydraulic parameter estimation

Groundwater resource management and protection relies strongly on the accurate estimation of hydrogeological parameters characterising aquifer flow and storage terms. The Transmissivity T $[L^2/T]$ refers to the groundwater flow rate through a saturated aquifer of a given thickness b $[L]$. T depends on the hydraulic conductivity (K) as given by:

$$T = Kb. \tag{34}$$

The groundwater storage capacity of an aquifer can be expressed by its storativity S. S refers to the sum of the two parameters specific yield (S_y) and specific storage (S_s). The specific yield tends to be of main interest in aquifer characterisation as it refers to the volume of water that can be extracted per unit of aquifer volume. It is a dimensionless value that is defined as the volume of water released per aquifer surface area per water level decrease (e.g. Fetter (2018)). In other words, S_y represents a drainable fraction of porosity n, also referred to as effective porosity. Specific storage (or specific retention) is water held back in the matrix due to capillary forces during drainage. This secondary storage may release water as a consequence of aquifer compression after water extraction. In unconfined aquifers, storativity is mainly defined by S_y. Total aquifer storage can be expressed as porosity (Bear (2012)), which is the sum of both storage terms:

$$n = S_y + S_s. \tag{35}$$

Estimates of hydrodynamic properties are required to predict the response of the aquifer flow field to injection or extraction. These parameters are conventionally obtained from hydraulic methods such as pumping tests. The system response to induced stress on the flow field is analysed, which usually equals a change in hydraulic head (in unconfined aquifers). This head

change is referred to as drawdown, measured at the pumping well, and at an observation well at a distance from the pumping well (Figure 6.1). Well-tests comprise extraction or injection (push / pull) (e.g. Fetter (2018)), step-tests at different pumping depths (Birsoy and Summers (1980)), slug tests (Butler Jr (2020)) and different versions of oscillatory pumping (e.g. Cardiff et al. (2013)). Change in head at a given location at a given time during pumping can be inverted into hydraulic parameters via various methods. In general, time-lapse hydraulic head measurements at the pumping well and observation wells are fitted to a suitable conceptual model to obtain the searched parameters. Commonly used interpretation techniques for cross-well tests have been proposed by e.g. Theis (1935). The Theis solution is based on Darcy's law and the continuity equation in a homogeneous aquifer. Meanwhile, numerous solutions have been developed that take different boundary conditions into account, such as variable well discharge (Hantush (1964)) or non-uniform aquifers characterised by areas of varying transmissivities (Butler (1988)). The effects of delayed drainage from the unsaturated zone have been included by e.g. Moench (2008) and Mishra and Neuman (2011). An overview of the steps in the model identification process is given by (Gringarten (2008), Figure 6.2).

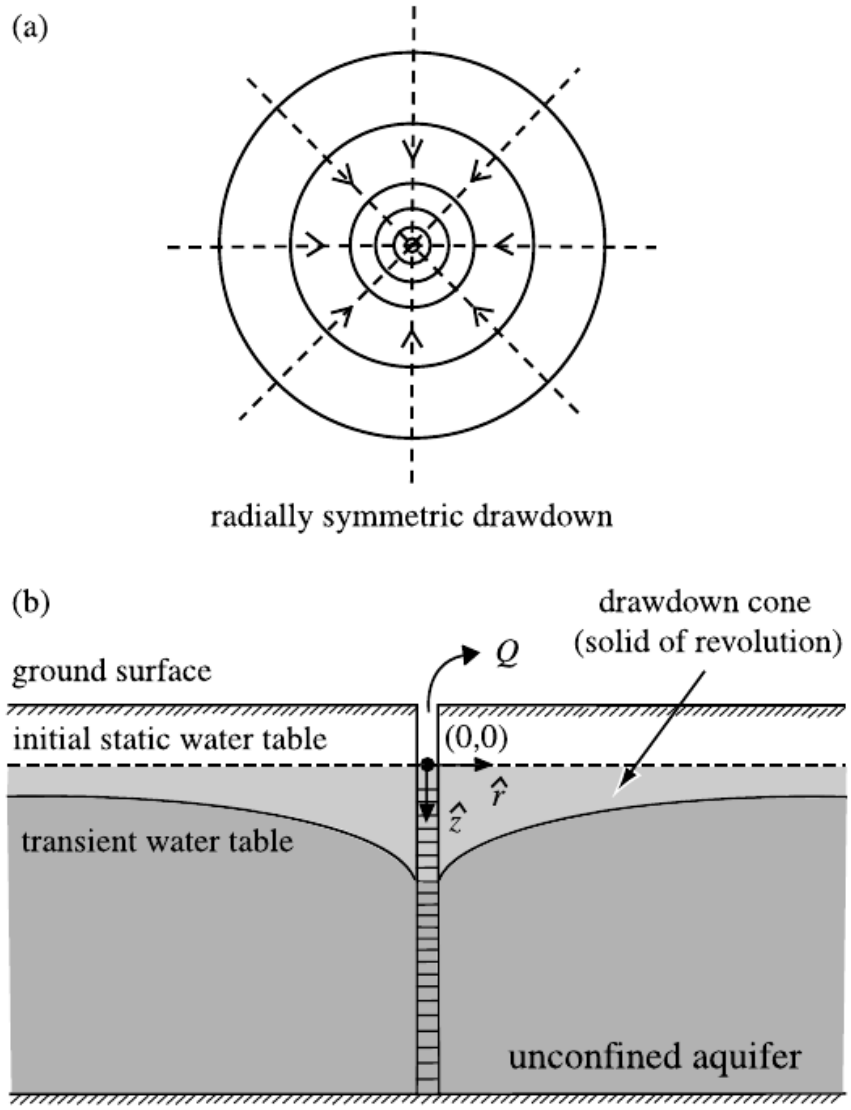

Figure 6.1: 'Idealized representation of model assumed for the simulations. (a) Equipotentials and streamlines. (b) Cross section with darker shaded area corresponding to saturated portion of aquifer during hydraulic testing and lighter shaded area to dewatered portion. Gravity observations are made along the ground surface. For mathematical convenience, the coordinate origin is located along the axis of the pumping well at the initial static water level; and r and z are the unit directional vectors.' Damiata and Lee, 2006, p.350

Hydraulic tomography expands the focus from individual wells and their radius of influence to larger areas and the estimation of the spatial variability of hydraulic conductivity and specific yield. Mapping of hydrodynamic properties of larger aquifer segments is achieved by the inversion of head change propagation in an array of distributed wells during and after injection or pumping sequentially carried out at numerous well locations (Zhu and Yeh (2005)).

6.2 Geodetic methods

Despite its ubiquitous application, the hydraulic method does come with its uncertainty, S_y estimate can be erroneous (e.g. Yeh and Huang (2009)). As well installation is time-consuming and costly, aquifers can be under-sampled and their spatial variability is underestimated. Another aspect is the quality, accessibility, and frequency of water level probing at the wells, which can vary depending on whether infrequent manual measurements or continuously measuring sensor equipment are available.

Apart from hydraulic methods, geodetic approaches have been tested. The added value of geodetic methods refers in particular to sites where drawdown data of sufficient quality is too difficult or too costly to be obtained. During hydraulic experiments, two geodetic observations can be made: Surface deformations (subsidence) as a response to water extraction may occur to a measurable extend. Subsidence is mainly determined by matrix properties and relates to the specific storage Ss. Moreover, a change in gravitational attraction can be observed that can be attributed to the change in mass due to the missing water volume of the drawdown cone. The gravimetric method is used to estimate the change in water mass which can be related to specific yield S_y. Usually, time-lapse gravity measurements are carried out at periods before, during, and after pumping. Chen et al. (2018) report the use of both methods in the same setting and measured subsidence in the field with levelling devices. The interest in improving observation and simulation of the gravity response to pumping tests has increased due to its non-invasive and integrative nature. Gravimetry's capability of describing groundwater storage and mass balance at various scales has been shown (e.g. Leirião et al. (2009); Christiansen, Binning, et al. (2011)). Specific yield estimates can be based on passive time-lapse gravity observations and head data in a recharge area as for instance shown by Wilson et al. (2011). However, it has also been proposed and investigated to measure gravity in particular during hydraulic testing.

6.2.1 Gravimetry for pumping tests: feasibility studies

Several studies on the use of gravimetry in aquifer testing have been published and conclude measurable gravity changes for a range of synthetic pumping experiments. One of the first theoretical assessments provided by Damiata and Lee (2006) was based on an analytical model to simulate the gravitational response to the hydraulic tests of unconfined aquifers. Blainey, Ferré, and Cordova (2007) extended this numerical experiment and compared the use of high- and low-quality drawdown and gravimetric data to estimate hydraulic conductivity and specific yield. The mentioned studies considered idealised conditions such as aquifer testing with a fully penetrating well and isotropic and homogeneous conditions. Herckenrath et al. (2012) extended the model for the more common case of partially penetrating wells in anisotropic

aquifers, including delayed drainage effects and possible data errors. In general, published feasibility studies consist of 2D-analytical solutions or 3D numerical forward-modelling (e.g. Leirião et al. (2009)).

Tsai et al. (2017) show in a stochastic study that mass balance constraints provided by gravimetry can improve hydraulic tomography over large areas. Best results have been expected for combined methods of both hydraulic and gravity data that further improve with an increasing number of gravity stations. As long as the well field is covered by the gravimeter's footprint, the exact location has been determined to be of minor importance. In a synthetic study, Fernández-Álvarez, González-Quirós, and D.Rubio-Melendi (2016) show the capability of gravity mapping in determining the principal directions of anisotropic transmissivities in unconfined aquifers during pumping tests.

Time-variable hydraulic head responses during earlier and later periods of the pumping provide further information on the hydrogeological context. In heterogeneous aquifers, temporal non-linearity of the pumped system response can point at flow field anisotropy (e.g. Pechstein et al. (2016)). A comprehensive overview of well-test interpretation methods using time-derivative approaches has been provided by e.g. Gringarten (2008) (Figure 6.2). The gravimetric response shows varying relative sensitivity to parameters during different time intervals: Maina and Guadagnini (2018) present a global sensitivity analysis of the probability distribution of gravity changes caused by well operation focusing on the first four statistical moments. They discussed that gravity performs well regarding aquifer storage terms and water retention curve parameters. Gravity's contribution to saturated and unsaturated hydraulic conductivity estimation appeared to be limited. The uncertainty in gravity changes was statistically highly influenced by parameters governing unsaturated flow. Gravity's sensitivity to the two storage components, specific storage and specific yield, changes during the development of the drawdown cone with time. At greater depth, gravity becomes more sensitive to specific yield and less sensitive to specific storage. The relative importance of the specific storage term and its impact on the drawdown decreases with time, as does gravity's sensitivity to it, whereas the importance of specific yield increases with time.

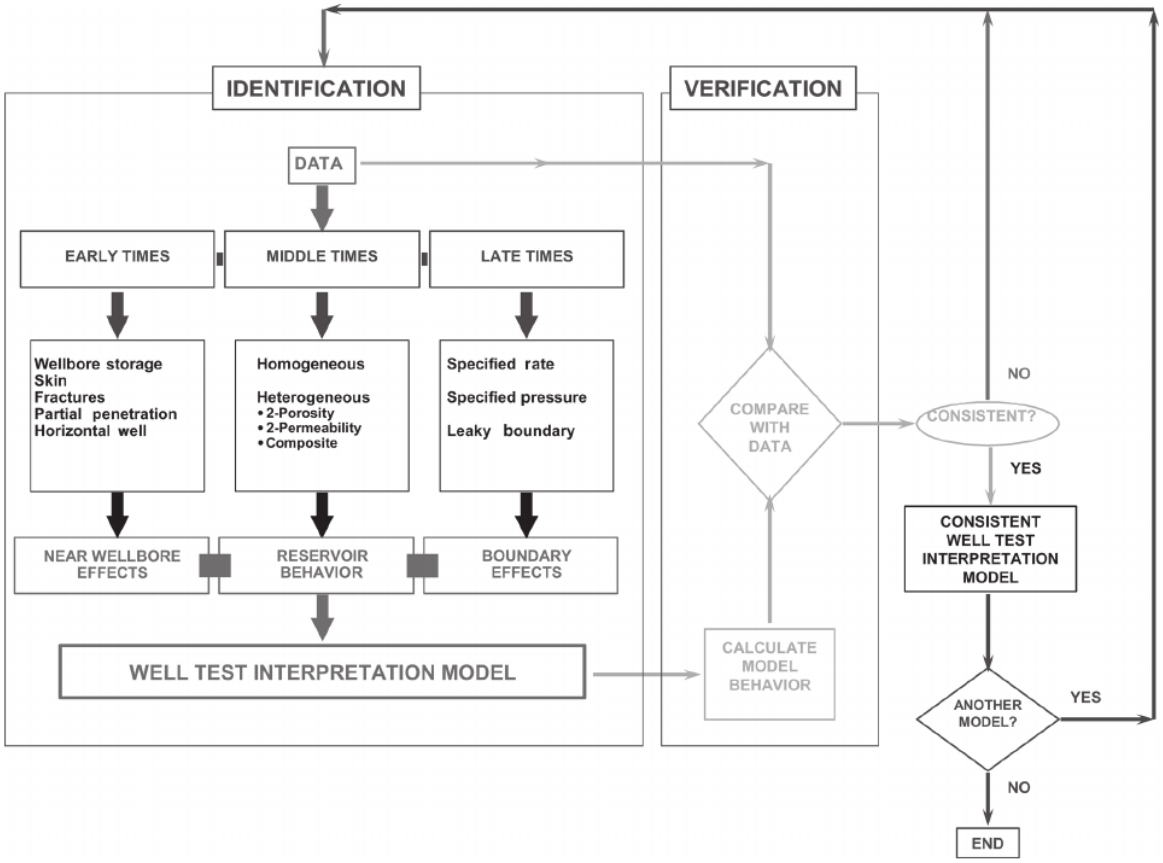

Figure 6.2: Procedure of determination of most suitable well test interpretation method, taking into account the hydrogeological context. From Gringarten et al., 2008, p. 47

6.2.2 Experiences from the field and added value of the gravimetric method

Apart from numerical experiments, field studies have reported the use of gravimetry in the context of aquifer testing. A recent, detailed assessment of gravimetric monitoring in small-scale field pumping tests has been provided by Chen et al. (2018). Prior to the field tests, they show numerically that the expected gravity response to aquifer pumping increases with larger S_y values and the volume of the drawdown cone. Furthermore, gravity is expected to be negatively correlated with horizontal distance between the pumped well and the gravity measurement and hydraulic head prior to pumping. These aspects need to be assessed beforehand in order to evaluate detectability and usefulness. Generally, sites with relatively large expected values for specific yield are recommended, as well as sites with measurement locations as close to the well as possible.

This is one of the reasons that such studies have been mainly conducted in the context of managed aquifer recharge in which large injection or pumping volumes have been achieved. Gravimetry has become of interest in the suitability assessment of aquifer segments for artificial groundwater recharge projects. For instance, Howle et al. (2003) monitored water injection with time-lapse

microgravity surveys and obtained specific yield. Gehman et al. (2009) conducted pumping and infiltration tests in a 3.2 km^2 similar facility that lead to a 460 nm·s^{-2} decrease in gravity near the pumping well. Gravimetric S_y estimates were found to be close to those derived from hydraulic methods and head changes predicted from gravity measurements agreed within $\pm$ 0.45 m.

Especially if hydraulic head data is of insufficient quality, additional gravity measurements can lead to improved storage estimates. Drawdown data of low quality was sufficient to estimate hydraulic conductivity, however, showed large uncertainty in specific yield estimation. Similarly, specific yield and hydraulic conductivity derived from gravity changes alone have been found to be imprecise. Joint interpretation of low-quality drawdown and gravimetric data leads to precise estimates of both (Christiansen, Binning, et al. (2011)).

It has been found that gravimetry can resolve horizontal and vertical anisotropy and contribute to solving the problem of insufficient spatial representativeness of single borehole measurements during hydraulic experiments. S_y derived from gravity measurements is representative of the S_y of the aquifer layer of the drawdown, whereas in hydraulic methods S_y corresponds to the material at the depths of the observation wells, as also observed by Chen et al. (2018). Combined hydraulic and gravimetric S_y estimation offers the possibility to confirm or to distinguish between depth-averaged and layer-specific S_y values. A study by Pool (2008) including 39 wells concludes that gravity measurements provide better storage estimates than head data alone in complex multiple-aquifer systems. Moreover, gravity data made it possible to identify unconfined, confined, and perched aquifers. The correlation between gravity and head changes can indicate the aquifer type. Head changes in confined or perched aquifers tend to rather represent pressure changes than mass changes, resulting in small gravity changes. Unconfined aquifers can generate positive, linear correlations, that become stronger with increasing specific yield. Gravimetry allowed to furthermore identify nonaquifer storage changes that were invisible in the head data, such as root zone storage after precipitation or streamflow infiltration (Pool (2008)).

In addition, the gravimetric method may provide valuable first estimates in data-scarce regions. The need for prior knowledge of subsurface physical properties is reduced. S_y estimates may solely be based on gravity and head change monitoring, given a known, volumetric pumping rate (e.g. Gehman et al. (2009)). Besides the analysis of well-test data, hydraulic tomography tends to rely on geological information and geostatistics (Zha et al. (2017)).

6.2.2.1 Possible applications for quantum hydrogravimetry

In practice, Chen et al. (2018) faced difficulties during the operation of a FG5 (Micro-g Lacoste,

Inc.) absolute gravimeter in field conditions. High noise levels in the gravity measurements was caused by external temperature changes. Possibilities to shield the instrument and to control external temperature were limited. At sites where the expected gravimetric response is already only a few tens of $nm \cdot s^{-2}$, the signal may in practice not be detectable. In larger experiments, the vibration noise during well operation can lead to erroneous gravity measurements (Howle et al. (2003)).

The absolute quantum gravimeter AQG#B01 combines several features that could be advantageous for applications similar to the mentioned studies. The AQG#B01 is relatively simple to transport and to restart, potentially allowing gravity measurements at different locations within a few hours. Most importantly, its reliable performance in the tested temperature ranges (Cooke et al., in review) opens up new possibilities. The high acquisition rate of an AQG could be beneficial to resolve temporal dynamics of water mass changes during pumping tests, potentially resolving the complementary effects of specific storage and specific yield in early and later time periods in the gravity signal. Depending on the transmissivity and the pumped volume, pumping and recession can last hours to several months. The possibility of continuous monitoring could make it possible to cover the entire duration of the experiment. High temporal resolution and sensitivity have been achieved in studies at artificial recharge facilities investigated infiltration processes deploying an "A-10 absolute gravimeter (Micro-g Lacoste, Inc.), two iGrav superconducting gravimeters (GWR Instruments, Inc.), and one gPhone gravimeter (Micro-g Lacoste, Inc.)" (Kennedy, Ferré, and Creutzfeldt (2016), p. 7247). A transportable absolute gravimeter could complement such studies with mobile acquisition at comparable performance, combined in one single instrument.

6.2.2.2 Pumping tests in heterogeneous aquifers: site example

A possible study site for future application of the AQG#B01 is in discussion. The study site is located close to Prades-le-Lez, 15 km North of the city of Montpellier, France. As the source area of the river Lez with drinking water facilities for the supply of Montpellier and surrounding villages, it is of scientific and societal interest. The Lez aquifer is a fractured karstic aquifer system in low-porosity carbonates. It shows strong hydraulic connectivity at local and regional scales due to flow-bearing structures located at stratigraphic interfaces. These structures are further fractured by conduit networks. At discontinuities of the large-scale structures, the aquifer appears to be compartmentalized (Dausse, Leonardi, and Jourde (2019)). A distinctively different behaviour during periods of lower and higher heads activates or deactivates the connectivity of faults and karst networks at a sub-unit of the Lez aquifer. The local aquifer productivity is thus dependent on the state of storage. Such a secondary karstic network is the Rieu Coullon

sub-site, with a transmissivity of 10^{-5} m^2s^{-1} that decreases with declining heads as the aquifer becomes increasingly split up into hydraulic compartments. During dry months, initial water heads at 32.2 to 44.5 m depth and drawdowns between approximately 5 and over 35 m have been reported, depending on the choice of pumping and observation wells, respectively (Clauzon (2019)).

Insights from gravity measurements that extend the information content of hydraulic head data could be expected regarding the mass balance of individual karst network compartments and the extend of connectivity beyond the well field. Hydraulic connectivity between some of the boreholes and the interaction with the larger network is still under investigation (Clauzon, personal communication). A comparison of the spatial heterogeneity of hydraulic parameters at time periods of high and low water levels, respectively, at the well locations and at additional locations could be envisioned using gravity monitoring. It is vital to conduct coupled hydro-gravimetrical simulations of the hydraulic heads and the corresponding gravity changes to estimate the expected gravity changes prior to experimental investigations. As the drawdown occurred at relatively large depths, specifications of the pumping procedure need to be chosen to produce measurable gravity signals.

The terrain offers several locations where bedrock surfaces. Whether these areas are suitable for stable gravimeter operation needs to be assessed. Possibly the installation of a supporting platform would be required. The site is furthermore accessible by car. The main drawback remains the lack of a shelter or access to electricity at the site, therefore the construction of a temporal shelter (tent) and the operation of a generator would be necessary. The development of future battery-powered field instruments is possible.

6.2.3 Outline of possible future research paths: Combined gravity and VGG measuring for aquifer property estimation

In this thesis, the possibility of delineating homogeneous and heterogeneous water mass distributions using vertical gravity gradient data in addition to gravity measurements has been investigated. VGG measurements in the discussed context focus on the monitoring of mass anomalies as a result of the interaction of external forcing and natural, subsurface heterogeneity. The drawdown cone resulting from pumping tests represents a strong spatial heterogeneity and it could be envisioned to conduct VGG estimates in such a setting. For instance, once the system reaches a stable state, the drawdown cone could be probed with spatially distributed measurements. The underlying hypothesis is that VGG data could be used to invert the shape of the hydraulic gradient geometrically, from which the corresponding hydraulic properties could be derived.

Figure 6.3 gives two examples of hydraulic head reduction as well as the corresponding gravity and VGG responses to pumping tests simulated for two simplified aquifers given a factor two difference in transmissivities. The drawdown was simulated using the R-package *rhytools* by Renard and Bertone (n.d.). The difference in maximal drawdown and cone shape is visible in panel (a). As can be seen in panel (b), the largest VGG are expected to be located close to the well and to decline with distance. Gravity residuals change more gradually with distance. Close to the well, the two transmissivities cause differences of $\sim$ 150 nm·s^{-2}. VGG differ a few E. These examples are based on a low-resolution model and serve as rough estimates. Stronger gravity and VGG changes require larger pumped volumes and different aquifer parameters. This example nevertheless illustrates that the ratio between gravity and VGG changes with distance and differs furthermore between the two cases with two transmissivities.

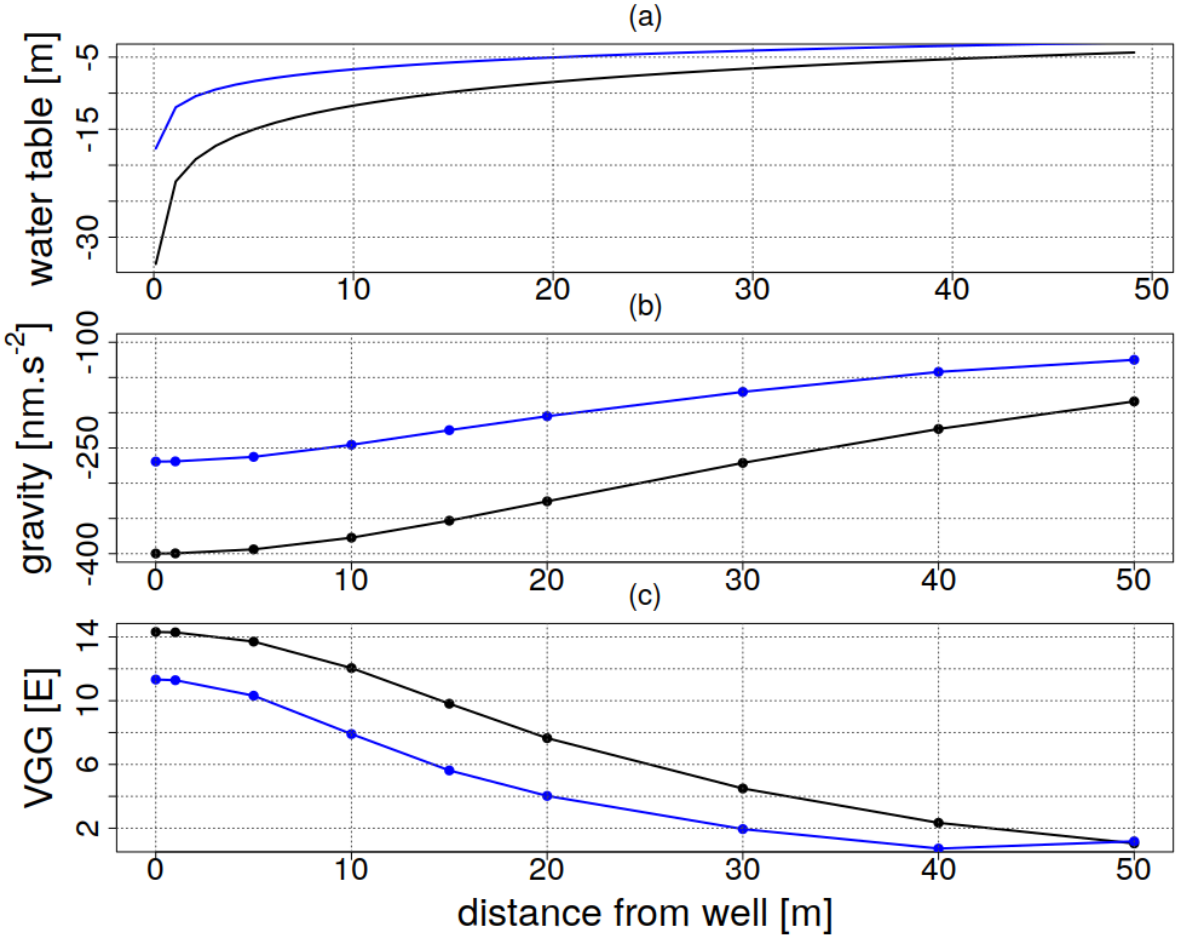

Figure 6.3: Simulated pumping test based on the analytical Theis solution for unconfined, homogeneous aquifers. Drawdown, corresponding gravity, and vertical gravity gradients at different distances from the pumping well (located at 0 m). The analytical solution was transferred into a 3D model of 1 m cell size. Parameters: Specific yield S_y =0.1, pumping rate of $3 imes 10^{-2} m^3 s^{-1}$, pumping duration 7 days, initial head at surface. Two values of transmissivity were tested T_1 =0.001 $m2s^{-1}$ (black lines) and T_1 =0.002 $m2s^{-1}$ (blue lines). Panel (a): Reduction in hydraulic head in meters, relative to surface. Panel (b): Gravity in nm.s^{-2} at 0.65 m measurement height. Panel (c): Vertical gravity gradients in E, based on from gravity difference at 0.65 and 1.32 m above surface.

The next step would be to simulate the spatial and temporal variability of expected gravity and VGG responses to pumping of different aquifer types, hydraulic boundary conditions, and pumping rates. More detailed simulations could focus on different storativities and transmissivities as well as varying degrees of spatial heterogeneity in a Monte Carlo framework. Inspired by Maina and Guadagnini (2018), a global sensitivity analysis approach is proposed, to similarly give an estimate on the influence of each hydraulic parameter on VGG measurements. Generally, the objective of such a study lies at responding to the following questions:

- Do measurable VGG changes occur for common subsurface conditions and pumping test designs?
- How does the feasibility of the VGG method vary for aquifer types and boundary conditions?
- What additional information content can be obtained from
  - inversion of combined gravity and VGG monitoring?
  - spatial differential VGG measurements at different locations above the drawdown cone at stable state?
  - temporal derivatives of the gravity and VGG series and possible changes in their relationship with time?
- Which aquifer properties would benefit from the incorporation of VGG data?
- To which extend do VGG practically provide an added value?

One possible objective that emerges from the vast range of possible research questions is the development of recommendations for joint gravity-VGG interpretation. It would be of interest to generate a systematic framework that can be used to relate gravity and VGG monitoring with the corresponding range of specific subsurface conditions and aquifer types. This could result in so-called diagnostic plots: Diagnostic plots are constructed from drawdown data and their logarithmic derivatives over time. These first qualitative classifications of the dominant aquifer characteristics can be used as a tool to choose a suitable conceptual model and provide information on the flow regime and boundary conditions (Gringarten (2008); Renard, Glenz, and Mejias (2008)). An overview of common diagnostic plots is given in Figure 6.4.

It would be worth investigating whether similar "diagnostic plots" for the response of gravity and vertical gravity could be derived. The idea is to evaluate whether characteristic ratios between relative gravity and VGG changes could be defined that are associated with distinguishable flow regimes? Further questions involve practical use and feasibility: Is the additional information

content compared to hydraulic methods worthwhile the effort? Are such relationships detectable with currently available instruments and typical acquisition protocols?

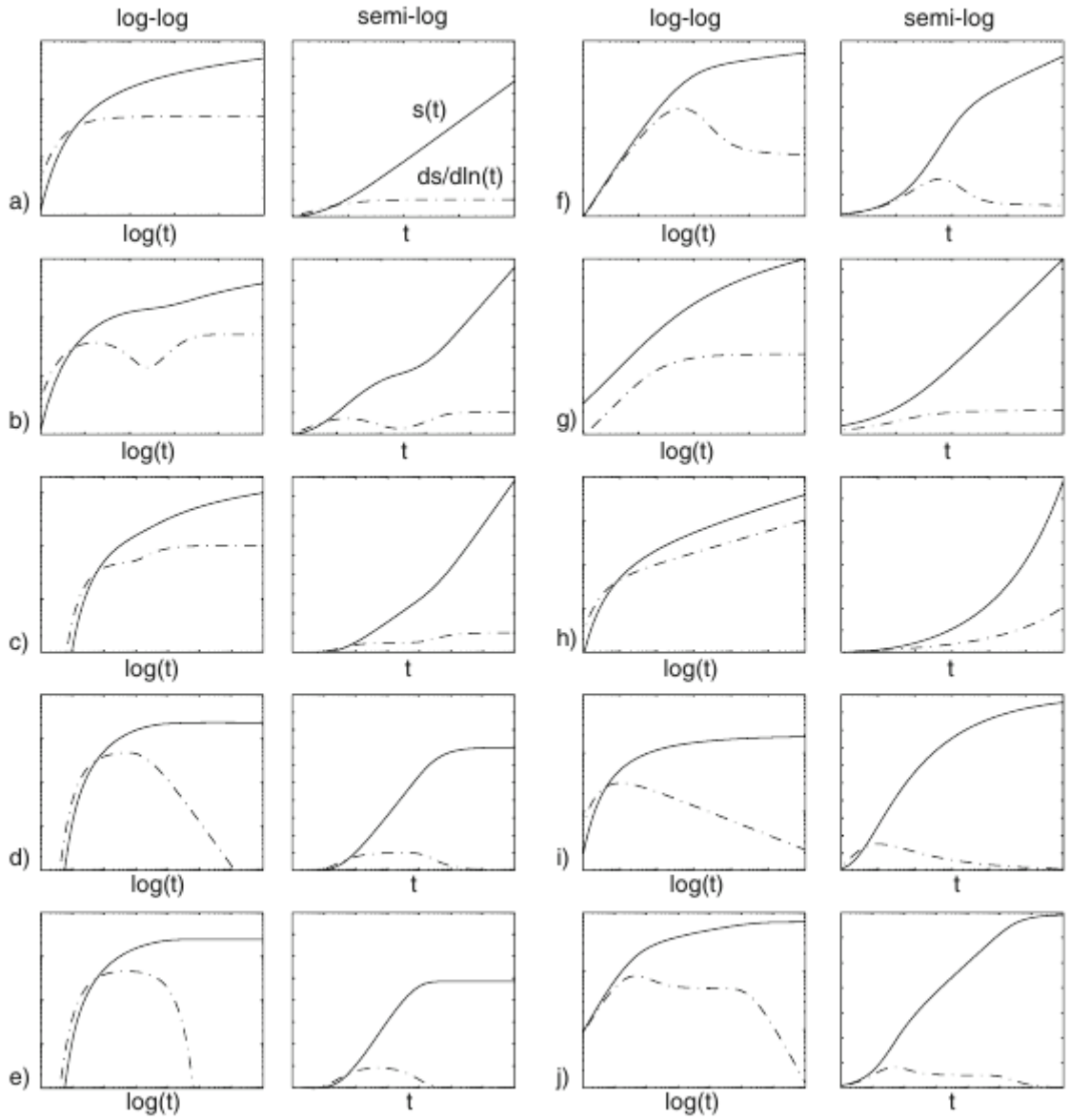

Figure 6.4: Diagnostic plots for common hydrogeological settings: 'a Theis model: infinite two-dimensional confined aquifer; b double porosity or unconfined aquifer; c infinite linear no-flow boundary; d infinite linear constant head boundary; e leaky aquifer; f well-bore storage and skin effect; g infinite conductivity vertical fracture.; h general radial flow—non-integer flow dimension smaller than 2; i general radial flow model—non-integer flow dimension larger than 2; j combined effect of well bore storage and infinite linear constant head boundary' (Renard et al., 2008; p.591)

7 Closing remark

Gravimetry has arrived in the 21st century. The journey started off with Newton and lead to a technology way beyond the understanding of his time: quantum gravimetry. The journey is yet to start. There is much to be explored and understood regarding the potential of gravimetry in solving a quest that is as old as civilization and nowadays of unprecedented urgency: the management of freshwater resources in a fast-changing world.

8 Appendix

8.1 Relative gravity surveys

Operator of all surveys was Anne-Karin Cooke. During survey eight a second person was briefly present. During survey 16 two other persons were present all day. The repeatability study on the same pillar was conducted in survey 16.

Survey	Date	time UTC	Instrument(s)	Pillars	Transport/relaxation time
1	20/12/2017	09:00:50 - 16:36:30	CG5 1151	1,2,3	arrival in morning, relaxation 0.5 h
2	11/01/2018	09:20:48 - 16:59:39	CG5 1151	1,2,3	arrival in morning, 0.5 h
3	02/02/2018	time	CG5 1151	1,2,3	arrival in morning, 0.5 h
4	24/03/2018	11:06:28 - 18:07:15	CG5 1151	1,2,3	arrival in morning, 0.5 h
5	19/04/2018	8:30 - 15:00	CG5 1151	1,2,3	arrival in morning, 1 h
6	27/04/2018	07:46:43 - 14:56:34	CG5 1151 and CG5 1215	1,2,3	arrival in morning, 1 h
7	17/05/2018	08:00:57 14:32:38	CG5 1151 and CG5 1215	1,2,3	1 hour in the morning
8	07/06/2018	07:46:51 14:45:49	CG5 1151 and CG5 1215	1,2,3	overnight relaxation
9	08/06/2018	07:14:56 - 13:28:55	CG5 1151	repeatability study 1,2,3	overnight relaxation
10	09/06/2018	07:12:13 - 13:34:58	CG5 1151	repeatability study 1,2,3	overnight relaxation
11	10/0620/18	07:19:53 - 13:32:54	CG5 1151	repeatability study 1,2,3	overnight relaxation
12	12/06/2018	14:02:33 - 22:15:45	CG5 1151 and CG5 1215	1,2,3	arrival in morning, 4 h
13	13/06/2018	06:41:26 - 10:17:05	CG5 1151 and CG5 1215	1,2,3	check this again
14	12/07/2018	09:15:17 - 16:31:04	CG5 1151 and CG6	1,2,3	1 hour relaxation
15	23/08/2018	02:35:04 - 10:05:36	CG5 1151 and CG6	1,2,3	short overnight relaxation
16	30/08/2018	07:22:46 - 16:26:53	CG5 1151 and CG6	2,3	overnight relaxation
17	11/09/2018	11:04:33 - 15:05:51	CG6	2,3	instruments in GEK for weeks, FG5 on p1
18	19/09/2018	12:00:00 - 20:00:03	CG5 1151 and CG6	1,2,3	4 h relaxation
19	22/10/2018	14:49:26 - 21:23:07	CG5 1151	1,2,3	1.5 h relaxation
20	15/11/2018	14:40:07 - 21:24:24	CG5 1151	1,2,3	4 h relaxation

8.2 Geostatistical simulations: Porosity distribution

8.2.1 Surface views

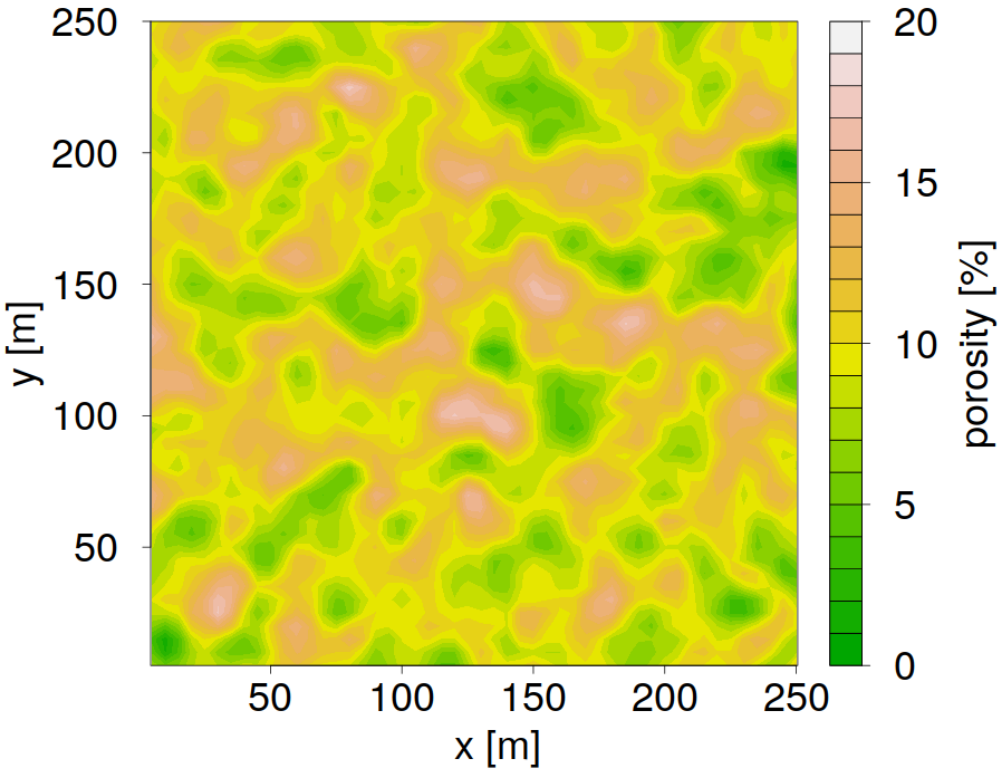

Figure 8.1: Porosity distribution: Surface view of simulation Gaussian (10m) nr. 251.

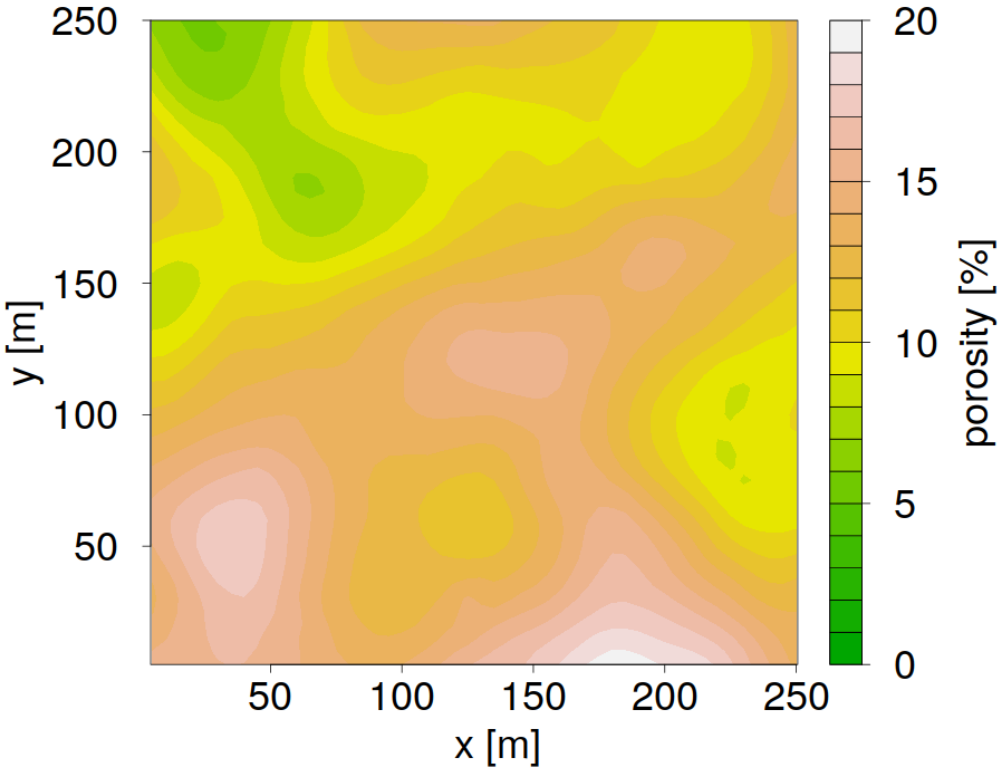

Figure 8.2: Porosity distribution: Surface view of simulation Gaussian (50m) nr. 251.

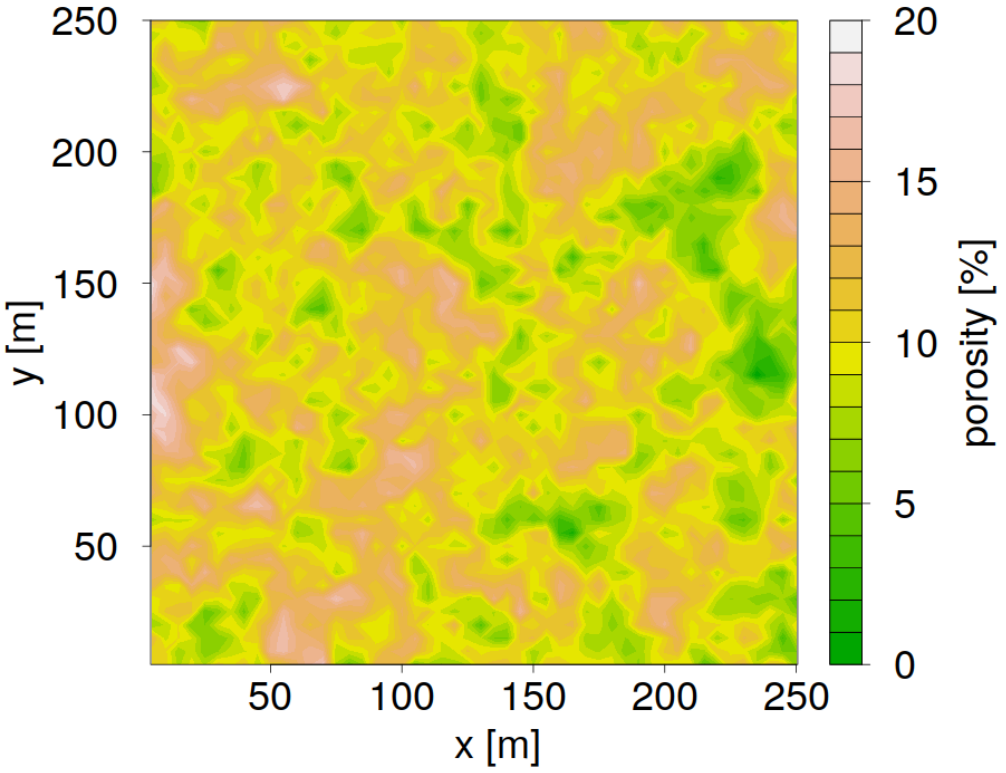

Figure 8.3: Porosity distribution: Surface view of simulation Exponential (10m) nr. 109.

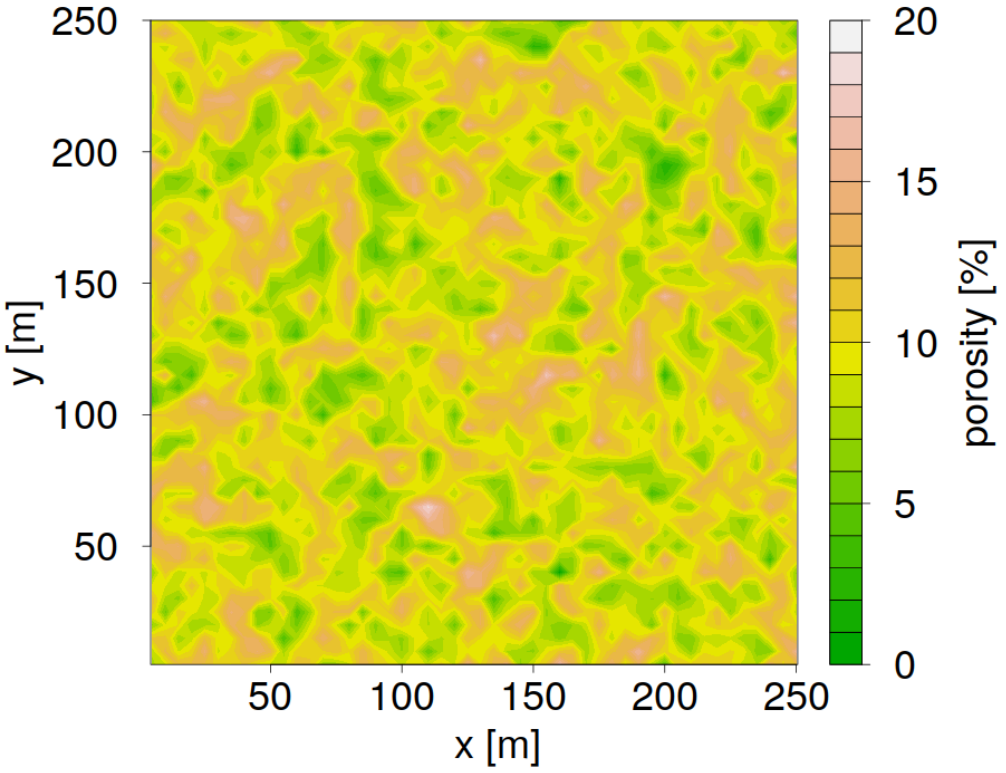

Figure 8.4: Porosity distribution: Surface view of simulation Spherical (10m) nr. 94.

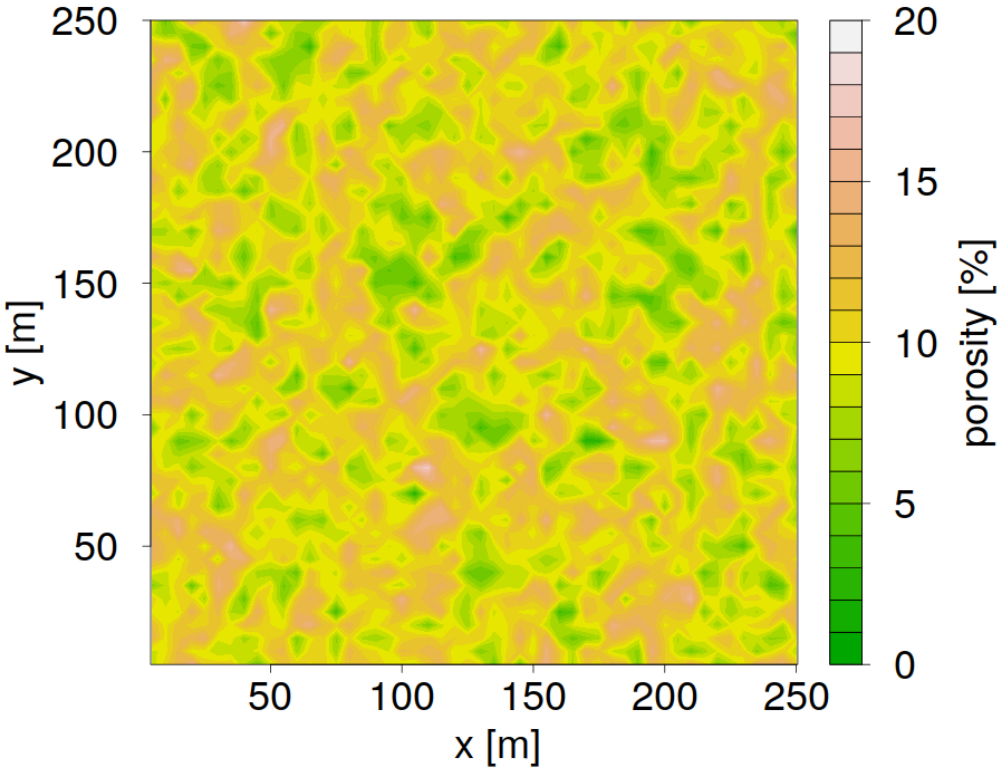

Figure 8.5: Porosity distribution: Surface view of simulation Spherical (10m) nr. 144.

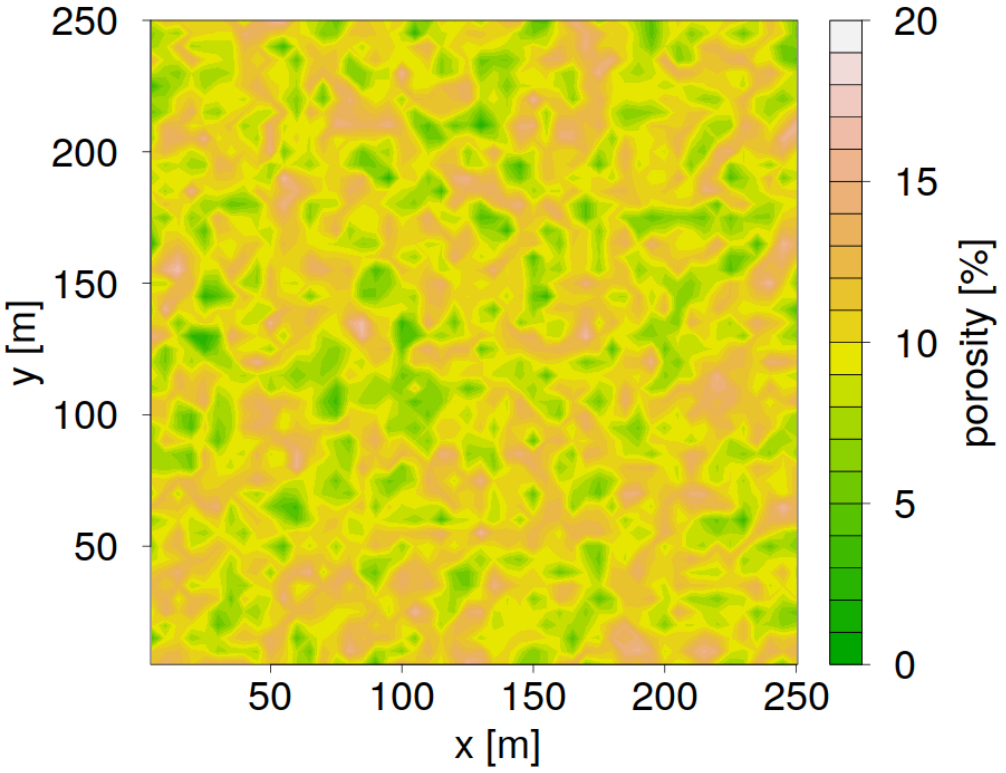

Figure 8.6: Porosity distribution: Surface view of simulation Spherical (10m) nr. 204.

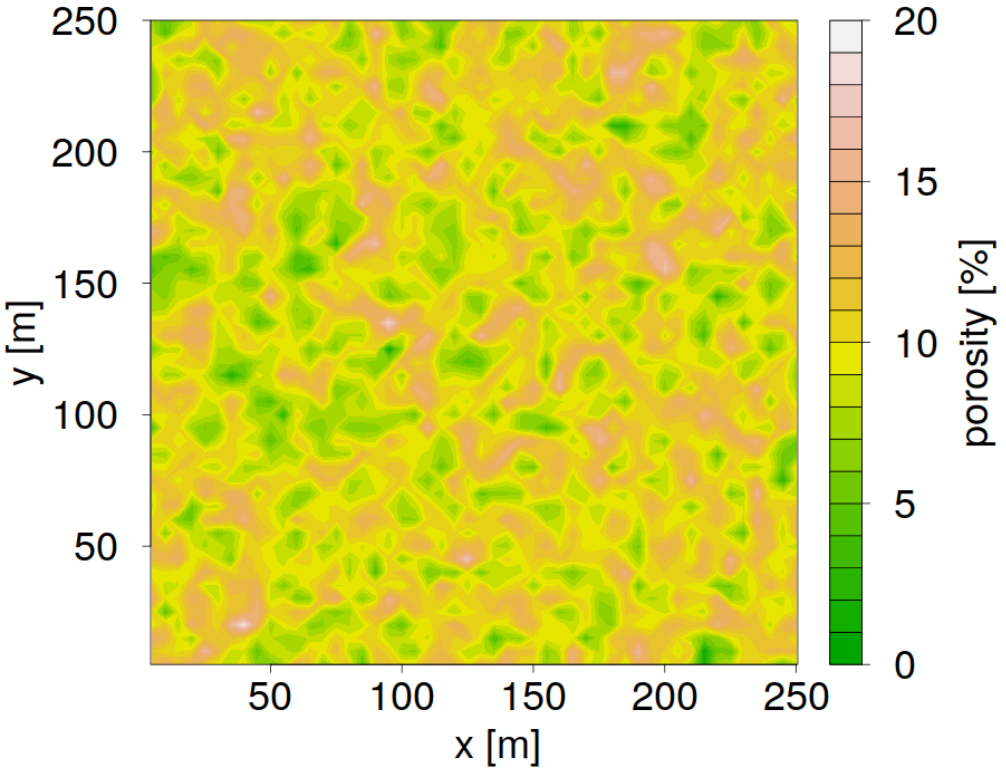

Figure 8.7: Porosity distribution: Surface view of simulation Spherical (10m) nr. 211.

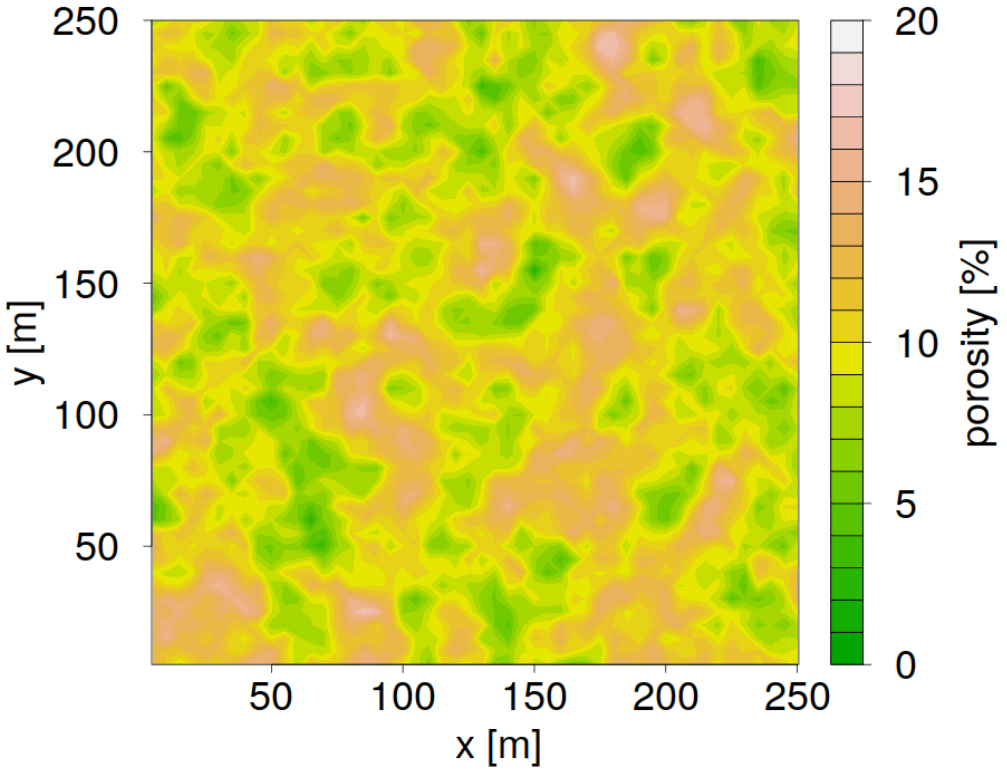

Figure 8.8: Porosity distribution: Surface view of simulation Spherical (20m) nr. 223.

8.2.2 W-E profiles

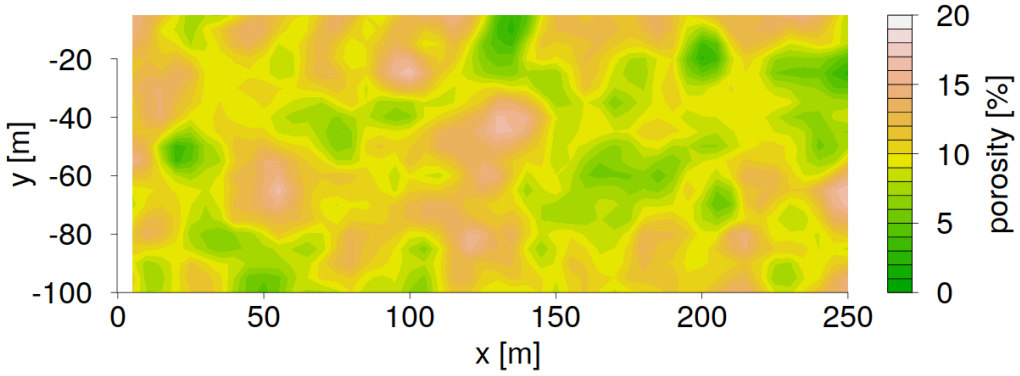

Figure 8.9: Porosity distribution: W-E profile of simulation Gaussian (10m) nr. 251.

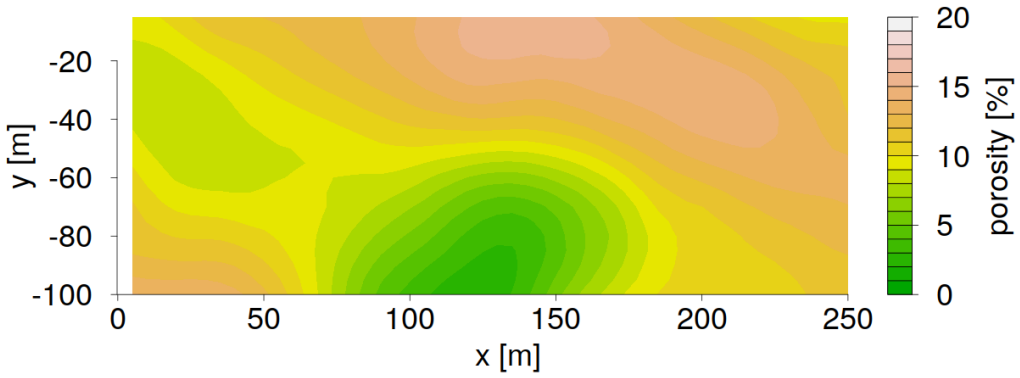

Figure 8.10: Porosity distribution: W-E profile of simulation Gaussian (50m) nr. 251.

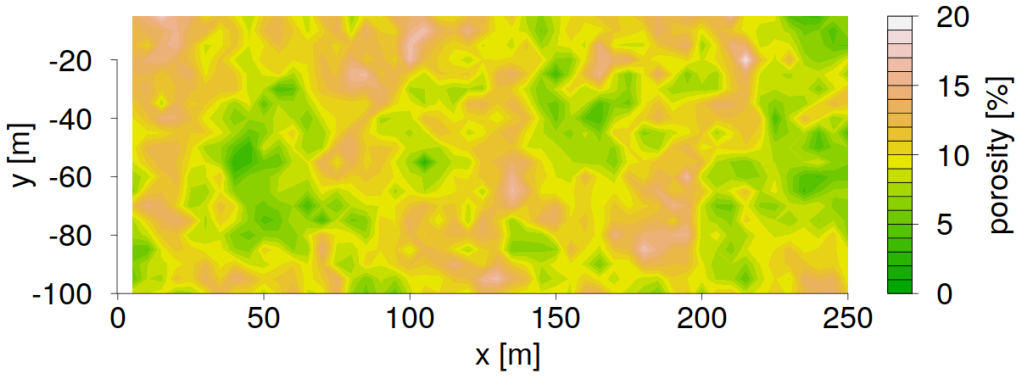

Figure 8.11: Porosity distribution: W-E profile of simulation Exponential (10m) nr. 109.

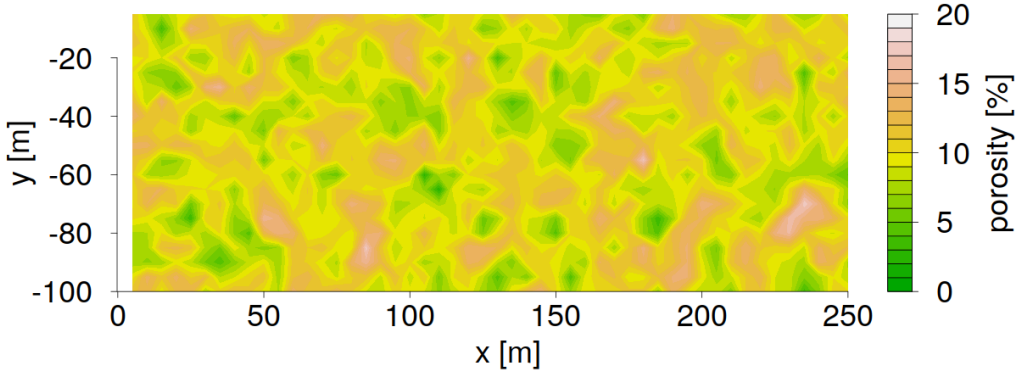

Figure 8.12: Porosity distribution: W-E profile of simulation Spherical (10m) nr. 94.

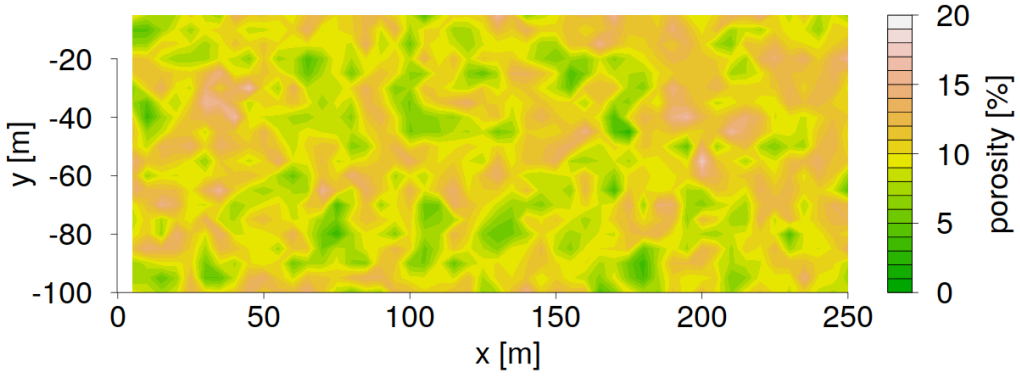

Figure 8.13: Porosity distribution: W-E profile of simulation Spherical (10m) nr. 144.

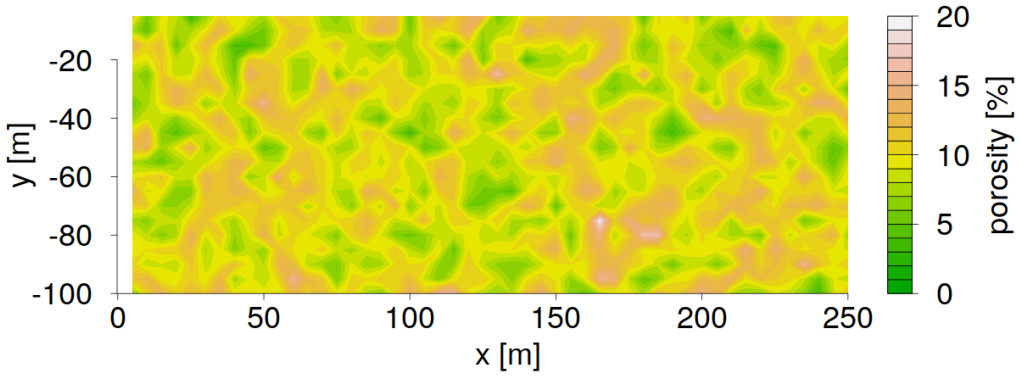

Figure 8.14: Porosity distribution: W-E profile of simulation Spherical (10m) nr. 204.

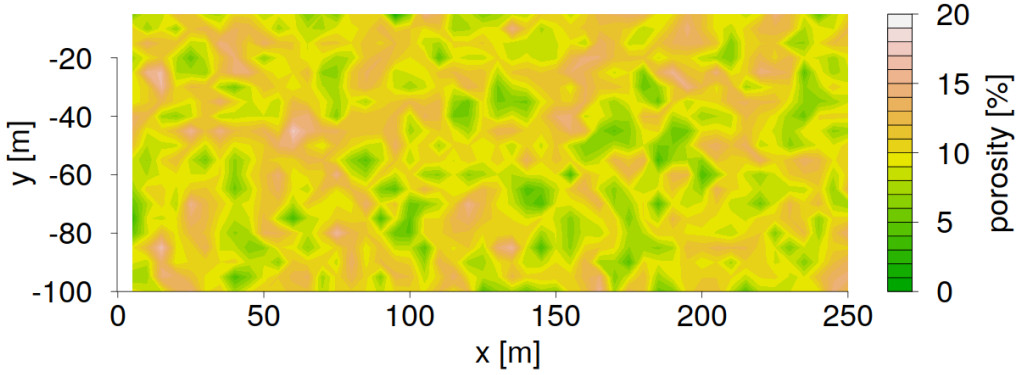

Figure 8.15: Porosity distribution: W-E profile of simulation Spherical (10m) nr. 211.

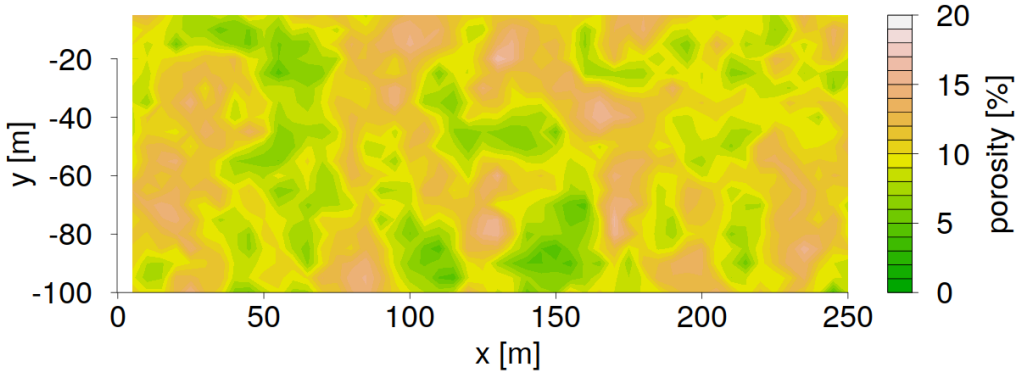

Figure 8.16: Porosity distribution: W-E profile of simulation Spherical (20m) nr. 223.

8.2.3 N-S profiles

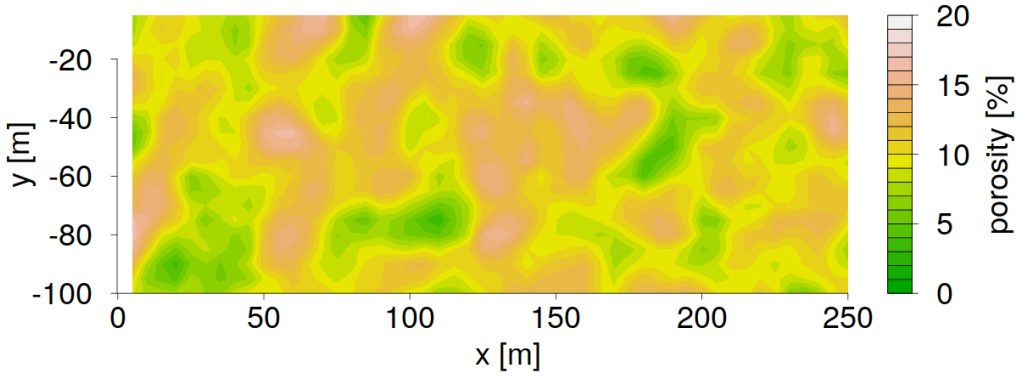

Figure 8.17: Porosity distribution: N-S profile of simulation Gaussian (10m) nr. 251.

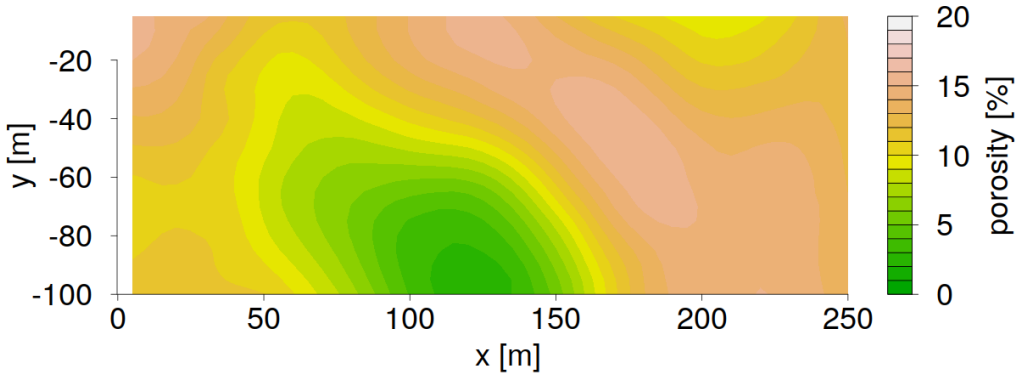

Figure 8.18: Porosity distribution: N-S profile of simulation Gaussian (50m) nr. 251.

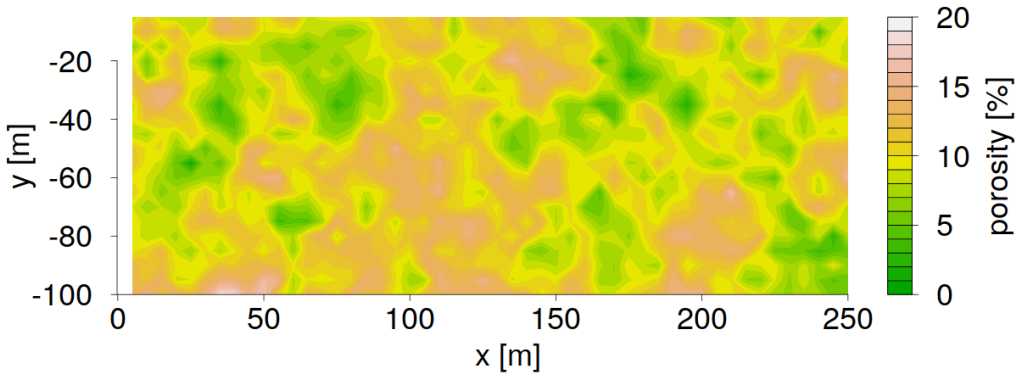

Figure 8.19: Porosity distribution: N-S profile of simulation Exponential (10m) nr. 109.

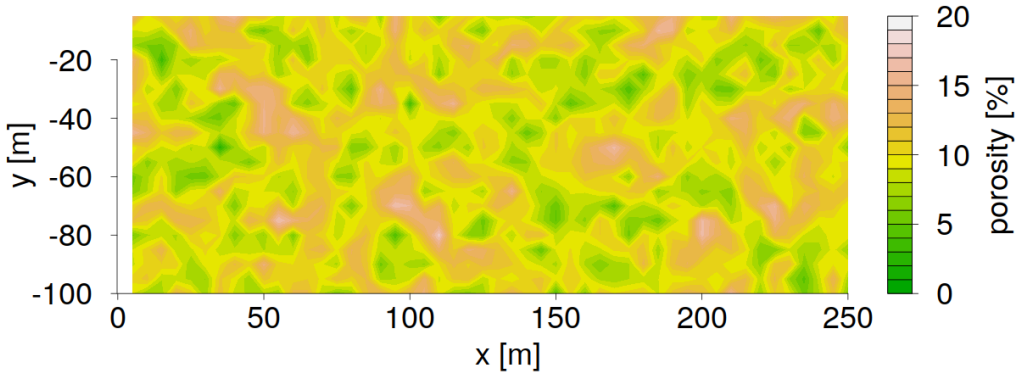

Figure 8.20: Porosity distribution: N-S profile of simulation Spherical (10m) nr. 94.

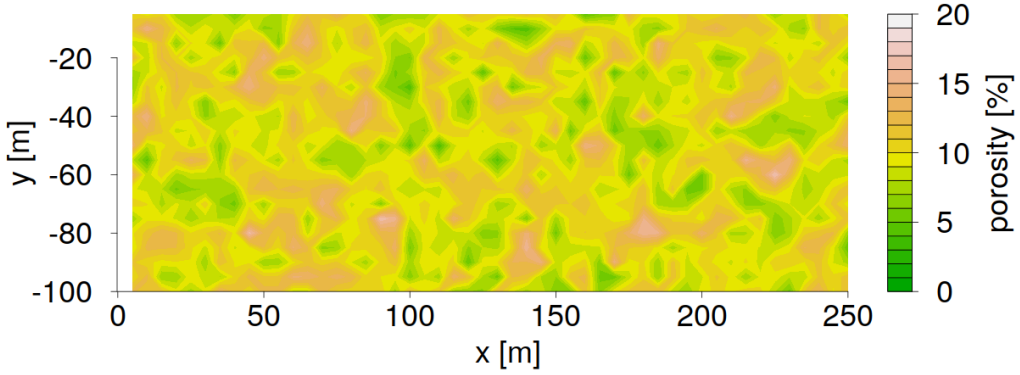

Figure 8.21: Porosity distribution: N-S profile of simulation Spherical (10m) nr. 144.

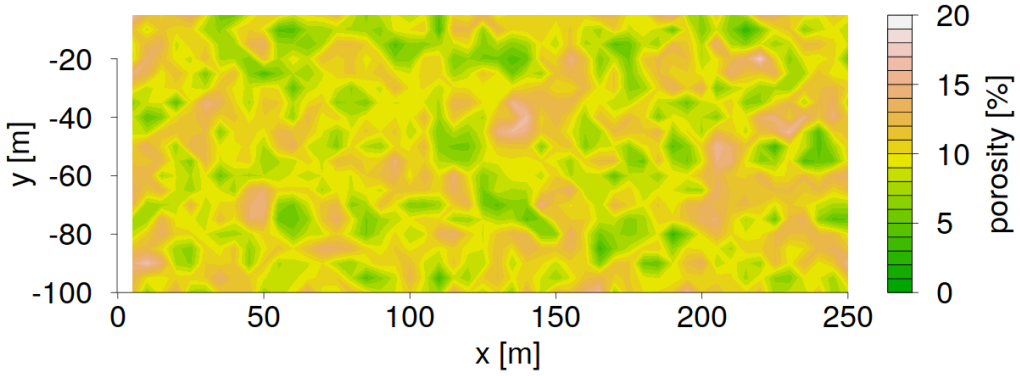

Figure 8.22: Porosity distribution: N-S profile of simulation Spherical (10m) nr. 204.

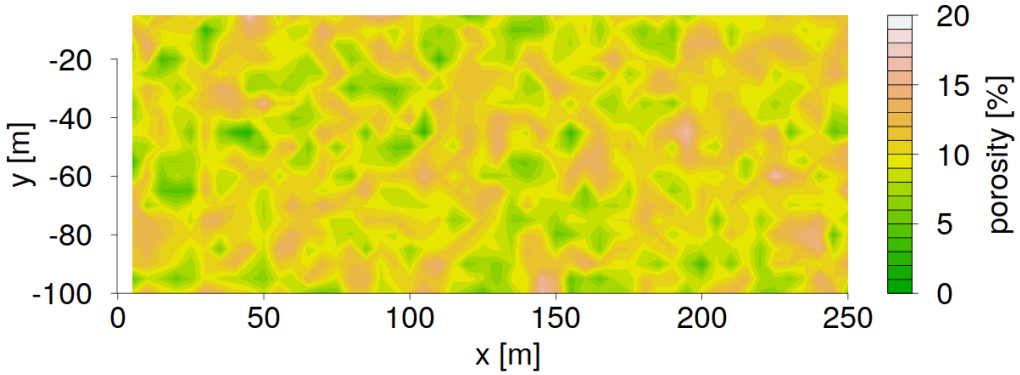

Figure 8.23: Porosity distribution: N-S profile of simulation Spherical (10m) nr. 211.

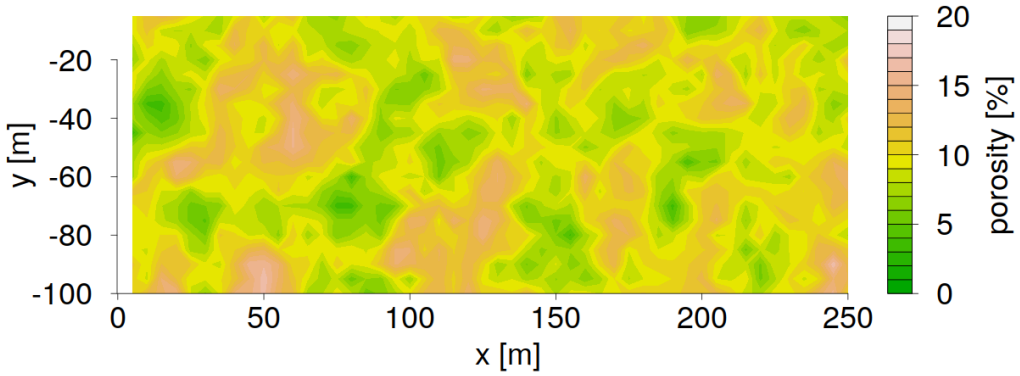

Figure 8.24: Porosity distribution: N-S profile of simulation Spherical (20m) nr. 223.

8.3 Geostatistical simulations: Directional variograms

The results of the directional variogram analysis is given for the simulated 3D subsurface porosity distributions. Several orientations given in degrees clockwise from N were tested: 0, 10, 20, 45, 90, 120, 135, 155, 180 and 270. This analysis was carried out for profiles in NS and WE direction and for the top view.

8.3.1 Surface views

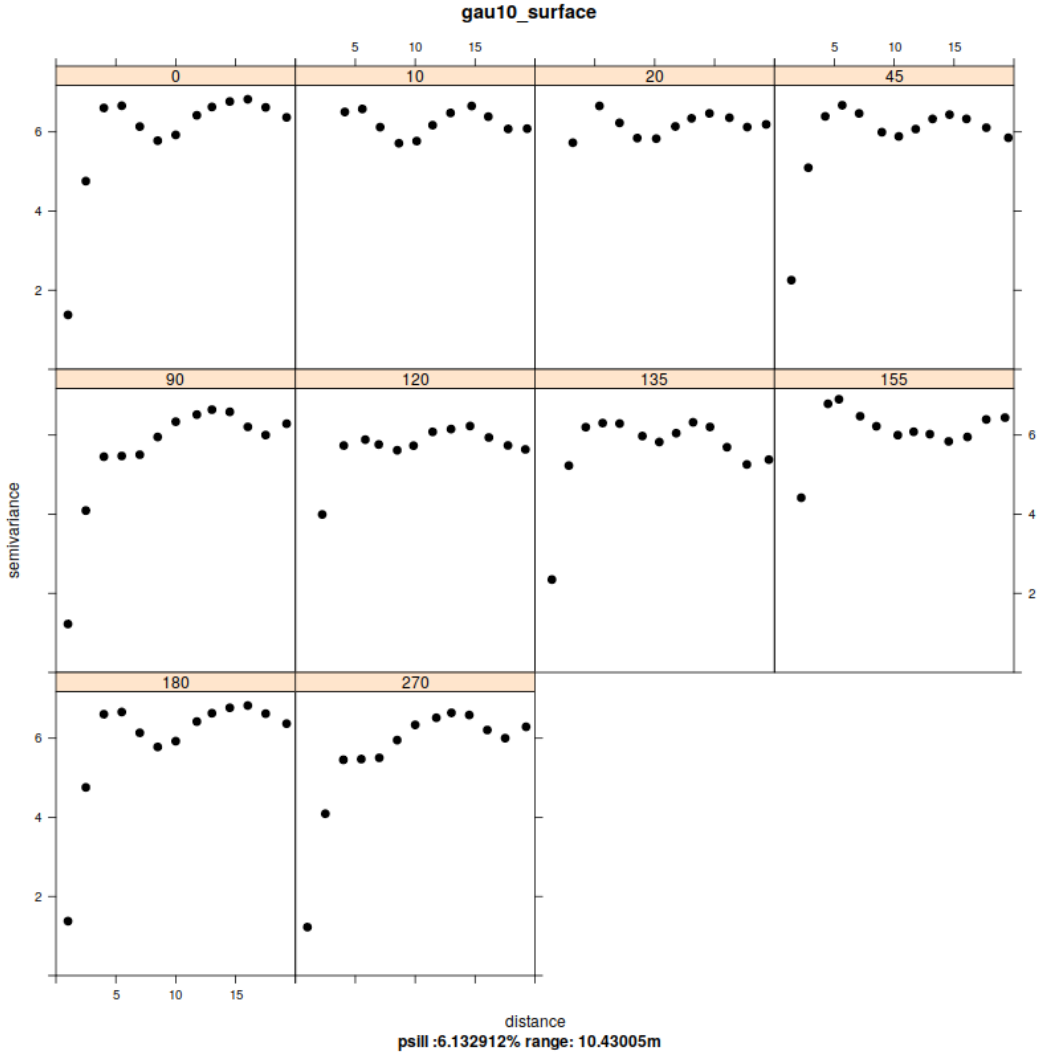

Figure 8.25: Directional variogram analysis of surface layer of the simulation Gaussian (10m) nr. 251.

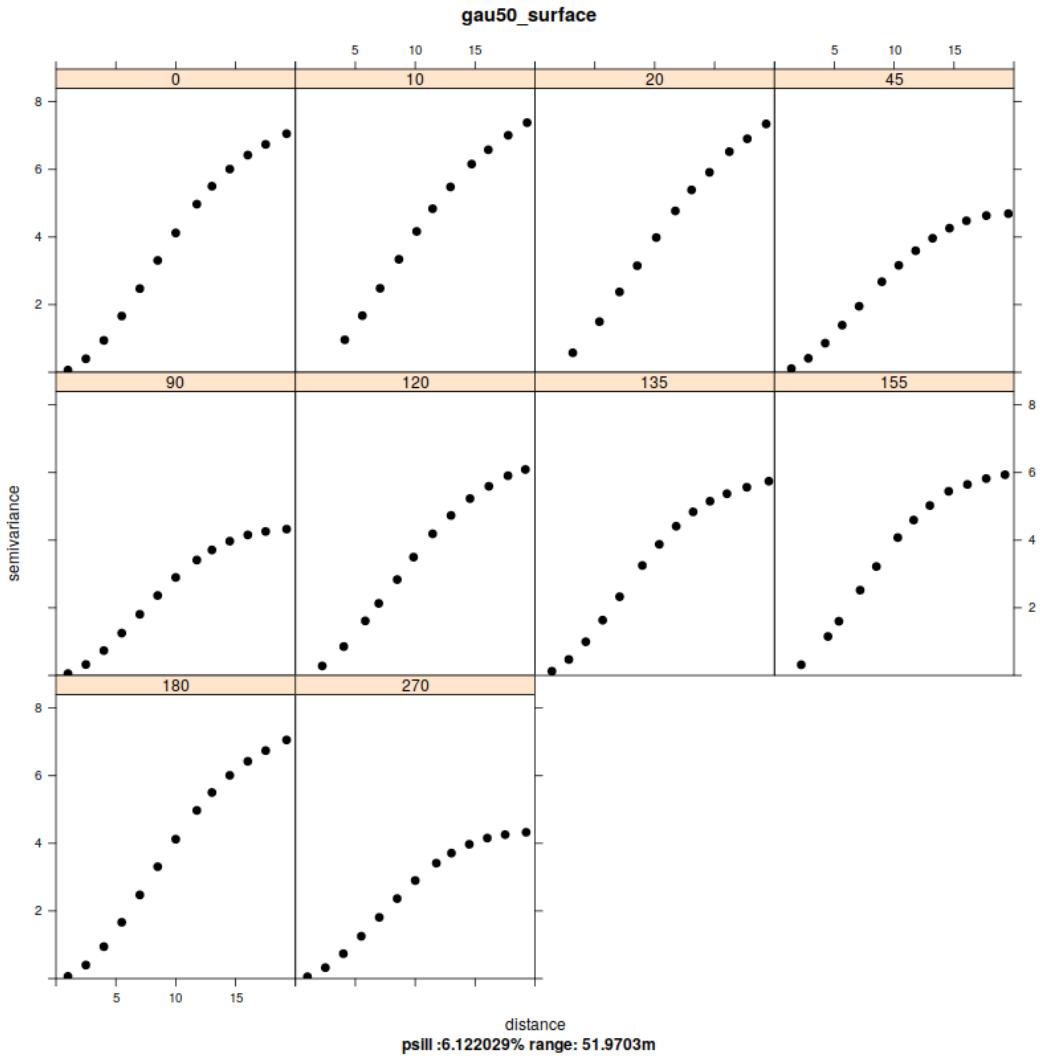

Figure 8.26: Directional variogram analysis of surface layer of the simulation Gaussian (50m) nr. 251.

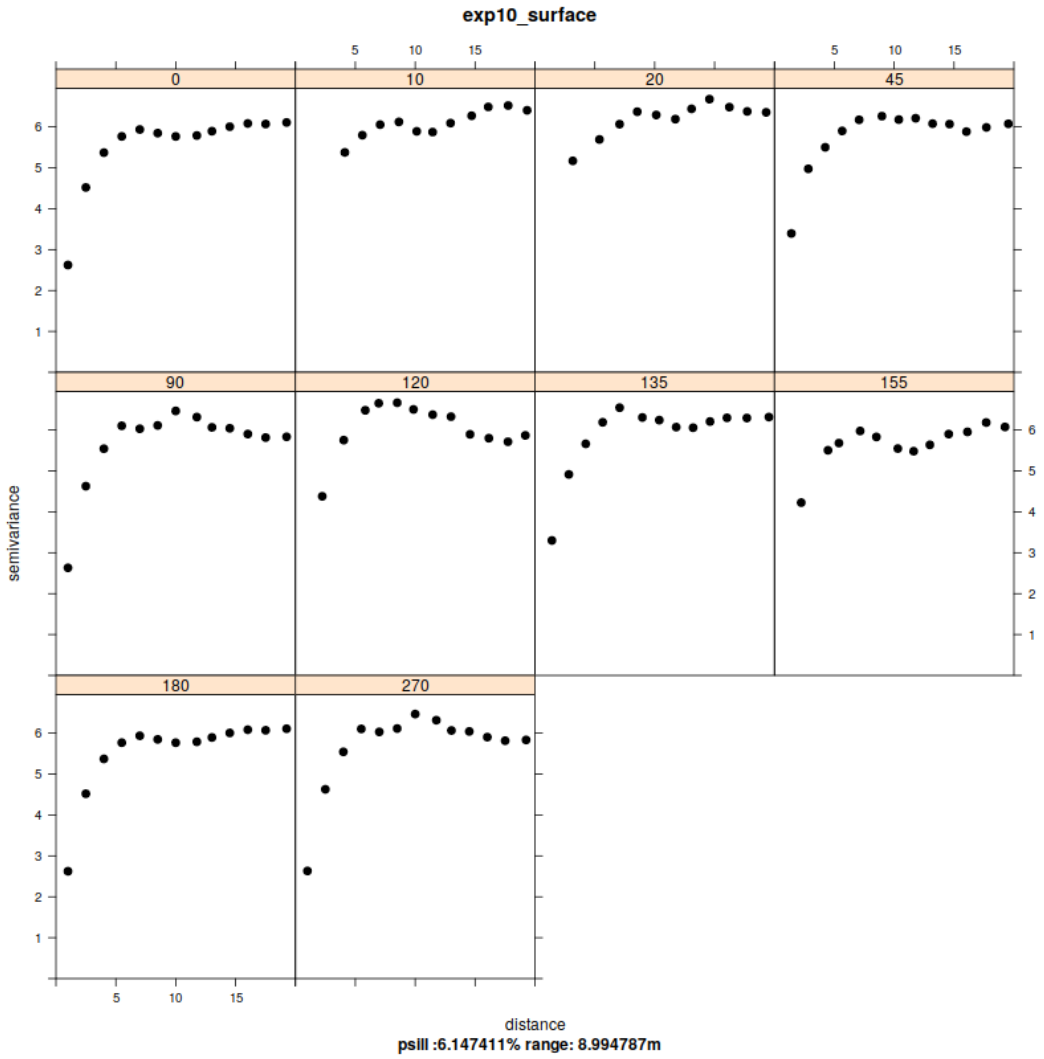

Figure 8.27: Directional variogram analysis of surface layer of the simulation exponential (10m) nr. 109.

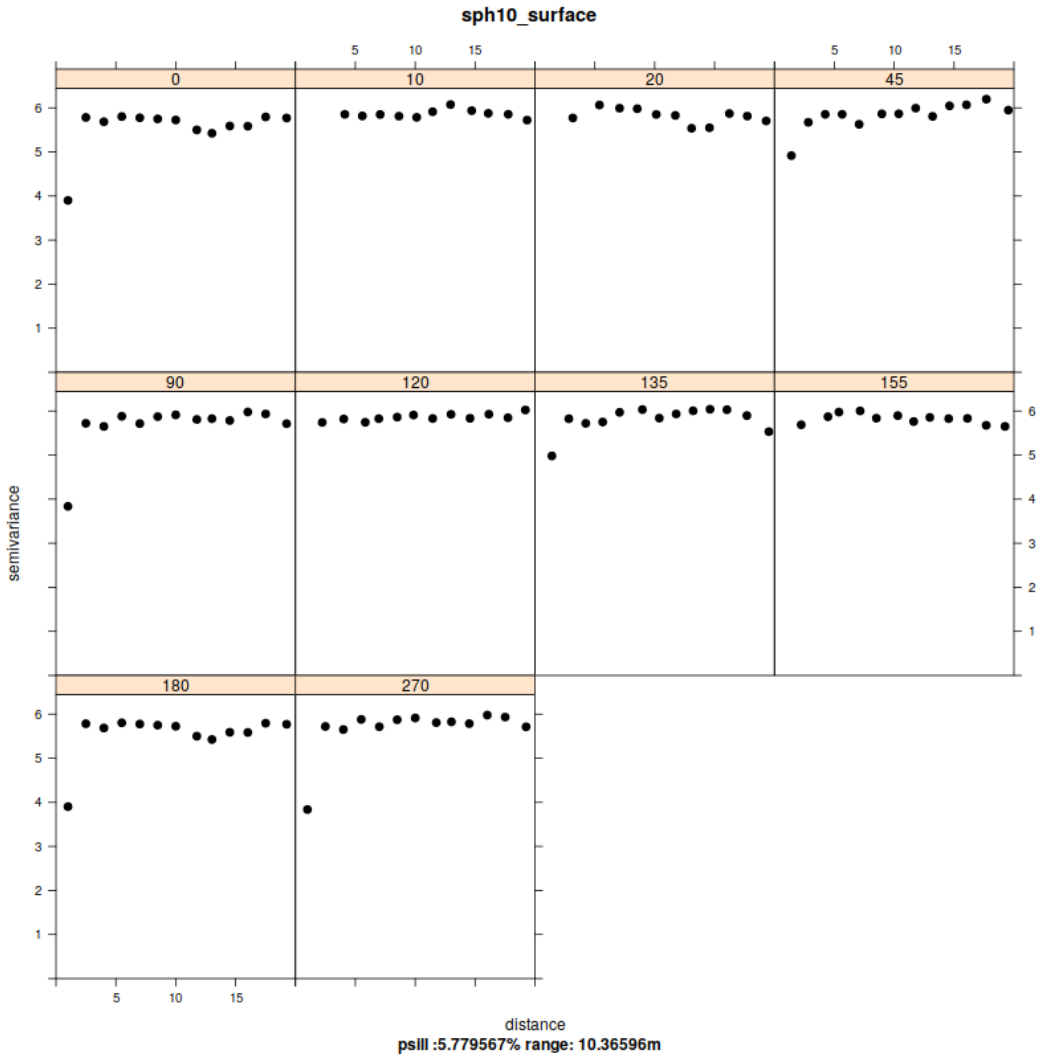

Figure 8.28: Directional variogram analysis of surface layer of the simulation spherical (10m) nr. 94.

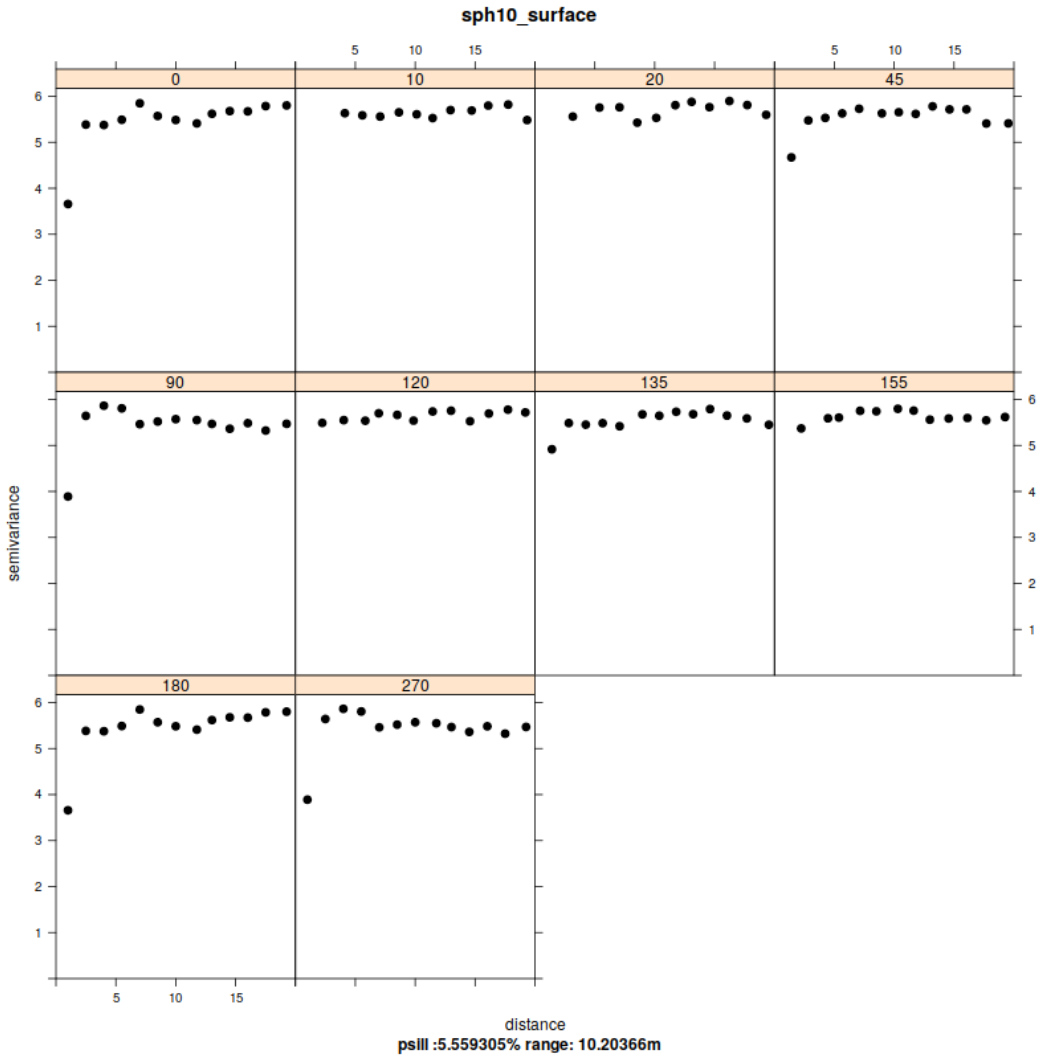

Figure 8.29: Directional variogram analysis of surface layer of the simulation spherical (10m) nr. 144.

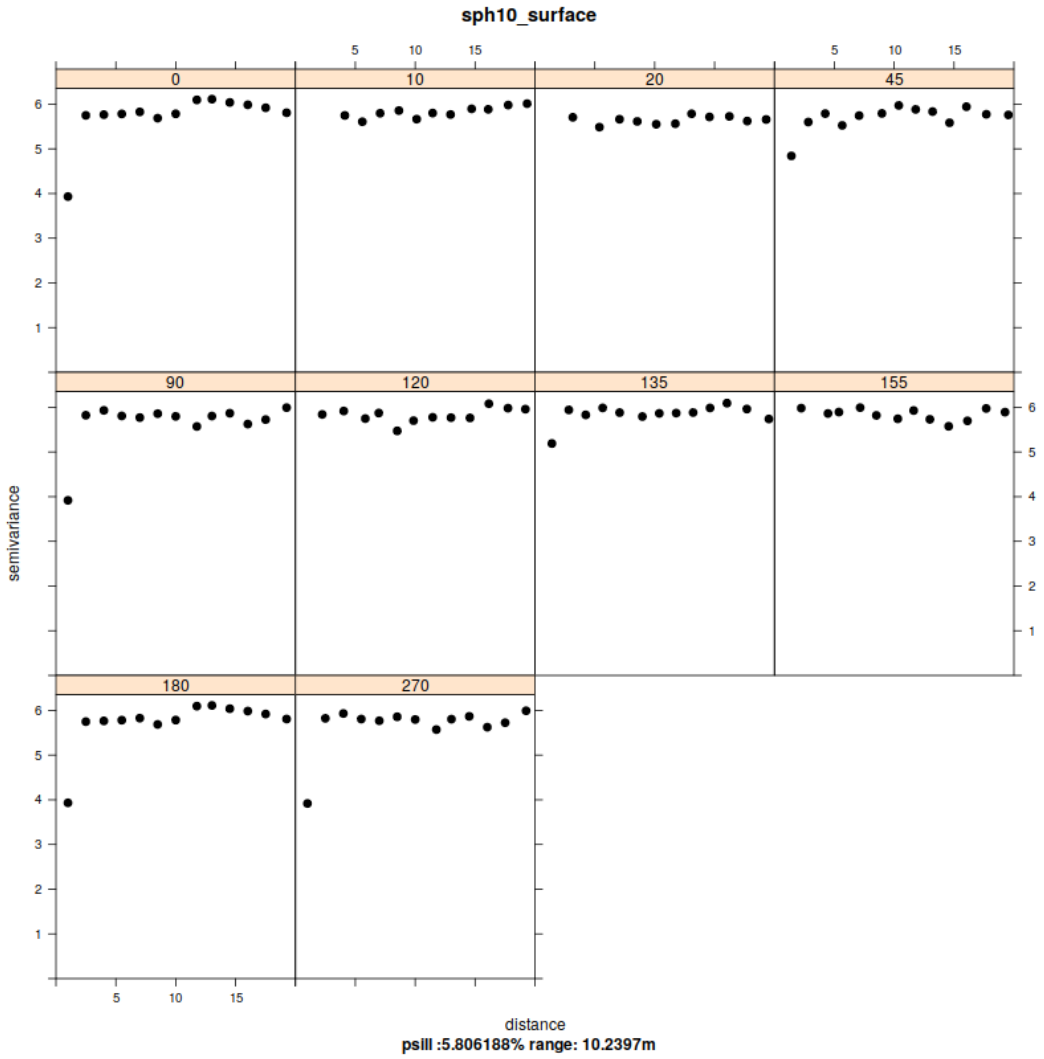

Figure 8.30: Directional variogram analysis of surface layer of the simulation spherical (10m) nr. 204.

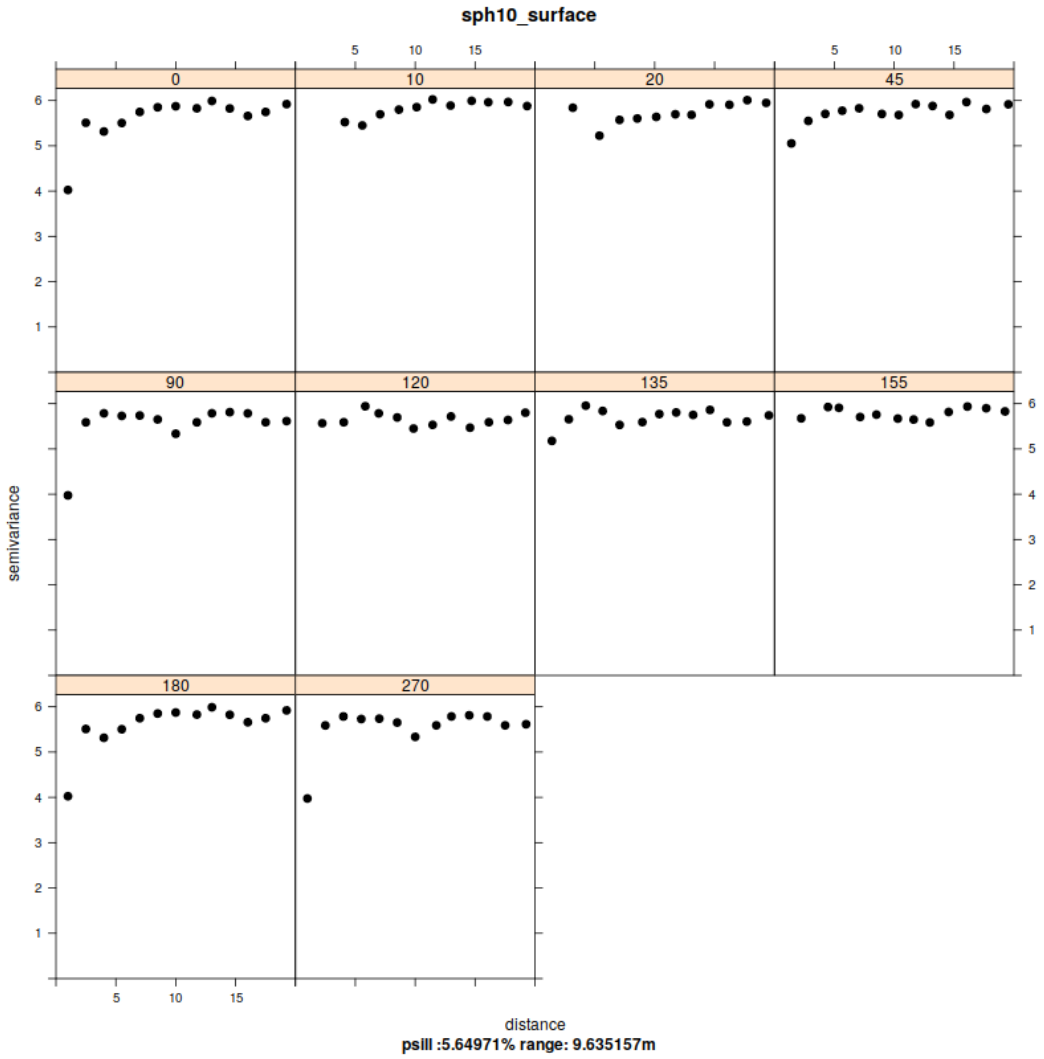

Figure 8.31: Directional variogram analysis of surface layer of the simulation spherical (10m) nr. 211.

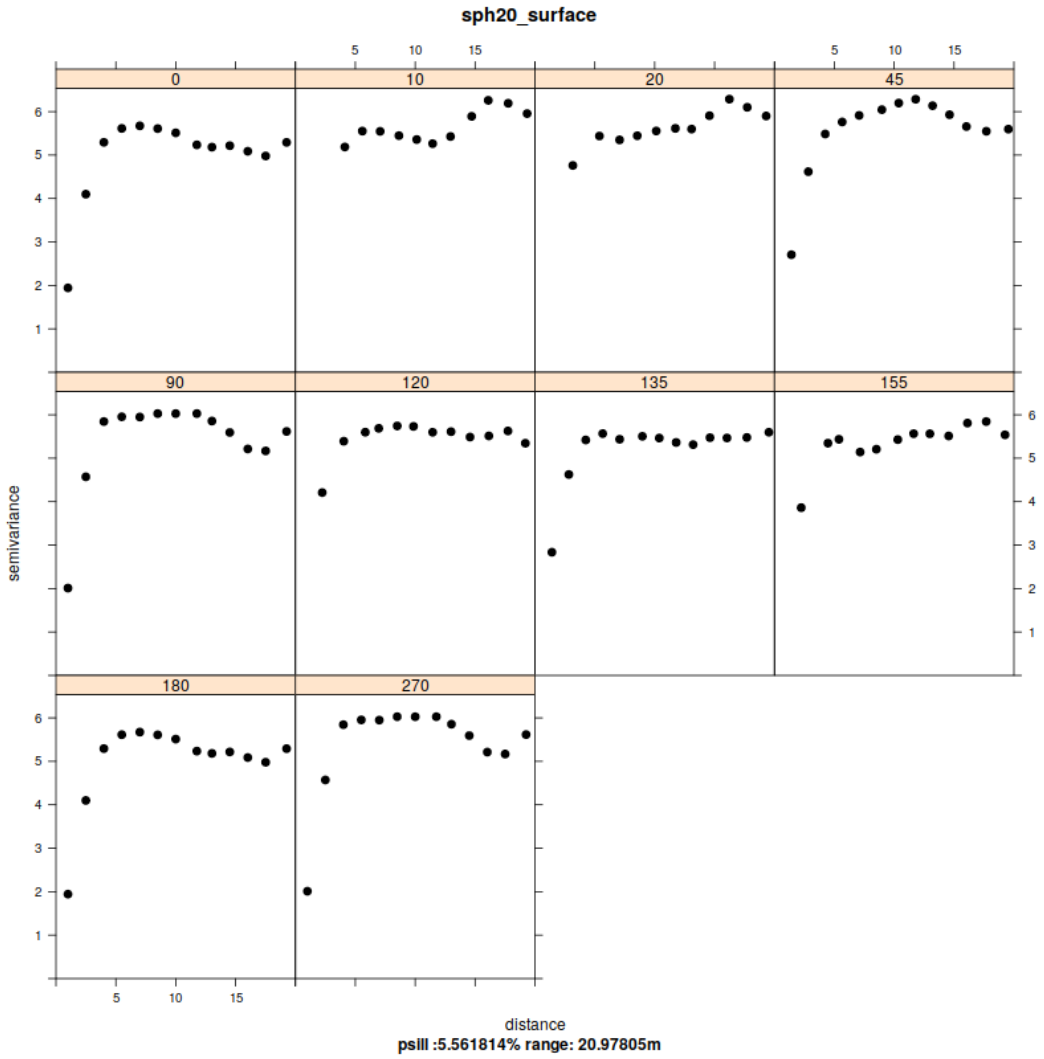

Figure 8.32: Directional variogram analysis of surface layer of the simulation spherical (20m) nr. 223.

8.3.2 W-E profiles

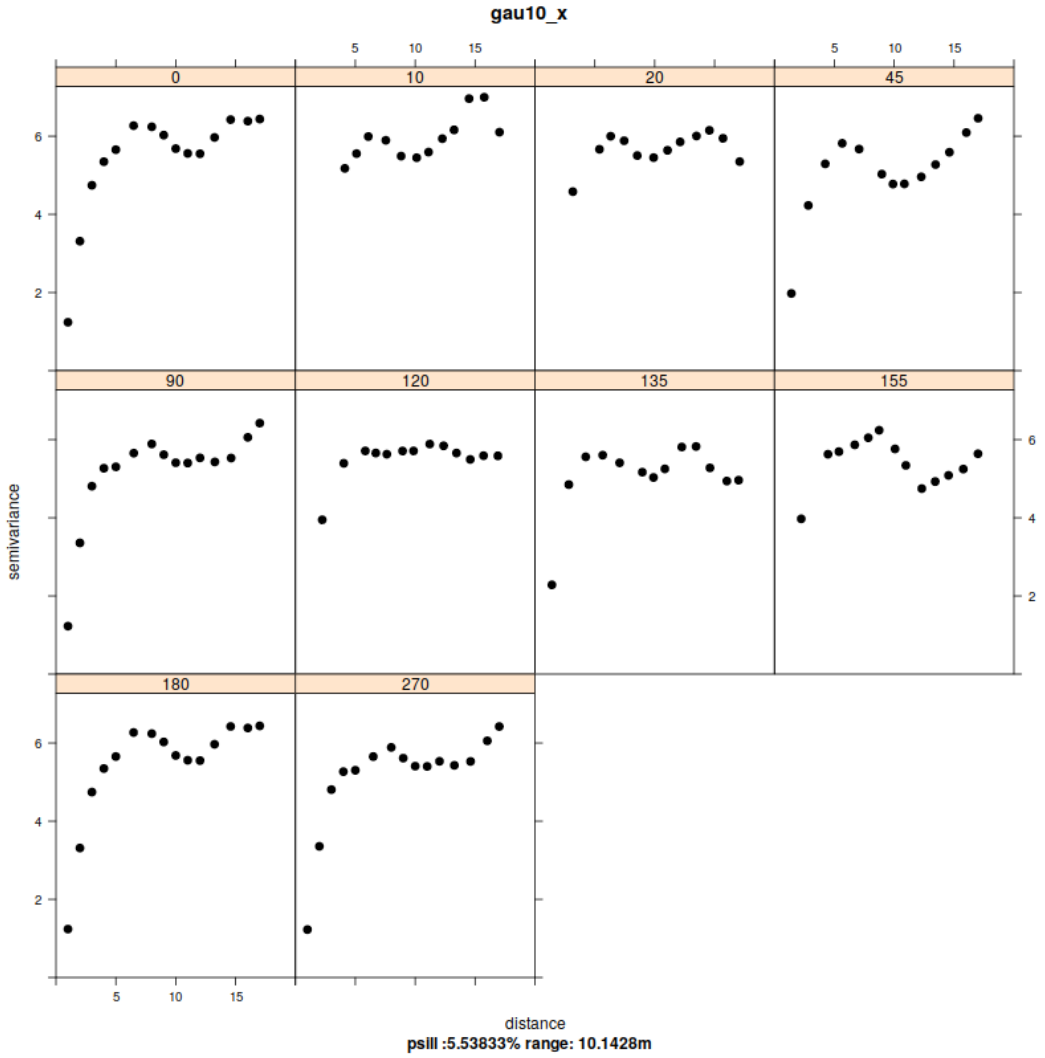

Figure 8.33: Directional variogram analysis of W-E profile of the simulation Gaussian (10m) nr. 251.

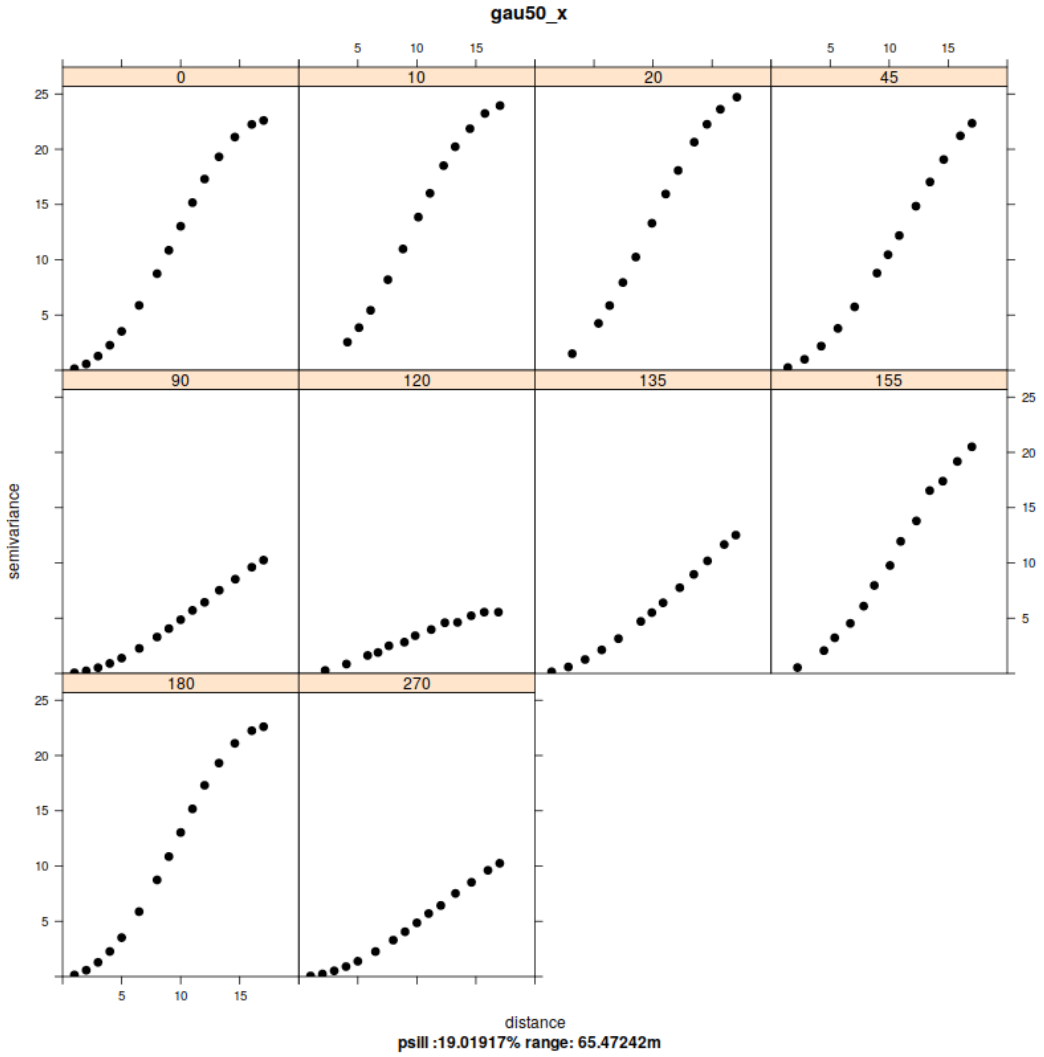

Figure 8.34: Directional variogram analysis of W-E profile of the simulation Gaussian (50m) nr. 251.

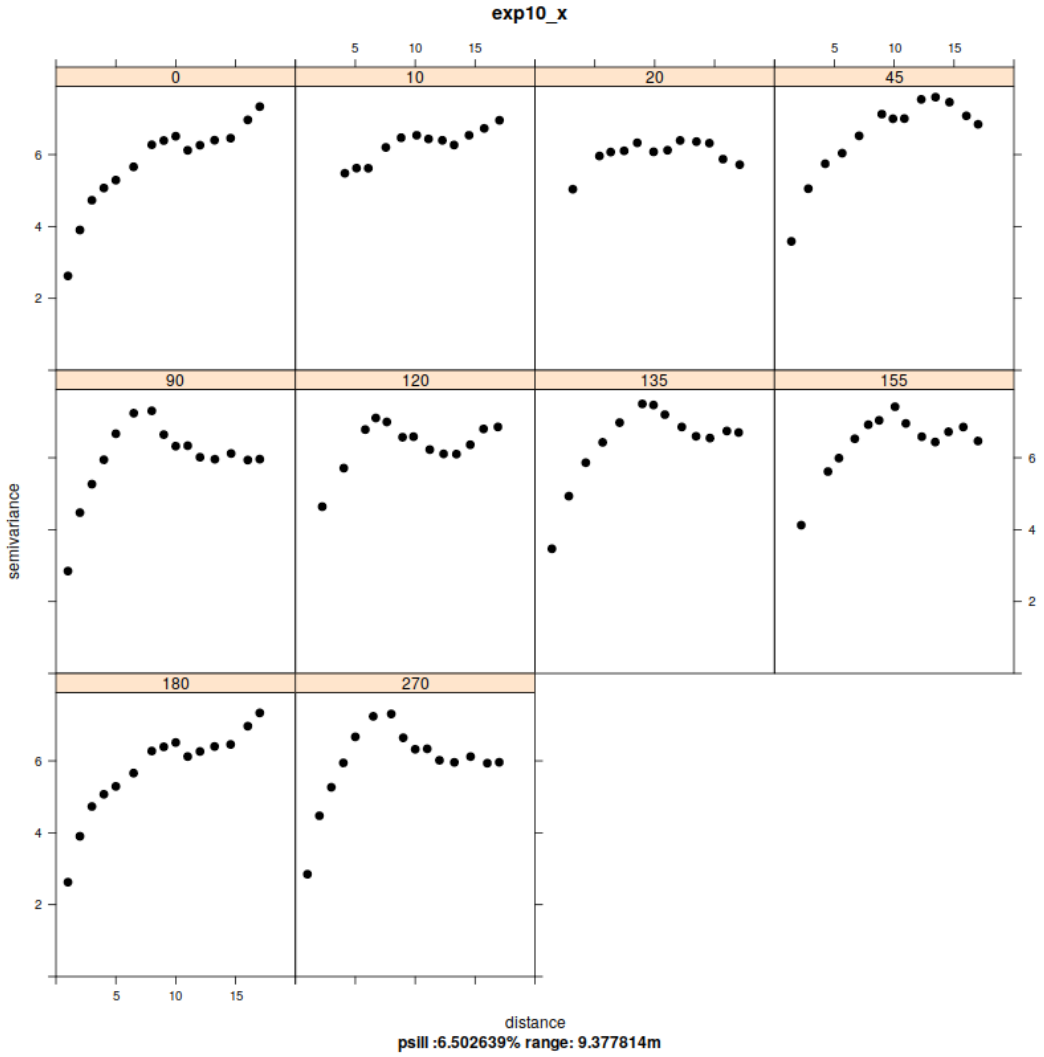

Figure 8.35: Directional variogram analysis of W-E profile of the simulation exponential (10m) nr. 109.

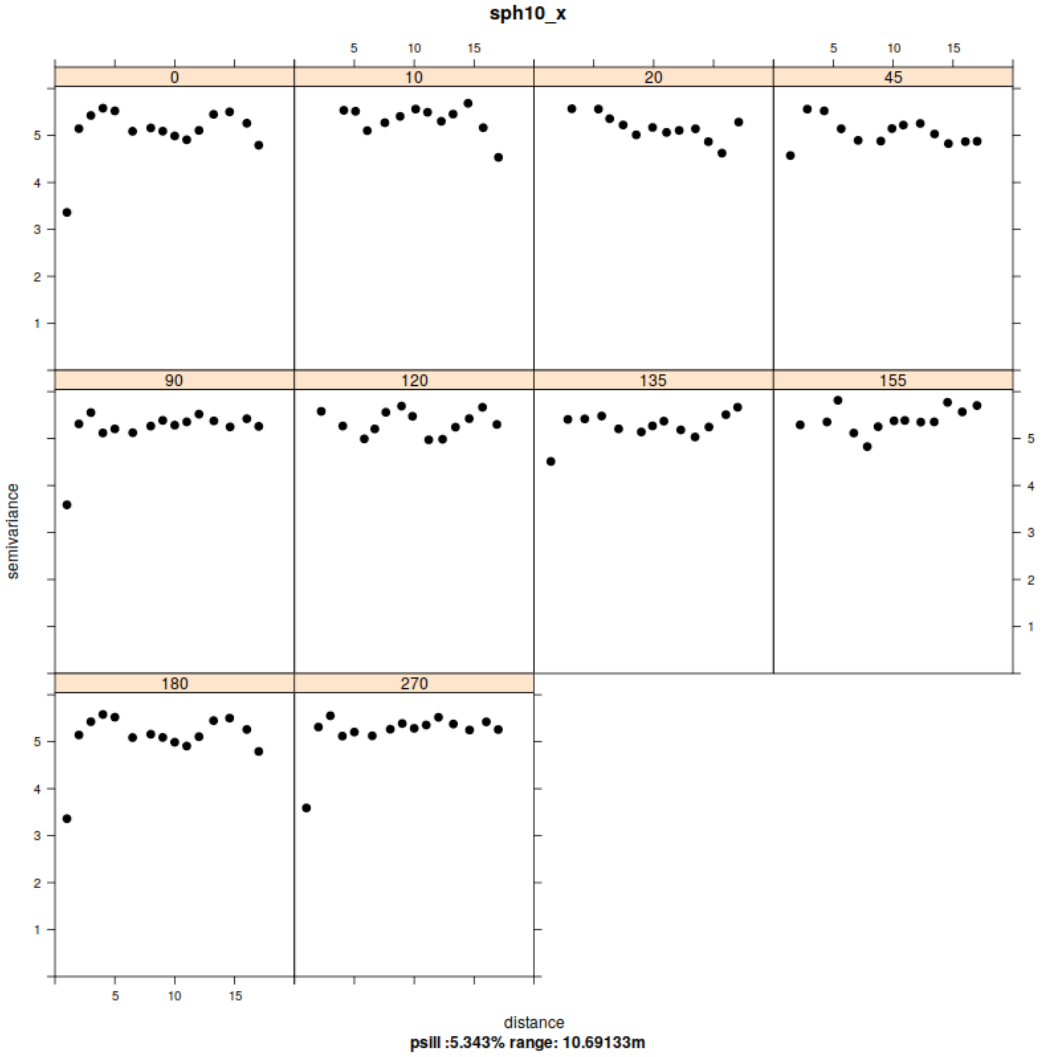

Figure 8.36: Directional variogram analysis of W-E profile of the simulation spherical (10m) nr. 94.

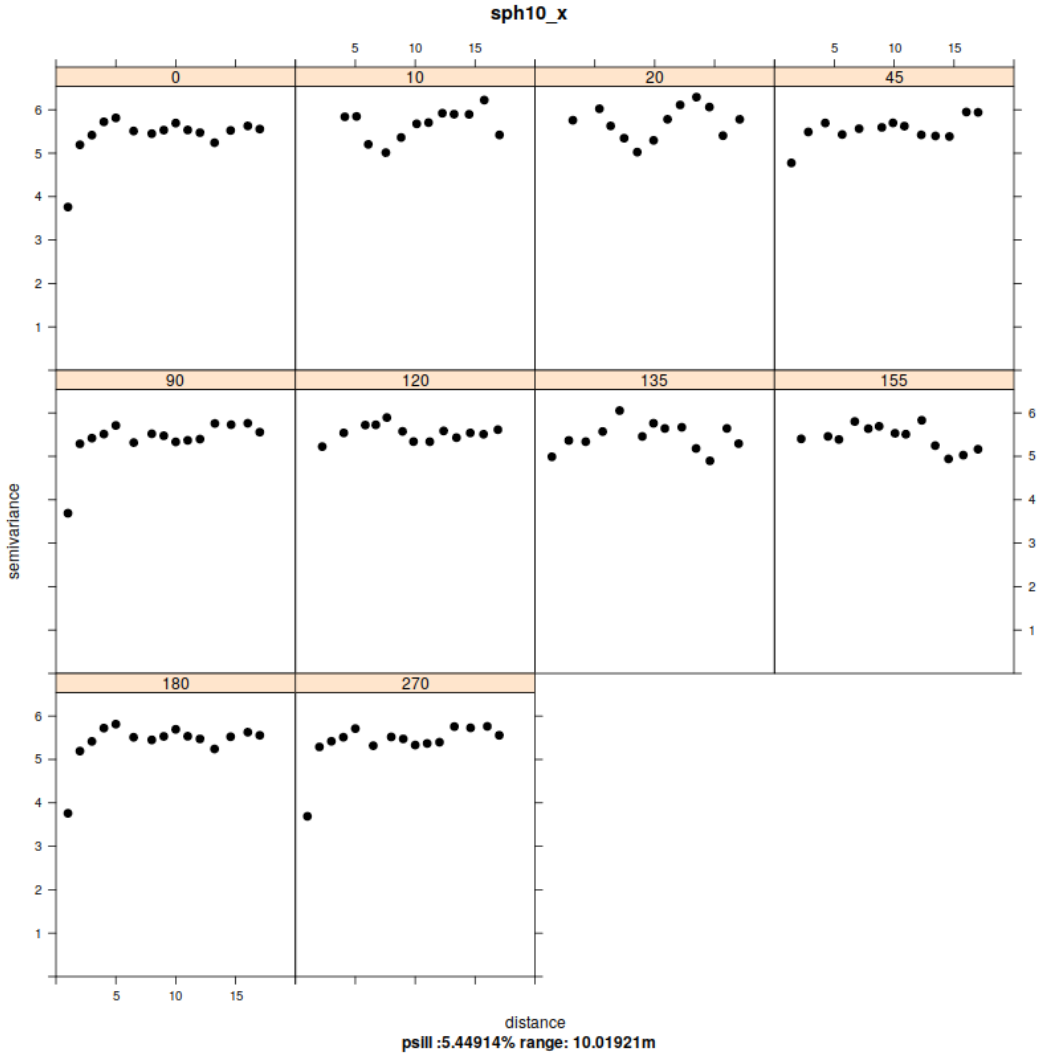

Figure 8.37: Directional variogram analysis of W-E profile of the simulation spherical (10m) nr. 144.

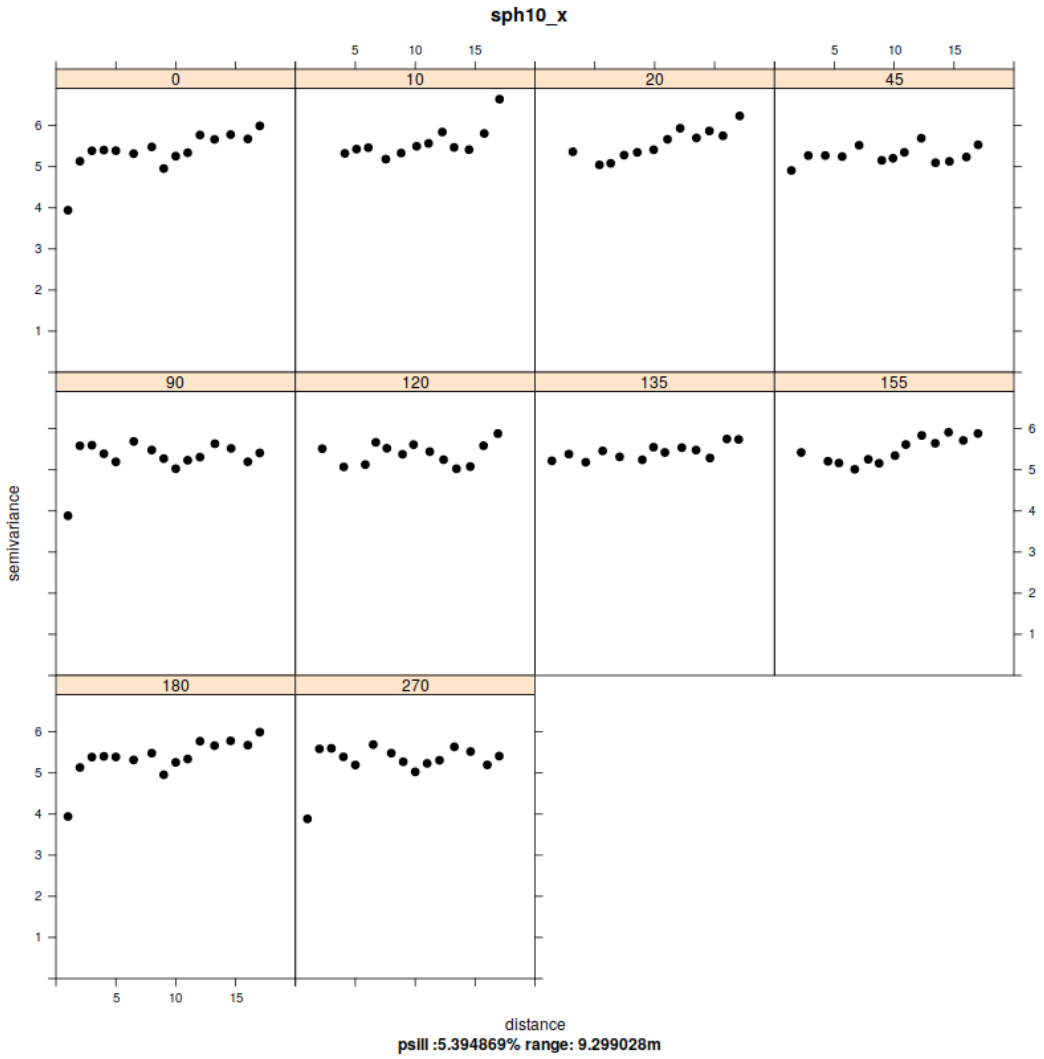

Figure 8.38: Directional variogram analysis of W-E profile of the simulation spherical (10m) nr. 204.

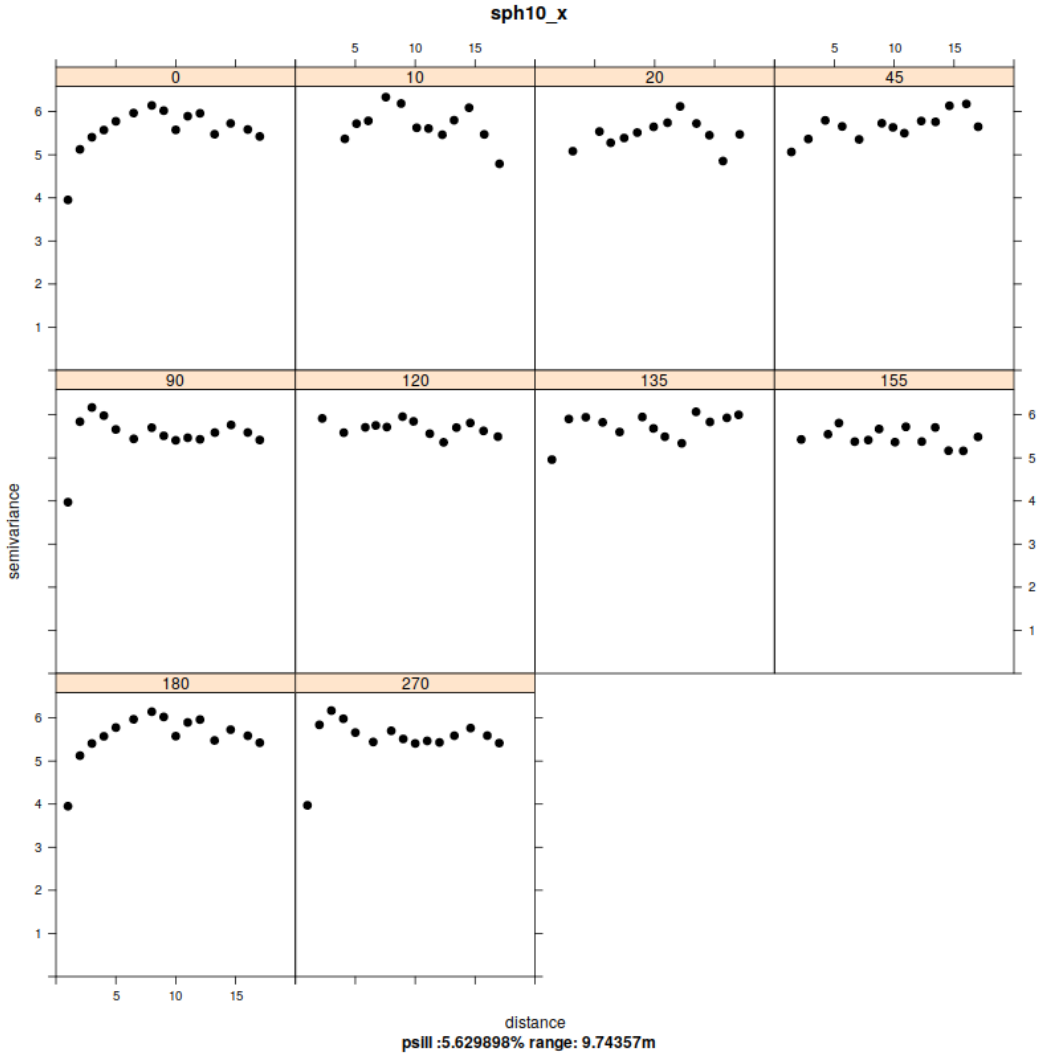

Figure 8.39: Directional variogram analysis of W-E profile of the simulation spherical (10m) nr. 211.

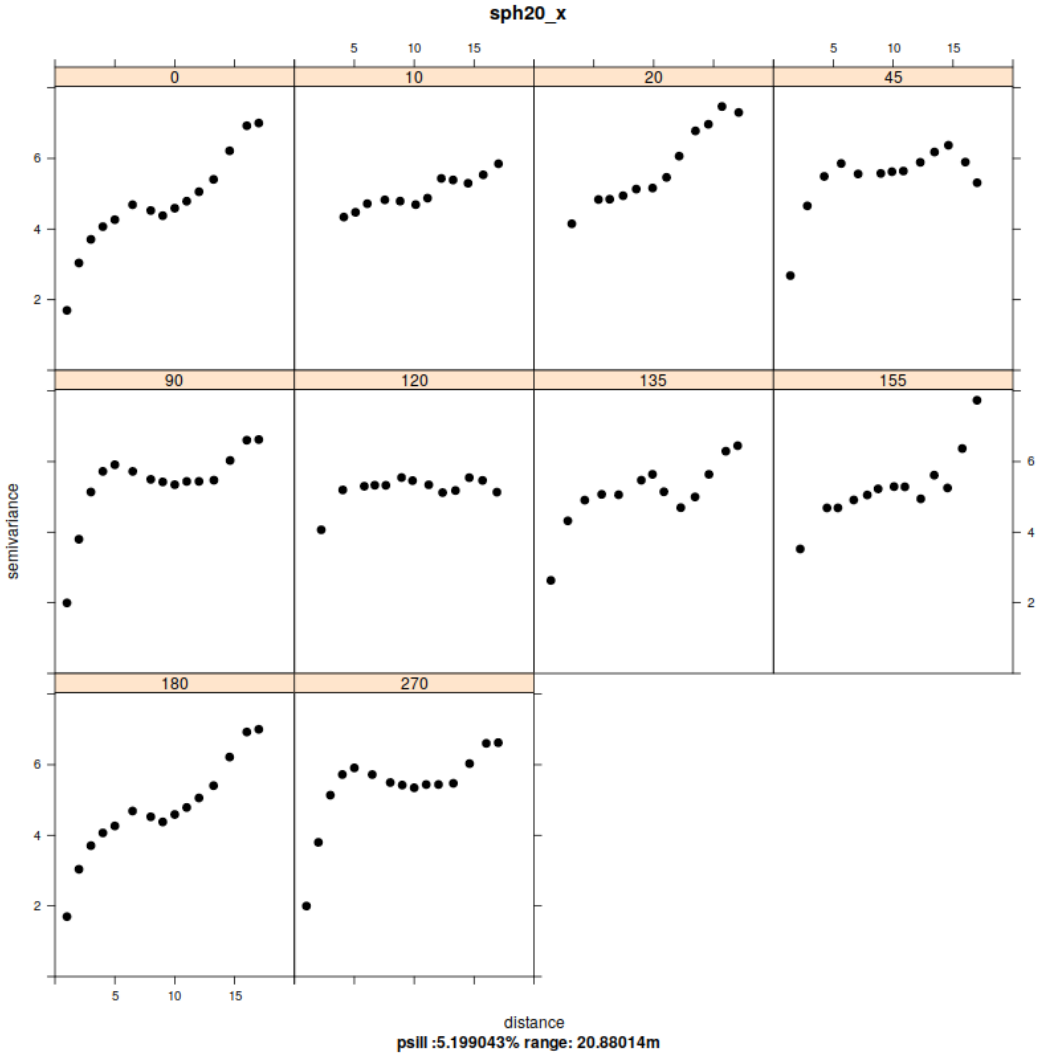

Figure 8.40: Directional variogram analysis of W-E profile of the simulation spherical (20m) nr. 223.

8.3.3 N-S profiles

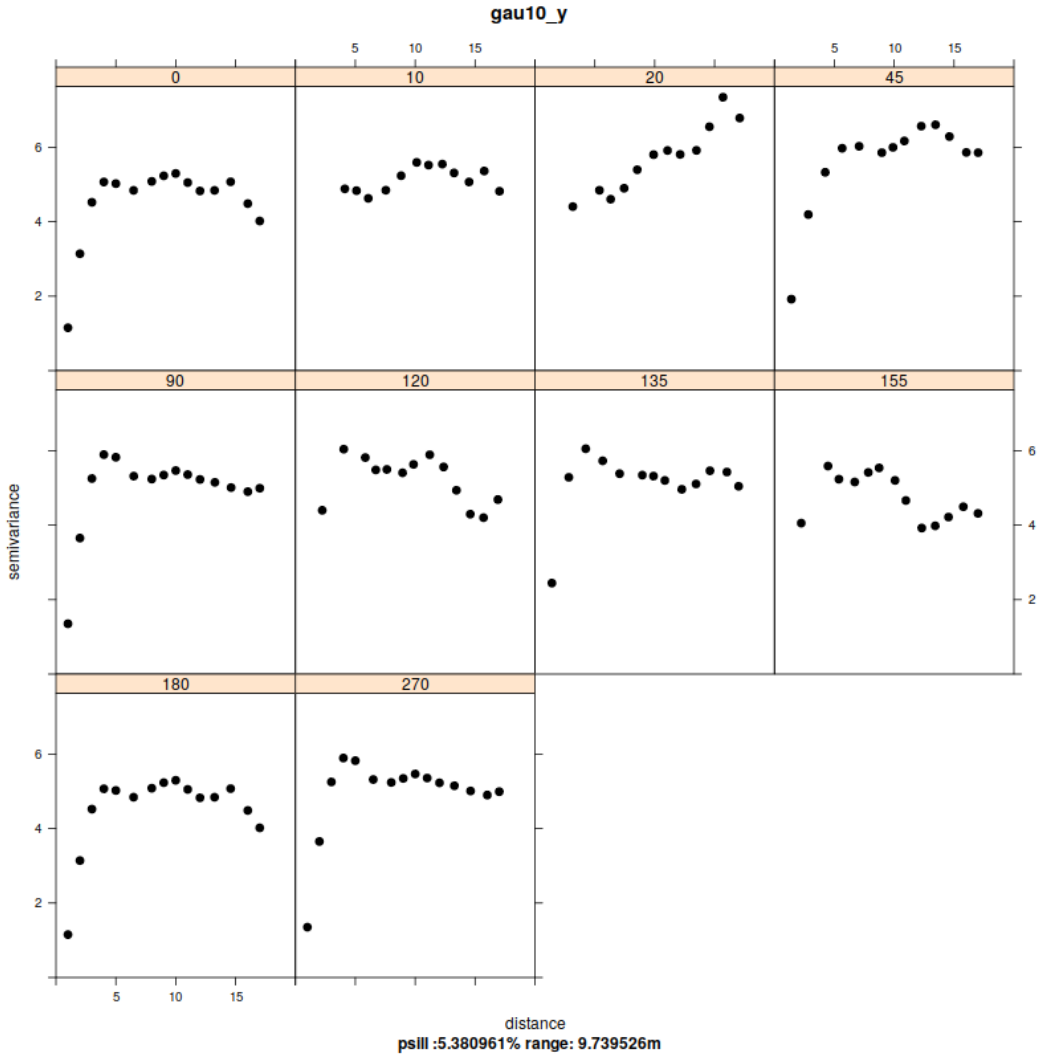

Figure 8.41: Directional variogram analysis of N-S profile of the simulation Gaussian (10m) nr. 251.

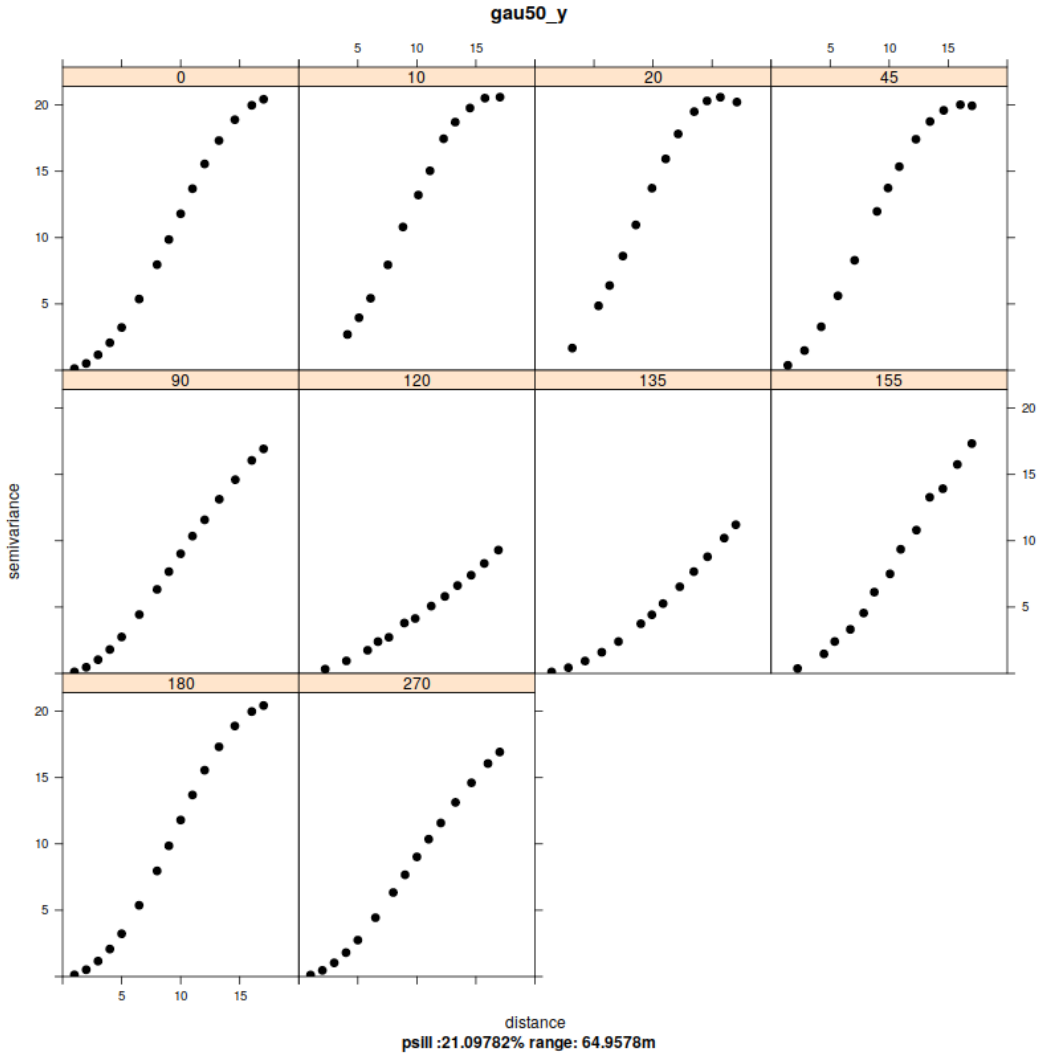

Figure 8.42: Directional variogram analysis of N-S profile of the simulation Gaussian (50m) nr. 251.

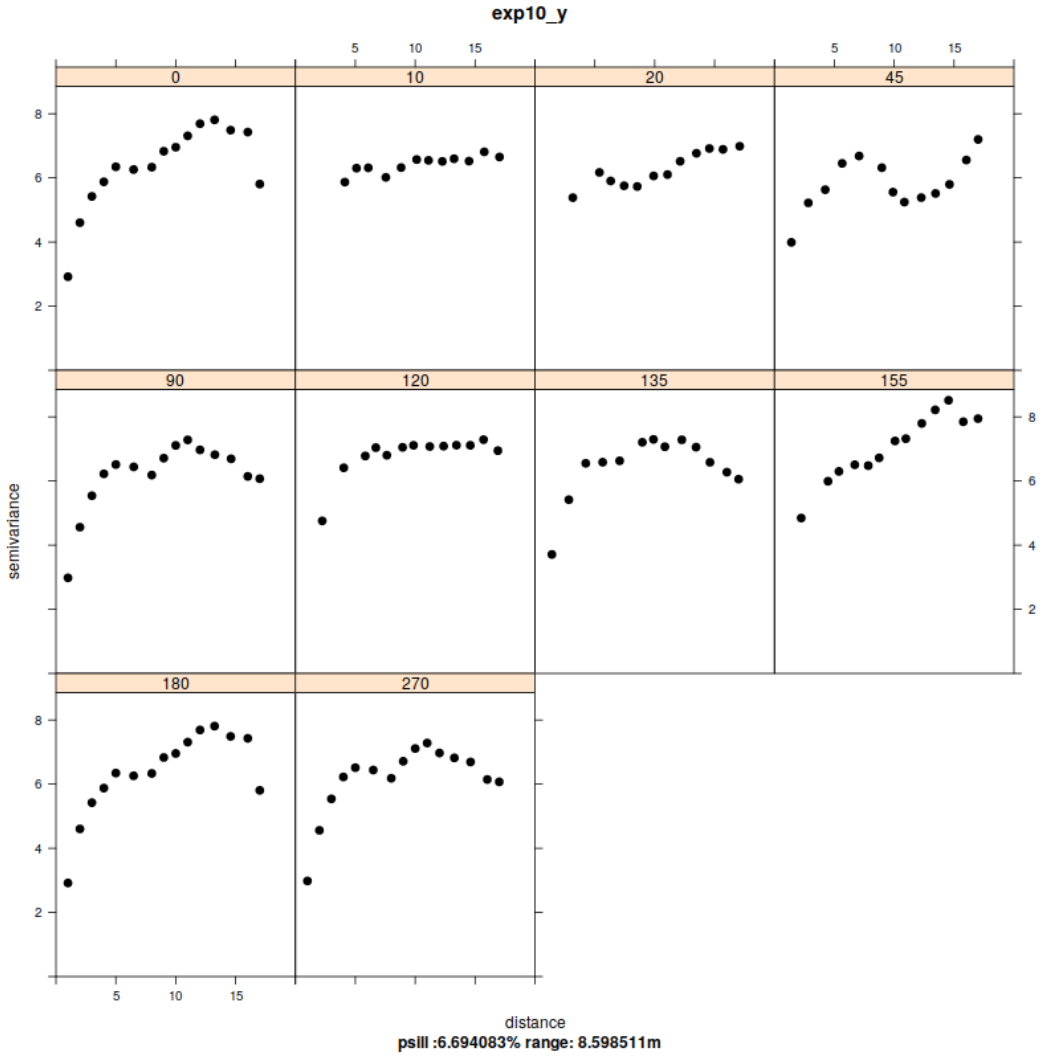

Figure 8.43: Directional variogram analysis of N-S profile of the simulation exponential (10m) nr. 109.

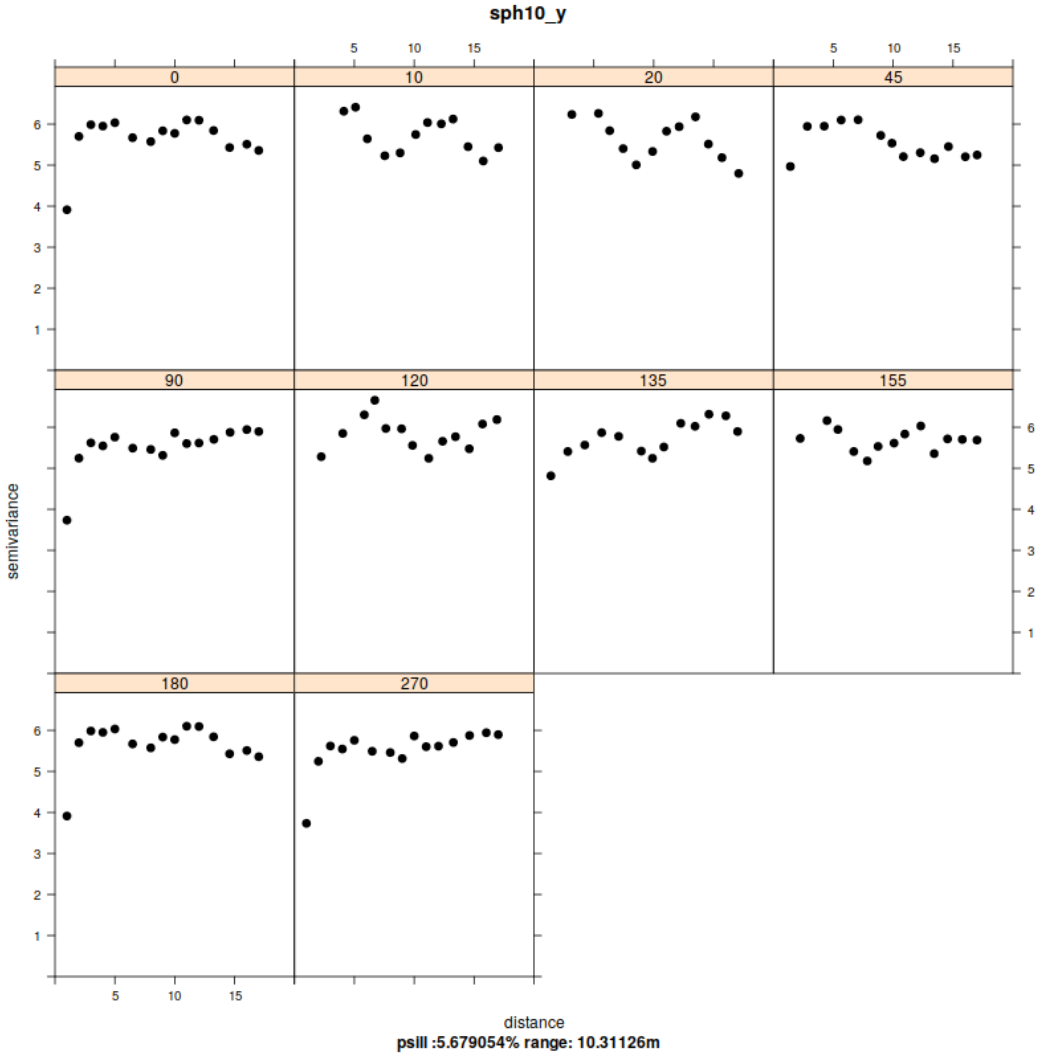

Figure 8.44: Directional variogram analysis of N-S profile of the simulation spherical (10m) nr. 94.

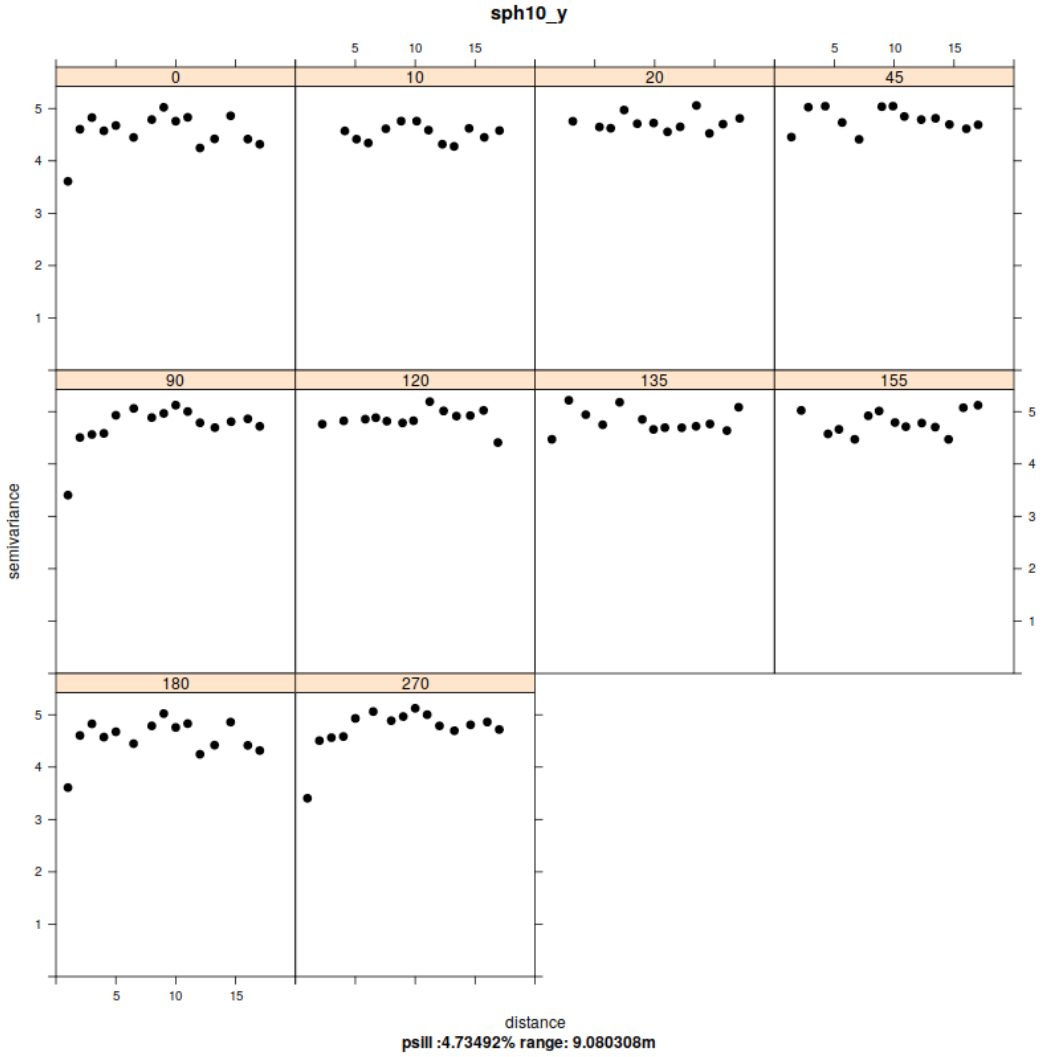

Figure 8.45: Directional variogram analysis of N-S profile of the simulation spherical (10m) nr. 144.

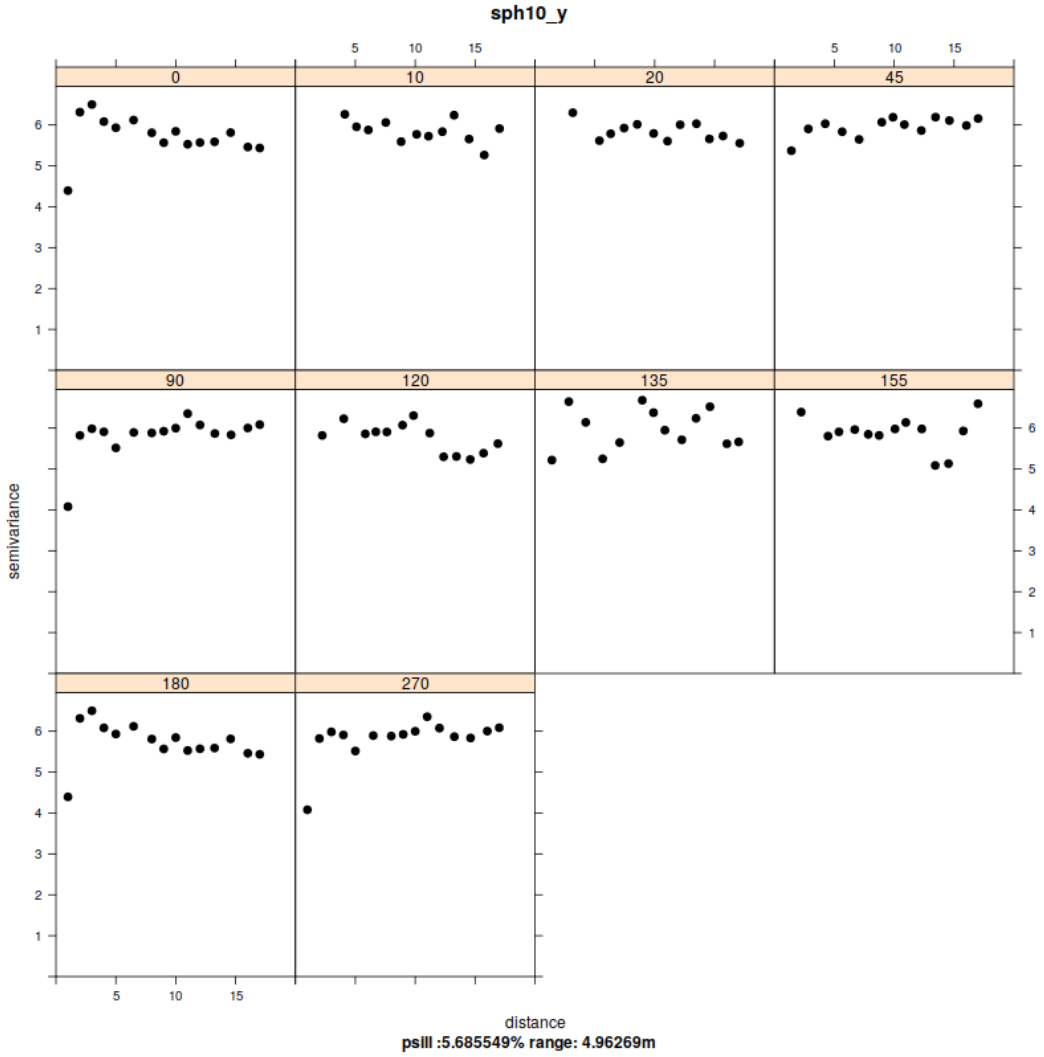

Figure 8.46: Directional variogram analysis of N-S profile of the simulation spherical (10m) nr. 204.

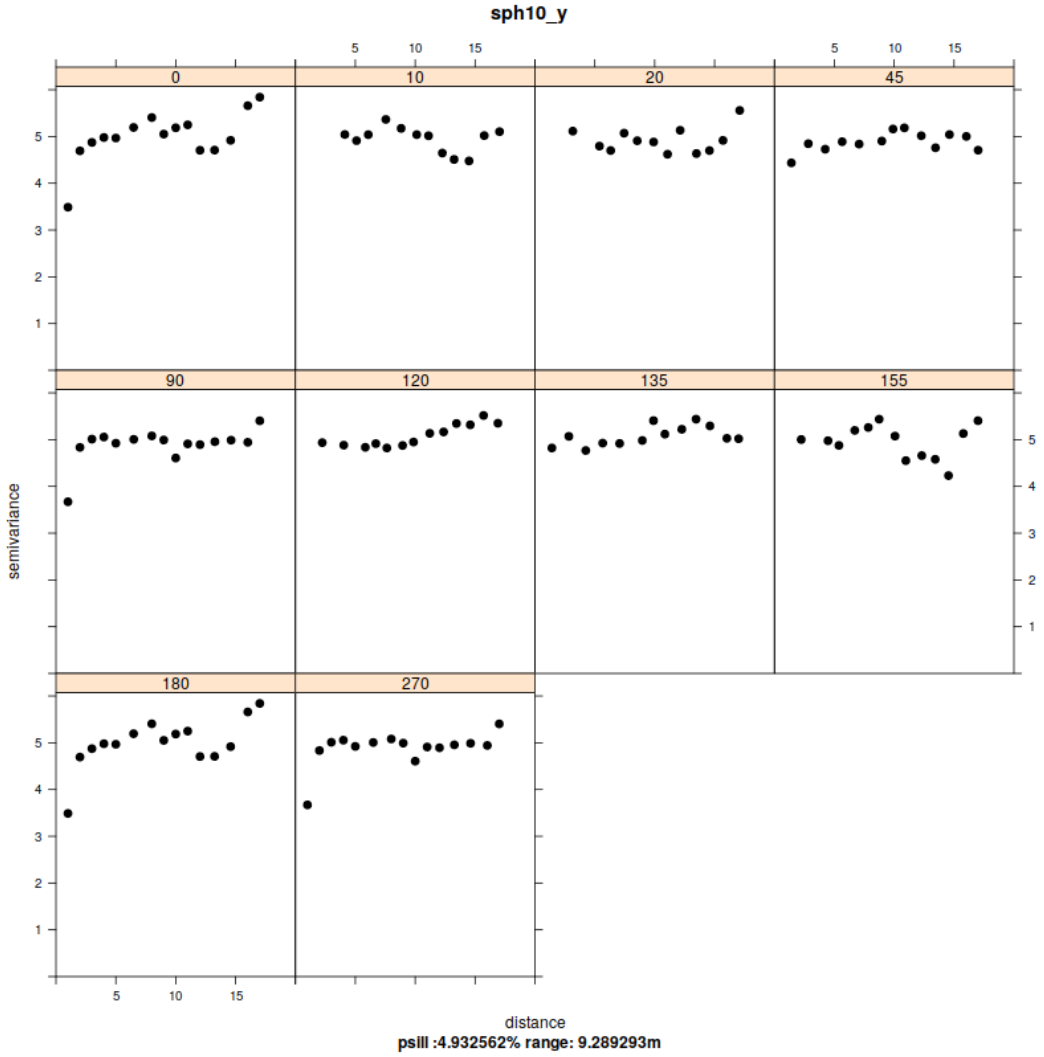

Figure 8.47: Directional variogram analysis of N-S profile of the simulation spherical (10m) nr. 211.

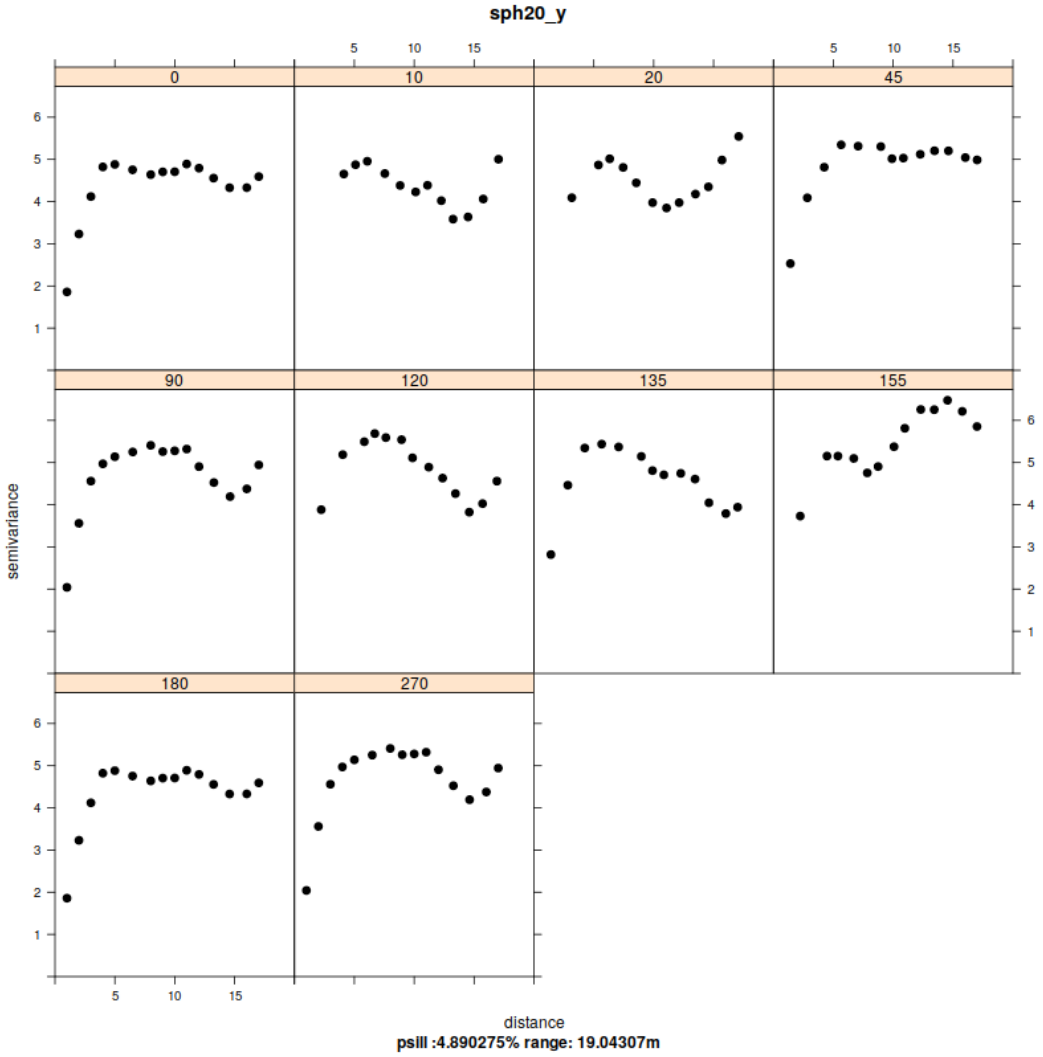

Figure 8.48: Directional variogram analysis of N-S profile of the simulation spherical (20m) nr. 223.

9 References

Agnew, D.C. 2015. "Earth Tides." In *Treatise on Geophysics*, 151–78. Elsevier. https://doi.org/10.1016/b978-0-444-53802-4.00058-0.

Allan, D.W. 1966. "Statistics of Atomic Frequency Standards." *Proceedings of the IEEE* 54 (2). Institute of Electrical; Electronics Engineers (IEEE): 221–30. https://doi.org/10.1109/proc.1966.4634.

Amalvict, M., J. Hinderer, J. Mäkinen, S. Rosat, and Y. Rogister. 2004. "Long-Term and Seasonal Gravity Changes at the Strasbourg Station and Their Relation to Crustal Deformation and Hydrology." *Journal of Geodynamics* 38 (3-5). Elsevier BV: 343–53. https://doi.org/10.1016/j.jog.2004.07.010.

Angelis, M. de, A. Bertoldi, L. Cacciapuoti, A. Giorgini, G. Lamporesi, M. Prevedelli, G. Saccorotti, F. Sorrentino, and G. M. Tino. 2008. "Precision Gravimetry with Atomic Sensors." *Measurement Science and Technology* 20 (2). IOP Publishing: 022001. https://doi.org/10.1088/0957-0233/20/2/022001.

Bear, J. 2012. *Hydraulics of Groundwater*. Mineola, New York, U.S.A.: Dover publications, Inc.

Bertrand, Véronique. 2019. "Scintrex Cg5 - Cg6 Relative Gravimeters from Résif's Gmob Instrumental Pool." https://medihal.archives-ouvertes.fr/medihal-02101748.

Binley, A., S. S. Hubbard, J. A. Huisman, A. Revil, D. A. Robinson, K. Singha, and L. D. Slater. 2015. "The Emergence of Hydrogeophysics for Improved Understanding of Subsurface Processes over Multiple Scales." *Water Resources Research* 51 (6). American Geophysical Union (AGU): 3837–66. https://doi.org/10.1002/2015wr017016.

Birsoy, Y. K., and W. K. Summers. 1980. "Determination of Aquifer Parameters from Step Tests and Intermittent Pumping Data." *Ground Water* 18 (2). Wiley: 137–46. https://doi.org/10.1111/j.1745-6584.1980.tb03382.x.

Bizouard, C., and D. Gambis. 2009. "The Combined Solution C04 for Earth Orientation Parameters Consistent with International Terrestrial Reference Frame 2005." In *Geodetic Reference Frames*, 265–70. Springer Berlin Heidelberg. https://doi.org/10.1007/978-3-642-00860-3_41.

Bizouard, C., S. Lambert, C. Gattano, O. Becker, and J.-Y. Richard. 2018. "The IERS EOP 14C04 Solution for Earth Orientation Parameters Consistent with ITRF 2014." *Journal of Geodesy* 93 (5). Springer Science; Business Media LLC: 621–33. https://doi.org/10.1007/s00190-018-1186-3.

Blainey, J. B., T. P. A. Ferré, and J. T. Cordova. 2007. "Assessing the Likely Value of Gravity and Drawdown Measurements to Constrain Estimates of Hydraulic Conductivity and Specific Yield During Unconfined Aquifer Testing." *Water Resources Research* 43 (12). American Geophysical Union (AGU). https://doi.org/10.1029/2006wr005678.

Blakely, R. 1995. *Potential Theory in Gravity and Magnetic Applications*. Cambridge, United Kingdom: Cambridge University Press.

Bodart, Q., S. Merlet, N. Malossi, F. Pereira Dos Santos, P. Bouyer, and A. Landragin. 2010. "A Cold Atom Pyramidal Gravimeter with a Single Laser Beam." *Applied Physics Letters* 96 (13). AIP Publishing:

134101. https://doi.org/10.1063/1.3373917.

Boddice, D., P. Atkins, A. Rodgers, N. Metje, Y. Goncharenko, and D. Chapman. 2018. "A Novel Approach to Reduce Environmental Noise in Microgravity Measurements Using a Scintrex CG5." *Journal of Applied Geophysics* 152 (May). Elsevier BV: 221–35. https://doi.org/10.1016/j.jappgeo.2018.03.022.

Bonvalot, S., M. Diament, and G. Gabalda. 1998. "Continuous Gravity Recording with Scintrex CG-3M Meters:A Promising Tool for Monitoring Active Zones." *Geophysical Journal International* 135 (2). Oxford University Press (OUP): 470–94. https://doi.org/10.1046/j.1365-246x.1998.00653.x.

Bordé, Ch.J. 1989. "Atomic Interferometry with Internal State Labelling." *Physics Letters A* 140 (1-2). Elsevier BV: 10–12. https://doi.org/10.1016/0375-9601(89)90537-9.

Bouman, J., J. Ebbing, M. Fuchs, J. Sebera, V. Lieb, W. Szwillus, R. Haagmans, and P. Novak. 2016. "Satellite Gravity Gradient Grids for Geophysics." *Scientific Reports* 6 (1). Springer Science; Business Media LLC. https://doi.org/10.1038/srep21050.

Boy, J.-P., and J. Hinderer. 2006. "Study of the Seasonal Gravity Signal in Superconducting Gravimeter Data." *Journal of Geodynamics* 41 (1-3). Elsevier BV: 227–33. https://doi.org/10.1016/j.jog.2005.08.035.

Boy, J.-P., L. Longuevergne, F. Boudin, T. Jacob, F. Lyard, M. Llubes, N. Florsch, and M.-F. Esnoult. 2009. "Modelling Atmospheric and Induced Non-Tidal Oceanic Loading Contributions to Surface Gravity and Tilt Measurements." *Journal of Geodynamics* 48 (3-5). Elsevier BV: 182–88. https://doi.org/10.1016/j.jog.2009.09.022.

Boy, J. P., and F. Lyard. 2008. "High-Frequency Non-Tidal Ocean Loading Effects on Surface Gravity Measurements." *Geophysical Journal International* 175 (1). Oxford University Press (OUP): 35–45. https://doi.org/10.1111/j.1365-246x.2008.03895.x.

Broglie, L.-V. de. 1924. "On the Theory of Quanta." *Ann. De Phys* 3.

Butler, J. J. 1988. "Pumping Tests in Nonuniform Aquifers the Radially Symmetric Case." *Journal of Hydrology* 101 (1-4). Elsevier BV: 15–30. https://doi.org/10.1016/0022-1694(88)90025-x.

Butler Jr, J. J. 2020. *The Design, Performance, and Analysis of Slug Tests*. 6000 Broken Sound Parkway NW, Suite 300, Boca Raton, FL 33487-2742, U.S.A.: CRC Press.

Camp, M. J. Van, O. de Viron, and R. J. Warburton. 2013. "Improving the Determination of the Gravity Rate of Change by Combining Superconducting with Absolute Gravimeter Data." *Computers & Geosciences* 51 (February). Elsevier BV: 49–55. https://doi.org/10.1016/j.cageo.2012.07.029.

Camp, M. Van, and O. Francis. 2006. "Is the Instrumental Drift of Superconducting Gravimeters a Linear or Exponential Function of Time?" *Journal of Geodesy* 81 (5). Springer Science; Business Media LLC: 337–44. https://doi.org/10.1007/s00190-006-0110-4.

Camp, M. Van, M. Vanclooster, O. Crommen, T. Petermans, K. Verbeeck, B. Meurers, T. van Dam, and A. Dassargues. 2006. "Hydrogeological Investigations at the Membach Station, Belgium, and Application to Correct Long Periodic Gravity Variations." *Journal of Geophysical Research* 111 (B10). American Geophysical Union (AGU). https://doi.org/10.1029/2006jb004405.

Camp, M. Van, and P. Vauterin. 2005. "Tsoft: Graphical and Interactive Software for the Analysis of Time Series and Earth Tides." *Computers & Geosciences* 31 (5). Elsevier BV: 631–40. https://doi.org/10.1016/j.cageo.2004.11.015.

Camp, M. Van, O. de Viron, H.-G. Scherneck, K.-G. Hinzen, S. D. P. Williams, T. Lecocq, Y. Quinif, and T. Camelbeeck. 2011. "Repeated Absolute Gravity Measurements for Monitoring Slow Intraplate Vertical Deformation in Western Europe." *Journal of Geophysical Research* 116 (B8). American Geophysical Union (AGU). https://doi.org/10.1029/2010jb008174.

Camp, M. Van, O. de Viron, A. Watlet, B. Meurers, O. Francis, and C. Caudron. 2017. "Geophysics from Terrestrial Time-Variable Gravity Measurements." *Reviews of Geophysics* 55 (4). American Geophysical Union (AGU): 938–92. https://doi.org/10.1002/2017rg000566.

Camp, M. Van, S. D. P. Williams, and O. Francis. 2005. "Uncertainty of Absolute Gravity Measurements." *Journal of Geophysical Research* 110 (B5). American Geophysical Union (AGU). https://doi.org/10.1029/2004jb003497.

Carbone, D., F. Cannavò, F. Greco, A. Messina, D. Contrafatto, G. Siligato, J. Lautier-Gaud, et al. 2020. "The NEWTON-G "Gravity Imager": A New Window into Processes Involving Subsurface Fluids," March. Copernicus GmbH. https://doi.org/10.5194/egusphere-egu2020-16329.

Carbone, D., and F. Greco. 2007. "Review of Microgravity Observations at Mt. Etna: A Powerful Tool to Monitor and Study Active Volcanoes." *Pure and Applied Geophysics* 164 (4). Springer Science; Business Media LLC: 769–90. https://doi.org/10.1007/s00024-007-0194-7.

Carbone, D., M. P. Poland, M. Diament, and F. Greco. 2017. "The Added Value of Time-Variable Microgravimetry to the Understanding of How Volcanoes Work." *Earth-Science Reviews* 169 (June). Elsevier BV: 146–79. https://doi.org/10.1016/j.earscirev.2017.04.014.

Cardiff, M., T. Bakhos, P. K. Kitanidis, and W. Barrash. 2013. "Aquifer Heterogeneity Characterization with Oscillatory Pumping: Sensitivity Analysis and Imaging Potential." *Water Resources Research* 49 (9). American Geophysical Union (AGU): 5395–5410. https://doi.org/10.1002/wrcr.20356.

Carrière, S. D., K. Chalikakis, G. Sénéchal, C. Danquigny, and C. Emblanch. 2013. "Combining Electrical Resistivity Tomography and Ground Penetrating Radar to Study Geological Structuring of Karst Unsaturated Zone." *Journal of Applied Geophysics* 94 (July). Elsevier BV: 31–41. https://doi.org/10.1016/j.jappgeo.2013.03.014.

Chalikakis, K., V. Plagnes, R. Guerin, R. Valois, and F. P. Bosch. 2011. "Contribution of Geophysical Methods to Karst-System Exploration: An Overview." *Hydrogeology Journal* 19 (6). Springer Science; Business Media LLC: 1169–80. https://doi.org/10.1007/s10040-011-0746-x.

Chen, Kuan-Hung, Cheinway Hwang, Liang-Cheng Chang, and Chien-Chung Ke. 2018. "Short-Time Geodetic Determination of Aquifer Storage Coefficient in Taiwan." *Journal of Geophysical Research: Solid Earth*, December. American Geophysical Union (AGU). https://doi.org/10.1029/2018jb016630.

Christiansen, L., P. J. Binning, D. Rosbjerg, O. B. Andersen, and P. Bauer-Gottwein. 2011. "Using Time-

Lapse Gravity for Groundwater Model Calibration: An Application to Alluvial Aquifer Storage." *Water Resources Research* 47 (6). American Geophysical Union (AGU). https://doi.org/10.1029/2010wr009859.

Christiansen, L., S. Lund, O. B. Andersen, P. J. Binning, D. Rosbjerg, and P. Bauer-Gottwein. 2011. "Measuring Gravity Change Caused by Water Storage Variations: Performance Assessment Under Controlled Conditions." *Journal of Hydrology* 402 (1-2). Elsevier BV: 60–70. https://doi.org/10.1016/j.jhydrol.2011.03.004.

Chu, S. 1998. "Nobel Lecture: The Manipulation of Neutral Particles." *Reviews of Modern Physics* 70 (3). American Physical Society (APS): 685–706. https://doi.org/10.1103/revmodphys.70.685.

Clauzon, V. 2019. "Caractérisation in Situ Multi-échelles Des Transferts de Fluide En Zone de Faille En Milieu Carbonaté." PhD thesis, Université de Montpellier. https://ged.biu-montpellier.fr/florabium/jsp/nnt.jsp?nnt=2019MONTG075.

Cooke, A.-K., C. Champollion, and N. Le Moigne. 2020. "Evaluation of the Capacities of a Field Absolute Quantum Gravimeter (AQG#B01)," August. Copernicus GmbH. https://doi.org/10.5194/gi-2020-22.

Creutzfeldt, B., A. Güntner, T. Klügel, and H. Wziontek. 2008. "Simulating the Influence of Water Storage Changes on the Superconducting Gravimeter of the Geodetic Observatory Wettzell, Germany." *GEOPHYSICS* 73 (6). Society of Exploration Geophysicists: WA95–WA104. https://doi.org/10.1190/1.2992508.

Creutzfeldt, B., A. Güntner, H. Wziontek, and B. Merz. 2010. "Reducing Local Hydrology from High-Precision Gravity Measurements: A Lysimeter-Based Approach." *Geophysical Journal International* 183 (1). Oxford University Press (OUP): 178–87. https://doi.org/10.1111/j.1365-246x.2010.04742.x.

Creutzfeldt, B., P. A. Troch, A. Güntner, T. P. A. Ferré, T. Graeff, and B. Merz. 2013. "Storage-Discharge Relationships at Different Catchment Scales Based on Local High-Precision Gravimetry." *Hydrological Processes* 28 (3). Wiley: 1465–75. https://doi.org/10.1002/hyp.9689.

Crossley, D., J. Hinderer, and U. Riccardi. 2013. "The Measurement of Surface Gravity." *Reports on Progress in Physics* 76 (4). IOP Publishing: 046101. https://doi.org/10.1088/0034-4885/76/4/046101.

Crossley, D., J. Hinderer, and S. Rosat. 2002. "Using the Atmosphere-Gravity Correlation to Derive a Time-Dependent Admittance." *Bull. Inf. Marées Terrestres* 136: 10809–20.

Damiata, B. N., and T.-C. Lee. 2006. "Simulated Gravitational Response to Hydraulic Testing of Unconfined Aquifers." *Journal of Hydrology* 318 (1-4). Elsevier BV: 348–59. https://doi.org/10.1016/j.jhydrol.2005.06.024.

Dausse, A., V. Leonardi, and H. Jourde. 2019. "Hydraulic Characterization and Identification of Flow-Bearing Structures Based on Multi-Scale Investigations Applied to the Lez Karst Aquifer." *Journal of Hydrology: Regional Studies* 26 (December). Elsevier BV: 100627. https://doi.org/10.1016/j.ejrh.2019.100627.

Davis, K., Y. Li, and M. Batzle. 2008. "Time-Lapse Gravity Monitoring: A Systematic 4D Approach with Application to Aquifer Storage and Recovery." *GEOPHYSICS* 73 (6). Society of Exploration

Geophysicists: WA61–WA69. https://doi.org/10.1190/1.2987376.

Dee, D. P., S. M. Uppala, A. J. Simmons, P. Berrisford, P. Poli, S. Kobayashi, U. Andrae, et al. 2011. "The ERA-Interim Reanalysis: Configuration and Performance of the Data Assimilation System." *Quarterly Journal of the Royal Meteorological Society* 137 (656). Wiley: 553–97. https://doi.org/10.1002/qj.828.

Delobbe, L., A. Watlet, S. Wilfert, and M. Van Camp. 2019. "Exploring the Use of Underground Gravity Monitoring to Evaluate Radar Estimates of Heavy Rainfall." *Hydrology and Earth System Sciences* 23 (1). Copernicus GmbH: 93–105. https://doi.org/10.5194/hess-23-93-2019.

Deville, S. 2013. "Caractérisation de La Zone Non Saturée Des Karsts Par La Gravimétrie et L'hydrogéologie." PhD thesis, Université Montpellier II - Sciences et Techniques du Languedoc. https://tel.archives-ouvertes.fr/tel-00829346.

Dietze, Michael. 2018. "The R Package "Eseis" a Software Toolbox for Environmental Seismology." *Earth Surface Dynamics* 6 (3). Copernicus GmbH: 669–86. https://doi.org/10.5194/esurf-6-669-2018.

Ducarme, B., A.P. Venedikov, J. Arnoso, and R. Vieira. 2006. "Analysis and Prediction of Ocean Tides by the Computer Program VAV." *Journal of Geodynamics* 41 (1-3). Elsevier BV: 119–27. https://doi.org/10.1016/j.jog.2005.08.001.

Falk, R., J. Müller, N. Lux, H. Wilmes, and H. Wziontek. 2011. "Precise Gravimetric Surveys with the Field Absolute Gravimeter a-10." In *Geodesy for Planet Earth*, 273–79. Springer Berlin Heidelberg. https://doi.org/10.1007/978-3-642-20338-1_33.

Ferguson, J. F., T. Chen, J. Brady, C. L. Aiken, and J. Seibert. 2007. "The 4D Microgravity Method for Waterflood Surveillance: Part II Gravity Measurements for the Prudhoe Bay Reservoir, Alaska." *GEOPHYSICS* 72 (2). Society of Exploration Geophysicists: I33–I43. https://doi.org/10.1190/1.2435473.

Fernández-Álvarez, J.-P., A. González-Quirós, and D.Rubio-Melendi. 2016. "Assessment of the Value of Microgravity to Estimate the Principal Directions of the Anisotropic Transmissivity of Aquifers from Pumping Tests: A Study Using a Hough Transform Based Automatic Algorithm." *Journal of Applied Geophysics* 134 (November). Elsevier BV: 172–82. https://doi.org/10.1016/j.jappgeo.2016.09.015.

Fetter, C. W. 2018. *Applied Hydrogeology*. 4180 IL Route 83, Suite 101, Long Grove, IL 60047-9580, U.S.A.: Waveland Press, Inc.

Fores, B. 2016. "Gravimétrie et Surveillance Sismique Pour La Modélisation Hydrologique En Milieu Karstique: Application Au Bassin Du Durzon (Larzac, France)." PhD thesis, Université de Montpellier. https://tel.archives-ouvertes.fr/tel-01649606.

Fores, B., C. Champollion, N. Le Moigne, R. Bayer, and J. Chéry. 2016. "Assessing the Precision of the iGrav Superconducting Gravimeter for Hydrological Models and Karstic Hydrological Process Identification." *Geophysical Journal International* 208 (1). Oxford University Press (OUP): 269–80. https://doi.org/10.1093/gji/ggw396.

Fores, B., C. Champollion, N. Le Moigne, and J. Chery. 2016. "Impact of Ambient Temperature on Spring-Based Relative Gravimeter Measurements." *Journal of Geodesy* 91 (3). Springer Science; Business

Media LLC: 269–77. https://doi.org/10.1007/s00190-016-0961-2.

Fores, B., G. Klein, N. Le Moigne, and O. Francis. 2019. "Long-Term Stability of Tilt-Controlled gPhoneX Gravimeters." *Journal of Geophysical Research: Solid Earth* 124 (11). American Geophysical Union (AGU): 12264–76. https://doi.org/10.1029/2019jb018276.

Francis, O., H. Baumann, T. Volarik, C. Rothleitner, G. Klein, M. Seil, N. Dando, et al. 2013. "The European Comparison of Absolute Gravimeters 2011 (ECAG-2011) in Walferdange, Luxembourg: Results and Recommendations." *Metrologia* 50 (3). IOP Publishing: 257–68. https://doi.org/10.1088/0026-1394/50/3/257.

Francis, O., and T. van Dam. 2002. "Evaluation of the Precision of Using Absolute Gravimeters to Calibrate Superconducting Gravimeters." *Metrologia* 39 (5). IOP Publishing: 485–88. https://doi.org/10.1088/0026-1394/39/5/9.

Frappart, F., and G. Ramillien. 2018. "Monitoring Groundwater Storage Changes Using the Gravity Recovery and Climate Experiment (GRACE) Satellite Mission: A Review." *Remote Sensing* 10 (6). MDPI AG: 829. https://doi.org/10.3390/rs10060829.

Gehman, Carter L., Dennis L. Harry, William E. Sanford, John D. Stednick, and Nathaniel A. Beckman. 2009. "Estimating Specific Yield and Storage Change in an Unconfined Aquifer Using Temporal Gravity Surveys." *Water Resources Research* 45 (4). American Geophysical Union (AGU). https://doi.org/10.1029/2007wr006096.

Geiger, R., A. Landragin, S. Merlet, and F. Pereira Dos Santos. 2020. "High-Accuracy Inertial Measurements with Cold-Atom Sensors." *AVS Quantum Science* 2 (2). American Vacuum Society: 024702. https://doi.org/10.1116/5.0009093.

Gelaro, R., W. McCarty, M. J. Suárez, R. Todling, A. Molod, L. Takacs, C. A. Randles, et al. 2017. "The Modern-Era Retrospective Analysis for Research and Applications, Version 2 (MERRA-2)." *Journal of Climate* 30 (14). American Meteorological Society: 5419–54. https://doi.org/10.1175/jcli-d-16-0758.1.

Gerbaux, G. 2009. *Impact de La Fracturation et de La Karstification Sur La Dynamique Des Eaux Souterraines Dans Le Larzac. Stage de Fin d'étude Master 2.* Université Montpellier 2.

Gillot, P., O. Francis, A. Landragin, F. Pereira Dos Santos, and S. Merlet. 2014. "Stability Comparison of Two Absolute Gravimeters: Optical Versus Atomic Interferometers." *Metrologia* 51 (5). IOP Publishing: L15–L17. https://doi.org/10.1088/0026-1394/51/5/l15.

Goodkind, J. M. 1999. "The Superconducting Gravimeter." *Review of Scientific Instruments* 70 (11). AIP Publishing: 4131–52. https://doi.org/10.1063/1.1150092.

Gouët, J. Le, T.E. Mehlstäubler, J. Kim, S. Merlet, A. Clairon, A. Landragin, and F. Pereira Dos Santos. 2008. "Limits to the Sensitivity of a Low Noise Compact Atomic Gravimeter." *Applied Physics B* 92 (2). Springer Science; Business Media LLC: 133–44. https://doi.org/10.1007/s00340-008-3088-1.

Green, T. R. 2016. "Linking Climate Change and Groundwater." In *Integrated Groundwater Management*, 97–141. Springer International Publishing. https://doi.org/10.1007/978-3-319-23576-9_5.

Gringarten, A. C. 2008. "From Straight Lines to Deconvolution: The Evolution of the State of the Art in Well Test Analysis." *SPE Reservoir Evaluation & Engineering* 11 (01). Society of Petroleum Engineers (SPE): 41–62. https://doi.org/10.2118/102079-pa.

Güntner, A., M. Reich, M. Mikolaj, B. Creutzfeldt, S. Schroeder, and H. Wziontek. 2017. "Landscape-Scale Water Balance Monitoring with an iGrav Superconducting Gravimeter in a Field Enclosure." *Hydrology and Earth System Sciences* 21 (6). Copernicus GmbH: 3167–82. https://doi.org/10.5194/hess-21-3167-2017.

Hantush, M. S. 1964. "Drawdown Around Wells of Variable Discharge." *Journal of Geophysical Research* 69 (20). American Geophysical Union (AGU): 4221–35. https://doi.org/10.1029/jz069i020p04221.

Harnisch, G., and M. Harnisch. 2006. "Hydrological Influences in Long Gravimetric Data Series." *Journal of Geodynamics* 41 (1-3). Elsevier BV: 276–87. https://doi.org/10.1016/j.jog.2005.08.018.

Hartmann, A., N. Goldscheider, T. Wagener, J. Lange, and M. Weiler. 2014. "Karst Water Resources in a Changing World: Review of Hydrological Modeling Approaches." *Reviews of Geophysics* 52 (3). American Geophysical Union (AGU): 218–42. https://doi.org/10.1002/2013rg000443.

Hasan, S., P. A. Troch, P. W. Bogaart, and C. Kroner. 2008. "Evaluating Catchment-Scale Hydrological Modeling by Means of Terrestrial Gravity Observations." *Water Resources Research* 44 (8). American Geophysical Union (AGU). https://doi.org/10.1029/2007wr006321.

Hauth, M., C. Freier, V. Schkolnik, A. Senger, M. Schmidt, and A. Peters. 2013. "First Gravity Measurements Using the Mobile Atom Interferometer GAIN." *Applied Physics B* 113 (1). Springer Science; Business Media LLC: 49–55. https://doi.org/10.1007/s00340-013-5413-6.

Hector, Basile, and Jacques Hinderer. 2016. "pyGrav, a Python-Based Program for Handling and Processing Relative Gravity Data." *Computers & Geosciences* 91 (June). Elsevier BV: 90–97. https://doi.org/10.1016/j.cageo.2016.03.010.

Hector, B., J. Hinderer, L. Séguis, J.-P. Boy, M. Calvo, M. Descloitres, S. Rosat, S. Galle, and U. Riccardi. 2014. "Hydro-Gravimetry in West-Africa: First Results from the Djougou (Benin) Superconducting Gravimeter." *Journal of Geodynamics* 80 (October). Elsevier BV: 34–49. https://doi.org/10.1016/j.jog.2014.04.003.

Hector, B., L. Séguis, J. Hinderer, J.-M. Cohard, M. Wubda, M. Descloitres, N. Benarrosh, and J.-P. Boy. 2015. "Water Storage Changes as a Marker for Base Flow Generation Processes in a Tropical Humid Basement Catchment (Benin): Insights from Hybrid Gravimetry." *Water Resources Research* 51 (10). American Geophysical Union (AGU): 8331–61. https://doi.org/10.1002/2014wr015773.

Herckenrath, D., E. Auken, L. Christiansen, A. A. Behroozmand, and P. Bauer-Gottwein. 2012. "Coupled Hydrogeophysical Inversion Using Time-Lapse Magnetic Resonance Sounding and Time-Lapse Gravity Data for Hydraulic Aquifer Testing: Will It Work in Practice?" *Water Resources Research* 48 (1). American Geophysical Union (AGU). https://doi.org/10.1029/2011wr010411.

Hinderer, J., D. Crossley, and R.J. Warburton. 2015. "Superconducting Gravimetry." In *Treatise on*

Geophysics, 59–115. Elsevier. https://doi.org/10.1016/b978-0-444-53802-4.00062-2.

Hinze, W.m J, R. R.B. Von Frese, and A. H. Saad. 2013. *Gravity and Magnetic Exploration: Principles, Practices, and Applications*. University Printing House, Cambridge CB2 8BS, United Kingdom: Cambridge University Press.

Howle, J. F., S. P. Phillips, R. P. Denlinger, and L. F. Metzger. 2003. "Determination of Specific Yield and Water-Table Changes Using Temporal Microgravity Surveys Collected During the Second Injection, Storage, and Recovery Test at Lancaster, Antelope Valley, California, November 1996 Through April 1997." *Water-Resources Investigations, Report*, 03–4019.

Huang, P.-W., B. Tang, X. Chen, J.-Q. Zhong, Z.-Y. Xiong, L. Zhou, J. Wang, and M.-S. Zhan. 2019. "Accuracy and Stability Evaluation of the 85Rb Atom Gravimeter WAG-H5-1 at the 2017 International Comparison of Absolute Gravimeters." *Metrologia* 56 (4). IOP Publishing: 045012. https://doi.org/10.1088/1681-7575/ab2f01.

Hwang, C., T.-C. Cheng, C.C. Cheng, and W.C. Hung. 2010. "Land Subsidence Using Absolute and Relative Gravimetry: A Case Study in Central Taiwan." *Survey Review* 42 (315). Informa UK Limited: 27–39. https://doi.org/10.1179/003962609x451672.

Imanishi, Y. 2004. "A Network of Superconducting Gravimeters Detects Submicrogal Coseismic Gravity Changes." *Science* 306 (5695). American Association for the Advancement of Science (AAAS): 476–78. https://doi.org/10.1126/science.1101875.

Imanishi, Y., Y. Tamura, H. Ikeda, and S. Okubo. 2009. "Permanent Gravity Changes Recorded on Superconducting Gravimeters from Earthquakes in Central JapanThe Noto Hantou and Niigataken Chuetsu-Oki Events in 2007." *Journal of Geodynamics* 48 (3-5). Elsevier BV: 260–68. https://doi.org/10.1016/j.jog.2009.09.013.

Jacob, T., R. Bayer, J. Chery, and N. Le Moigne. 2010. "Time-Lapse Microgravity Surveys Reveal Water Storage Heterogeneity of a Karst Aquifer." *Journal of Geophysical Research* 115 (B6). American Geophysical Union (AGU). https://doi.org/10.1029/2009jb006616.

Jacob, T., K. Samyn, A. Bitri, F. Quesnel, T. Dewez, P. Pannet, and B. Meire. 2018. "Mapping Sand and Clay-Filled Depressions on a Coastal Chalk Clifftop Using Gravity and Seismic Tomography Refraction for Landslide Hazard Assessment, in Normandy, France." *Engineering Geology* 246 (November). Elsevier BV: 262–76. https://doi.org/10.1016/j.enggeo.2018.10.007.

Jiang, Z, V Pálinkáš, F E Arias, J Liard, S Merlet, H Wilmes, L Vitushkin, et al. 2012. "The 8th International Comparison of Absolute Gravimeters 2009: The First Key Comparison (CCM.G-K1) in the Field of Absolute Gravimetry." *Metrologia* 49 (6). IOP Publishing: 666–84. https://doi.org/10.1088/0026-1394/49/6/666.

Karst3D Team. 2019. "Karst3D." OSU OREME. https://doi.org/10.15148/940C2882-49F1-49DB-A97E-12303CACE752.

Kasevich, M., and S. Chu. 1991. "Atomic Interferometry Using Stimulated Raman Transitions." *Physical*

Review Letters 67 (2). American Physical Society (APS): 181–84. https://doi.org/10.1103/physrevlett.67.181.

Kater, H. 1818. "IV. An Account of Experiments for Determining the Length of the Pendulum Vibrating Seconds in the Latitude of London." *Philosophical Transactions of the Royal Society of London* 108 (December). The Royal Society: 33–102. https://doi.org/10.1098/rstl.1818.0006.

Kennedy, J., T. P. A. Ferré, and B. Creutzfeldt. 2016. "Time-Lapse Gravity Data for Monitoring and Modeling Artificial Recharge Through a Thick Unsaturated Zone." *Water Resources Research* 52 (9). American Geophysical Union (AGU): 7244–61. https://doi.org/10.1002/2016wr018770.

Kennedy, J. R., and T. P.A. Ferré. 2015. "Accounting for Time- and Space-Varying Changes in the Gravity Field to Improve the Network Adjustment of Relative-Gravity Data." *Geophysical Journal International* 204 (2). Oxford University Press (OUP): 892–906. https://doi.org/10.1093/gji/ggv493.

Krause, P., M. Naujoks, M. Fink, and C. Kroner. 2009. "The Impact of Soil Moisture Changes on Gravity Residuals Obtained with a Superconducting Gravimeter." *Journal of Hydrology* 373 (1-2). Elsevier BV: 151–63. https://doi.org/10.1016/j.jhydrol.2009.04.019.

Kroner, C. 2001. "Hydrological Effects on Gravity at the Geodynamic Observatory Moxa." *Journal of the Geodetic Society of Japan* 47 (1). The Geodetic Society of Japan: 353–58. https://doi.org/10.11366/sokuchi1954.47.353.

LaCoste, Micro-g. 2008. "A-10 Portable Gravimeter User's Manual." 401 Horizon Ave., Lafayette, CO 80026 USA: Micro-g LaCoste. http://microglacoste.com/support/product_manuals/.

———. 2013. *GPhoneX*. 401 Horizon Ave., Lafayette, CO 80026 USA: Micro-g LaCoste. http://microglacoste.com/support/product_manuals/.

———. 2020. "FG5-X Absolute Gravity Meters." 401 Horizon Ave., Lafayette, CO 80026 USA: Micro-g LaCoste. http://microglacoste.com/product/fg5-x-absolute-gravimeter/.

Lampitelli, C., and O. Francis. 2010. "Hydrological Effects on Gravity and Correlations Between Gravitational Variations and Level of the Alzette River at the Station of Walferdange, Luxembourg." *Journal of Geodynamics* 49 (1). Elsevier BV: 31–38. https://doi.org/10.1016/j.jog.2009.08.003.

Lederer, M. 2009. "Accuracy of the Relative Gravity Measurement." *Acta Geodyn. Geomater* 6 (3): 155.

Leirião, S., X. He, L. Christiansen, O. B. Andersen, and P. Bauer-Gottwein. 2009. "Calculation of the Temporal Gravity Variation from Spatially Variable Water Storage Change in Soils and Aquifers." *Journal of Hydrology* 365 (3-4). Elsevier BV: 302–9. https://doi.org/10.1016/j.jhydrol.2008.11.040.

Le Moigne, N., S. Bonvalot, A.-K. Cooke, G. Gabalda, and C. Champollion. 2019. "AQG-A01: Evaluation of the Instrument; Continuous Monitoring in Laboratory; Daily Observati on at Different Location." In *EGU General Assembly*. EGU2019-15991. Vienna, Austria.

Linage, C. De, J. Hinderer, and Y. Rogister. 2007. "A Search for the Ratio Between Gravity Variation and Vertical Displacement Due to a Surface Load." *Geophysical Journal International* 171 (3). Oxford University Press (OUP): 986–94. https://doi.org/10.1111/j.1365-246x.2007.03613.x.

Llubes, M., N. Florsch, J. Hinderer, L. Longuevergne, and M. Amalvict. 2004. "Local Hydrology, the Global Geodynamics Project and CHAMP/GRACE Perspective: Some Case Studies." *Journal of Geodynamics* 38 (3-5). Elsevier BV: 355–74. https://doi.org/10.1016/j.jog.2004.07.015.

Longuevergne, L., J.P. Boy, N. Florsch, D. Viville, G. Ferhat, P. Ulrich, B. Luck, and J. Hinderer. 2009. "Local and Global Hydrological Contributions to Gravity Variations Observed in Strasbourg." *Journal of Geodynamics* 48 (3-5). Elsevier BV: 189–94. https://doi.org/10.1016/j.jog.2009.09.008.

Louchet-Chauvet, A., T. Farah, Q. Bodart, A. Clairon, A. Landragin, S. Merlet, and F. Pereira Dos Santos. 2011. "The Influence of Transverse Motion Within an Atomic Gravimeter." *New Journal of Physics* 13 (6). IOP Publishing: 065025. https://doi.org/10.1088/1367-2630/13/6/065025.

Maina, F. Z., and A. Guadagnini. 2018. "Uncertainty Quantification and Global Sensitivity Analysis of Subsurface Flow Parameters to Gravimetric Variations During Pumping Tests in Unconfined Aquifers." *Water Resources Research* 54 (1). American Geophysical Union (AGU): 501–18. https://doi.org/10.1002/2017wr021655.

Marson, I. 2012. "A Short Walk Along the Gravimeters Path." *International Journal of Geophysics* 2012. Hindawi Limited: 1–9. https://doi.org/10.1155/2012/687813.

Mazzilli, N., H. Jourde, T.s Jacob, V.t Guinot, N.Le Moigne, M. Boucher, K. Chalikakis, H. Guyard, and A. Legtchenko. 2012. "On the Inclusion of Ground-Based Gravity Measurements to the Calibration Process of a Global Rainfall-Discharge Reservoir Model: Case of the Durzon Karst System (Larzac, Southern France)." *Environmental Earth Sciences* 68 (6). Springer Science; Business Media LLC: 1631–46. https://doi.org/10.1007/s12665-012-1856-z.

Mazzotti, S., A. Lambert, N. Courtier, L. Nykolaishen, and H. Dragert. 2007. "Crustal Uplift and Sea Level Rise in Northern Cascadia from GPS, Absolute Gravity, and Tide Gauge Data." *Geophysical Research Letters* 34 (15). American Geophysical Union (AGU). https://doi.org/10.1029/2007gl030283.

Mazzotti, S., A. Lambert, J. Henton, T. S. James, and N. Courtier. 2011. "Absolute Gravity Calibration of GPS Velocities and Glacial Isostatic Adjustment in Mid-Continent North America." *Geophysical Research Letters* 38 (24). American Geophysical Union (AGU): n/a–n/a. https://doi.org/10.1029/2011gl049846.

McNamara, J. P., D. Tetzlaff, K. Bishop, C. Soulsby, M. Seyfried, N. E. Peters, B. T. Aulenbach, and R. Hooper. 2011. "Storage as a Metric of Catchment Comparison." *Hydrological Processes* 25 (21). Wiley: 3364–71. https://doi.org/10.1002/hyp.8113.

Merlet, S., Q. Bodart, N. Malossi, A. Landragin, F. Pereira Dos Santos, O. Gitlein, and L. Timmen. 2010. "Comparison Between Two Mobile Absolute Gravimeters: Optical Versus Atomic Interferometers." *Metrologia* 47 (4). IOP Publishing: L9–L11. https://doi.org/10.1088/0026-1394/47/4/l01.

Merlet, S., A. Kopaev, M. Diament, G. Geneves, A. Landragin, and F. Pereira Dos Santos. 2008. "Micro-Gravity Investigations for the LNE Watt Balance Project." *Metrologia* 45 (3). IOP Publishing: 265–74. https://doi.org/10.1088/0026-1394/45/3/002.

Merriam, J. B. 1992. "Atmospheric Pressure and Gravity." *Geophysical Journal International* 109 (3). Oxford University Press (OUP): 488–500. https://doi.org/10.1111/j.1365-246x.1992.tb00112.x.

Meurers, B. 2002. "Aspects of Gravimeter Calibration by Time Domain Comparison of Gravity Records." *Bull Inf Marées Terr* 135: 10643–50.

Meurers, B., M. Van Camp, and T. Petermans. 2007. "Correcting Superconducting Gravity Time-Series Using Rainfall Modelling at the Vienna and Membach Stations and Application to Earth Tide Analysis." *Journal of Geodesy* 81 (11). Springer Science; Business Media LLC: 703–12. https://doi.org/10.1007/s00190-007-0137-1.

Ménoret, V., P. Vermeulen, N. Le Moigne, S. Bonvalot, P. Bouyer, A. Landragin, and B. Desruelle. 2018. "Gravity Measurements Below 10-9 G with a Transportable Absolute Quantum Gravimeter." *Scientific Reports* 8 (1). Springer Science; Business Media LLC. https://doi.org/10.1038/s41598-018-30608-1.

Middlemiss, R., S. Bramsiepe, R. Douglas, J. Hough, D. Paul, S. Rowan, and G. Hammond. 2017. "Field Tests of a Portable MEMS Gravimeter." *Sensors* 17 (11). MDPI AG: 2571. https://doi.org/10.3390/s17112571.

Middlemiss, R. P., A. Samarelli, D. J. Paul, J. Hough, S. Rowan, and G. D. Hammond. 2016. "Measurement of the Earth Tides with a MEMS Gravimeter." *Nature* 531 (7596). Springer Science; Business Media LLC: 614–17. https://doi.org/10.1038/nature17397.

Mikolaj, M., M. Reich, and A. Güntner. 2019. "Resolving Geophysical Signals by Terrestrial Gravimetry: A Time Domain Assessment of the Correction-Induced Uncertainty." *Journal of Geophysical Research: Solid Earth* 124 (2). American Geophysical Union (AGU): 2153–65. https://doi.org/10.1029/2018jb016682.

Mishra, P. K., and S. P. Neuman. 2011. "Saturated-Unsaturated Flow to a Well with Storage in a Compressible Unconfined Aquifer." *Water Resources Research* 47 (5). American Geophysical Union (AGU). https://doi.org/10.1029/2010wr010177.

Mochales, T., A. M. Casas, E. L. Pueyo, O. Pueyo, M. T. Román, A. Pocovı', M. A. Soriano, and D. Ansón. 2007. "Detection of Underground Cavities by Combining Gravity, Magnetic and Ground Penetrating Radar Surveys: A Case Study from the Zaragoza Area, NE Spain." *Environmental Geology* 53 (5). Springer Science; Business Media LLC: 1067–77. https://doi.org/10.1007/s00254-007-0733-7.

Moench, A. F. 2008. "Analytical and Numerical Analyses of an Unconfined Aquifer Test Considering Unsaturated Zone Characteristics." *Water Resources Research* 44 (6). American Geophysical Union (AGU). https://doi.org/10.1029/2006wr005736.

Moigne, N. Le. 2019. "Gravimeter Superconductor Gwr iGrav Gwr at the Larzac Observation Site." https://hal.archives-ouvertes.fr/medihal-02101723.

Mouyen, M., L. Longuevergne, K. Chalikakis, N. Mazzilli, C. Ollivier, S. Rosat, J. Hinderer, and C. Champollion. 2019. "Monitoring of Groundwater Redistribution in a Karst Aquifer Using a Superconducting Gravimeter." Edited by K. Coulié, P. Febvre, and G. Micolau. *E3S Web of Conferences* 88. EDP

Sciences: 03001. https://doi.org/10.1051/e3sconf/20198803001.

Mouyen, M., F. Masson, C. Hwang, C.-C. Cheng, N. Le Moigne, C.W-. Lee, R. Kao, and W.-C. Hsieh. 2012. "Erosion Effects Assessed by Repeated Gravity Measurements in Southern Taiwan." *Geophysical Journal International* 192 (1). Oxford University Press (OUP): 113–36. https://doi.org/10.1093/gji/ggs019.

Muquans. 2020. Institut d'Optique d'Aquitaine, Rue François Mitterrand, 33400 Talence, France: Muquans. https://www.muquans.com/product/absolute-quantum-gravimeter/.

Naujoks, M., C. Kroner, A. Weise, T. Jahr, P. Krause, and S. Eisner. 2010. "Evaluating Local Hydrological Modelling by Temporal Gravity Observations and a Gravimetric Three-Dimensional Model." *Geophysical Journal International*, May. Oxford University Press (OUP), no–no. https://doi.org/10.1111/j.1365-246x.2010.04615.x.

Naujoks, M., A. Weise, C. Kroner, and T. Jahr. 2007. "Detection of Small Hydrological Variations in Gravity by Repeated Observations with Relative Gravimeters." *Journal of Geodesy* 82 (9). Springer Science; Business Media LLC: 543–53. https://doi.org/10.1007/s00190-007-0202-9.

Neumeyer, J., F. Barthelmes, O. Dierks, F. Flechtner, M. Harnisch, G. Harnisch, J. Hinderer, et al. 2006. "Combination of Temporal Gravity Variations Resulting from Superconducting Gravimeter (SG) Recordings, GRACE Satellite Observations and Global Hydrology Models." *Journal of Geodesy* 79 (10-11). Springer Science; Business Media LLC: 573–85. https://doi.org/10.1007/s00190-005-0014-8.

Neumeyer, J., F. Barthelmes, C. Kroner, S. Petrovic, R. Schmidt, H. Virtanen, and H. Wilmes. 2008. "Analysis of Gravity Field Variations Derived from Superconducting Gravimeter Recordings, the GRACE Satellite and Hydrological Models at Selected European Sites." *Earth, Planets and Space* 60 (5). Springer Science; Business Media LLC: 505–18. https://doi.org/10.1186/bf03352817.

Newton, I. 1686. "Philosophiae Naturalis Principia Mathematica." *Reg. Soc. Praeses, London* 2: 1–4.

Niebauer, T. 2015. "Gravimetric Methods Absolute and Relative Gravity Meter: Instruments Concepts and Implementation." In *Treatise on Geophysics*, 37–57. Elsevier. https://doi.org/10.1016/b978-0-444-53802-4.00057-9.

Niebauer, T. M., G. S. Sasagawa, J. E. Faller, R. Hilt, and F. Klopping. 1995. "A New Generation of Absolute Gravimeters." *Metrologia* 32 (3). IOP Publishing: 159–80. https://doi.org/10.1088/0026-1394/32/3/004.

Okabe, M. 1979. "Analytical Expressions for Gravity Anomalies Due to Homogeneous Polyhedral Bodies and Translations into Magnetic Anomalies." *GEOPHYSICS* 44 (4). Society of Exploration Geophysicists: 730–41. https://doi.org/10.1190/1.1440973.

Olsson, P.-A., K. Breili, V. Ophaug, H. Steffen, M. Bilker-Koivula, E. Nielsen, T. Oja, and L. Timmen. 2019. "Postglacial Gravity Change in Fennoscandiathree Decades of Repeated Absolute Gravity Observations." *Geophysical Journal International* 217 (2). Oxford University Press (OUP): 1141–56. https://doi.org/10.1093/gji/ggz054.

Pacheco-Martı'nez, J., S. Wdowinski, E. Cabral-Cano, M. Hernández-Marı'n, J. A. Ortiz-Lozano, T. Oliver-Cabrera, D. Solano-Rojas, and E. Havazli. 2015. "Application of InSAR and Gravimetric Surveys for Developing Construction Codes in Zones of Land Subsidence Induced by Groundwater Extraction: Case Study of Aguascalientes, Mexico." *Proceedings of the International Association of Hydrological Sciences* 372 (November). Copernicus GmbH: 121–27. https://doi.org/10.5194/piahs-372-121-2015.

Pearson-Grant, S.C., P. Franz, and J. Clearwater. 2018. "Gravity Measurements as a Calibration Tool for Geothermal Reservoir Modelling." *Geothermics* 73 (May). Elsevier BV: 146–57. https://doi.org/10.1016/j.geothermics.2017.06.006.

Pechstein, A., S. Attinger, R. Krieg, and N. K. Copty. 2016. "Estimating Transmissivity from Single-Well Pumping Tests in Heterogeneous Aquifers." *Water Resources Research* 52 (1). American Geophysical Union (AGU): 495–510. https://doi.org/10.1002/2015wr017845.

Peters, A., K. Y. Chung, and S. Chu. 2001. "High-Precision Gravity Measurements Using Atom Interferometry." *Metrologia* 38 (1). IOP Publishing: 25–61. https://doi.org/10.1088/0026-1394/38/1/4.

Piccolroaz, S., B. Majone, F. Palmieri, G. Cassiani, and A. Bellin. 2015. "On the Use of Spatially Distributed, Time-Lapse Microgravity Surveys to Inform Hydrological Modeling." *Water Resources Research* 51 (9). American Geophysical Union (AGU): 7270–88. https://doi.org/10.1002/2015wr016994.

Pool, D. R. 2008. "The Utility of Gravity and Water-Level Monitoring at Alluvial Aquifer Wells in Southern Arizona." *GEOPHYSICS* 73 (6). Society of Exploration Geophysicists: WA49–WA59. https://doi.org/10.1190/1.2980395.

Reich, M., and A. Güntner. 2020. "A Concept of Hybrid Terrestrial Gravimetry and Cosmic Ray Neutron Sensing for Investigating Hydrological Extreme Events," March. Copernicus GmbH. https://doi.org/10.5194/egusphere-egu2020-13624.

Renard, P., and F. Bertone. n.d. *Rhytool: Hytool Library for R Users*. https://CRAN.R-project.org/package=rhytool.

Renard, P., D. Glenz, and M. Mejias. 2008. "Understanding Diagnostic Plots for Well-Test Interpretation." *Hydrogeology Journal* 17 (3). Springer Science; Business Media LLC: 589–600. https://doi.org/10.1007/s10040-008-0392-0.

RESIF. 2020. "Le Réseau Sismologique et Géodésique Français Résif." 3, rue Michel-Ange, 75794 Paris cedex 16 – France. https://www.resif.fr/en.

Reudink, R., R. Klees, O. Francis, J. Kusche, R. Schlesinger, A. Shabanloui, N. Sneeuw, and L. Timmen. 2014. "High Tilt Susceptibility of the Scintrex CG-5 Relative Gravimeters." *Journal of Geodesy* 88 (6). Springer Science; Business Media LLC: 617–22. https://doi.org/10.1007/s00190-014-0705-0.

Riccardi, U., S. Rosat, and J. Hinderer. 2011. "Comparison of the Micro-G LaCoste gPhone-054 Spring Gravimeter and the GWR-C026 Superconducting Gravimeter in Strasbourg (France) Using a 300-Day Time Series." *Metrologia* 48 (1). IOP Publishing: 28–39. https://doi.org/10.1088/0026-1394/48/1/003.

Rodell, M., P. R. Houser, U. Jambor, J. Gottschalck, K. Mitchell, C.-J. Meng, K. Arsenault, et al. 2004.

"The Global Land Data Assimilation System." *Bulletin of the American Meteorological Society* 85 (3). American Meteorological Society: 381–94. https://doi.org/10.1175/bams-85-3-381.

Rosat, S. 2005. "High-Resolution Analysis of the Gravest Seismic Normal Modes After the 2004 Mw= 9 Sumatra Earthquake Using Superconducting Gravimeter Data." *Geophysical Research Letters* 32 (13). American Geophysical Union (AGU). https://doi.org/10.1029/2005gl023128.

Santos, F. Pereira dos, and S. Bonvalot. 2016. "Cold-Atom Absolute Gravimetry." In *Encyclopedia of Geodesy*, 1–6. Springer International Publishing. https://doi.org/10.1007/978-3-319-02370-0_30-1.

Schäfer, F., P. Jousset, A. Güntner, K. Erbas, J. Hinderer, S. Rosat, C. Voigt, T. Schöne, and R. Warburton. 2020. "Performance of Three iGrav Superconducting Gravity Meters Before and After Transport to Remote Monitoring Sites." *Geophysical Journal International* 223 (2). Oxford University Press (OUP): 959–72. https://doi.org/10.1093/gji/ggaa359.

Schäfer, F., P. Jousset, T. Toledo, A. Güntner, T. Schöne, D. Naranjo, K. Erbas, E. Juliusson, and R. Warburton. 2020. "Integrated Microgravimetric and Seismic Monitoring Approach in the Þeistareykir Volcanic Geothermal Field (North Iceland)." March. Copernicus GmbH. https://doi.org/10.5194/egusphere-egu2020-11801.

Schmerge, D., and O. Francis. 2006. "Set Standard Deviation, Repeatability and Offset of Absolute Gravimeter A10-008." *Metrologia* 43 (5). IOP Publishing: 414–18. https://doi.org/10.1088/0026-1394/43/5/012.

Schmidt, R., F. Flechtner, U. Meyer, C. Reigber, F. Barthelmes, C. Förste, R. Stubenvoll, R. König, K.-H. Neumayer, and S. Zhu. 2006. "Static and Time-Variable Gravity from GRACE Mission Data." In *Observation of the Earth System from Space*, 115–29. Springer-Verlag. https://doi.org/10.1007/3-540-29522-4_9.

Scintrex, L. 2014. "CG-5 Scintrex Autograv Tm System Operation Manual." 222 Snidercroft Road, Concord, Ontario, Canada, L4K 2K1: Scintrex Limited. https://scintrexltd.com.

———. 2018. "CG-6 Scintrex Autograv Tm System Operation Manual." 222 Snidercroft Road, Concord, Ontario, Canada, L4K 2K1: Scintrex Limited. https://scintrexltd.com.

Singh, P. K., P. Dey, S. K. Jain, and P. Mujumdar. 2020. "Hydrology and Water Resources Management in Ancient India," May. Copernicus GmbH. https://doi.org/10.5194/hess-2020-213.

Stock, M. 2012. "Watt Balance Experiments for the Determination of the Planck Constant and the Redefinition of the Kilogram." *Metrologia* 50 (1). IOP Publishing: R1–R16. https://doi.org/10.1088/0026-1394/50/1/r1.

Sueur, J., T. Aubin, and C. Simonis. 2008. "Seewave: A Free Modular Tool for Sound Analysis and Synthesis." *Bioacoustics* 18: 213–26. http://www.tandfonline.com/doi/abs/10.1080/09524622.2008.9753600.

Sugihara, M., and T. Ishido. 2008. "Geothermal Reservoir Monitoring with a Combination of Absolute and Relative Gravimetry." *GEOPHYSICS* 73 (6). Society of Exploration Geophysicists: WA37–WA47. https://doi.org/10.1190/1.2991105.

Sugihara, M., Y. Nishi, H. Ikeda, K. Nawa, and T. Ishido. 2017. "Monitoring CO2 Injection at the Tomakomai Field Using High-Sensitivity Continuous Gravimetry." *Energy Procedia* 114 (July). Elsevier BV: 4020–7. https://doi.org/10.1016/j.egypro.2017.03.1542.

Tamura, Y., T. Sato, M. Ooe, and M. Ishiguro. 2007. "A Procedure for Tidal Analysis with a Bayesian Information Criterion." *Geophysical Journal International* 104 (3). Oxford University Press (OUP): 507–16. https://doi.org/10.1111/j.1365-246x.1991.tb05697.x.

Tapley, B. D. 2004. "GRACE Measurements of Mass Variability in the Earth System." *Science* 305 (5683). American Association for the Advancement of Science (AAAS): 503–5. https://doi.org/10.1126/science.1099192.

Telford, WM, L.P. Geldart, and R.E. Sheriff. 1990. *Applied Geophysics*. Cambridge University Press.

Theis, C. V. 1935. "The Relation Between the Lowering of the Piezometric Surface and the Rate and Duration of Discharge of a Well Using Ground-Water Storage." *Transactions, American Geophysical Union* 16 (2). American Geophysical Union (AGU): 519. https://doi.org/10.1029/tr016i002p00519.

Tinkham, M. 2004. *Introduction to Superconductivity*. Courier Corporation.

Trimeche, A., M. Langlois, S. Merlet, and F. Pereira Dos Santos. 2017. "Active Control of Laser Wavefronts in Atom Interferometers." *Physical Review Applied* 7 (3). American Physical Society (APS). https://doi.org/10.1103/physrevapplied.7.034016.

Tsai, J.-P., T.-C. J. Yeh, C.-C. Cheng, Y. Zha, L.-C. Chang, C. Hwang, Y.-L. Wang, and Y. Hao. 2017. "Fusion of Time-Lapse Gravity Survey and Hydraulic Tomography for Estimating Spatially Varying Hydraulic Conductivity and Specific Yield Fields." *Water Resources Research* 53 (10). American Geophysical Union (AGU): 8554–71. https://doi.org/10.1002/2017wr020459.

UN. 2020. *The United Nations World Water Development Report 2020*. UN. https://doi.org/10.18356/e2014dcb-en.

Van Camp, M., O. de Viron, G. Pajot-Métivier, A. Casenave F.and Watlet, A. Dassargues, and M. Vanclooster. 2016. "Direct Measurement of Evapotranspiration from a Forest Using a Superconducting Gravimeter." *Geophysical Research Letters* 43 (19). Wiley Online Library: 10–225. https://doi.org/10.1002/2016GL070534.

Vörösmarty, C. J., C. Léveque, C. Revenga, R. Bos, C. Caudill, J. Chilton, EM. Douglas, et al. 2005. "Fresh Water." *Millennium Ecosystem Assessment* 1. Island Press Washington: 165–207.

Wahr, J. M. 1985. "Deformation Induced by Polar Motion." *Journal of Geophysical Research* 90 (B11). American Geophysical Union (AGU): 9363. https://doi.org/10.1029/jb090ib11p09363.

Wang, R., F. Lorenzo-Martı'n, and F. Roth. 2006. "PSGRN/PSCMPa New Code for Calculating Co- and Post-Seismic Deformation, Geoid and Gravity Changes Based on the Viscoelastic-Gravitational Dislocation Theory." *Computers & Geosciences* 32 (4). Elsevier BV: 527–41. https://doi.org/10.1016/j.cageo.2005.08.006.

Warburton, R.J., H. Pillai, and R.C. Reineman. 2010. "Initial Results with the New Gwr iGrav Superconducting Gravity Meter." In *Extended Abstract Presented at 2nd Asia Workshop on Superconducting Gravimetry Taipei, Taiwan*.

Watlet, A., O. Kaufmann, A. Triantafyllou, A. Poulain, J. E. Chambers, P. I. Meldrum, P. B. Wilkinson, et al. 2018. "Imaging Groundwater Infiltration Dynamics in the Karst Vadose Zone with Long-Term ERT Monitoring." *Hydrology and Earth System Sciences* 22 (2). Copernicus GmbH: 1563–92. https://doi.org/10.5194/hess-22-1563-2018.

Wenzel, H.-G. 1996. "The Nanogal Software: Earth Tide Data Processing Package Eterna 3.30." *Bull. Inf. Marées Terrestres* 124: 9425–39.

Wilson, C. R., H. Wu, L. Longuevergne, B. Scanlon, and J. Sharp. 2011. "The Superconducting Gravimeter as a Field Instrument Applied to Hydrology." In *Geodesy for Planet Earth*, 291–95. Springer Berlin Heidelberg. https://doi.org/10.1007/978-3-642-20338-1_35.

Wolf, P., and P. Tourrenc. 1999. "Gravimetry Using Atom Interferometers: Some Systematic Effects." *Physics Letters A* 251 (4). Elsevier BV: 241–46. https://doi.org/10.1016/s0375-9601(98)00881-0.

Wziontek, H., H. Wilmes, P. Wolf, S. Werth, and A. Güntner. 2009. "Time Series of Superconducting Gravimeters and Water Storage Variations from the Global Hydrology Model WGHM." *Journal of Geodynamics* 48 (3-5). Elsevier BV: 166–71. https://doi.org/10.1016/j.jog.2009.09.036.

Yeh, H.-D., and Y.-C. Huang. 2009. "Analysis of Pumping Test Data for Determining Unconfined-Aquifer Parameters: Composite Analysis or Not?" *Hydrogeology Journal* 17 (5). Springer Science; Business Media LLC: 1133–47. https://doi.org/10.1007/s10040-008-0413-z.

Zha, Y., T.-C. J. Yeh, W. A. Illman, H. Onoe, C. M. W. Mok, J.-C. Wen, S.-Y. Huang, and W. Wang. 2017. "Incorporating Geologic Information into Hydraulic Tomography: A General Framework Based on Geostatistical Approach." *Water Resources Research* 53 (4). American Geophysical Union (AGU): 2850–76. https://doi.org/10.1002/2016wr019185.

Zhu, J., and T.-C. J. Yeh. 2005. "Characterization of Aquifer Heterogeneity Using Transient Hydraulic Tomography." *Water Resources Research* 41 (7). American Geophysical Union (AGU). https://doi.org/10.1029/2004wr003790.

Zreda, M., D. Desilets, T. P. A. Ferré, and R. L. Scott. 2008. "Measuring Soil Moisture Content Non-Invasively at Intermediate Spatial Scale Using Cosmic-Ray Neutrons." *Geophysical Research Letters* 35 (21). American Geophysical Union (AGU). https://doi.org/10.1029/2008gl035655.